Anatomy of detachment fault zones in a nearly amagmatic mid-ocean ridge setting : map to sample scale observations at the Southwest Indian Ridge, 64°40'E

Souradeep Mahato

Université Paris Cité

École doctorale [STEP'UP – ED N°560]

IPGP- Équipe de Géosciences marines

Anatomy of detachment fault zones in a nearly amagmatic mid-ocean ridge setting: map to sample scale observations at the Southwest Indian Ridge, 64°40'E

Par Souradeep MAHATO

présentée et soutenue publiquement le 4 décembre 2023

Thèse de doctorat de Sciences de la Terre et de l'environnement
dirigée par : Mathilde Cannat

Et par Isabelle MARTINEZ

Devant un jury composé de:

Daniel SAUTER,	DR CNRS Université de Strasbourg	Rapporteur
Barbara E. JOHN,	Prof. University of Wyoming	Rapportrice
Gianreto MANATSCHAL,	Prof. Université de Strasbourg	Examinateur
Javier ESCARTÍN,	DR CNRS École normale supérieure, Paris	Examinateur
Muriel ANDREANI,	DR Université Claude Bernard Lyon 1.	Examinatrice
Nathalie FEUILLET,	Phys. Université Paris Cité	Examinatrice
Mathilde CANNAT,	DR CNRS Université Paris Cité	Directrice de thèse
Isabelle MARTINEZ	Prof. Univ. Paris Cité	Invitée

Résumé

L'Est de la dorsale sud-ouest indienne (SWIR) est un end-member peu magmatique du système des dorsales médio-océaniques. Dans certaines zones presque amagmatiques de plus de 50 km de large, la divergence des plaques se fait le long de failles de détachement (Ocean Detachment Faults ; ODF), qui exhument des roches dérivées du manteau. Ces ODF ont une durée de vie de 1 à 2 millions d'années, puis une nouvelle ODF prend le relais avec une polarité opposée. On parle de « flip-flop detachment faulting ». Cette thèse utilise la bathymétrie, les observations de plongée ROV et des échantillons de roches pour étudier la géologie, la tectonique et les processus de déformation de ces ODF presque amagmatiques.

Le mur de la vallée axiale dans la zone d'étude (64°35'E SWIR) correspond au plancher d'un ODF actif jeune, D1. Le sommet de ce mur correspond au domaine dit de « breakaway » de D1. Il comprend des blocs glissés qui exposent une séquence de déformation d' ~100m d'épaisseur, avec des niveaux de gouges et de microbrèches de serpentinite intercalées avec des péridotites serpentinisées moins déformées. D'après sa géométrie, on attribue cette séquence à la zone de faille de l'ODF D2. Ceci renforce l'interprétation des ODFs D1 et D2 comme flip-flop.

Notre étude montre une variation significative des déformations liées à D1 le long de l'axe. A l'est de la zone d'étude, la zone de faille exhumée est lisse, à l'ouest elle présente des corrugations similaires à celles documentées dans des ODF plus magmatiques. La région corruguée présente également plusieurs crêtes de quelques centaines de mètres de large, orientées NNE, que nous interprétons comme des méga-corrugations formées en raison de l'existence de phacoïdes d'échelle comparable dans la zone d'endommagement du détachement. Le domaine corrugué a aussi un relief plus marqué et des petites failles normales antithétiques, absentes dans la région non corruguée. Les horizons de microbrèches/gouges sont plus épais et plus continus dans la région non corrugué et nos observations de terrain suggèrent que des fluides hydratés favorisent la formation de ces gouges dans la zone de faille. Tout cela suggère une faille et un plancher D1 plus résistants à la déformation dans la région corruguée. Les corrugations font un angle de 15-25° sur la direction d'expansion NS. La résistance variable de la faille et de son plancher le long de l'axe pourrait causer une rotation locale du champ de déformation.

Les microbrèches et gouges de D1 et D2 résultent de la fracturation cassante de péridotites déjà serpentinisées. Ces roches contiennent des microdomaines riches en clastes et des microdomaines foliés pauvres en clastes avec une matrice de chrysotile à grain fin dans laquelle nous avons observé des indices de dissolution et de précipitation

syntectoniques. Les données expérimentales indiquent que la résistance à la friction des gouges de chrysotile à des températures < 100°C est très faible, similaire à celle du talc, mais qu'elle augmente à des températures et des pressions plus élevées. Les processus de dissolution-précipitation favorisés par les fluides affaiblissent cependant probablement les gouges de chrysotile dans ces domaines plus profonds. En outre, l'épaisseur, l'étendue et la connectivité des horizons de gouge et de microbrèche jouent également un rôle crucial dans la détermination de la résistance de la faille.

Cette étude montre deux différences nettes entre les ODFs D1 et D2. et les ODFs corrugués plus magmatiques. Les horizons les plus déformés de D1 et D2 sont des gouges et des microbrèches à chrysotile, tandis que dans les ODF plus magmatiques, il s'agit de serpentinites cisaillées contenant du talc, de l'amphibole et/ou de la chlorite. Les ODFs presque amagmatiques D1 et D2 auraient aussi un domaine endommagé plus épais. Nous proposons que cette zone d'endommagement épaisse est héritée d'une déformation moins localisée dans la transition fragile/ductile de ces ODF presque amagmatiques.

Keywords: Dorsale médio-océanique (MOR), expansion océanique avec faible apport magmatique, faille de détachement amagmatique jeune et active, zone d'endommagement de faille, corrugations, failles antithétiques, gouge de faille de serpentine, localisation de la déformation, distribution granulométrique (PSD), déformation du mur de faille (footwall).

Abstract

The easternmost region of the Southwest Indian Ridge (SWIR) represents a melt-poor end-member of the global mid-ocean ridge system. It features >50 km wide, nearly amagmatic corridors, where seafloor spreading is accommodated mainly by large offset detachment faults (ODFs), leading to the exposure of mantle-derived rocks on the seafloor. These ODFs have a lifetime of 1-2 myr, then a new ODF takes over with an opposite polarity. This process is known as flip-flop detachment faulting. This thesis uses bathymetry, ROV dive observations, and rock samples to study nearly amagmatic ODF's geology, tectonics, and deformation processes.

The axial valley wall in the study area (64°35'E SWIR) corresponds to the footwall of a young active ODF, D1. It exposes variably deformed serpentinized peridotites with rare gabbro dikes. This south-facing wall's top comprises km-long scarps representing the degraded D1 breakaway. The outcrops along these scarps feature highly deformed serpentinite microbreccia and gouge-bearing horizons interlayered with less deformed serpentinized peridotites. These deformed lithologic packages are up to ~100m thick. Based on their geometry, they are related to D2 ODF zone, which strengthens the interpretation of nearly amagmatic ODFs as flip-flop, consistent with prior research.

Our study found significant along-strike variations in D1 footwall features. The eastern part of the study area is smooth, the western part displays corrugations similar to those documented in more magmatic, domal, and corrugated ODFs. The corrugated region in our study area also has several hecto-to-kilometers-wide NNE-trending ridges, interpreted as mega-corrugations that formed due to hecto-to-kilometer-scale phacoids between linked fault splays in the detachment damage zone. The corrugated domain also has a higher footwall, and minor-offset antithetic faults, absent in the non-corrugated region. Highly deformed microbreccia/gouge layers are thicker and more extensive in the non-corrugated region, and field observations suggest that hydrous fluids in the fault zone could enhance the formation of such gouges. Together, these observations suggest a more robust D1 fault and footwall in the corrugated region. Corrugations show a 15-25° clockwise orientation to the NS spreading direction. We propose this may be due to local rotations of the principal strain directions, caused by variable fault and footwall strength along the axis, possibly linked to hydrothermal fluid availability.

The deformation microtextures of serpentinite microbreccia and gouges from the D1 and D2 fault zones formed due to the brittle fracturing of already serpentinized peridotites. They contain clast-rich microdomains and clast-poor foliated microdomains with a fine-grained chrysotile matrix in which we observed evidence for syntectonic dissolution and precipitation processes. Experimental data indicates that the frictional strength of chrysotile gouge at temperatures < 100°C is very low, similar to that of talc, but increases at higher temperatures and pressures. However, fluid-enhanced dissolution-precipitation processes likely weaken the chrysotile gouge in these deeper domains. In addition, the thickness, extent, and connectivity of gouge and microbreccia horizons also play a crucial role in determining fault strength.

This study documents several differences between the studied eastern SWIR nearly amagmatic ODFs and more magmatic corrugated dome-shaped ODFs. The most deformed horizons in nearly amagmatic ODFs are chrysotile-bearing gouges and microbreccia, while at more magmatic ODFs they are talc, amphibole, and chlorite-bearing sheared serpentinites. Nearly amagmatic ODFs also appear to have a thicker damage domain with hector to kilometer-sized phacoids of less deformed serpentinized peridotite. We propose that this thick damage zone is a legacy of less localized deformation in the transition between brittle and ductile domains of these nearly amagmatic ODFs.

Keywords: Mid-oceanic ridge (MOR), Magma starved seafloor spreading, young and active amagmatic detachment fault, fault damage zone, corrugations, antithetic faults, serpentine fault gouge, strain localization, Particle size distribution (PSD), Footwall deformation

Acknowledgments

Whew, the calendar flipped to a new year, marking a new chapter, and that means finally wrapping up these thesis acknowledgments! Four years flew by like a jolt of espresso on an empty stomach, punctuated by countless meetings (some more caffeinated than others). Buckle up because I will attempt to thank everyone who helped navigate this research ship to shore.

Firstly, I would like to express my gratitude to the members of the jury who have agreed to evaluate my work, participate in the early morning defense from the other side of the Atlantic (UTC-7), and engage in the intense discussions that followed. I extend my thanks to Daniel Sauter, Barbara Jhon, Gianreto Manatschal, Javier Escartín, Muriel Andreani, and Nathalie Feuillet for their valuable time and effort and left me with insights permanently etched in my brain.

No thesis would be possible without a phenomenal thesis director, and mine was the absolute best. Mathilde Cannat, thank you for taking a chance on me, for patiently teaching me how to think and do the science (even when my ideas were as scattered as a toddler's toy box), and for always having my back, even when I needed a gentle reality check. I owe you more than words can express (and hopefully, many future publications!). Also, thank you for providing travel and conference opportunities and even letting me join the MOMARSAT 2021 campaign and an unforgettable Nautile dive. To Isabelle Martinez, co-director extraordinaire, a big thank you for opening the door to the fascinating world of stable isotopes (of course, COVID-19 made it difficult, but don’t worry, I’m on it)

To all my collaborators: Stephan Borensztajn, thanks for all the SEM sessions with the Mandalorian soundtrack. Nicolas Rividi and your microprobe-wielding colleague, thanks for the good vibes. Pascale Besson, your rock-pulverizing patience. Thanks to Sophie Nowak, Nelly Assayag, and Charles Le Losq for your aid and the 3rd-floor crew for the countless coffee-fueled laughter sessions.

Marie-Dominique Rocheron, thank you for coordinating all the travels and the paperwork jungle! Mihai and Yujin, you're my tech support – many thanks to you. And to the entire Marine Geosciences team, you guys rock.

Now, onto the amazing people who made this journey more than just science: my "Cannat siblings." Manon, my thesis-big-sis, thanks for always being a call away and for your eagle-eyed proofreading. Jie, the kung fu master and software guru, your humor and expertise were lifesavers. Benjamin, my translator, foodie, and travel advisor, you made Paris a breeze (and way more fun!). Finally, the youngsters Antoine

and Sampriti. Thanks, Antoine, for making numerical models more understanding in a geologist's eye, and Sampriti, I know thank you is not enough, but you never let me feel the 6000 km of distance.

Last but not least, to my incredible friends and colleagues, Nirmit and Soumya, congratulations on the doctorates! Thanks for being the best pandemic flatmate a person could ask for. Valentine and Pierre, cheers to surviving French bureaucracy together and all the laughter-filled moments. And to everyone I met on my seafaring adventures, especially Tom and Lise, merci for the memories.

This thesis may be done, but the adventure has just begun. Here's to new discoveries, more coffee (obviously!), and even more acknowledgments in future publications!

“চিত্ত যেথা ভয়শূন্য, উচ্চ যেথা শির,
জ্ঞান যেথা মুক্ত, যেথা গৃহের প্রাচীর
আপন প্রাঙ্গণতলে দিবসশর্বরী
বসুধারে রাখে নাই খণ্ড ক্ষুদ্র করি,”

“Where the mind is without fear and the head is held high;
Where knowledge is free;
Where the world has not been broken up into fragments by narrow domestic walls;
Where words come out from the depth of truth;”

- Rabindranath Tagore

Table of Contents

Introduction (English)

The global mid-ocean ridge (MOR) system is ~60,000 kilometers long, forming the Earth's most extensive mountain chain under every major ocean. The MOR system is created by the movement of tectonic plates that diverge at varying rates. The global MOR system is broken up into several major ridges, including the fast-spreading East-Pacific Rise (spreading rate up to 160 mm/yr.), the slow-spreading Mid-Atlantic ridge (MAR, average ~25 mm/yr.), and the ultra-slow (~14mm/yr.) spreading eastern Southwest Indian ridge (SWIR). In sections of slow and ultra-slow spreading ridges with reduced magma supply, plate divergence is partly accommodated by large-offset (between 5 and more than 25 km) normal faults. These faults are known as oceanic detachment faults (ODFs). Along these ODFs, mantle-derived rocks are exhumed to the seafloor, hydrothermally altered, and intruded by variable quantities of magma: this assemblage of variably altered mantle-derived rocks and magmatic intrusions represents a significant proportion (~25%) of the ocean crust created at slow and ultraslow spreading mid-ocean ridges. ODFs are, therefore, a key component of divergent plate tectonics, and understanding how these faults form and develop, the role they play in channeling hydrothermal fluids into the axial lithosphere, and their relations with magmatism are key questions to better understand the formation of new lithosphere at mid-ocean ridges.

ODFs can be categorized based on their morphology, their geophysical properties, and the nature of the rocks exposed in their footwall:

- Corrugated detachments showcase dome-like topographies with distinct undulations of the seafloor, also called corrugations. Corrugations are parallel to plate divergence directions and are believed to result from brittle strain localization on networks of anastomosing linked fractures. Active corrugated-dome-shaped detachments extend up to ~20-30 km along the ridge axis, exposing gabbro and serpentinized peridotite and

facing volcanic seafloor in the hanging wall side. The exposed fault surfaces in the ODFs footwall show brittle to semi-brittle deformation localized in talc±chlorite±amphibole+serpentine bearing assemblages with rare cataclasites. Local seismicity indicates that these ODFs root at the base of the brittle axial lithosphere at depths of ~10-15 km, with a high dipping angle (~60-70°). The ductile domain below is thought to be magma-rich.

- The easternmost region of the ultraslow-spreading SWIR (between 61°E and 67°E) and some regions of the Gakkel Ridge in the Arctic are end members of the global MOR system because of their low overall melt supply. In these regions, exposures of serpentinized peridotites, with very few magmatic rocks, are exposed on both diverging plates in nearly amagmatic spreading corridors between zones of higher volcanic activity. Gakkel Ridge is less studied and partly sedimented. Much of what is known of these nearly amagmatic ODFs comes from studies of the eastern SWIR, our study area. They form broad ridges extending ~25-95 km along the ridge axis. These ridges do not bear corrugations, at least as seen in shipboard bathymetry. They expose primarily serpentinized peridotite (with minor gabbros and basalts) on both flanks and are interpreted as the exhumed footwalls of successive ODFs with opposite polarity, commonly known as "flip-flop" ODFs. Microseismicity extends to depths of ~15 km, hinting at the minimum depth to the brittle-ductile transition. Unlike the microseismicity patterns seen in corrugated detachments, microearthquakes are not confined to the ODF footwall and fault zone but also occur in the hanging wall. ODFs formed in this nearly amagmatic context may be comparable to those documented in fossil Ocean Continental Transition settings (OCTs).

This thesis focuses on the presently active, south-facing, nearly amagmatic ODF (D1) at 64°35'E on the SWIR. It cuts through the footwall of an earlier ODF (D2) with opposite polarity. D1 is still in its early development stages. In December 2016-

January 2017, during the ROVSMOOTH cruise of RV Pourquoi Pas?, the D1 footwall and part of the D2 exposed fault surface were mapped (high-resolution bathymetry and magnetics) and explored and sampled with the ROV Victor 6000. This thesis work uses ROVSMOOTH high-resolution bathymetry, ROV dive observations, and a selection of the most deformed samples collected during the ROV dives in the D1 and D2 exposed fault zones, together with earlier shipboard bathymetry to address the following questions:

How does strain localize during mid-ocean ridge detachment faulting in an environment where serpentinized peridotites are the dominant rock type, and there is little to no magma or magmatic rocks? What can we learn about the anatomy of the fault zone at flip-flop ODFs? And what can we infer about the overall strength of their fault zone and footwall?

According to numerical models, it becomes difficult to form ODFs when the brittle axial lithosphere thickens to more than 10 km. In the case of our SWIR study area, the brittle axial lithosphere is at least 15 km thick, based on microseismicity. For detachment faults to form in such conditions, numerical models introduce a reduction of the rocks' friction coefficient above a critical amount of strain. The study of actual ODF fault rocks is essential to constrain these models. Such studies have, to this date, mostly concerned ODFs that formed in contexts of low to moderate magmatism at both the MAR and SWIR.

In these magmatically active settings, ODF fault zones typically contain semi-brittle shear zones with deformed and recrystallized hydrous minerals such as amphibole, chlorite, serpentine, and/or talc. With the exception of serpentine, these minerals mostly result from the hydrothermal alteration of peridotites containing veins of gabbroic rocks or from the hydrothermal alteration of peridotites by Al, Si, and Fe-enriched hydrothermal fluids produced by prior alteration of gabbroic rocks. The presence of a substantial amount of magmatic rocks, therefore, appears key to achieve strain localization in the fault zone of these ODFs. By contrast, at the nearly amagmatic eastern SWIR ODFs, dredge samples collected before the ROVSMOOTH cruise show that the proportion of serpentinized peridotite samples that contain veins of gabbroic

material is low in exposed fault zones and that the role of their hydrous alteration products to localize deformation is minimal. Previous studies based on these dredged samples have addressed strain localization in the deep lithosphere at and below the brittle-ductile transition (BDT). This thesis presents the first map to outcrop to sample-scale description of fault and strain localization structures that formed in the upper brittle and hydrothermally altered domains of nearly amagmatic SWIR ODFs.

The first chapter of the thesis is a bibliographic review of the concepts needed to understand the work. It is divided into four parts. The first part covers a general description of slow and ultraslow mid-oceanic ridges. The second part presents the geologic setting of oceanic detachment faults and their morphology and internal structures. The third part introduces observations on strain localization at oceanic detachment faults. The fourth part describes the geological and geophysical context of the eastern part of the Southwest Indian Ridge (62-65°E), specifically the 64°35’E region.

The second chapter of the thesis is a combined map to outcrop scale study on the geology and deformation of the D1 and D2 ODFs. It is written as an article in preparation entitled: *Footwall geology and deformation at a magma-starved young axial detachment fault: 64°35'E Southwest Indian Ridge (SWIR)*. This manuscript is intended to be submitted to *Geochemistry, Geophysics, Geosystems*. It focuses on the anatomy of the exposed D1 and D2 detachment fault zones and the thickness of their overall damage zone, the geometry of linked fractures, the distribution and extent of cataclastic deformation, the role of fluid in strain localization, and the origin of recent small offset antithetic normal faults, and of corrugations that are locally seen in the high-resolution bathymetry.

The third chapter of the thesis is a microstructural study of the most highly deformed fault zone samples collected during the ROV dives. It is written as an article in preparation entitled: *Strain localization in the brittle domain during detachment faulting in a nearly amagmatic ultraslow spreading context: 64°35'E Southwest Indian Ridge*. This manuscript is intended to be submitted to *Geochemistry, Geophysics, Geosystems, or to Lithos*. The studied samples are cataclastic

microbreccia and serpentine gouges. The chapter describes their microstructures, including clast size distribution, analyzes the major element composition of the clasts and matrix, and uses RAMAN spectra to discriminate between serpentine species. It discusses the possible consequences of these results in terms of the effective strength of the fault rocks in the brittle region of nearly amagmatic ODFs.

The last part of the thesis is a general discussion, main conclusions, and future perspectives based on results from chapters two and three.

The appendix contains supplementary figures and tables for chapters two and three.

This thesis was fully funded by the ANR project Ridge-Factory-Slow (ANR-18-CE010002-01). The work started in the fall of 2019 with a different scope, focusing on the geological context, mineralogy, and geochemistry of the carbonated ultramafic rocks documented and sampled during the ROVSMOOTH cruise, particularly next to the Old City hydrothermal field, a serpentinization-fueled vent field discovered during the cruise. The initial title of the thesis was "*Fluid-rock interactions in the context of mantle exhumation at slow-spreading ridges: 64°E SWIR"*. However, after a few months of preparatory work (bibliography, getting a grasp of the available data), the COVID-19 crisis started. We could not as planned, go to the sample storage facility in the early spring and had to wait till the next fall. Then, the stable isotopes lab at IPGP was closed for several more months. This thesis was therefore re-oriented to focus on ODF strain localization at map to sample scale. Sample preparation, then analytical work on carbonated samples, was nonetheless performed in the 3rd and 4th year of this thesis. A paper (not included in this thesis) is in the early writing stages.

Introduction (Français)

Le système mondial des dorsales médio-océaniques s'étend sur environ 60 000 kilomètres, formant la chaîne de montagnes la plus étendue de la Terre sous tous les grands océans. Ce système résulte du mouvement des plaques tectoniques, qui divergent à des vitesses variables. Le système mondial des dorsales comprend plusieurs dorsales majeures, notamment la dorsale Est-Pacifique, à taux d'expansion rapide aux d'expansion rapide (jusqu'à 160 mm/an), la dorsale médio-atlantique (MAR), à taux d'expansion lent (en moyenne ~25 mm/an) et la dorsale Sud-Ouest Indienne (SWIR), à taux d'expansion ultra-lent (~14 mm/an). Dans les régions des dorsales d'étalement lentes et ultra-lentes où l'approvisionnement en magma est réduit, la divergence des plaques est partiellement assurée par des failles normales à grand rejet (de 5 à plus de 25 km). Ces failles sont connues sous le nom de failles de détachement océanique. Le long de ces détachements, des roches dérivées du manteau sont exhumées sur le plancher océanique, altérées par l'hydrothermalisme et intrudées par des quantités variables de magma: cet assemblage de roches dérivées du manteau altérées de façon variable et d'intrusions magmatiques représente une proportion significative (~25%) de la croûte océanique créée au niveau des dorsales lentes et ultralentes. Les détachements sont donc un élément clé de la tectonique divergente des plaques. La compréhension de la formation et du développement de ces failles, du rôle qu'elles jouent dans l'acheminement des fluides hydrothermaux dans la lithosphère axiale et de leurs relations avec le magmatisme sont des questions essentielles pour mieux comprendre la formation de nouvelle lithosphère au niveau des dorsales médio-océaniques.

Les détachements océaniques peuvent être classées en fonction de leur morphologie, de leurs propriétés géophysiques et de la nature des roches exposées dans leur mur (footwall) :

- Les détachements dits corrugués présentent des topographies en forme de dôme avec des ondulations distinctes du plancher océanique, également

appelées corrugations. Les corrugations sont parallèles aux directions de divergence des plaques et résulteraient de la localisation des déformations fragiles sur des réseaux de fractures anastomosées. Les détachements corrugués s'étendent jusqu'à ~20-30 km le long de l'axe de la dorsale, exposant des gabbros et des péridotites serpentinisées et faisant face à un plancher océanique volcanique du côté de leur mur (hanging wall). Les surfaces de faille exposées dans le plancher de ces détachements présentent une déformation cassante à semi-cassante localisée dans des assemblages de talc±chlorite±amphibole+serpentine, avec de rares cataclasites. La sismicité locale indique que ces détachements s'enracinent à la base de la lithosphère axiale fragile à des profondeurs de ~10-15 km, avec un pendage fort (~60-70°). On pense que le domaine ductile sous-jacent est riche en magma.

- La région la plus orientale de la SWIR (entre 61°E et 67°E) et certaines régions de la dorsale de Gakkel dans l'Arctique sont des end-members du système mondial des dorsales pour leur faible budget magmatique. Dans ces régions, il existe des couloirs d'expansion océanique presque amagmatique, situés entre des zones d'activité magmatique plus soutenue. Dans ces couloirs, des péridotites serpentinisées, avec très peu de roches magmatiques, affleurent sur les deux plaques divergentes. La dorsale de Gakkel est moins étudiée et partiellement sédimentée. Ce que l'on sait de ces détachements presque amagmatiques provient donc d'études sur la SWIR, dans notre zone d'étude. Dans la topographie, ils se traduisent par des buttes allongées sur ~25 à 95 km le long de l'axe de la dorsale. Ces buttes ne présentent pas de corrugations, du moins pas dans la bathymétrie acquise depuis les navires. Elles mettent à l'affleurement des péridotites serpentinisées (avec très peu de gabbros et de basaltes) sur leurs deux flancs. Elles sont interprétées comme formées par les planchers exhumés de détachements successifs de polarité opposée, communément appelés détachements "flip-flop". A l'axe, des séismes sont détectés

jusqu'à ~15 km de profondeur, ce qui indique la profondeur minimale de la transition fragile-ductile. Contrairement à la microsismicité relevée près des détachements corrugués, ces microséismes ne sont pas limités à à la zone de faille du détachement actif et à son plancher, mais se produisent également son mur. Les détachements formés dans ce contexte presque amagmatique sont de potentiels analogues pour ceux documentés dans les contextes fossiles de transition océan-continent (OCT).

Cette thèse concerne le détachement actif (D1), à pendage sud du couloir presque amagmatique de 64°35'E sur la SWIR. Ce détachement recoupe le plancher d'un détachement antérieur (D2) de polarité opposée. D1 en est encore à ses premiers stades de développement. En décembre 2016-janvier 2017, lors de la campagne ROVSMOOTH du RV Pourquoi Pas ?, le plancher exposé de D1 et une partie de la surface de la faille exposée de D2 ont été cartographiés (bathymétrie et magnétisme à haute résolution) et explorés et échantillonnées à l'aide du ROV Victor 6000. Ce travail de thèse utilise la bathymétrie de haute résolution acquise pendant ROVSMOOTH, les observations des plongées ROV et une sélection des échantillons les plus déformés collectés lors de ces plongées dans les zones de faille exposées D1 et D2 pour aborder les questions suivantes :

Comment la déformation se localise-t-elle lors de la formation de failles de détachement océaniques dans un environnement où les péridotites serpentinisées sont le type de roche dominant, et où il y a peu ou pas de magma ou de roches magmatiques ? Que pouvons-nous apprendre sur l'anatomie de la zone de faille de ces détachements ? Et que pouvons-nous en déduire quant à la résistance (strength) de ces failles et de leur plancher ?

D'après les modèles numériques, il devient difficile de former des détachements lorsque la lithosphère axiale fragile fait plus de 10 km. Dans le cas de notre zone d'étude sur la SWIR, la lithosphère axiale fragile a une épaisseur d'au moins 15 km, d'après la microsismicité. Pour que des failles de détachement se forment dans de telles conditions, les modèles numériques introduisent une réduction du coefficient de friction des roches au-delà d'une quantité critique de déformation. L'étude des roches

de failles des détachement est essentielle pour contraindre ces modèles. Jusqu'à présent, cette étude a surtout porté sur des détachements corrugués formés dans des contextes de magmatisme faible à modéré dans plusieurs régions de la MAR et de la SWIR.

Dans ces environnements magmatiques actifs, les zones de failles de détachement contiennent généralement des zones de cisaillement semi-fragiles avec des minéraux hydratés déformés et recristallisés tels que l'amphibole, la chlorite, la serpentine et/ou le talc. À l'exception de la serpentine, ces minéraux résultent principalement de l'altération hydrothermale de péridotites contenant des veines de roches gabbroïques ou de l'altération hydrothermale de péridotites par des fluides hydrothermaux enrichis en Al, Si et Fe lors de l'altération antérieure de roches gabbroïques. La présence d'une quantité substantielle de roches magmatiques semble donc essentielle pour localiser les déformations dans la zone de faille de ces détachements. En revanche, dans les détachements presque amagmatiques de la SWIR, les échantillons de dragage effectués avant la campagne ROVSMOOTH ont montré que la proportion des péridotites serpentinisées contenant des veines de matériau gabbroïque est faible et que le rôle de leurs produits d'altération hydrothermale dans la localisation de la déformation est minime. Des études antérieures basées sur ces échantillons dragués ont abordé la localisation de la déformation dans la lithosphère axiale profonde au niveau et en dessous de la transition fragile-ductile (BDT). Cette thèse présente la première description, aux échelles de la carte, de l'affleurement et de l'échantillon, des structures de localisation et des déformations dans les domaines fragiles et hydrothermalisés plus superficiels de détachements presque amagmatiques.

Le premier chapitre de la thèse est une revue bibliographique des concepts nécessaires à la compréhension du travail. Il est divisé en quatre parties. La première partie traite d'une description générale des dorsales médio-océaniques lentes et ultra-lentes. La deuxième partie présente le contexte géologique des failles de détachement océaniques ainsi que leur morphologie et leurs structures internes. La troisième partie introduit des observations sur la localisation de la déformation aux failles de détachement océaniques. La quatrième partie décrit le contexte géologique et géophysique de la

partie orientale de la Dorsale Sud-Ouest Indienne (62-65°E), spécifiquement la région 64°35'E

Le deuxième chapitre de la thèse est une étude combinée, à l'échelle de la carte et de l'affleurement, de la géologie et de la déformation des détachements D1 et D2. Il est rédigé sous la forme d'un article en préparation intitulé *Footwall geology and deformation at a magma-starved young axial detachment fault: 64°35'E Southwest Indian Ridge (SWIR).* Ce manuscrit est destiné à être soumis à Geochemistry, Geophysics, Geosystems. Il concerne l'anatomie des zones de faille de détachement D1 et D2, l'épaisseur de leur zone d'endommagement, la géométrie des fractures et des surfaces de failles, la distribution et l'étendue de la déformation cataclastique, le rôle des fluides dans la localisation des déformations. Il aborde également l'origine de failles normales à faible rejeu antithétiques au détachement D1, et de corrugations sont localement visibles dans la bathymétrie à haute résolution.

Le troisième chapitre de la thèse est une étude microstructurale des échantillons les plus déformés de la zone de faille collectés pendant les plongées ROV. Il s'agit d'un article en préparation intitulé : *Strain localization in the brittle domain during detachment faulting in a nearly amagmatic ultraslow spreading context: 64°35'E Southwest Indian Ridge.* Ce manuscrit est destiné à être soumis à Geochemistry, Geophysics, Geosystems, ou à Lithos. Les échantillons étudiés sont des microbrèches cataclastiques et des gouges de serpentine. Le chapitre décrit leurs microstructures, y compris la distribution de la taille des clastes, analyse la composition en éléments majeurs des clastes et de la matrice, et utilise les spectres RAMAN pour discriminer les espèces de serpentine. Il discute des conséquences possibles de ces résultats en termes de résistance effective des roches de faille dans le domaine fragile des détachements presque amagmatiques.

La dernière partie de la thèse est une discussion générale, suivie des principales conclusions et des perspectives d'avenir, basées sur les résultats des chapitres deux et trois.

L'annexe contient des figures et des tableaux supplémentaires pour les chapitres deux et trois.

Cette thèse a été entièrement financée par le projet ANR Ridge-Factory-Slow (ANR-18-CE010002-01). Le travail a débuté à l'automne 2019, avec un objectif différent, qui concernait le contexte géologique, la minéralogie et la géochimie des roches ultramafiques carbonatées documentées et échantillonnées lors de la campagne ROVSMOOTH, en particulier à côté du champ hydrothermal Old City (un champ alimenté par la serpentinisation, découvert lors de la campagne). Le titre initial de la thèse était *"Fluid-rock interactions in the context of mantle exhumation at slow-spreading ridges: 64°E SWIR"*. Cependant, après quelques mois de travail préparatoire (bibliographie, reconnaissance des données disponibles), la crise COVID-19 a commencé. Nous n'avons pas pu, comme prévu, nous rendre au centre de stockage des échantillons au début du printemps et avons dû attendre l'automne suivant. Ensuite, le laboratoire d'isotopes stables de l'IPGP a été fermé pendant plusieurs mois. Cette thèse a donc été réorientée pour se concentrer sur la localisation des déformations associées aux détachements, de l'échelle de la carte à l'échelle de l'échantillon. La préparation des échantillons carbonatés, puis le travail analytique sur ces échantillons, ont néanmoins été réalisés au cours des 3ème et 4ème années de cette thèse. Un article (non inclus dans cette thèse) est en cours de rédaction.

Chapter 1

1.1 Fast, intermediate, slow, and ultraslow mid-ocean ridges

Mid-ocean ridges (MORs) are the longest underwater mountain chains on Earth, stretching over 60,000 kilometers (Heezen, 1960; Bird, 2003). They form where tectonic plates move apart, causing volcanic activity, faulting, and hydrothermal vents. These regions have relatively shallow seafloors, high heat flow, and seismic activity less than 20 kilometers deep. MORs are classified by how fast they spread (MacDonald et al., 1982; Small and Sandwell, 1992):

- Fast-spreading ridges, like the East Pacific Rise, spread at rates exceeding 80 mm/year.
- Intermediate-spreading ridges, like the Juan de Fuca Ridge, spread at 40-80 mm/year.
- Slow-spreading ridges (for example, the Mid-Atlantic Ridge; MAR) spread at less than 40 mm/year. Among slow ridges, ultra-slow spreading ridges, like the Southwest Indian Ridge (SWIR), spread at less than 20 mm/year (Dick et al., 2003). Slow and ultraslow ridges represent about 50% of the total length of the present-day MOR system (Bird, 2003).

The topography of MORs varies with their spreading rate. Fast-spreading ridges have axial highs (Figure 1.1a) that rise up to 400 meters. In contrast, slow-spreading ridges have axial valleys that can be 1-4 kilometers deep and 10-30 kilometers wide (Figure 1.1b-c), flanked by normal faults that indicate a strong contribution of tectonics to plate divergence (Tapponnier and Francheteau, 1978; Phipps Morgan et al., 1987; Buck et al., 2005). Another key difference between fast and slow-ultraslow ridges is that in addition to large transform faults, slow and ultraslow ridges are segmented (Lin et al., 1990; Detrick et al., 1994; Gente et al., 1995) at scales of 30 to 100 km (Sandwell et al., 2001). Segments may be offset from one another by a few tens of km, but

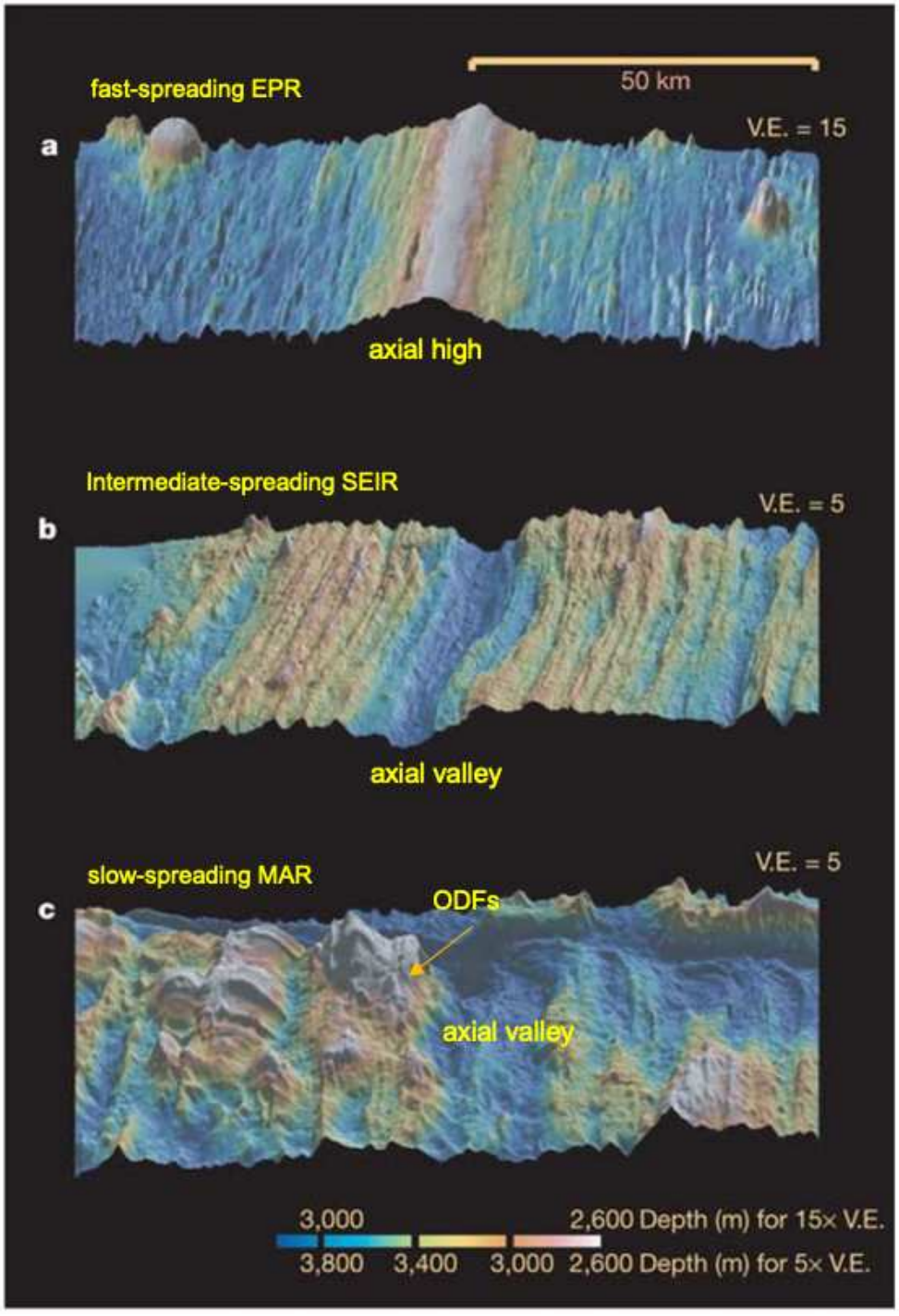

Figure 1-1 Mid-ocean ridge (MOR) morphology variation with spreading rate, adapted from Buck et al. (2005). Each image shows 40 km along the ridge axis and 110 km across the axis. At fast-spreading ridges, such as the East Pacific Rise (EPR), the axial morphology is characterized by axial high and small amplitude abyssal hills parallel to the spreading axis. At slower-spreading ridges (MAR), the axial morphology becomes more complex, with a negative axial relief and the development of corrugated surfaces in the axial valley walls. These corrugated surfaces represent the exhumed footwalls of detachment faults.

their definition is primarily based on changes in the along-axis topography: the axial valley at segment centers is shallower; the axial valley at segment ends is deeper and commonly broader.

The average thickness of the oceanic crust, determined by seismic methods, is, in most cases, a useful proxy to estimate the flux of melt at MORs (Chen, 1992; Christensen et al., 2002; White et al., 1992). While it can reach 30 km at hot spot-dominated ridges such as Iceland, it is remarkably even at most other ridge regions, at 6-7 km. At slow and ultraslow ridges, however, seismic and gravity-derived crustal thicknesses are highly variable at the scale of individual ridge segments (Tolstoy et al., 1993; Lin et al., 1990). The crust is thicker (typically 7-8 km-thick) at segment centers and thinner (typically 3-5 km-thick) at segment ends (Hooft et al., 2000). The geology at the seafloor is also distinct: basalts crop out at segment centers, while variably serpentinized, mantle-derived peridotites and gabbros are exposed at segment ends (Figure 1.2: Cannat et al., 1995; Dick, 1989). Outcrops of mantle-derived and gabbroic rocks display evidence of both ductile and brittle deformation and are most commonly faulted into one of the axial valley walls, the other exposing basalts (Karson and Dick, 1983; Cannat, 1993). Improved mapping techniques in the late 1990s and early 2000s have led to a breakthrough in understanding these exhumation tectonics with the discovery of corrugated and dome-shaped fault surfaces associated with these ultramafic and gabbroic outcrops (Cann et al., 1997; Smith et al., 2005). These large offset fault surfaces are known as Oceanic Core Complexes (OCCs; Cann et al., 1997; Tucholke et al., 1998) because of their similarities to continental core complexes also exhumed by detachment fault tectonics (John, 1987). OCCs form as the exhumed footwalls of large offset normal faults called Oceanic Detachment Faults (ODFs). In areas such as the northern Mid-Atlantic Ridge, segment end-type areas dominated by ODFs account for ~50% of the ridge length (Escartín et al., 2008), forming ~25% of the newly accreted seafloor (Cannat et al., 1995). At ultraslow ridges such as the SWIR and Gakkel ridge in the Arctic, some regions display anomalously low average crustal thickness, with isolated volcanic centers separated by long (up to 100 km) ridge domains of nearly amagmatic accretion (Dick et al., 2003; Standish et al., 2008;

Cannat et al., 2006; Sauter et al., 2013; Michael et al., 2003). These nearly amagmatic domains expose serpentinized peridotites with little gabbros and basalts over large portions of the ridge and commonly on both plates. Accretion there is almost fully accommodated by ODFs.

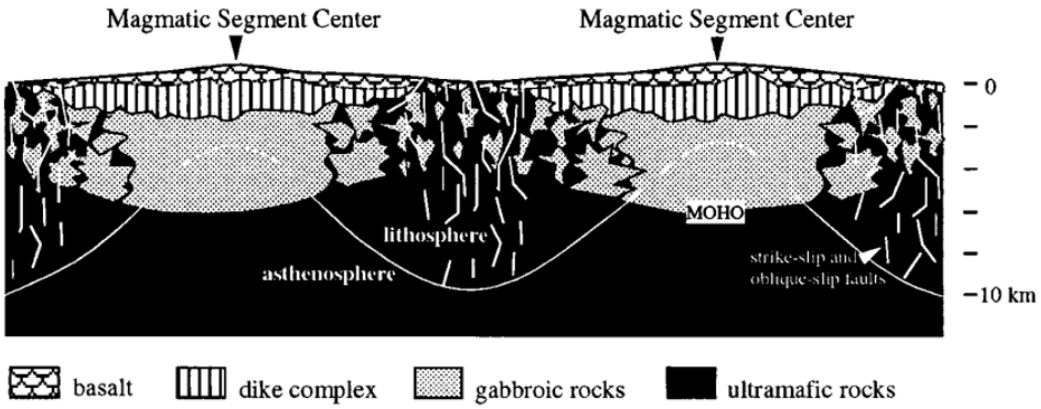

Figure 1-2: Along-axis conceptual section of two segments of the slow-spreading Mid-Atlantic Ridge in the 22°N region (Cannat et al., 1995). These segments have a thicker geophysically defined crust at the center, which is hypothesized to be fully magmatic and lay layered. At segment ends, mantle-derived peridotites intruded by gabbros are exposed on at least one of the axial valley walls. The base of the lithosphere (marked by the white line) is sketched here as thicker beneath the segment ends than beneath the more magmatic segment centers.

1.2 Geologic setting of oceanic detachment faults, their morphology, and internal structure:

Oceanic detachment faults (ODFs) play a significant role in plate divergence in sections of slow-spreading ridges with limited magma supply, which are common towards the end of ridge segments (Buck et al., 2005; Cann et al., 1997; Escartín et al., 2008; Escartín & Cannat, 1999; Sauter et al., 2013; Smith et al., 2008). Studies at the mid-Atlantic ridge (MAR) have revealed that these normal faults have offsets of 5 to 35 km and can persist up to 2.6 million years (Tucholke et al., 1998). The majority of the exposed fault surfaces in the footwall of these ODFs have a gentle slope of less than

20° and exhibit a dome-like topography. These surfaces frequently feature corrugations parallel to the spreading direction (Cann et al., 1997; Tucholke et al., 1998), mirroring patterns seen in continental detachment faults (John, 1987). However, a key distinction exists: continental detachment faults are interpreted as rooting into ductile crustal regions at a shallow angle (Figure 1.3b), while ODFs and their ductile roots, as plate boundaries, dissect the axial lithosphere (Figure 1.3a). Oceanic detachment faults expose gabbro and variably serpentinized peridotites. They initiate at high angles, and in their shallower regions, they acquire gentler slopes over time (John and Cheadle, 2010). This contrasts with continental detachments, which predominantly feature quartz and feldspar-rich lithologies. In the following sections, we discuss the geological context of ODFs, their morphology, internal configurations, the origin of the corrugation patterns, and the variations of these characteristics depending on the magma supply. We also provide some context on another type of trans-lithospheric detachment fault that forms at magma-poor ocean continental transitional (OCT) settings.

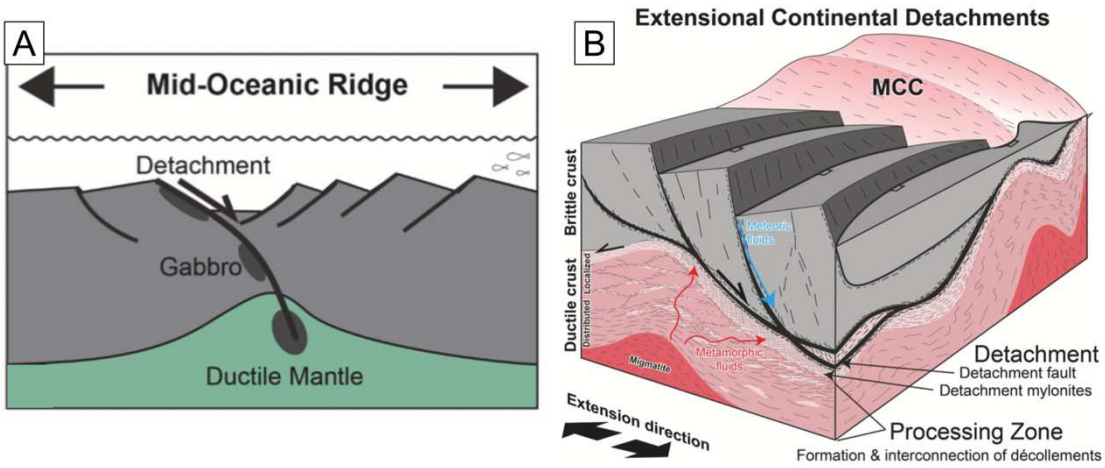

Figure 1-3: The sketch illustrates key differences between oceanic detachments (a) and continental detachment faults (b). (a) adapted from Whitney et al. (2013), shows the steep dipping deeper portion of the ODFs dissects the entire lithosphere, whereas the continental detachment faults roots at a shallow angle along the top of the ductile crust (b), adapted from Wiest et al., 2019

1.2.1. Geologic settings of ODFs:

Plate separation at mid-ocean ridges is a balance between magmatism and tectonic displacements. Detachment faults form at mid-ocean ridges where magmatism is reduced. This reduction in magmatism is commonly observed near the ends of slow spreading ridge segments (Lin et al., 1990; Tolstoy et al., 1993; Hooft et al., 2000). ODFs expose lower crustal and upper mantle lithologies on the seafloor, typically within the inside corner regions of first- and second-order ridge discontinuities (Figure 1.4; Tucholke & Lin, 1994; Cann et al., 1997; Karson, 1998; Tucholke et al., 1998; Karson, 1999; Cheadle & Grimes, 2010). Studies have shown that ODFs can also form in outside corner settings and far from transform offsets as long as melt delivery is reduced (Escartín & Cannat, 1999; Okino et al., 2004; Smith et al., 2006; Escartín et al., 2008). At the Southwest Indian Ridge (SWIR) between 61°E and 66°E, nearly 40% of the seafloor on both the African and the Antarctic plates appears to have been formed at ODFs (Cannat et al., 2006).

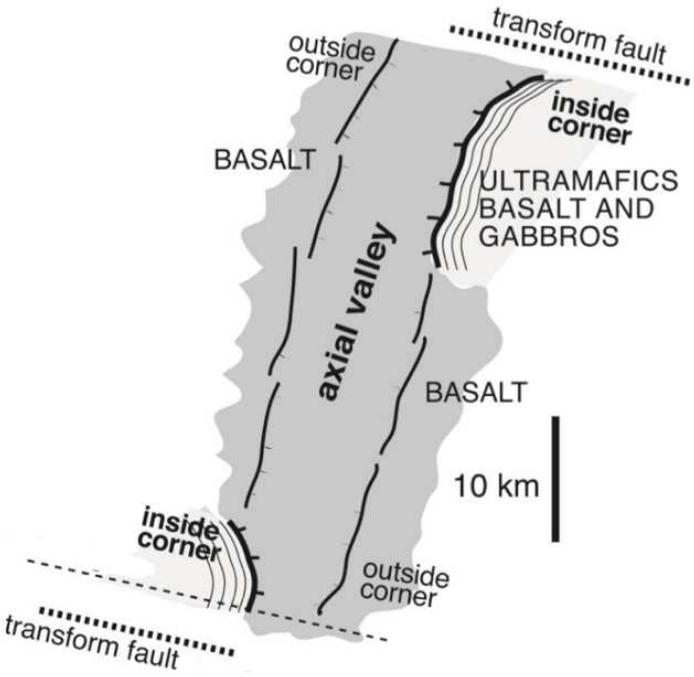

Figure 1-4: Based on Cannat et al. (2010), an interpretative diagram depicts the MAR ridge segment structure. Basalts and dolerites are visible at the surface of the axial valley and outer corners. In contrast, the inner corners showcase ultramafic rocks, specifically peridotites and gabbroic intrusions. The segment is defined by an axial valley surrounded by transform discontinuities.

Buck et al. (2005) proposed the *M* factor to measure how melt supply influences the tectonic activity of MORs. This factor quantifies the portion of plate separation attributed to magma emplacement, with the balance attributed to tectonic extension (faulting). Numerical modeling shows that when melt contributes 95% to plate separation, a symmetrical faulting pattern emerges, which then moves away from the ridge axis (Figure 1.5a). As the melt contribution decreases to 50%, on-axis faults with large offsets (>15 km) in one plate become prominent (Figure 1.5b). Over time, as a long-offset fault moves away from the axis into a thicker lithosphere, it becomes increasingly difficult for slip to occur, prompting a new on-axis fault to form, rendering the older fault inactive. When the melt contribution drops below 50%, the fault system is predicted to drift across-axis into the hanging wall (Tucholke et al., 2008). According to these models, a critical transition occurs when melt accounts for 30-50% of plate divergence, during which persistent, long-lasting detachment faults emerge (Tucholke et al., 2008).

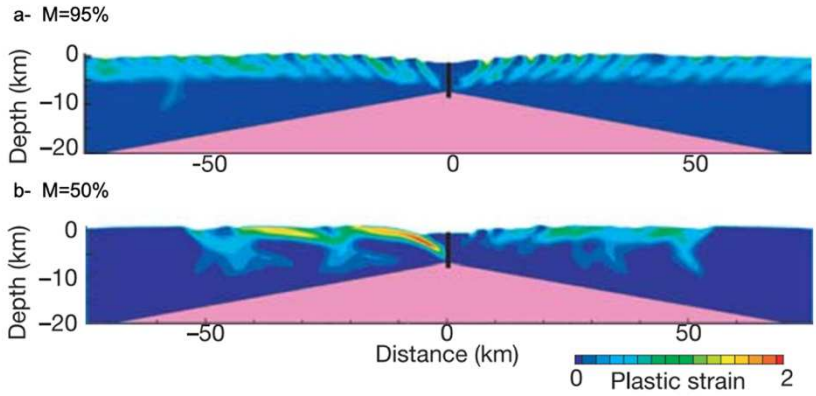

Figure 1-5: The adapted model of Buck et al. (2005) of fault behavior during plate spreading: (a) Dike-only spreading: Strains are localized, forming symmetric short-offset normal faults that migrate off-axis. (b) Asymmetric spreading (50% diking, 50% tectonics): Long-offset normal faults develop on one plate. Faults can become abandoned, and new faults develop as plates spread.

It is worth noting, however, that these models assume a 6 km-thick brittle lithosphere on the axis, the same thickness as the global average oceanic crust. In natural slow-ultraslow settings where ODFs form, the seismic crust is less than 6 km thick (Tolstoy et al., 1993; Hooft et al. 2000), while microseismicity data suggests that the brittle lithosphere is ~8-12 km thick at the MAR (de Martin et al., 2007; Parnell-

Turner et al., 2018), and 15-20 km-thick at the Southwest Indian Ridge (SWIR; Yu et al., 2018; Schlindwein & Schmid, 2016; Grevemeyer et al., 2019; Chen et al., 2023). With a brittle layer that is up to 3 times thicker than the layer potentially formed by magmatic dikes, the M ratio is still a useful concept, but the correspondence between a given M value and the characteristics of axial tectonics is likely more complicated (see discussions in Cannat et al., 2019; Olive et al., 2020).

1.2.2. Morphology of ODFs

The exposed footwalls of ODFs are characterized by a topographically high and an undulating smooth surface compared to the surrounding seafloor (Cann et al., 1997). In the Mid-Atlantic Ridge (MAR), these detachment faults extend up to ~20-30 km along the ridge axis, and the observed fault surfaces extend up to ~35 km across the ridge axis (Tucholke et al., 1998). In one case, an horizontal offset of about a hundred km has been documented (Godzilla Mullion, Ohara, et al., 2001; 2003).

ODFs are typically characterized by two distinct features. Firstly, a linear, outward-tilting breakaway ridge can be observed on the older side that lies away from the ridge axis. This corresponds to the detachment initiation area where it has cut the ocean floor (Figure 1.6a-b). Secondly, on the younger side facing towards the ridge axis, there is a boundary that can either be a high-angle fault scarp or a low dipping emergence. This boundary marks the location where the most recent material has been exhumed to the seafloor (Figure 1.6a-b: Smith et al., 2006; Escartín et al., 2017). Active detachment faults typically have an emergence angle of less than 35° and sometimes less than 10° (Cann et al., 1997; Smith et al., 2006). The vicinity of detachment faults and their exhumed footwall often shows a variety of debris flow morphologies and complex mass-wasting structures (Cann et al., 1997; Smith et al., 2006; Cannat et al., 2013; Escartín et al., 2017; 2022). The hanging wall side of active scooped-shaped and corrugated detachment faults always faces volcanic seafloor

(Figure 1.6a-b), such as at the 13°20’ and 13°30’N ODFs and the TAG Hydrothermal Field at 16°36’N on the MAR.

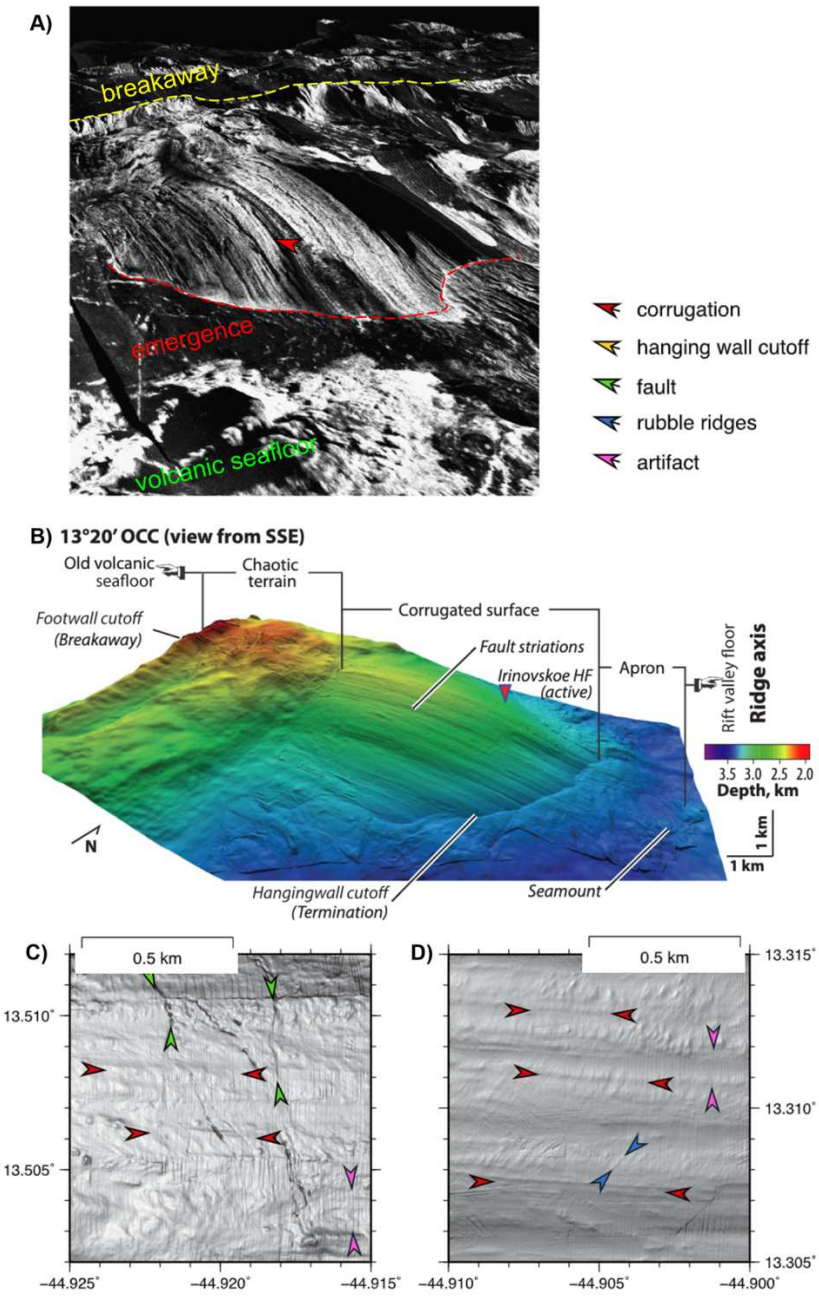

Figure 1-6: Three-dimensional perspectives of the MAR 13°20’N ODF (A) seafloor reflectivity mosaic (TOBI) draped over bathymetry, viewed from SE (adapted from MacLeod et al., 2009), and (B) micro bathymetry of the same area, viewed from the SSE, showcase various structural domains such as the dome-shaped corrugated surface, breakaway ridge, and what is termed as termination here, the detachment emergence, based on adaptation from Escartín et al., 2017. On the other hand, (C-D) presents detailed examinations of corrugated fault surfaces. Adapted from Parnell-Turner et al. (2018), these views highlight corrugation highs (red arrows), rubble ridges (blue arrows), cross-cutting faults (green arrows), and instances of artifacts (pink arrows).

On a wide range of spatial scales, bathymetry data on scooped-shaped exhumed detachment surfaces show spreading parallel undulations (Figure 1.6b, c-d) similar to those of onland normal faults (Figures 1.3b and *1.7c,* e.g., Whitney et al., 2013). These are called corrugations, and they have wavelengths ranging from tens of meters to ~1 km and amplitudes of meters to tens of meters. Along the spreading parallel direction, corrugations are up to ~2 km long (Figure 1.6b-d; Cann et al., 1997; Ohara et al., 2001; MacLeod et al., 2002; Reston et al., 2002; Cannat et al., 2003; Searle et al., 2003; Smith et al., 2006; Cannat et al., 2009; Escartín et al., 2017). These corrugations are characteristic features of MAR dome-shaped, relatively magmatic (the hanging wall exposes volcanic rocks, and gabbro exposures are common in the footwall) ODFs. They are also common along the ultraslow-spreading SWIR ridge: the easternmost SWIR between 61°E and 67°E shows domal corrugated structures over ~4% of the mapped area (Cannat et al., 2006). Among those, the FUJI dome corrugated detachment, at 63.55°E, emerges at an angle of less than 15° (Searle et al., 2003).

By contrast, ~40% of off-axis areas mapped in the 61°E to 67°E SWIR region show broad ridges that extend ~25-95 km parallel to the local ridge axis (Cannat et al., 2019, 2006). These broad ridges form in nearly amagmatic spreading corridors between more volcanic domains and do not appear corrugated in shipboard bathymetry (Cannat et al., 2006). Both flanks of these ridges expose mostly (~90%) serpentinized peridotite (Sauter et al., 2013) to the seafloor. Both flanks of these ridges are interpreted as exhumed footwalls of successive and opposite polarity detachment faults (Sauter et al., 2013). This type of detachment is known as flip-flop (Reston and McDermott, 2011), where a new detachment fault cuts through the footwall of a preceding detachment fault with opposite polarity. The exhumed footwalls of these 'flip-flop' ODFs face a sparsely magmatic and ultramafic-dominated hanging wall (Sauter et al., 2013; Cannat et al., 2006).

1.2.3. How do ODFs' Corrugation Form?

Several hypotheses have been proposed to explain the genesis of ODFs' corrugations:

- The 'continuous casting' theory (Spencer, 1999). It suggests that the footwall material is weaker than the materials found above, in the hanging wall. During the detachment fault movements, this weaker material conforms to the irregular surface of the more rigid upper plate material.
- Tucholke et al. (2008) updated the continuous casting hypothesis to suggest that the corrugations on oceanic detachment fault surfaces, which are spaced hundreds of meters apart, are formed due to variable and intermittent magmatism. The uneven brittle–plastic transition, a consequence of sporadic magma intrusion at the spreading center, plays a pivotal role in creating these corrugations by fostering depth-dependent fault initiation. The theory further suggests that the rheological irregularities influence the corrugation's wavelength in the hanging wall, potentially due to changes in the melt supply or varying degrees of serpentinization. This hypothesis rests on the continuous casting hypothesis, where the cool hanging wall continually molds the footwall (Tucholke et al., 2008).
- Parnell-Turner et al. (2018) argue that serpentinization is unlikely to be the cause of corrugations on oceanic detachment fault surfaces: fault rocks are not serpentinized at all ODFs (e.g., samples from the corrugated surface at the 13°20’N OCC are primarily quartz-cemented basaltic breccias; Bonnemains et al., 2017; Escartín et al., 2017). They also argue against an origin due to magma induced thermal anomalies because these would need to be sustained for a sufficiently long time for corrugations to form. They calculate that the thermal contrast would need to be sustained for 0.2-0.5 million years to form a typical corrugation. In addition, these thermal anomalies would need to be very closely spaced (about 100 meters apart to explain the typical spacing of corrugations) and thermal anomalies of the required wavelength could not be sustained for long enough. Instead, they propose (Figure 1.8) that corrugations on oceanic detachments originate from the 3D geometry of linked and anastomosing

fractures in the fault zone (Escartín et al., 2017; Karson et al., 2006). In this interpretation, corrugations are a general outcome of brittle strain localization, irrespective of rock type and deformation history (Parnell-Turner et al., 2018).

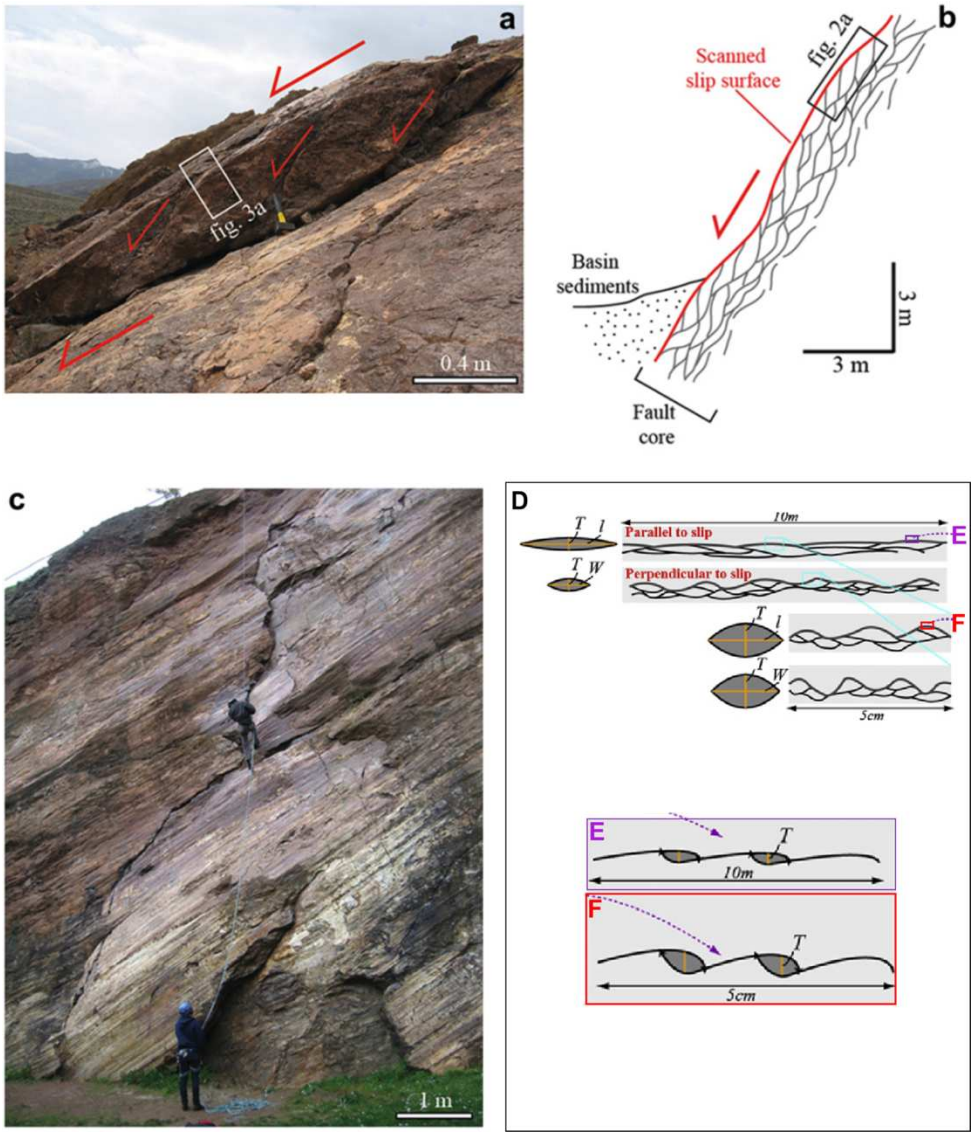

Figure 1-7: The Dixie Valley fault zones in Nevada, USA, and Corona Heights are characterized by an intricate mesh of anastomosing sliding planes of different scales that separate individual sigmoidal lenses. (a, b, c). The cross-section of the Dixie Valley fault zone displays a major sigmoidal lens made up of three smaller ones (a). A schematic representation of an outcrop cross-section is presented (b). A diagram illustrates how the fault's surface consists of aggregated multi-scale lenses from a lateral segment linkage process (d). T represents the thickness of the sigmoidal lens, l its elongation parallel to the fault slip, and W its width perpendicular to the slip. The figure is adapted from Candela and Renard (2012).

At continental normal faults, which are also in several cases corrugated, corrugations are also believed to form from mechanisms related to the 3D geometry of the fault zone: re-activation of existing faults or linkage of en-echelon segment faults (Figure 1.7a, b-d; Ferrill et al., 1999; Jackson and McKenzie, 1999). In this interpretation, individual rupture segments extend sideways until they link (Figure 1.7d, Candela and Renard, 2012; Childs et al., 1995; Peacock, 2002). This interconnected array of fault segments produces an undulating fault surface where the pronounced ridges align with the intersections of the fault segments (Ferrill et al., 1999). When these structures emerge, they imprint subtle topographies on the core complex dome (Figures 1.6a-b and 1.8). This interpretation suggests that the varied corrugation wavelengths arise from fault segment linkages across different scales (Figures 1.7d and 1.8).

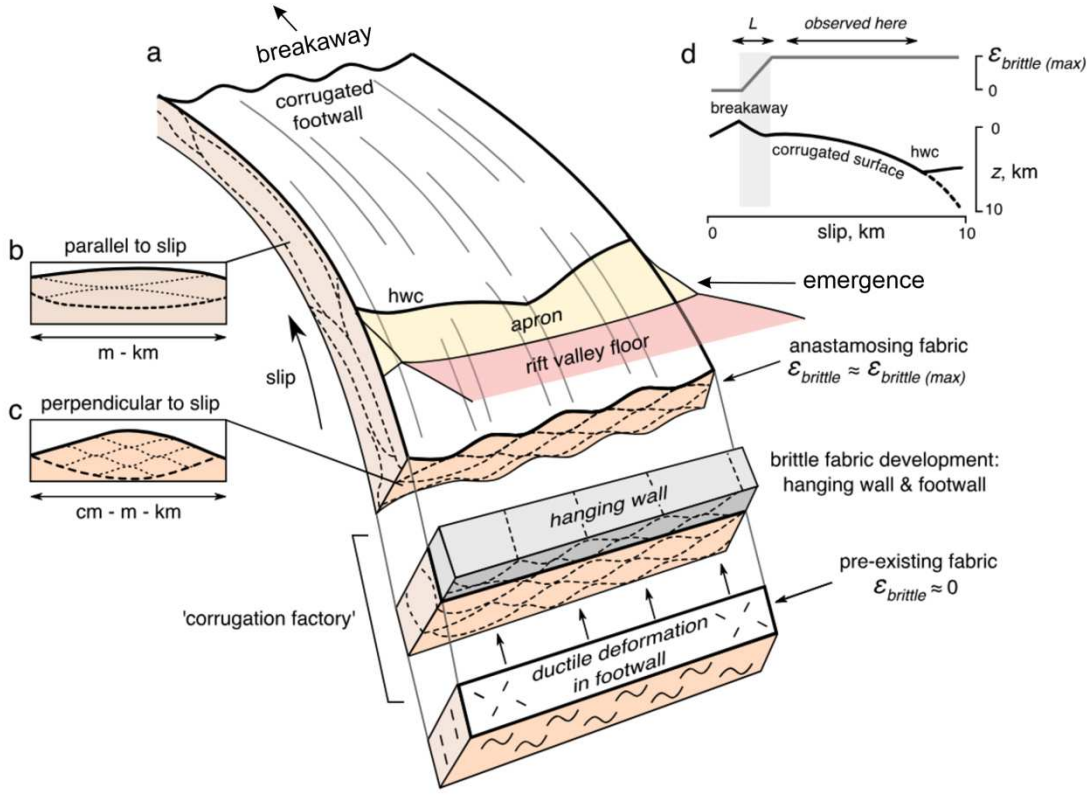

Figure 1-8: The illustration depicts the genesis of corrugations via strain localization. It presents a view of an oceanic detachment fault. This fault transitions from a footwall with a pre-existing ductile fabric (shown in the lower block) to a corrugation factory (central block) and finally to exhumation (the upper curved block). The footwall's upper surface is indicated in white, while its corrugations are represented by gray lines. As the footwall material (shown in tan) passes through the corrugation factory, it acquires an anastomosing fabric, denoted by

dashed lines. The hanging wall material, seen as a gray block, also forms this anastomosing fabric. The rift valley floor, or the hanging wall, is colored pink. The talus deposits, shaded yellow, extend up to the fault emergence. The figure is adapted from Parnell-Turner et al. (2018)

1.2.4. The internal structure of ODFs in magmatic vs. amagmatic settings:

Several expeditions to magmatically active and corrugated oceanic detachment faults at slow and ultraslow ridges, alongside ROV sampling, have enhanced our understanding of their internal structures. At site IODP U1309D, located in the domal footwall section of Atlantis Massif (MAR), drilling recovered approximately 1.4 km of primarily gabbroic material with some ultramafic layers (Blackman et al., 2006; Ildefonse et al., 2007). This discovery at Atlantis Massif is consistent with prior drillings in the 15°20'N FZ area (Kelemen et al., 2004) and at Atlantis Bank at 57°15'E on the SWIR, which also found a significant amount of gabbroic rock (Dick et al., 2000). Seismic imaging also reveals high-velocity bodies beneath corrugated ODFs' domed surfaces, as highlighted by multiple studies (Figure 1.9a, Canales et al., 2004, 2007, 2008; deMartin et al., 2007; Planert et al., 2010). Geophysical interpretation is complex due to similarities in the properties of ~20-75% serpentinized crustal gabbroic and peridotite mantle (Christensen, 1978; Miller and Christensen, 1997). However, Canales et al. (2008) pointed the good correspondence between higher velocity bodies in the shallow crust and gabbro outcrops. By contrast, flip-flop detachment faults in the nearly amagmatic SWIR spreading corridors expose primarily serpentinized peridotites, and gabbroic veins are sparse (Sauter et al., 2013; Paquet et al., 2016).

Detachment faults have been modeled numerically, and it has been suggested that they start with a steep slope deep down and curve in more shallow areas (Lavier et al., 1999; Poliakov & Buck, 1998). As a result, the inactive and exposed part of the detachment fault reaches a very low or even inverse slope. These models fit bathymetric observations. At the TAG and 13°20'N MAR ridge, microseismicity

distribution suggests an initiation at depths of 8 to 12 km at an angle of 70° (Figure 1.9a; de Martin et al., 2007; Parnell-Turner et al., 2018), effectively following a concave profile. Paleomagnetic data acquired on IODP drilling samples at the top of corrugated domes of the MAR ridge confirm the idea of a rotation of the fault wall, ranging from 45 to 80° (Garcés & Gee, 2007; Morris et al., 2009).

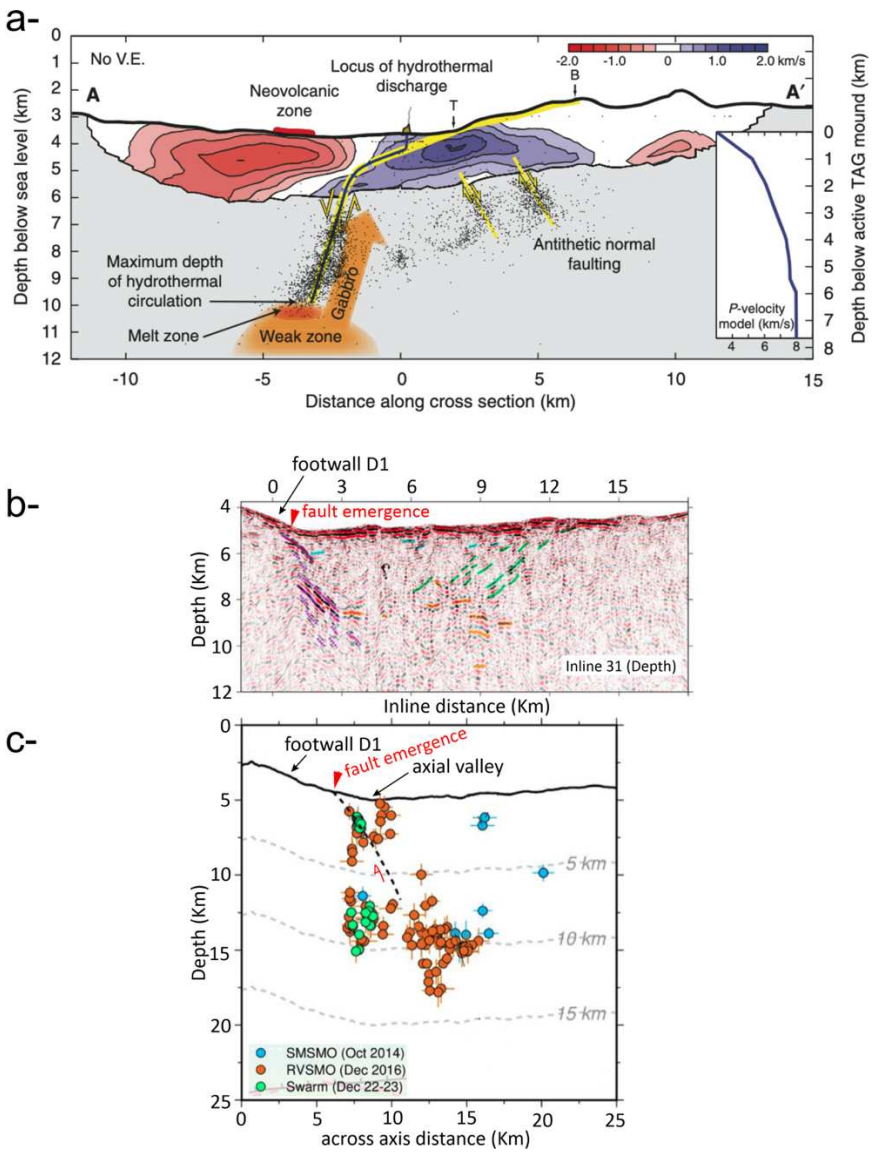

Figure 1-9: (a) The fault emergence, represented as T, is where the fault surfaces, while B indicates the breakaway point. A schematic showcases high-velocity material at shallow depth under a young detachment fault located at the TAG, Mid-Atlantic Ridge (26°N). The fault descends steeply (~70°) to about 7 km beneath the seafloor, as outlined by the gathered micro-earthquake hypocenters (black dots) and velocity anomalies (deMartin et al., 2007). The visible fault surface is believed to be the footwall, rotated by an angle of approximately 50°. (b) A depth-converted, across-axis *section of the P-wave velocity model from 64°35'E SWIR showing*

the internal structure (reflectors) of the amagmatic footwall and its hanging wall. Reflectors in magenta are interpreted as due to detachment fault damage. This figure is adapted from Momoh et al., 2017. (c) Micro earthquake distributions in the axial domain of 64°35'E SWIR, adapted from Chen et al., 2023. The black dashed line indicates the proposed trace of the active detachment fault.

Seismic reflectors indicate that the active flip-flop detachment fault in the nearly amagmatic SWIR 64°E spreading corridor has a dip of 45-50° at depths down to 5 km below the seafloor (Momoh et al., 2017). The seismic experiment was not designed to image deeper, and local seismicity does not focus along the inferred fault zone (Chen et al., 2023) as it does at more magmatic ODFs de Martin et al., 2007; Parnell-Turner et al., 2018), so that the dip of the fault further down into the brittle lithosphere is not known. These reflectors, that are found over ~1.5 km in the across-fault direction, are interpreted as fault damage associated with the ODF (Figure 1.9b, Momoh et al., 2017). Other sub-horizontal reflectors are interpreted as magmatic sill-like intrusions (Momoh et al., 2017). Microseismicity is recorded down to 15 km below the seafloor, indicating the local depth to the brittle-ductile transition (Figure 1.9c, Chen et al., 2023). In contrast to what has been documented in MAR corrugated detachments (deMartin et al., 2007; Parnell-Turner et al., 2020, 2017), earthquakes are not focused along the fault zone and in the detachment footwall but also occur in the hanging wall.

These observations collectively indicate notable differences in deformation processes and strain localization between the more prevalent corrugated-volcanic mode of detachment faulting along more magmatically active ridge areas and the almost entirely amagmatic flip-flop mode of detachment faulting.

1.2.5. Detachment Faulting, deformation, and Mantle Exhumation along magma-poor Ocean Continental Transition Zone

Serpentinized mantle-derived peridotites have also been discovered in multiple locations along the ocean continent transition domains (OCTs) of continental margins.

Currently, the exhumed mantle in OCTs has been penetrated by five drill holes. The Galicia margin was drilled at ODP Site 637. The Iberia margin (Figure 1.10a) has three drill holes at ODP Sites 897, 1068, and 1070. Additionally, ODP Site 1277 is situated at the conjugate Newfoundland margin (Müntener and Manatschal, 2006; Tucholke and Sibuet, 2007). While exhumed serpentinized peridotites are prevalent at the Iberia margin, they have also been observed at the South Australian Margin (Nicholls et al., 1981; Beslier et al., 2004) and as fossil relicts of the Alpine Tethys in the Alps (Manatschal and Bernoulli, 1999). These rocks are thought to have been exhumed by detachment faults that cut throughout the continental mantle lithosphere as part of the final stages of past continental rifting events (Whitmarsh et al., 1996). The ocean-continent transition domain lies oceanward of the last blocks of the continental lithosphere (Figure 1.10a). The whole margin is structured into a proximal domain with stretched continental crust, a necking zone showcasing a drastic reduction in crustal thickness, and the ocean-continent transition (Péron-Pinvidic and Manatschal, 2009; Manatschal et al., 2001; Whitmarsh et al., 2001).

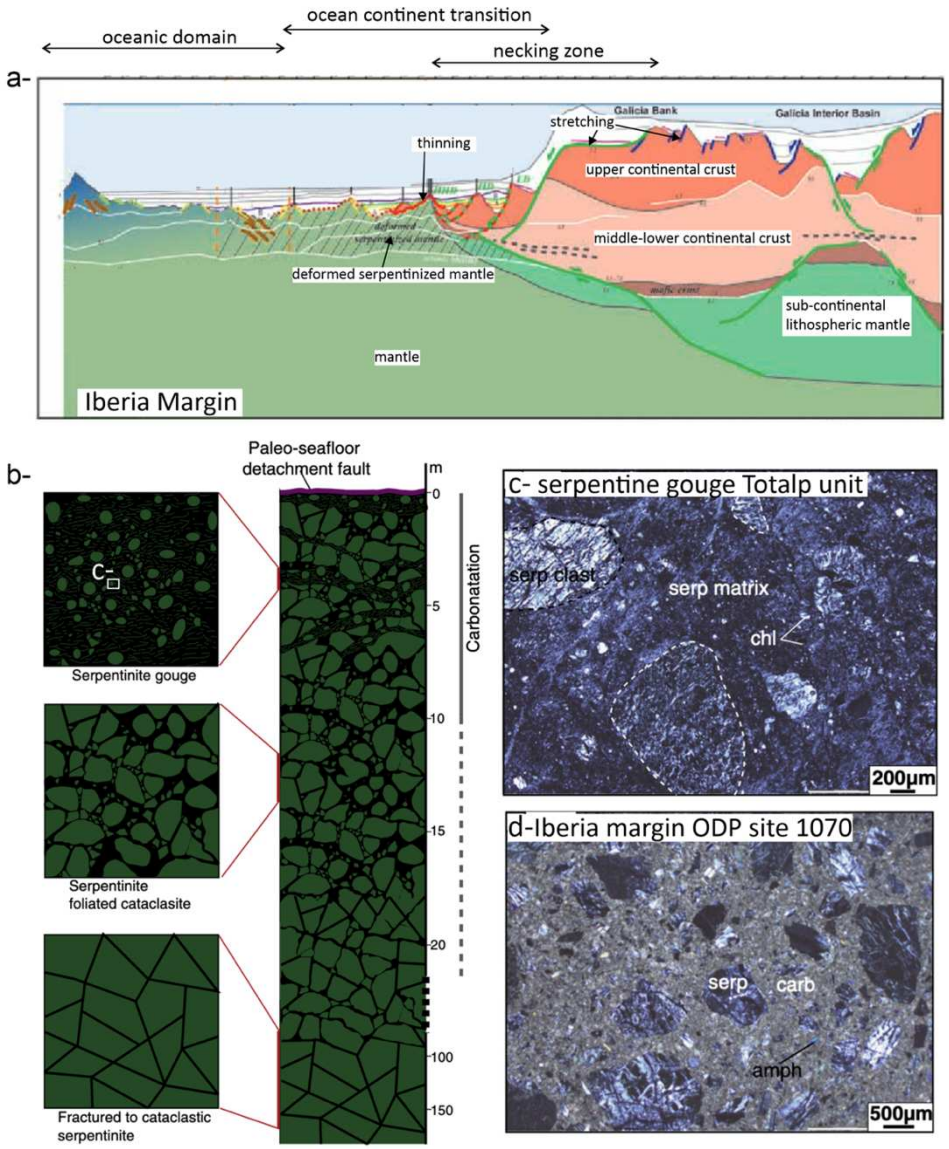

Figure 1-10: A sketch, adapted from Péron-Pinvidic and Manatschal (2009), depicts the magma-poor ocean-continental transitional setting of the Iberia margin, which has a vertical thickness of 30 km. This depiction is based on seismic reflection, refraction data, and results from four ocean drilling programs. The structure is segmented into three distinct parts: Firstly, the necking zone, where both the continental crust and subcontinental lithospheric mantle thin out as they transition toward the oceanic domain. This thinning is due to polyphase deformation along both shallow faults (highlighted in red) and deep crust, sub-continental lithospheric mantle-piercing faults (in green). Secondly, the ocean-continental transition zone showcases the exhumation of the deformed serpentinized mantle through a detachment fault (in green). Lastly, seafloor spreading results in the formation of the magmatic oceanic crust. Black vertical lines represent ODP drilling sites (b) Another sketch, adapted from Picazo et al. (2013), offers a detailed view of the deformation textures under the Totalp paleo seafloor in SE Switzerland, which is interpreted as a fossil magma-poor ocean-continent transitional setting. This illustration shows deformation facies in serpentinites such as serpentinite gouges/cataclasites, foliated cataclasites, and fractured serpentinized peridotites. (c) A representative thin section from the Totalp unit displays a cataclastic gouge sample

characterized by a fine-grained matrix and clasts that range from rounded to subrounded shapes. (d) Drilled samples from the Iberian Ocean-continental transitional setting reveal a texture similar to the cataclastic gouge. Microphotographs c-d are sourced from Picazo et al., 2013.

Picazo et al. (2013) performed field mapping of the Totalp unit, a relict of the Jurassic seafloor (Bernoulli and Weissert, 1985) in SE Switzerland. This unit is interpreted as the exhumed surface of an OCT detachment fault. It exposes a ~150 m thick sequence of deformed serpentinites (Figure 1.10b). The petro-structural examination of this sequence shows that deformation occurred after partial serpentinization of the mantle-derived material. A deformation gradient was identified in the ~150 m thick sequence, ranging from bottom to top from cataclasis to serpentine gouge formation (Figure 1.10b; Picazo et al., 2013). Semi-brittle deformation is identified in the most highly strained gouge horizons (Figure 1.10c). Picazo et al. (2013) compared the Totalp deformation microstructures to those of serpentine breccia and cataclastic gouges from ODP site 1070 (Figure 1.10d) at the Iberia margin. ODP Hole 1070A unveiled 604 m of post-rift sediments from recent to early Oligocene, beneath which lies 54 m of late Aptian syn-rift sediments, approximately 1 m of sedimentary ultramafic breccia, and 18 m of tectonic ultramafic breccia (Whitmarsh et al., 1998). The tectonic breccia, made of serpentinite clasts, is believed to have formed post-serpentinization. Its deformation microstructures are very similar to the texture of serpentine gouges and foliated cataclastic rocks described in the Totalp fossil-detachment fault area (Picazo et al., 2013).

1.3 Strain localization at oceanic detachment faults. Observations and numerical modeling.

Microseismicity data from the Mid-Atlantic Ridge (MAR) suggests that the brittle lithosphere below corrugated and domal ODFs is ~8-12 km thick (de Martin et al.,

2007; Parnell-Turner et al., 2018). At the ultraslow Southwest Indian Ridge (SWIR), microearthquakes have been detected at depths of up to ~15 km (Yu et al., 2018) below a corrugated domal ODF at ~54°E, in a region of the ridge that has an overall "normal" seismic crustal thickness. In the nearly amagmatic portions of the SWIR (64-65°E region) where flip-flop ODFs develop (Sauter et al., 2013), microearthquakes are also up to 15-20 km deep (Schlindwein & Schmid, 2016; Grevemeyer et al., 2019; Chen et al., 2023).

Numerical models that rely only on cohesion weakening as a function of increasing strain to stabilize normal faults predict that large offset detachment faults do not develop in a brittle axial lithosphere that is thicker than ~10 kilometers (Lavier et al., 2000; Lavier & Buck, 2002). These models instead generate multiple faulted half-grabens. Additional weakening mechanisms involving a larger decrease in the effective strength of the fault rocks are therefore needed for detachment faults to form in a thick axial lithosphere. Geological studies and sampling at ODFs inform on these weakening mechanisms.

MAR corrugated detachment faults probably root in high-temperature-solidifying gabbroic bodies, evidenced by mylonitic deformation microtextures in gabbros (e.g., Cannat et al., 1991; Dick et al., 2002) and by studies of gabbro infiltrated ultramafic samples (Picazo et al., 2012; Hansen et al., 2013; Schroeder & John, 2004; Jons et al., 2009; Albers et al., 2019). Outcrops from exposed corrugated ODFs surfaces also reveal anastomosing fractures and schistose rocks (serpentinized peridotite, gabbros or basalts). Highly deformed ultramafic samples in these exposed fault zones typically contain assemblages of weak hydrous minerals such as talc, tremolite, chlorite, and serpentine. These assemblages result from the hydrothermal alteration of melt-impregnated peridotites (Boschi et al., 2006; Jons et al., 2009; Picazo et al., 2012; Albers et al., 2019), and/or from the alteration of peridotites by Si-Al-Fe rich hydrothermal fluids, produced by prior interactions with gabbroic materials (Escartín et al., 2003; Picazo et al., 2012; Boschi et al., 2006; McCaig et al., 2007; Früh-Green et al., 2017). Among these minerals, talc is the weakest (with friction coefficients of 0.16-0.23; Moore and Lockner, 2008) and is stable up to 800°C

(Chernosky et al., 1985; Jenkins et al., 1991), while serpentine is stable only up to ~400°C (Evans, 2004). Amphibole and chlorite found in corrugated ODFs ultramafic fault rocks may also form at a temperature higher than serpentine stability (up to ~500-600°C; Picazo et al., 2012; Albers et al., 2019).

It has been argued that the rheology of talc could control the strength of corrugated ODFs (Cannat et al., 2009; Ildefonse et al., 2007; Hansen et al., 2013). Massive serpentinites, primarily made up of lizardite and fibrous serpentines, exhibit a frictional coefficient (μ = 0.30) (Escartin et al., 1997, 2001; Raleigh & Paterson, 1965). Antigorite's friction is relatively higher, with values ranging from (μ=0.50) to (μ= 0.75), comparable to the typical friction of rocks, which ranges between (μ = 0.60) and (μ mu = 0.85) (Moore et al., 1997; Takahashi et al., 2011; Byerlee, 1978). Antigorite, however, is not abundant in abyssal serpentinites. The frictional coefficient for saturated lizardite gouges varies between (μ = 0.29) and (μ = 0.56) (Behnsen & Faulkner, 2012; Moore et al., 1997; Moore & Lockner, 2011), while that of saturated chrysotile gouge lies between (μ= 0.1) and (μ = 0.55) (Moore et al., 1997, 2004). Above 100°C, the frictional strength of water-saturated gouges from both lizardite and chrysotile is noted to markedly rise, nearing their dry strength of (μ = 0.6) to (μ = 0.7), possibly due to water desorption from the mineral surfaces (Moore et al., 1997; Summers & Byerlee, 1977). Adding a relatively small amount of talc can substantially weaken a lizardite gouge: at 200°C, and 100 MPa pressure, adding 20 wt% talc to a lizardite gouge lowers its coefficient of friction to $\mu \approx 0.25$ from $\mu \geq 0.5$ (Moore and Lockner, 2011).

Thus, strain localization at corrugated ODFs appears favored by magmatic rocks and their alteration products, weakening the footwall and its flexural rigidity (e.g., Cannat et al., 2009). This may explain observations from the MAR near 13°N, where the corrugated dome-shape detachment fault appears to rotate ~35° within just the upper 5 km below the fault's emergence (Smith et al., 2006; Escartin et al., 2017). At flip-flop, nearly amagmatic ODFs, magmatic rocks, and their alteration products are rare (Sauter et al., 2013; Rouméjon et al., 2015; Bickert et al., 2023; Paquet et al., 2016). Deformation microstructures acquired in exhumed peridotites prior to

serpentinization, at temperatures of ~800-1000°C, correspond to poorly localized semi-brittle to ductile conditions and point to a strong brittle ductile transition domain (BDT): the ODF there does not root into a weak magma-rich mantle (Bickert et al., 2020; 2021). Strain localization in the fault above the BDT at these magma-starved ODFs has not been documented before; it is the object of this thesis.

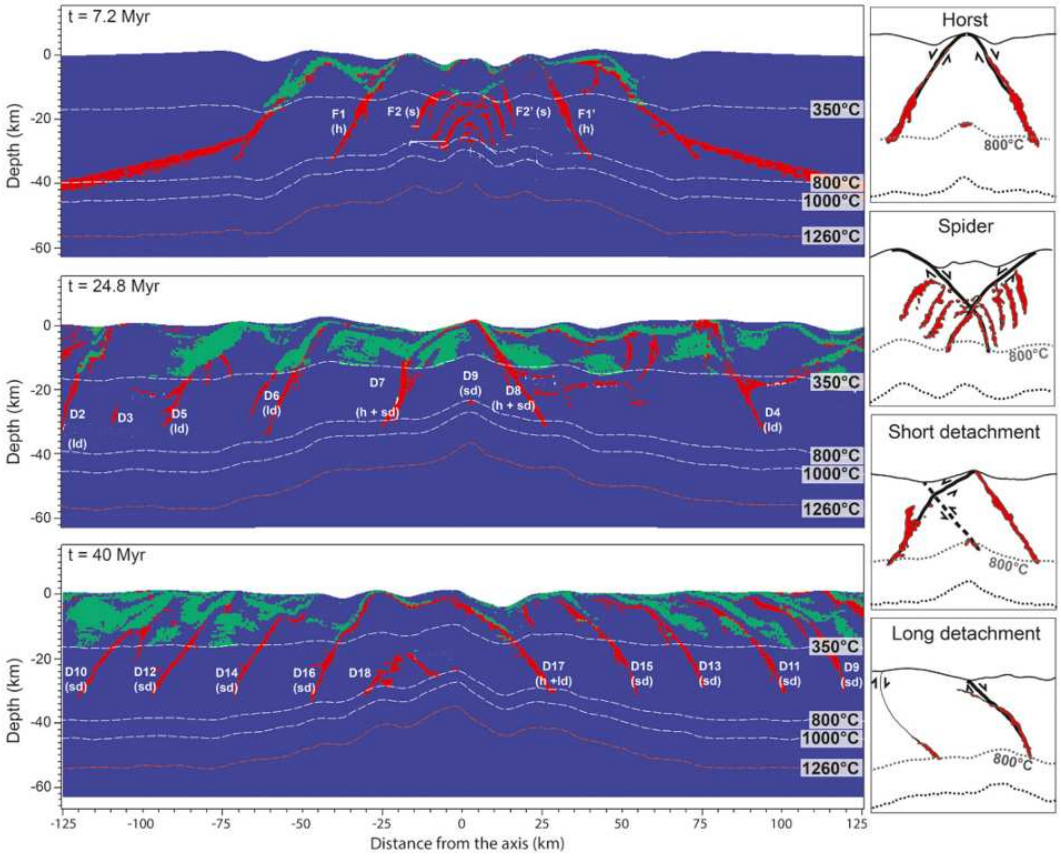

Figure 1-11: Adapted from Bickert et al. (2020). The figure shows a timeline of the deformation modes: horst mode (h), spider mode (s), short detachment mode (sd), and long detachment mode (ld), with examples of each mode on the right. Grain Size reduction zones are shown in red; serpentinized domains are in green; serpentine-free and mantle that is not affected by grain size reduction are shown in blue. Faults (F) and detachments (D) are numbered sequentially.

Numerical experiments by Bickert et al. (2020) explore ultraslow amagmatic spreading with a 15 km-thick brittle lithosphere and two plausible localization mechanisms: one is grain size reduction in fresh peridotite in the brittle-ductile transition domain (as constrained by sample studies), and the other is a reduction of the friction coefficient in domains that are modelled as serpentinized (serpentinization

is set to occur at T < 400°C above a total work threshold; Bickert et al., 2020). These models show that two types of faults can form: detachment faults and shorter-lived conjugate faults. This results in several tectonic modes: short-lived faults create a spider pattern or form horsts (Figure 1.11); detachment faults flip-flop with variable regularity. Overall, in this flip-flop mode, the lifetime and offset of successive detachments compare well with observations at 64°E on the SWIR (Sauter et al., 2013). Detachment faults root in shear zones near the apex of the axial thermal structure, which in these models is fixed. Flip-flop ODFs and horsts are also reproduced in numerical models by Sandiford et al. (2021) and Mezri et al. (submitted), which also reduce the friction coefficient above a critical amount of strain in serpentinized domains, with an axial thermal regime that is recalculated at each step.

1.4 Geological and Geophysical context of the SWIR

The Southwest Indian Ridge (SWIR) spans ~7,700 km between the Bouvet Triple Junction in the southern Atlantic Ocean and the Rodrigues Triple Junction (RTJ) in the Indian Ocean. This ridge, which separates the African and Antarctic plates, is characterized by its ultraslow slow spreading rate of 14 mm per year (Sauter & Cannat, 2010; Patriat & Segoufin, 1988). Magnetic anomalies suggest that the initiation of the SWIR ridge was around 155 Ma ago, occurring between the Prince Edward and Discovery II transform faults (Sauter et al., 2010). The SWIR's expansion rate has decreased over time from 30 to 24 mm/year approximately 24 Ma ago and then from 16 to 14 mm/year about 20 Ma ago (Patriat & Segoufin, 1988). The younger, easternmost parts of the axis (close to the Rodrigues triple junction; Figure 1.12a) started forming about 20 Ma ago. The Bouvet and Rodrigues triple junctions' migration since the formation of the SWIR is responsible for the obliquity seen in several ridge regions (Sauter & Cannat, 2010). Ridge obliquity relative to the plate divergence varies from 15° between 64° and 67.5°E to 51° between 10° and 15°E

(Sauter & Cannat, 2010). The axis displays numerous transform faults, typically with an NNE-SSW orientation (Figure 1.12a).

Several studies have highlighted the absence of significant volcanic activity over large parts of the SWIR axis in two regions where mantle-derived rocks predominantly outcrop on the seafloor (Dick et al., 2003; Seyler et al., 2003; Cannat et al., 2006; Standish et al., 2008). One of these regions is located east of the Melville transform fault between 61 and 67.5°E (Figure 1.12a-b), and the other is the oblique segment that spans from 9 to 25°E (Figure 1.12a-b).

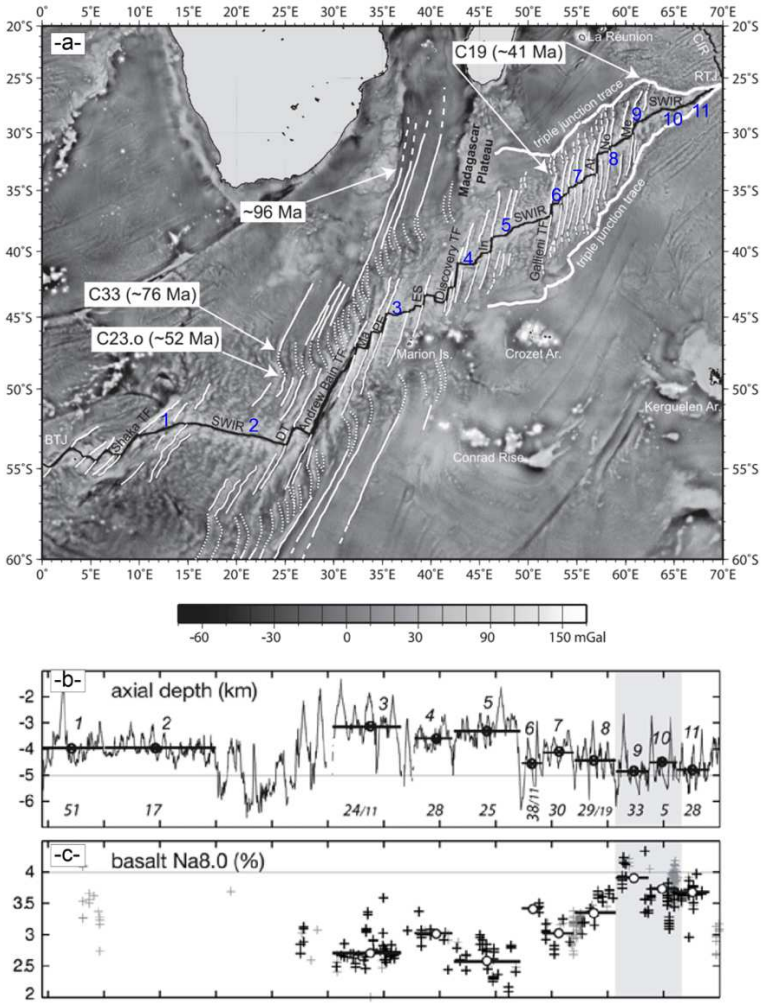

Figure 1-12: (a) The trace of the Southwest Indian Ridge in the black line between the BTJ at the west and RTJ at the east is illustrated by free-air gravity anomalies adapted from Sauter and Cannat (2010). The RTJ trace is highlighted by thick white lines. Fracture zones are indicated by thin white and dotted lines. The acronyms are defined as: BTJ for Bouvet Triple Junction, RTJ for Rodrigues Triple Junction, DT for Du Toit, Ma for Marion, PE for Prince Edward, ES for Eric Simpson, In for Indomed, At for Atlantis, No for Novara, Me for Meville, Marion Is for Marion Island, Crozet Ar for Crozet Archipelago, Kergulen Ar for Kergumen

Archipelago, CIR for Central Indian Ridge, and SWIR for Southwest Indian Ridge. It is notable that between the Melville transform fault and the Rodrigues Triple Junction, there is an absence of mapped transform faults. Magnetic anomalies with their respective ages are represented as C19, C23, and C33. The numerals 1 to 11 (blue in Figure a-, and black in Figure b-) indicate segments as per the classification of Cannat et al. (2008), which are differentiated based on changes in ridge orientation or their division by transform faults. (b) shows axial depth variation along the traced ridge axis located in (a), and (c) shows the Na8.0 content of basalts along the same ridge axis. Both (b) and (c) are adapted from Cannat et al., 2008. The content of Na8.0 is derived by correcting the Na2O value based on a reference MgO value of 8 wt% (Klein & Langmuir, 1987).

In the easternmost SWIR region (Figure 1.13), magmatic activity is concentrated in 3 large axial volcanic centers (#14, #11, and #8 in Figure 1.13; Cannat et al., 1999). The axial regions between these volcanic centers have an average axial valley depth of ~4700 m and are devoid of significant volcanic formations (Cannat et al., 2006; Sauter & Cannat, 2010). This correlates with a thinner seismic crust. It averages around 3 km, in the P wave model of Muller et al. (1999), and ranges between 3 and 5 km in more recent models by Momoh et al.(2017) and Corbalan et al. (2021).

Based on bathymetry and gravity data over the off-axis regions of this easternmost SWIR region, Cannat et al. (2006) described three distinct seafloor types (Figures 1.13 and 1.14).: volcanic-volcanic seafloor, with volcanic terranes on both plates; corrugated-volcanic seafloor, representing only 4% of the total mapped surface of figures 1.13, with corrugated ODFs footwalls on one plate and volcanism in the conjugate hanging wall plate; and the smooth seafloor, characterized by broad and elongated ridges devoid of volcanic cones or scarps. These ridges can stretch up to ~90 km along-axis and vary in height from 500 to 2500 m (Cannat et al., 2006). They align with the local ridge trend at their time of formation. The smooth seafloor constitutes around 40% of the entire area mapped in Figure 1.13.

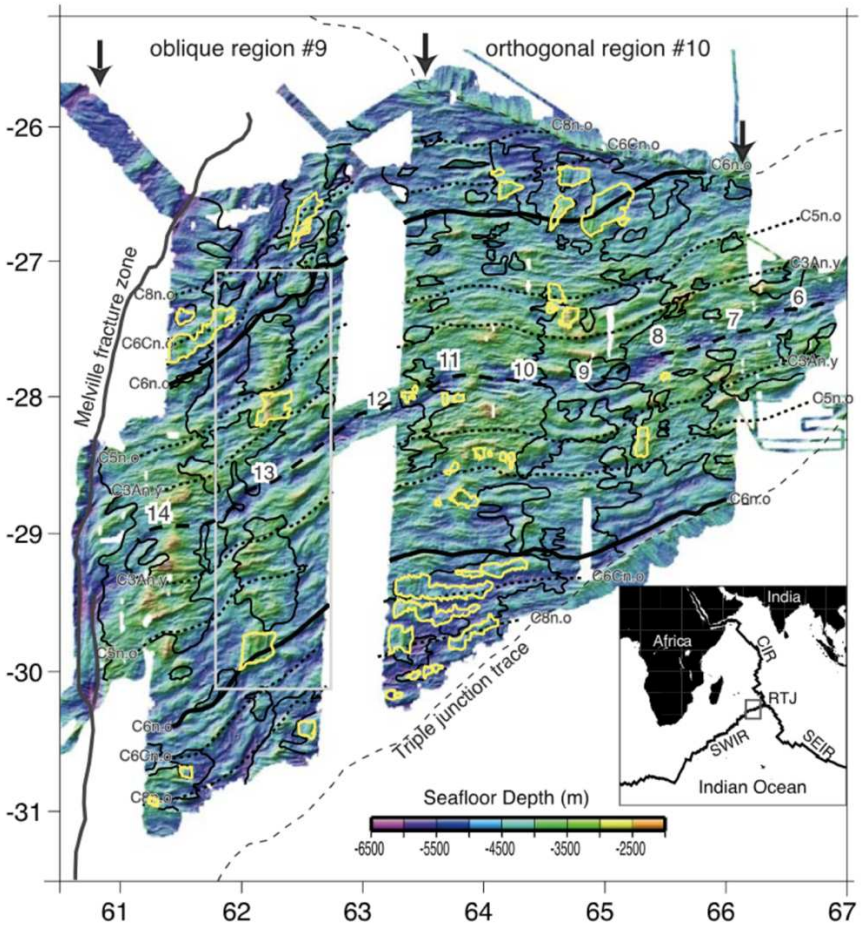

Figure 1-13: Based on Cannat et al. (2008), the bathymetry of the easternmost SWIR is presented. Numeric labels correspond to SWIR axial segments as categorized by Cannat et al. (2003). The bold black dotted line represents the ridge axis. Regions enclosed in yellow highlight seafloor sections believed to be exhumed by corrugated detachment surfaces. The finer black dotted lines, aligned with the ridge axis, indicate magnetic isochrones. Zones outlined by thinner black lines feature terrains abundant with scarps and volcanic cones.

Three oceanographic cruises have focused on the smooth seafloor in this eastern SWIR region: SMOOTHSEAFLOOR in 2010 (PI-D. Sauter and M. Cannat), SISMOSMOOTH in 2014 (PI-S. Leroy and M. Cannat) and ROVSMOOTH in 2016 (PI-M. Cannat). These cruises have confirmed that the “smooth seafloor” predominantly exposes serpentinized peridotites (Figure 1.15, Sauter et al., 2013), and have brought the observations that lead to the flip-flop ODFs hypothesis (Sauter et al., 2013).

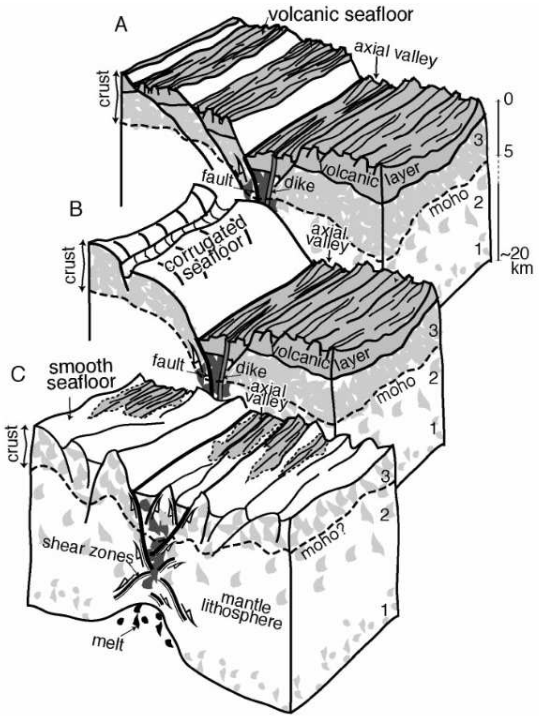

Figure 1-14: Seafloor classifications at the eastern ultraslow-spreading SWIR (a) Terrain where magmatic rocks form on both tectonic plates, termed volcanic-volcanic. (b) The corrugated-volcanic category is where one plate accumulates magmatic rocks, and the other reveals exhumed lower-crustal or variably hydrothermally altered mantle rocks; the corrugated seafloor is characterized by striations or undulations parallel to the spreading direction. (c) A smooth seafloor interspersed with patches of volcanic seafloor, indicating the placement of mantle rocks on both plates without prevalent magmatism and corrugations. These sketches are adapted from Cannat et al. (2006).

Microseismicity data acquired during the SISMOSMOOTH and ROVSMOOTH cruises shows microearthquakes occurring down to a depth of ~15 km in the 64°E SWIR nearly amagmatic corridor (Figure 1.17b; Chen et al., 2023). A microseismicity survey conducted in the nearly amagmatic domains near axial volcano #8 (Figure 1.16) was initially interpreted with hypocenter depths down to 35 km (Figure 1.16c, Schlindwein & Schmid, 2016). This was reinterpreted by Grevemeyer et al. (2019), who updated this maximum depth to ~20 km. Êarthquake hypocenters are shallower below the axial volcano (Figure 1.16d, Schlindwein & Schmid, 2016).

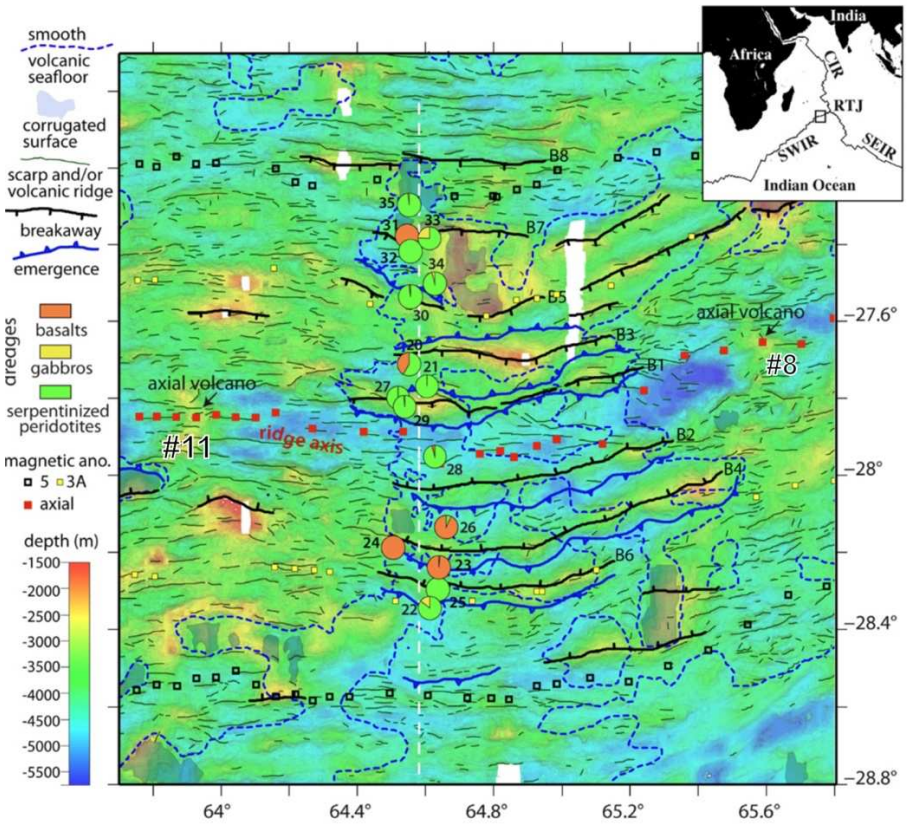

Figure 1-15: A zoomed-in view (adapted from Cannat et al., 2019) of Figure 1.4.2 between axial volcanic centers #11 and #8, The profile cross-section along the NS trending white dashed line is shown in Figure 1.4.9b. This sketch map highlights key tectonic features, like the breakaways (B1 to B8) and sequential emergences of successive detachment faults. The detachment fault breakaway B1 is currently active and about 300 kyr old, while the B8 was initiated about 11 Ma ago, based on magnetic anomaly 5. The seafloor to the east and west of this amagmatic NS corridor is characterized by volcanic scarps and narrow ridges.

Figure 1.18c shows an interpretative sketch of the reflectors imaged using data acquired during the SISMOSMOOTH cruise beneath the emergence of the D1 detachment (Momoh et al., 2017). It shows several dipping and sub-horizontal reflectors interpreted as damage zones in the fault and as minor faults and thin magmatic intrusions in the hanging wall (Figure 1.18c). Processing of SISMOSMOOTH seismic refraction data has led to models of P-wave velocity distribution that point to depths of 3-5 km for the 7.5 km/s iso-velocity contour (Momoh et al., 2017; Corbalan et al., 2021). This is proposed to correspond to the base of a geophysically-defined crust made of variably serpentinized peridotite.

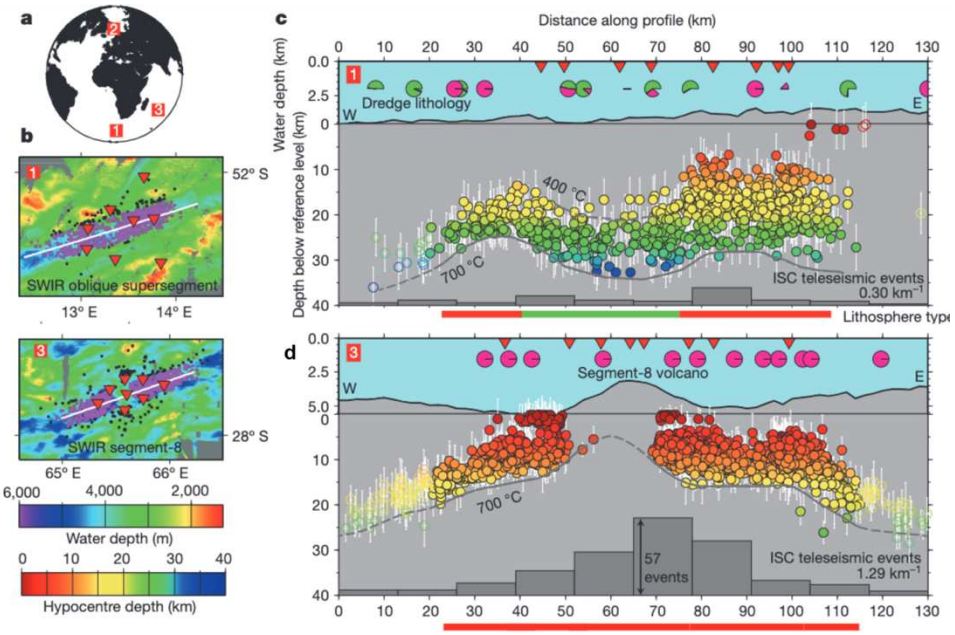

Figure 1-16: Earthquake distribution along the selected eastern and western sections of SWIR ridge. (b-c) Section of the ultra-slow spreading Southwest Indian Ridge at 13°E: The left panel displays bathymetry with ocean-bottom seismometers (red triangles) and earthquake epicenters (black dots). The right panel shows a cross-section and rock types from dredges (large circles) and earthquake hypocenters (small circles). (d) Magmatic segment: Differences in earthquake depths highlight a thicker brittle lithosphere in amagmatic sections. Histograms represent teleseismic event counts. 'Segment 8' volcano is shown in (d); the figure is adapted from Schlindwein and Schmid (2016).

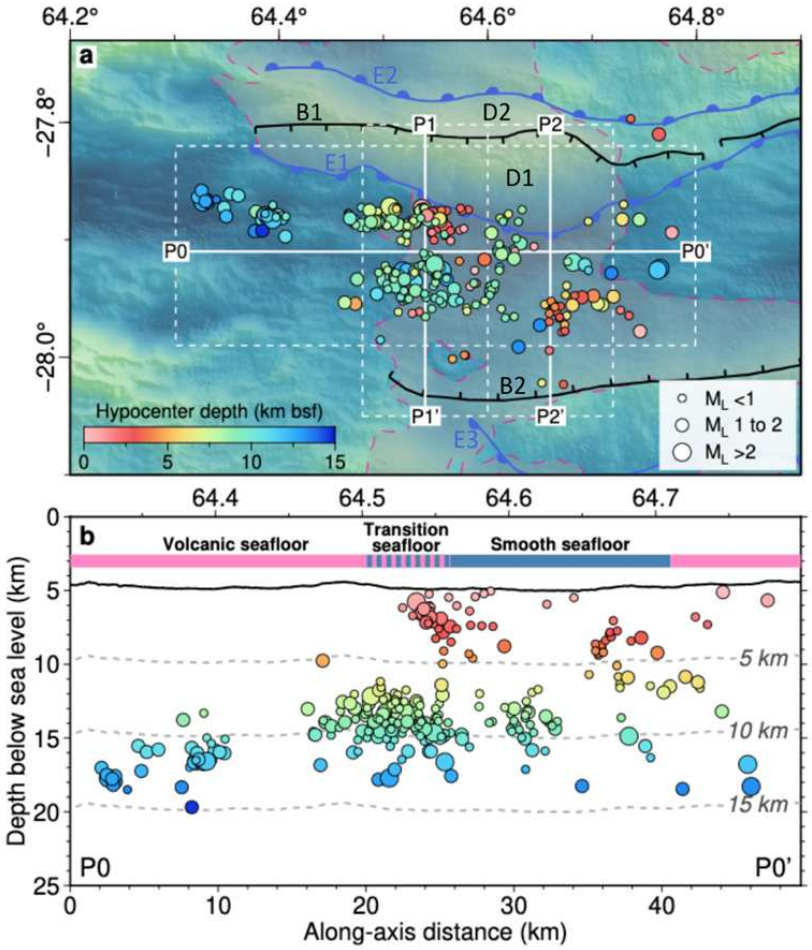

Figure 1-17: (a) A zoomed-in view of the bathymetry map showing the axial region within the NS corridor at 64°E in the SWIR region (see figure 1.4.4). The area outlined by light pink dashed lines indicates a smooth seafloor, while the surrounding open area denotes a more volcanic seafloor. (b) Presents a cross-section along the P0-P0' line as shown in (a). Earthquake locations in this section are color-coded by hypocenter depth, with the circle size indicating local magnitude (ML). Acronyms include: B1 and B2 representing successive detachments 1 and 2, from younger to older; E1-E3 indicating successive detachment fault emergences corresponding to breakaways 1 through 3; and D1 and D2 marking the exhumed footwall of these detachments. This figure is adapted from Chen et al. (2023).

Bickert et al. (2021) investigated the deformation and strain localization processes that predated serpentinization of the peridotites in the root zones of the flip-flop detachments (Figure 1.18d, BDT). Bickert et al. (2023) also found evidence in some samples for the percolation of small amounts of seawater-derived fluids in the detachment fault zone down to the BDT domain (Figure 1.18d).

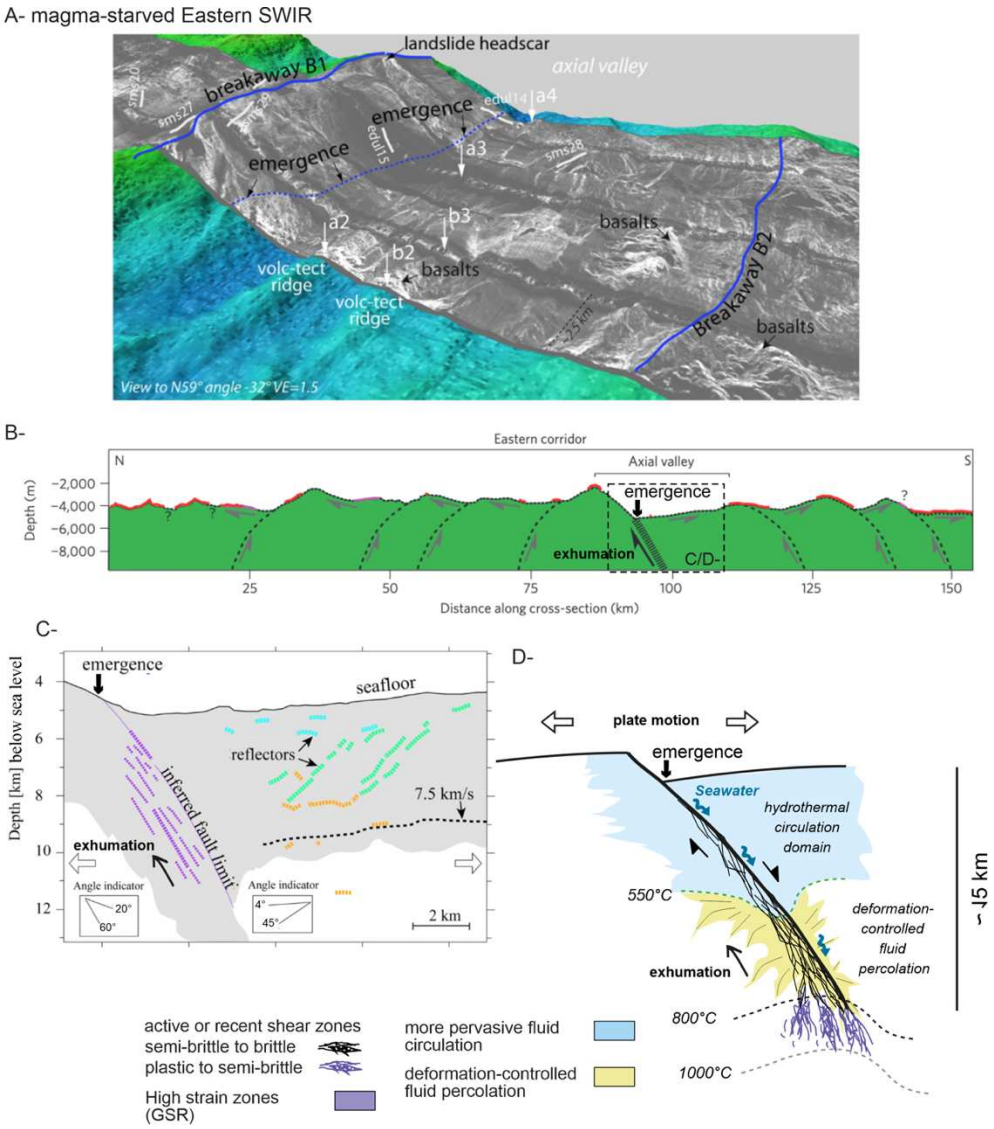

Figure 1-18: *(a) TOBI reflectivity image (with a perspective view towards NE) draped on bathymetry, showing the south-sloping active detachment footwall between the emergence and breakaway B1, near the 64°E SWIR axial region. Hummocky basaltic outcrops rest on less reflective ultramafic seafloor. This Figure is adapted from Cannat et al. (2019) (b) Simplified geological section of smooth seafloor along the NS trending profile located in Figure 1.4.4, based on the bathymetry and dredged data. Mantle-derived rocks are represented in green; volcanic seafloor in red; Thick black half arrow in the axial domain represents the presently active detachment fault; curved with steep dipping black dashed lines represent abandoned detachment faults; sub-horizontal gray half arrows under the undulatory black dashed lines represents mantle exhumation surfaces. This figure is adapted from Sauter et al. (2013). (c) An integrated illustration of the axial domain (can be relocated in Figure b-) combines findings from the 3-D seismic reflection and the wide-angle P wave velocity model. Purple south dipping reflectors are interpreted as due to the detachment fault damage. The primary fault plane, marking the boundary between the hanging wall and footwall plate, is depicted as a solid purple line. Reflectors with a northern (towards the left) inclination in the axial valley domain (hanging wall of the active detachment fault) are shown with green dashed lines. Sub-horizontal reflectors are interpreted as incipient magmatic bodies. The base of the crust is*

drawn along the 7.5 km/s velocity contour, which corresponds to a transition from fresh mantle to serpentinized peridotite (in grey) (Momoh et al., 2017). (d) Interpretative sketches of hydration and deformation processes in the root zone of the eastern SWIR detachment faults (modified after Bickert et al., 2021 and 2023); in the absence of magma, the strain is localized in the root zone of the detachment fault by grain size reduction in fresh peridotite and forming a system of anastomosing plastic to semi-brittle shear zones (represented by dark purple lines). The seawater-derived fluids (blue arrows) percolate through the network of microfractures, forming the detachment. As the mantle blocks are exhumed along the fault network, then under the hydrothermal circulation domain, hydration becomes more widespread.

The proportion of serpentinized peridotite samples that contain veins of gabbroic material is much lower in this area compared to more magmatically robust ODFs (Paquet et al., 2016; Rouméjon et al., 2015; Bickert et al., 2023). The textural and chemical characteristics of these plagioclase-bearing ultramafic rocks and olivine gabbros are interpreted as due to reactions between the peridotite host rock and small volumes of basaltic melts in the deep axial lithosphere (Paquet et al., 2016; Figure 1.19). Previous sample studies have also focused on the serpentinization processes (Rouméjon and Cannat, 2014; Rouméjon et al., 2015), leading to a model in which serpentinization initiates in the peridotites as it is exhumed through the BDT and cools to serpentine stability conditions. Thermal and tectonic stresses near the BDT would create microcracks that will serve as pathways for the serpentinizing fluids (Figure 1.20, Rouméjon and Cannat, 2014).

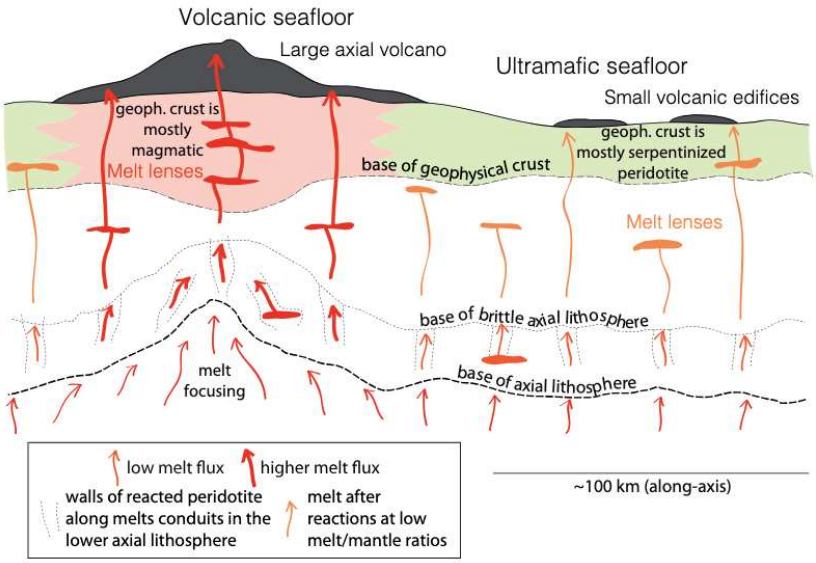

Figure 1-19: The cartoon illustrates the dynamics of melt emplacement in volcanic domains vs ultramafic-dominated smooth seafloor. It shows a similar degree of partial melting (indicated by the similar thickness red arrows below the base of the axial lithosphere) of a common mantle source below both the seafloor types, then preferentially melt focusing (Dick, 1989) leads to a higher melt flux (thick red arrows) below the volcanic centers result in the formation of thicker magmatic crust (Cannat, 2003; Standish et al.,2008). Below the ultramafic seafloor, the melt fluxes are low (orange arrows) along the reactive domains, as indicated by overall low melt/rock ratios. This is followed by fractional crystallization in melt lenses positioned at different levels within the axial lithosphere. The figure is sourced from Paquet et al., 2016.

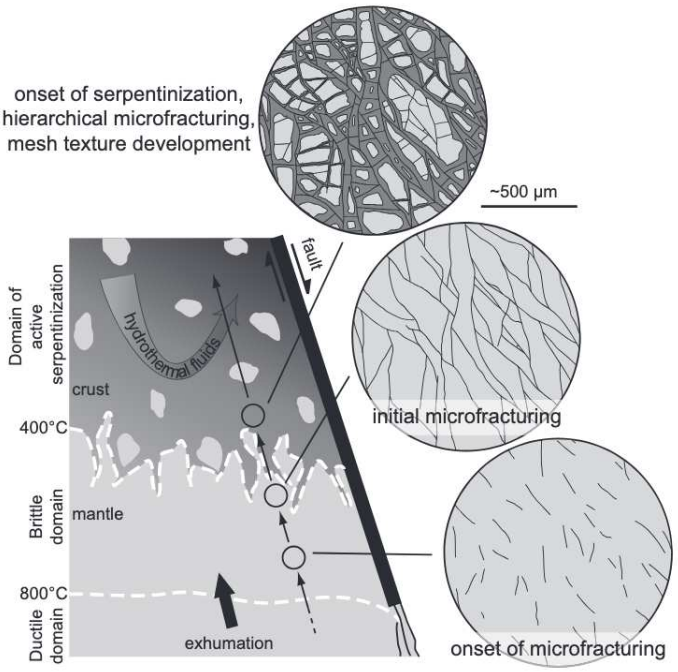

Figure 1-20: The conceptual drawing adapted from Roumejon and Cannat, (2014) depicts the evolution of a serpentine mesh texture and microfracture within the footwall and several hundred meters from the mid-oceanic ridge detachment fault. As fresh peridotite exhumes

along the fault, it transitions from a ductile to a brittle domain. In this brittle zone, a mix of anisotropic thermal shrinkage and tectonic stresses results in extensive microfracture development. When temperatures drop below 400° C, fluids seep into these early microfractures, leading to serpentinization and the emergence of further complex microfractures.

Chapter 2

Footwall geology and deformation at a magma-starved young axial detachment fault: 64°35'E Southwest Indian Ridge (SWIR)

Souradeep Mahato & Mathilde Cannat

Key points: Magma starved seafloor spreading, detachment fault, damage zone, corrugations, antithetic faults.

2.1 Abstract

The eastern Southwest Indian Ridge (SWIR) is a melt-poor end-member region of the global MOR system. The available magma focuses on axial volcanoes, leaving >50 km-wide, nearly amagmatic ridge sections, where seafloor spreading occurs via large offset detachment faults. We utilize shipboard bathymetry, microbathymetry, and ROV dive observations to present map-to-outcrop scale observations of the footwall geology and deformation associated with two successive detachments (D1 and D2) in the 64°35'E region of the SWIR. In situ rock sampling shows that outcrops are made of variably deformed serpentinized peridotites, with very few gabbro dikes. The upper slopes of the axial valley wall show km-sized bench-like structures and is interpreted as the degraded breakaway region of D1. The head scarp along the top of the axial valley wall exposes a ~100 m section of the D2 detachment fault zone, which features a sequence of variably deformed fabric interlayered with anastomosing sigmoidal phacoids, planar fractures, and serpentine breccia/microbreccia/gouge bearing horizons. At the map scale, the active emergence of D1 shows a cusp-and-lobe shape geometry. The lower slopes of the D1 footwall show two distinct domains. The domain to the west features N25° trending corrugations, several NNE trending broad ridges up to 5 km long, and a series of WNW-trending antithetic small offset normal faults. The domain to the east is devoid of these ridges and antithetic faults and also lacks corrugations. This indicates an along-strike variation in the tectonic structure of the D1 exposed fault surface. Sampling and dive observations indicate that the key difference between the corrugated and non-corrugated regions of the D1 fault zone is in the abundance and thickness of horizons of serpentinite microbreccia and gouge, which we propose form preferentially in the fault zone where hydrous fluids are available during deformation. These fluids favor semi-brittle deformation and gouge formation, resulting in a weaker fault zone in the non-corrugated domain compared to the corrugated domain. We interpret the NNE-trending ridges as large undulations of the exposed D1 fault surface, i.e., mega corrugations. Our results suggest that these ridges and the indentations and lobes along the D1 emergence trace result from the activation of linked sigmoidal fault splays surrounding large phacoids (~ 600 thick) of less

intensely deformed serpentinized peridotite in a broad D1 fault zone. This damage zone anatomy would be consistent with seismic reflection observations (Momoh et al., 2017) in the area. The NNE trend of the ridges and the overall N25° trend of the documented corrugations are oblique to the NS spreading direction. We propose that this could result from a local clockwise rotation of strain directions in the more rigid western domain of the D1 footwall. It is not possible with the data available to determine whether these complexities, and the along-axis contrast in D1 fault structures exist because D1 is a young detachment, in the early stages of its development. When compared with corrugated ODFs, the whole damage zone of the flip-flop D1 and D2 ODFs is substantially thicker. Within this thick damage zone, individual exposed fault splays exhibit strain localization over comparable thicknesses (~100 m against ~70 m at documented corrugated ODFs), but the nature of the deformed rocks is different: we did not observe talc-amphibole and/or chlorite bearing sheared serpentinites, and instead documented intensely cataclastic serpentinites, with intervals of gouge and microbreccia up to 8 m-thick.

2.2 Introduction

Oceanic detachment faults (ODFs) accommodate a part of the plate divergence in sections of slow-spreading ridges that have a reduced magma supply, typically but not exclusively, at the end of ridge segments (Buck et al., 2005; Cann et al., 1997; Escartín et al., 2008; Escartín & Cannat, 1999; Sauter et al., 2013; Smith et al., 2008). Observations made at the mid-Atlantic ridge (MAR) show that these detachment faults have large offsets (~5-35 km) and lifetimes ranging between ~1-2.6 myr (Tucholke et al., 1998). Most exhumed fault surfaces are gently dipping (<20°) and show dome-shaped topography. They commonly bear corrugations that are aligned parallel to the spreading direction (Cann et al., 1997; Tucholke et al., 1998), similar to observations initially made on continental exhumed detachment fault surfaces (John, 1987). Several interpretations have been proposed for the origin of ODF's corrugations

(Spencer, 1999; Tucholke et al., 1998; 2008). The most recent papers on the subject reassess these interpretations and propose as an alternative that corrugations form due to brittle strain localization on a network of anastomosing linked fractures (Escartín et al., 2017; Parnell-Turner et al., 2018). Presently, active MAR dome-shaped and corrugated detachments extend between ~7-12 km along the ridge axis (Escartín et al., 2017; MacLeod et al., 2009; Smith et al., 2006, 2014). Micro-earthquakes (deMartin et al., 2007; Parnell-Turner et al., 2017) reveal that the fault initiates at depths of ~7-12 km with a high dipping angle (~60-70°). Dredging, drilling and in situ sampling on a handful of near and off-axis MAR ODFs recovered variably deformed gabbroic rocks, serpentinized peridotite, basaltic breccia, and lesser diabase lithologies (Cannat et al., 1997, 1995; Casey, 1997; Kelemen et al., 2007; MacLeod et al., 2002; Mével et al., 1991; Schroeder et al., 2007). Along the north MAR, areas of asymmetrical accretion dominated by detachment faulting account for ~50% of the ridge length (Escartín et al., 2008) or ~25% of the newly accreted seafloor (Cannat et al., 1995).

The best-studied detachment fault systems along the MAR show that while semi-brittle to brittle fault rocks may be found ~100 m or more below the corrugated surface (Escartín et al., 2017; Karson et al., 2006; MacLeod et al., 2002), the most intensely deformed samples are concentrated in the upper 10 m of the exposed fault zone (Schroeder & John, 2004). When available, submersible observations also reveal the lack of a plurimeter-thick cataclastic domain below the exposed fault (Karson et al., 2006). Such an example has been documented in fossil ocean-continent transition (OCT) detachments (Picazo et al., 2013). Corrugated ODFs at the MAR and other slow-ultraslow ridges typically expose both gabbro and serpentinized peridotites and face volcanic seafloor in the hanging wall (Smith et al., 2006; MacLeod et al., 2009; Cannat et al., 2006). Sample studies and numerical modeling suggest that corrugated ODFs root into a magma-rich, hot ductile domain (Dick et al., 2000; Olive et al., 2010; Casini et al., 2021). Their exposed fault surfaces show brittle to semi-brittle deformation localized in talc-chlorite-amphibole-serpentine bearing greenschist facies assemblages, with rare cataclasites (Boschi et al., 2006; Dick et al., 2002; Escartín et

al., 2003; Hansen et al., 2013; Picazo et al., 2012; Schroeder & John, 2004) One exception is the 13°20'N active MAR detachment, where the exhumed fault exposes silica cemented basaltic cataclastic breccia probably incorporated from the volcanic formations in the hanging wall (Bonnemains et al., 2017).

The easternmost region of the ultraslow-spreading SWIR (east of Melville Fracture Zone) is an end member of the global MOR system in terms of its low overall melt supply (Cannat et al., 2008, 1999; Minshull et al., 2006). It shows domal corrugated structures similar to MAR ODFs, over ~4% of the mapped area (Cannat et al., 2006). By contrast, ~40% of the mapped area shows broad ridges that extend ~25-95 km parallel to the local ridge axis (Cannat et al., 2019, 2006). These broad ridges form in nearly amagmatic spreading corridors between more volcanic domains and do not appear corrugated in shipboard bathymetry (Cannat et al., 2006). They expose mostly (~90%) serpentinized peridotite (Sauter et al., 2013). Both flanks of these ridges are interpreted as exhumed footwalls of opposite polarity (flip-flop) ODFs (Sauter et al., 2013). Compressional wave velocity models indicate that the upper part (down to ~5 km bsf) of the lithosphere in these smooth seafloor domains has crustal physical properties and probably consists of fractured serpentinized peridotites with incipient magmatic bodies (Corbalán et al., 2021; Momoh et al., 2017). Studies of partially serpentinized dredged samples indicate that eastern SWIR detachments root into a brittle-ductile transition region that is made primarily of fresh peridotites, generating high-stress distributed deformation and grain size reduction zones (Bickert et al., 2021, 2020).

The presently active D1 axial detachment at 64°35E (Figure 1) is the focus of the present study. It faces south and has been active for ~300 kyr, cutting through detachment D2, which had an opposite vergence and was active for ~1.5 myr (Cannat et al., 2019). Detachment D1 is, therefore, at an early stage of its development. Its footwall faces sparsely volcanic to non-volcanic ultramafic seafloor on the hanging wall side (Sauter et al., 2013), with increasing magmatism toward the west (Cannat et al., 2006). Seismic reflectors are interpreted as due to detachment-related damage, dip ~50° at ~5 km bsf beneath the D1 emergence (Momoh et al., 2017). Several such

reflectors are imaged over a width of ~0.5-1.8 km, suggesting that the detachment fault damage zone is that broad (Momoh et al., 2017; 2020). Microseismicity is recorded down to a depth of ~15 km bsf in the 64°35E axial region, providing a minimum estimate for the local depth to the brittle-ductile transition (Chen et al., 2023). In contrast to what has been documented in MAR corrugated detachments (deMartin et al., 2007; Parnell-Turner et al., 2020, 2017), earthquakes are not focused along the fault zone and in the detachment footwall but also occur in the hanging wall. All these observations concur to suggest significant differences in the way deformation is accommodated and localized between the more common corrugated-volcanic spreading mode (Cannat et al., 2006) and the nearly amagmatic (i.e., nearly fully tectonic) flip-flop plate divergence mode identified in the eastern SWIR.

This paper presents the first outcrop-scale study of the geology and deformation of the 64°35E SWIR flip-flop fault zones. We use microbathymetry and seafloor exploration videos acquired with the ROV (Remotely Operated Vehicle) VICTOR during the ROVSMOOTH 2017 cruise of RV Pourquoi Pas? These observations take us from the emergence of the D1 detachment in the axial valley to the top of its footwall (top of northern axial valley wall, Figure. 1b) and allow us to document the lithologies and deformation facies associated with the D1 and D2 exposed fault zones. Our results concern the anatomy of these fault zones, the geometry of linked fractures, the distribution and extent of cataclastic deformation, the role of fluids in strain localization, the origin of ODFs corrugations, and the overall thickness of the detachment damage zone. We also bring new constraints on the active internal deformation of the footwall of the young D1 detachment. Together, these results represent new observational constraints on the faulting behavior of the axial lithosphere at ultraslow and magma-starved mid-ocean ridges.

2.3 Data and Methods

[1] The shipboard bathymetry data (50 m grid spacing) used in this study were acquired (and processed, using the Caraibes 5.0 software @Ifremer) during the ROVSMOOTH cruise onboard RV Pourquoi Pas?, with a RESON 7150 multibeam echosounder (12 KHz frequency, beam opening angle of 151°, and a ship velocity of 6 nm/hr). High-resolution bathymetry data (1 m grid spacing) used in this study were acquired during three dives of ROV Victor 6000 (dives 639, 642 and 650; Figure 1b) using a RESON 7125 echosounder mounted on the ROV frame, with an operating frequency of 400 kHz, a beam opening angle of 120°, a velocity of ~0.3 m/s, and maintaining an altitude ~50 m above the seafloor. Ultra-short baseline ROV positioning was not perfect due to the steep and irregular slopes of the study area. Onboard processing of the data was therefore carried out track by track (using the Caraibes 5.0 software @Ifremer). Ifremer then provided us with reprocessed positioning data (using the DELPH'INS 2.3 software (@IXblue). However, most overlapping grids for individual tracks still did not fit correctly. Maps used in this paper are the result of a track-by-track manual adjustment of these grids using the GlobalMapper software (@BlueMarble).

[2] We jointly analyzed high-resolution topography, seafloor ROV exploration videos, and sampling of the footwall of presently active detachment D1. We illustrate dive observations with a selection of video snapshots (field of view ~15-20 m in the foreground unless specified otherwise). We also performed a preliminary optical and SEM (Scanning Electron Microscopy) microstructural study of selected deformed samples (the more detailed study is presented in Chapter 3). We also used side scan sonar data acquired with the TOBI (Towed Ocean Bottom Instrument) during the SmoothSeafloor 2010 cruise of RV Marion Dufresne (Sauter et al., 2013). Map scale data integration and analyses were carried out with the Global Mapper software (@BlueMarble). ROV exploration dives 643, 644, 647, and 649 (Figure 1a) produced seafloor video footage along a total of ~30 km of dive tracks and recovered 118 rock samples. Out of these, 105 samples come from confirmed outcrops (as opposed to talus). The ROV navigation and orientation information (heading direction, pan, and

camera tilt) are used in the areas of interest (e.g., fault scarp sections) to estimate the orientation of structural planes like rock cleavage and schistosity.

2.4 Results

The footwall of the active D1-detachment (the south-facing axial valley wall; Figure 1b and 2a) has a relief of ~2,600 m relative to the axial valley floor, with an average slope of ~30°. The D1 detachment fault zone emerges from the seafloor at or near the base of the wall (Figure 1). ROV observations are too scarce to precisely locate this emergence at the regional scale. In Figures 1 and 2, we thus trace the bottom of the axial valley wall as the southernmost possible location for the emergence of the D1 fault zone, except where dive data brings confirmation on the actual location. ROV dives 643, 647, 644, and 649 recovered variably serpentinized and deformed peridotites (90 out of a total of 118 samples; Figure 1b), with minor gabbros (1 sample in dive 643) and hydrothermal carbonates from the Old City hydrothermal field (20 samples, dives 644 and 649; Lecoeuvre et al., 2021). As will be shown, observations at three different scales, e.g., shipboard bathymetry, microbathymetry, and ROV exploration dives, indicate that the lower (~5,000-3,000 mbsl) and upper (~3,000-2,200 mbsl) slopes of the axial valley wall are very distinct in terms of their morphology and tectonic structure. Three domains will be described consecutively. They are, from bottom to top (Figures. 1b & 2c):

(1) *The exposed fault zone (EFZ) domain:* it covers the lower slopes from north of active fault emergence (E1) up to a slope break that occurs at depths of ~2700 to ~3000 mbsl.

(2) *The degraded exposed fault zone (DEFZ) domain:* it covers an area of convex downward slopes with intermittent exposures of the exhumed D1 fault zone.

(3) *The degraded breakaway (DB) domain:* a ~700-1,500 m wide domain below the top of the axial valley wall, characterized by several hectometers to kilometer-sized benches that represent slid blocks of the degraded D1 breakaway (Figure 2b).

In the following sections, we describe the geology and the structure of each domain, from the base of the wall upward to the top of the axial valley wall, where the seafloor formed by the previous D2 detachment fault is exposed (Figure. 1b).

2.4.1. The Exposed Fault Zone (EFZ) domain

[1] The exposed fault zone domain has an average slope of ~26°. It is structured by north-northeast trending ridges (Figures 1b, & 2a), up to ~300 m wide and ~200 m high, distant by 1 to 2 km, labeled 'A,' 'B,' and 'C' in Figures 2a & 3a. Between these ridges, the topography is lower, and in some instances (as in between ridges B and C; Figure. 3a), gully shaped. This ridge/gully or ridge/lower topography structure has about the same wavelength (1-2 km) as lobate domains visible near the base of the axial valley wall (Figure 2a). In Figure 3a, high-resolution bathymetry allows us to see that the narrow gully between NNE-trending ridges B and C, and the tip of ridge B, collectively correspond to a recess between two lobate domains at the bottom of the wall. In addition to this ridge/lower topography structure, the EFZ domain displays several E-W trending lineaments, characterized by narrow (up to ~160 m wide) slope breaks in shipboard bathymetry (labeled 1 to 4 in Figure. 3a). Some of these lineaments (for example those shown in Figures 3b & c) are traceable up to 4.5 km laterally (Figures 3a, 1b, & 2a). Microbathymetry reveals that these lineaments correspond to north-facing, antithetic fault scarps a few meters high (Figures 3b & c), some of which offset recent talus (Figure 3c). Finally, visible only in the

microbathymetry data are two other types of north-northeast trending lineaments: actual corrugations (~1 to ~30 m high and up to ~400 m long; Figures 3a, b, & c) and faint undulations of the seafloor (less than 1m high and up to 140 m-long; Figure 3b). We now describe these structures and the local geology from observations made during ROV dives 649 and 644.

[2] Dive 649 starts at a depth of ~5085 meters at the bottom of the axial valley wall. High-resolution mapping was unfortunately not acquired there (due to a technical problem), but dive observations are consistent with the high-resolution topographic data acquired ~1 km further west (Figure 3d). A slope break, from 5-10° below to ~30±5° above, is marked by a ~5 m high, ~15-50 m wide bulge, with northward-facing slopes of 25°-35°. This is similar to the hanging wall cut-off observed at the 13°20' and 16°35'N active MAR detachment faults (Escartín et al., 2017; Smith et al., 2014). We interpret this slope break as the trace of the emergence of the active D1 detachment fault. In the area of Figure 3d, this trace curves inward and upward to the north, diverging from the base of the axial valley wall. In the side-scan sonar (TOBI) image (Sauter et al., 2013), the narrow bulge and its adjacent slope break coincide with a 130 m wide lobate band of acoustically bright seafloor (Figure. 2d). A broader (300 m) and more rectilinear E-W band of reflective seafloor that corresponds to locally steeper slopes is found at depths of ~5060 to 5015 mbsl (Figure 2d) and was crossed during dive 649. Other features of the TOBI record in these lower axial valley wall slopes are scaly-shaped narrow reflectors that extend ~400-500 m and trend NW-SE (Figure 2d). Two of these reflectors, in the eastern part of the TOBI coverage, correspond to lobate topography at the base of the wall.

Geological observations made near the base of the axial valley wall at the beginning of ROV dive-649 show lightly sedimented south-dipping planar surfaces that extend several tens of meters along the slope (Figure. 4b & c). These planar surfaces correspond to meter-scale alternations of blocky serpentinized peridotite and horizons of foliated breccia and microbreccia. Outcrops are covered by a thin iron-manganese crust that is commonly eroded off, showing the bluish-white tint of the brecciated intervals (Figures 4a, c, & d). Talus of iron-manganese crust-free rubble also suggests

recent local erosion of these lower slopes (Supplementary Figure. 2, photo 2). In situ ROV sampling of the brecciated intervals (Figure 4a) yields fragile, gouge samples with angular, sub-rounded, rounded, and elongated clasts of serpentinized peridotite and serpentinite in a foliated matrix made of sheared serpentine (Figure 4d & g). Under the microscope, using a retardation plate in polarized light shows that the sheared serpentine has a crystallographic preferred orientation, indicating that crystal plastic deformation mechanisms were activated in these most deformed intervals (Figure 4f).

In the field, the serpentine gouge and microbreccia horizons are <1 m (Figure 4c) to ~8 m-thick (Figure 4a). The intervening layers of blocky, more massive serpentinized peridotite are cut by a dominant, parallel family of fractures and by secondary sets of fractures, the most developed being more steeply south-dipping fractures, which we interpret as Riedel brittle shears (Figures 4c & 5a). A closer look at a recently eroded scarp in one of these blocky horizons (Figure 5a) shows a ~0.5 m-thick greenish-white serpentinite shear zone subparallel to the upper surface of the outcrop (other horizons of this serpentine gouge plus microbreccia material form the local slope, visible in the background of Figure 5a). Serpentinized peridotite blocks above the shear zone are slightly rotated along antithetic sheared fractures (Figure 5b). These fractures are also filled with the whitish-sheared serpentine material (Figure 5b). The serpentinized peridotites below the shear zone are distinctly schistose over at least ~0.5 m (Figure 5a). The schistosity also dips south but more gently than the shear zone. Together, these observations are consistent with a top-to-south shear displacement. The serpentinized peridotites below the shear zone are also cut by several steeper south-dipping fractures, similar to those in the background of Figure 4c, some also lined by white serpentine material (Figure 5a). Outcrops that offer a view to the north (orthogonal to the slope and the plate divergence direction), also locally show an anastomosing fault zone fabric with a wavelength of ~10-15 m below the exposed fault surface (Figure 5c). This anastomosing fabric defines sigmoidal rock bodies (phacoids) that are ~10 m wide and ~4 m thick. The sigmoid peripheral and the neck zone between two sigmoids commonly develop thin greenish-white gouge-bearing microbreccia intervals, whereas the sigmoid core is less deformed (Figure 5c).

[3] In the deepest portion of NE-trending ridge C and the adjacent gully (Figures 3d and 6a), the D1 emergence turns north and upward. The footwall, with WSW to SW-facing, ~30-35° slopes, emerges from a domain of shallower slopes (~13-19°) to the west that is covered by blocky talus (Figure 6a). Moving upslope along the dive 649 path, the outcrops are first barely emerging from the south-dipping slopes and exposing the same assemblage of blocky, fractured, and locally brecciated serpentinites and occasional bluish-white serpentinite gouge. After passing over the tip of ridge C and going toward the N-S trending trace of the emergence (Figures 3a & 6a), the topography is a bit more roughed, with faint undulations that trend N27°-N35°, probably related to the observed anastomosing fault fabric (Figures 6b & c). A massive serpentinized peridotite outcrop a few tens of meters to the east of the emergence (Figure 6d) shows slope parallel curved scaly fault planes (Figure 6d), discordant on an earlier set of meter-spaced, planar, south to southeast dipping fractures that recall those in Figure 4b, with a perpendicular set of secondary joints. Closer to the emergence, at location 9 (Figure 6a), a >1 m thick interval of serpentine gouge and microbreccia sits structurally above these fractured massive serpentinites and coincides with more gentle slopes (Figure 6e). To the north of location 9, there is a domain of smoother southwest-facing slopes that were not explored during dive 649. It displays several faint, N25° to 30° undulations, extending up to 130 m (Figure 6a). These lineaments are not detected in the shipboard bathymetry but are very similar to the small-scale corrugations described in high-resolution bathymetric maps of MAR corrugated detachments (Escartín et al., 2017; Parnell-Turner et al., 2018; Smith et al., 2014).

[4] ROV dive 649 then continues across a domain of gentle south-facing slopes (~20°), covered by talus generated by a horseshoe-shaped erosional scarp, ~100 m high (Figure 6a). This scarp offers a view of multiple ~5-10 m high steps (Figure 6a). Although not explored with the ROV, these steps could correspond to the edges of stacked and anastomosing fault surfaces. Further to the west, the D1 emergence, with slopes of 33-35°, shows undulations at wavelengths of ~20-50 m (Figure 6a). Moving upward onto the tip of NNE-trending ridge B (Figure 3a), the high-resolution

bathymetry shows NNE-trending, east-facing slope breaks or scarps (Figure 6a), revealing a faint slope-parallel planar fabric that could also correspond to stacked fault surfaces (Figure 6a). The most prominent slope break is ~6-12 m high and ~300 m long. The slope (26-27°) above and to the west of this slope break bears a faint N20° trending lineament that can be followed for 27 m (Figure 6a). At a depth of ~ 4530 m, ROV dive 649 crosses the southern end of a prominent corrugation, ~30 m high, 140 m wide, that trends N21°, extends at least 450 m (Figure 3c) and coincides with the local top of NNE-trending ridge B (Figure 3a). Further upslope, the high-resolution bathymetry documents two other faintly corrugated exposed fault zone regions at depths between 3080 and 4020 m, with lineaments trending N357° and N16°, respectively (Figure 3b). These corrugated middle-lower slopes are light to heavily sedimented. Outcrops are characterized by slope parallel, planar (Figure 6f), or curved and undulating fault surfaces (Figures 6g & h), with local occurrences of the greenish-white serpentine gouge (Figures 6f, g & h). Scarps that offer a view below these fault surfaces typically show a few decimeters of gouge and microbreccia, then ~1 m of extensively brecciated serpentinite overlies more massive yet fractured serpentinized peridotite (Figure 6f).

[6] A striking characteristic of these middle-lower slopes of the axial valley wall is the occurrence of several N, NNE, or NNW-facing scarps that offset the exposed detachment surface (Figures 3b & c) and some of the recent talus (Figure 3c). It can be followed up to ~4.5 km in the shipboard bathymetry (Figure 3a). In the high-resolution bathymetry, they range in height between 1 m or less for the NE-trending array that offsets the talus in Figure 3c and 23 m for the scarp numbered #3 in Figures 3a & b. Scarp #2 (Figure 3a) was explored during ROV dive 644 (Figure 7). It exposes a north-dipping fault plane with down-dip to NNW-trending striations and scaly and pullout structures that indicate normal down-to-north displacement (Figure 7b). Beneath this fault plane are a few decimeters of a non-cohesive, yellowish gouge and microbreccia formation (Figures 7c & d). We calculate an average local dip of 35° for this antithetic fault plane using ROV navigation, immersion data, and trigonometry.

Assuming fault dips of 35° scarps #1 to 4 in Figure 3a would amount to a cumulated horizontal throw of ~55 m.

[7] NNE-trending ridge A continues up to ~ 3300 mbsl into the upper slopes of the EFZ domain, just below the Old City vent site (Figure 9a). NNE-trending ridges B and C (Figure 2a) and two other ridges to the west of ridge A (A' and D; Figure 9a) extend up to similar depths. Overall, the topography in the upper slopes of the EFZ domain is more chaotic than in the lower regions, with evidence for substantial mass wasting in the form of hectometer-sized landslide lobes (Supplementary Figure 3). Yet outcrops of decameter-scale fault surfaces remain common (Figures 9b & c). As in the deeper parts of the EFZ domain, these fault surfaces are associated with brecciated, locally schistose serpentinite, with occasional decimeter-scale horizons of pale green serpentine gouge (Figure 9c). Other serpentinite outcrops are more massive, displaying the now typical planar to sigmoidal fracture patterns (Supplementary Figure 4, photos 3-8).

ROV dive 644 explores the NNE trending ridge A from a depth of 4320 m upward. The geology there is more rocky than documented by ROV dive 649 over the same depth range on the western flank of ridge B (Figure 3a). Outcrops of serpentinized peridotites display a range of fracturation facies: from planar fractures, spaced by 1 m or more, with sets of perpendicular joints (Figure 8b) to more pervasively fractured outcrops with decimeter to plurimeter-spaced planar and sigmoidal fractures (Figures 8a, c, & e), and occasional decimeter-thick intervals of the green-white serpentine gouge formation (Figure 8a, & c). These facies can be interpreted in terms of increasing strain. In several instances, the exposed D1 fault surface corresponds to the development of tight concordant fractures, or schistosity (Figures 9d & e), transitioning to meter-spaced sigmoidal fractures ~5 m below (Figure 8d). In other instances, decameter-scale, slope-parallel fault surfaces are discordant on the least deformed fractured facies (Figure 8b). In terms of geometry, the dominant dip of decameter-scaled exposed planar, undulated, and sigmoidal fault surfaces along ridge A varies from southwest-ward (locations 14, 15, and 16; Figures 8a, b & c) to southward (location 19; Figure 8d), then southeast-ward on the eastern

side of ridge A (location 20; Figure 8e). This suggests that the ridge-like topography could be due to kilometer-scale undulations (very large corrugations) of the exposed fault surface.

North-facing, antithetic fault scarps that can be followed a few km in the shipboard bathymetry also remain common in the upper EFZ slopes (Figure 9a). Most active vents of the Old City hydrothermal field (Lecoeuvre et al., 2021) are located along scarp #8 (Cannat et al., in preparation). High-resolution bathymetry in the Old City area reveals at least 6 such scarps, not all of which are detectable in the ship bathymetry. These scarps offset Ridge A', are up to ~30 m high, and distant by ~50-200 m. Collectively, assuming fault dips of 35° (as documented for scarp #2, Figures 7a & b), they would amount to a cumulated horizontal throw of ~200 m.

2.4.2. The degraded exposed fault zone (DEFZ) domain

[9] The DFZ domain is characterized by a bumpy and locally convex upward topography, with more gentle slopes (<25°) than in the EFZ domain below. The limit between the two structural domains corresponds to a slope break at 3000 to 3100 mbsl and to the upper end of the NNE-trending ridges (Figure 9a). Some of the N-facing, antithetic fault scarps that are visible near the Old City vents extend into the DEFZ domain. Observations made during ROV dive 647 show that south-facing DEFZ slopes expose the same combination of decameter-scale, breccia-lined fault surfaces (which might, in most cases, be decameter-sized blocks, Figures 10a & d) and fractured serpentinites (Figures 10b, & c) as the EFZ domain. Most fractures dip south. They form networks and range from pluri-meter spaced with conjugate joints (Figure 10b) to decimeter-scaled with local schistose intervals (Figure 10c). The last probable outcrop of an exposed fault surface was encountered at a depth of 2771 mbsl (Figure 10d). North-facing slopes and the depressions associated with the antithetic scarps are covered by pelagic sediments and talus, including fresh talus without sediment cover (Supplementary Figures 3 & 4, photo 26).

2.4.3. The degraded breakaway (DB) domain

[10] At 2603 mbsl, ROV dive 647 encountered a 1 to 2-m-thick outcrop of semi-indurated pelagic sediment, with a cm-thick crust of iron-manganese oxide (Figure 10e), very similar to outcrops found over the top of the axial valley wall (Figure 11b). This old (based on the thickness of the oxide crust) and thick sedimentary formation sign the location of the deepest slid block of the DB domain. Topographically, there is no clear break with the DEFZ domain below: the transition occurs within the region of convex upward slopes that extend between ~2500 and ~2770 mbsl at the latitude of dive 647 (Figures 2c, 9a & Supplementary Figures 7a, & d). Above this region of convex upward slopes, the uppermost portion of the wall is structured in a series of gently north or south-facing benches and steeper and eroded south-facing slopes (Figures 11a & 12a). The benches are 100 m to ~2 km in length, and 20 m to 450 m in width. They represent the top surfaces of coherent blocks that have slid downslope from the top of the wall (Figures 12a & c). The intervening south-facing scarps are 45 m to ~250 m high. They bear decameter-scale erosional ridges and gullies that connect to multiple generations of overlapping debris cones at the base of these scarps (Figure 12a). Several north-facing, E-W to WNW trending antithetic faults offset these erosional ridges and gullies (Figures 12a, b & d).

[11] Going upslope from the first outcrop of thick sediments at 2603 mbsl (Figure 10e), ROV dive 647 encountered smooth sedimented terrains, sedimented talus (Supplementary Figures 3 & 4 photos 31 & 34), and a hectometer-sized patch of recent (non-oxide-coated) carbonate-indurated sediments (Supplementary Figure 4 photo 34; dive 647). The first notable scarp, at 2434 mbsl (location 32 in Figure 11a), exposes a chaotic formation of serpentinite gouge and microbreccia with an irregular foliation (Figure. 10f). This outcrop is unconformably covered by ~1 m of semi-consolidated sedimented talus, and pelagic sediments. It is free of oxide coating and, therefore, has been recently rejuvenated. Dive 647 then explored the main, up to 55 m-high scarp

just below the top of the axial valley wall (Figure 11a). At the top, ~2315 mbsl, there is a 1-2 m-thick, oxide-coated indurated sediment formation (Figure 11b) similar to that encountered at ~2603 mbsl at the base of the DB domain (Figure 10e). The edge of the scarp exposes extensively brecciated serpentinites, with a thinner oxide-coating, or in several locations, oxide-free with recent talus, indicating recent mass wasting. These brecciated outcrops display meter to plurimeter-thick pale green, serpentine gouge-bearing horizons (Figure 11d), intercalated with brecciated and locally schistose serpentinite with sigmoidal phacoids (Figure 11c). Pale green gouge-bearing horizons are found at the top of the wall but also deeper down the scarp (the outcrop in Figure 11d is ~55 m below the top). The schistosity, the alternation of more and less schistose horizons, and the gouge-bearing horizons all have a moderate dip to the north, sub-parallel to the dominant slope at the top of the wall, indicating that this deformation sequence relates to the D2 detachment fault.

[13] The top of the axial valley wall was also mapped (MAP-639; Figure 1b) and explored further to the west during ROV dive 643 (Figure 1b). This is a geologically more complex and under-documented region of the wall. There are several volcanic ridges in the axial valley and in the lower slopes of the wall at the same longitude (Figure 1b) and (Sauter et al., 2013), and dive 643 did sample a few gabbroic samples, in addition to serpentinized peridotites (Figure 1b). Topographically, it is also a complex region: the top of the wall bends southward just west of the area explored during ROV dive 643 (Figure 1b), and the north-facing slopes of the wall are affected by significant mass wasting (Supplementary Figure 5b with 3D view). As a result, the top of the axial valley wall is a steep crest (Figure 13a), with slopes > 50° on the north-facing scarp, that locally exposes nearly continuous outcrops over a ~100 m drop.

[14] ROV exploration dive 643 first explored the north-western slopes of the area mapped during ROV dive 639, structured by narrow (≤ 20 m-wide) slope-parallel benches separated by 35 to 40°, NW-facing, eroded slopes (Figure 13a). These eroded slopes expose slope-parallel (i.e., dominantly NW-facing), breccia-lined fault planes (Figure 13b), and variably schistose and brecciated serpentinite with sigmoidal fractures (Figure 13c), and occasional decimeter-thick intervals of pale green

serpentine gouge, also dipping to the north-west (Supplementary Figure 6 photos 2, 4-6). At the crest-shaped top of the ridge valley wall, the topography is smooth, exposing brecciated serpentinite with a north-dipping schistosity (Figure. 13d) or a chaotic formation of microbreccia with gently dipping horizons of pale green serpentine gouge intervals (Figure 13e), that hardly emerges from the topography. The shallowest sections of the crest (< 2500 mbsl), exposing this microbreccia formation, form small polygonal platforms, dipping <15° to the south or to the north (Figure 13a). To the south of one of these platforms, the microbathymetry reveals ~5-20 m high steps that appear to be the trace of an ESE-dipping planar fabric (Figure 13a). ROV dive 643 explored the eroded south-dipping slopes to the east of these steps and documented fractured to schistose and brecciated to massive serpentinites with slope-parallel fractures (Supplementary Figure 6 photos 24, 25, & 27- 29).

ROV dive 643 then performed two traverses of the nearly continuous outcrops that form the ~100 m high scarp on the north side of the summit crest (Figure 13a). The outcrop contains a few decimeter-thick gabbro dikes (identified based on sampling and on the prominence of sub-orthogonal joints; Figure 14f). The top 5-15 m consist of extensively brecciated serpentinites, with a gently north-dipping schistosity and local, vein-like pale green serpentine gouge horizons (Figures 14a, b, & c). Below this brecciated horizon, the dominant fabric consists of sets of fractures similar to those observed in association with D1 fault zone exposures further down the axial valley wall, with a progression from massive outcrops with orthogonal fracture sets (Figure 14f) to brecciated and locally schistose outcrops with anastomosing fractures that define sigmoidal phacoids (Figure 14d, h & i). This fabric dips to the ESE and, therefore, is discordant to the schistosity in the overlying breccia (Figure. 14a). It is also discordant to decameter-sized fault planes (Figure 14e) and plurimeter-thick schistose intervals (Figure 14g) that also dip to the north at several locations within the fractured sequence. Such discordant relations between the most deformed (fault surfaces, schistose horizons, gouge, and foliated microbreccia) and the less deformed (planar and sigmoidal-shaped fractures) intervals are also very similar to those observed in association with D1 fault zone exposures (Figures 6d & 8b). The outcrops

described in Figure 14 extend ~300 m along-slope, and the ESE-dipping fabric there could well correspond to the planar fabric observed south of the summit crest and another ~200 m to the southeast.

2.5 Discussion

2.5.1. Test of the flip-flop hypothesis and age of the D1 axial detachment fault

Our observations confirm that the southern slopes of the axial valley wall expose serpentinized peridotite, which confirms that the D1 detachment is nearly amagmatic (Sauter et al., 2013). Our observations also confirm that the northern slopes of the axial valley wall expose older, north-facing fault surfaces with scaly and pullout structures indicative of normal, top-to-the-north displacement (Figure 13b) and fault rocks with north-dipping structures (Figures 11c and d, and 13c, d and e). These outcrops are covered with 1-2 m of sediments, with a cm-thick coating of iron-manganese oxides (Figure 11b). This is consistent with the flip-flop hypothesis proposed by Sauter et al. (2013), in which these northern slopes represent the older exposed fault surface of the north facing D2 detachment (Figure 1b). Our observations also show that the upper slopes of the footwall of the D1detachment are made of hectometer to kilometer-sized blocks of the former breakaway that have slid downslope due to gravity (Figure 12). Following Cannat et al. (2019), we propose that these large blocks formed early in detachment D1 life, probably because, in its initial stages, it emerged with a dip that exceeded the stability of the exhumed serpentinized peridotites (Cannat et al., 2013). Similar degraded breakaways have been documented in MAR corrugated detachments (Smith et al., 2014; Escartín et al., 2017). Exposures of the older and sedimented D2 fault surface some 1.9 km to the south of the top of the wall on the dive 647 track (Figures 9a and 10e) allow us to constrain the width of this D1 degraded breakaway domain. It is consistent with the width hypothesized by Cannat et al. (2019) based on their interpretation of shipboard bathymetry. Our observations, therefore, also support the ~300 kyr age estimated for the initiation of

D1 by these authors (based on the horizontal distance between the emergence and the reconstructed breakaway, assuming a fully tectonic plate divergence).

2.5.2. The D1 exposed fault: NNE-trending ridges, smooth vs corrugated seafloor

Below the degraded breakaway, our observations document a narrow (~350-1200 m-wide) domain with a rather chaotic topography that exposes blocks and occasional in-situ exposures of south-facing normal fault surfaces (Figure 10a and d). We interpret these as the youngest preserved D1 fault structures and propose that, in this domain (degraded exposed fault zone or DEFZ), the young D1 fault zone dissected slid blocks of the degraded breakaway (see the conceptual sketch in Figure 15b). Below the DEFZ domain and down to the base of the D1 footwall, the ROV dives document frequent outcrops of fault surfaces and of deformed serpentinized peridotites. There are talus (Figures 3b, 3c, and 6a), and erosional scarps (Figure 6a), but most of this terrane is made of in-situ D1 fault material. At the scale of the shipboard bathymetry map (Figure 2a), this exposed fault zone (EFZ) domain is topographically complex. To the east, it is smooth and bumpy, the bumps corresponding with lobate scale-like structures seen in TOBI images (Figure 2d). To the west, and over most of the area covered in this study, it is structured by the A, B, and C prominent NNE-trending ridges (Figure 2a), themselves cut by WNW-trending benches which we have shown to be arrays of recent small offset antithetic normal faults (Figures 3b, 3c, 7 and 12d).

Prior to our study, with only shipboard bathymetry, the nature of the NNE-trending ridges was enigmatic, and the prevalent, although not convincing, interpretation was that the ridges, and the intervening gullies, were large mass-wasting structures (erosional ridges and canyons). We now interpret these ridges as very large (up to 380 m in amplitude and 0.5-2 km in wavelength) members of the corrugation family (i.e., undulations of the fault surface itself). Our key supporting observation is that going up slope ridge A along dive 644 (Figure 3a), fault surfaces and dominant fractures dip to the SW, S, or SE parallel to the local slope (Figure 8).

The ridge is, therefore, shaped by undulations of the D1 fault structures. Smaller, hectometer-spaced undulations (up to 45 m in amplitude) that unambiguously belong to the family of ODF corrugations (Cann et al., 1997; Smith et al., 2006; MacLeod et al., 2009; Escartín et al., 2017) are also visible in the microbathymetry map of ridge B (Figures 3b and c). These can be followed up to 350 m downslope across the microbathymetry coverage, so they might be longer. Given their size, they would also be visible in shipboard bathymetry, were it not for the complex ridge-gully shaped topography. Finally, there are numerous instances of outcrop-scale undulations of the exposed fault surface, < 1 m in amplitude (Figures 6c, 6g, 6h, 8f). These outcrop-scale undulations are most likely the cause of the fainter lineaments seen in the microbathymetry (Figures 3b and 6a). Dive observations show that they result from decameter-scale pullout structures on the exposed fault (Figures 6g and h), and from the sigmoidal phacoids outcrop-scale structuration of the fault zone (Figure 6c). For these hectometer and decameter-spaced corrugations, our results, therefore, fully support the interpretation proposed by Escartín et al. (2017) and further detailed by Parnell-Turner et al. (2018): they record strain localization structures associated with the ODF activity.

Although the correspondence is not perfect, there is a connection between the tip of the NNE-trending ridges, indentations of the trace of the D1 emergence, and lobate slope breaks near the base of the axial valley wall (Figure 3a). In the initial shipboard topography-based interpretation, these lobate structures were envisioned as possible kilometer-wide debris lobes. Microbathymetry and observations made during ROV dive 649 support an alternative interpretation of the ridges, indentations, and lobes: we propose that they result from the activation of fault splays surrounding hectometer to km-sized phacoids (megaphacoids) in a broad D1 fault zone (Figure 15b). The indentation of D1 emergence around the tip of ridge C is about 1.2 km long (Figure 3a). In our interpretation, it results from the activation of a more internal sigmoidal fault splay, taking most, if not all, of the displacement over from another fault splay that emerged further down near the base of the wall (Figure 3a). Assuming the same 30° emergence angle for the two proposed fault splays, this 1.2 km distance

corresponds to an across-fault splays distance (i.e., a megaphacoid thickness) of ~600 m. We thus propose that the D1 damage zone is at least that broad and comprised of anastomosing domains of more localized deformation (i.e., fault splays) that can change activation status through time. Those splays that are active at the shallowest depths are exposed at the seafloor in the footwall (Figure 15b). In this interpretation, the NNE-trending ridges develop near the linkages between these fault splays; therefore, although they correspond to fault surface undulations that are much larger than the corrugations reported so far at ODFs, in our interpretation, these ridges also record strain localization structures associated with ODF activity.

NNE-trending ridges are absent in the eastern part of our study area (east of ridge C; Figure 2a). Hectometer-spaced corrugations are not visible in the sparse bathymetric coverage (Figure 6a), nor are they visible in the TOBI seafloor reflectivity images (Figure 2d). At the outcrop scale, sigmoidal phacoids are locally observed (Figure 5c) and might produce faint undulations visible in the microbathymetry (Figure 6a), but most ROV dive 649 observations in the eastern lower slopes of the axial valley wall point to extensive (up to 8 m-thick; Figure 4a) outcrops of gouge-bearing brecciated serpentinites, intercalated with fractured and locally schistose serpentinized peridotites (Figures 4b, 4c, 5a and 6e). In the thin section, the gouge and microbreccia intervals display foliated microshear domains with a fine matrix of serpentine crystals with both a shape and a crystallographic preferred orientation (Figure 4d, e, and f). Our interpretation is that these fibers crystallized during the deformation at the expense of serpentinite microclasts (Figure 4g) and that the deformation mechanisms involved are, therefore, semi-brittle. Dive observations also suggest that the gouge and microbreccia intervals originate in fractures of the more coherent serpentinized peridotite intervals (Figure 5a). We propose that these cracks create pathways for hydrous fluids and that these fluids then favor the local recrystallization of serpentine, leading to strain localization and further semi-brittle deformation.

Exposures of the D2 fault zone near the top of the axial valley wall show thick intervals of gouge and microbreccia (Figures 11c, 11d, and 13e). Outcrops of gouge-bearing

brecciated serpentinites are, by contrast, far less common in the corrugated domain to the west: they line some fault planes (Figures 6f, 6g, 6h, and 8d), and the peripheral domains of sigmoidal phacoids (Figure 8a and c). When present, they are also thinner (a few decimeters, up to 1 m in Figure 8d). The overall rheology of the fault zone in the corrugated domain is, therefore, closer to purely brittle and probably also stronger. A contrast in footwall strength between the two regions is also consistent with the higher relief of the footwall in the corrugated domain (Figures 2a and 15b). However, a contrast in strength is probably not the direct cause for the presence or absence of corrugations. Rather, in the interpretation proposed by Parnell-Turner et al. (2018), which we support, the fault surface is expected to present sub-parallel undulations or corrugations if fractures link in such a way as to define phacoids that are elongated in the direction of fault displacement. If hydrous fluids lead to enhanced displacement along fractures that form in relatively little deformed serpentinized peridotite (such as in Figure 5a), it is possible to envision that phacoids will be more easily subdivided into less elongated and more flattened shapes that would not produce corrugations, but possibly instead create the scale-like lobate structures seen in the TOBI image (Figure 2d).

With the exception of the gouge-microbrecciated horizons, the pattern of deformation is the same in the corrugated and non-corrugated regions: from orthogonal fractures to linked fractures, sigmoidal phacoids, and brecciated serpentinized peridotite (see for example Figure 8, and Figure 14a). Our hypothesis is, therefore, that the key difference between corrugated and non-corrugated regions of the exposed ODF surfaces in our study area is that hydrous fluids were more readily available during deformation in the non-corrugated regions.

2.5.3. The D1 damage zone at depth

From what precedes, we derive several constraints to draw the conceptual sketches in Figure 15: 1- the D1 damage zone contains megaphacoids that are of the

order of 600 m wide in the across-fault direction and about the same along-axis (based on the dimensions of indentations and lobes in the emergence region; Figure 3a); 2- fault splays, both active and formerly active, between these megaphacoids are probably up to ~200 m-thick (based on the lithostructural log in Figure 14a), if the most intensely strained region, which will ultimately form the exhumed fault surface, is centered relative to the megaphacoids; 3- there are significant variations in the rheology of these fault splays depending on the abundance of semi-brittle microshear zones, which we relate to the availability of hydrous fluids. Seismic reflection constraints on the dip of the fault (50° at 5 km depth; Momoh et al., 2017) consist in several planar reflectors with that dip, interpreted as zones of fault damage, the most far apart of which are distant by about 1.5 km (Momoh et al., 2017). We take this as the across-fault width of the D1 damage zone at those depths (Figure 15b) and draw a thinner damage zone up in the DEFZ and EFZ regions of the footwall that expose a younger D1 fault. Compared to exposed fault zones documented at the Atlantis Massif (Boschi et al., 2006) and 13°20'N (Escartín et al., 2017; Parnell-Turner et al., 2018) dome-shaped corrugated ODFs, the estimated thickness of the exhumed fault zone is comparable, but here we have several fault splays and km-sized phacoids, that are not documented at the dome-shaped ODFs, and make for a much thicker damage zone. At the 13°20'N ODF, the fault zone is described as ~75m thick, with individual fault rock exposures up to 10 m high that show brittle deformation structures (in basalts, for the most part) comparable to those documented in the least deformed portions of Figure 14a (Escartín et al., 2017). The real difference is that dome-shaped corrugated ODFs do not expose the meter to decameter-thick sections of cataclastic microbreccia and gouges documented here in non-corrugated regions, although isolated samples have been reported (Schroeder and John, 2004; Schroeder et al., 2007; Picazo et al., 2013; Bonnemains et al., 2017). The other key difference is that the most deformed intervals in ultramafic rocks exposed at these more magmatic ODFs contain talc, amphibole, and or chlorite-bearing serpentinite, which we have not documented in the D1 and D2 exposed fault zones.

In the vertical damage zone section of Figure 15b, about 3 km south of the D1 emergence, we propose a simplified case in which brittle deformation further down has produced similar-sized megaphacoids in both the corrugated and the non-corrugated regions. In Figures 15c and d, we then zoom into the fault zone at an intermediate depth, about 1 km to the south of its emergence (Figure 15b), in order to illustrate how fault splay geometry could then evolve in the corrugated and non-corrugated regions. In corrugated regions, the original megaphacoids have been further fractured, but few fractures have evolved into high-strain shear zones so that the overall ridge and gully-shaped topography of the active fault splay have been maintained. By contrast, in the non-corrugated region, new fractures in the original megaphacoids have evolved into high-strain fault splays, thanks to the activation of semi-brittle deformation mechanisms, so that the original fault splay topography has been leveled.

2.5.4. Antithetic normal faults, the direction of corrugations, and the strength of the D1 footwall and fault zone

The antithetic, north-facing normal faults documented in this study have small, estimated offsets (we estimated a cumulated horizontal offset of only ~255 m for antithetic faults numbered 1 to 10 in Figures 3a and 9a). They are very recent and probably active (they dissect recent talus and erosional ridges; Figures 3c and 12b), have a relatively shallow dip (~35° for the exposed fault plane in Figure 7), and are found from the base of the EFZ domain (Figure 3a), all the way up the wall into the DB domain (Figure 12b). They do not, however, occur in the non-corrugated eastern part of our study area (Figure 2a). Their development, therefore, appears connected to the rheological behavior of the D1 footwall in the corrugated and NNE-trending ridge-bearing domain.

Small offset normal faults that deform the exhumed footwall have been reported at continental detachment fault systems (Little et al., 2019; Mizera et al., 2019) and in

other geological studies of corrugated domal ODFs at the MAR (Atlantis Massif; Karson et al., 2006; 13°N; Escartín et al., 2017). They have also been inferred from the distribution of microseismicity (TAG; deMartin et al., 2007). However, none of these occurrences is really similar to the tight network of small offset normal faults documented here. In the case of the 13°N detachment, the small normal faults developed at the end of the ODF activity (Escartín et al., 2017). Numerical models of ODF formations suggest three perspectives to discuss the normal faults in our study area. Kinematic models that involve flexural deformation of the ODF footwall as a response to unloading stresses caused by detachment faulting do predict extension in the shallow footwall and compression in the lower half of the plate (Buck et al., 1988). Reverse faults documented in gabbros drilled at the Atlantis Massif (Pressling et al., 2012), and reverse faulting earthquakes recorded at depths > 3km in the footwall of the 13°20'N MAR domal ODF (Parnell-Turner et al., 2017) have been interpreted in this frame. A different approach, proposed by Sandiford et al. (2021), models footwall exhumation as a solid block rotation controlled by the concave downward shape of the detachment. In this frame, normal faulting in the footwall accommodates the transition from solid block rotation in the detachment to horizontal plate divergence after exhumation. Finally, there is the modeling approach of Bickert et al. (2020), who do not specifically address the origin of the flexural stresses responsible but identify antithetic normal faulting of the footwall as a component of what they call the "short detachment" spreading mode in a model setting with no magma input and a thick (and therefore strong) axial lithosphere. In their model, which was specifically designed to explore the formation of flip-flop ODFs in our study area, antithetic faulting is focused in a single secondary fault zone that eventually (ODFs in their runs last 1 to 2 myr, similar to flip-flop detachments in the SWIR 64°E region; Sauter et al., 2013) takes over as the main (flip-flop) ODF. The natural case documented here is different: antithetic normal faulting is distributed over the whole height of the footwall. However, as D1 is young, this could represent the early stages of this short detachment mode.

Another thing to take into account when comparing nature to 2D numerical models, is that ODFs are, in fact, 3D. This is clearly true for corrugated dome-shaped detachment faults: their exhumed footwall is typically longer across-axis than in the along-axis direction (Smith et al., 2006; MacLeod et al., 2009; Cannat et al., 2009). ODFs in the SWIR 64°E region are much longer along-axis the, D1, for example, can be followed along the axis at least 45 km and up to 85 km (Cannat et al., 2019), far beyond the area of our study (Figure 1a). Two observations do, however, point to a not insignificant role of along-axis variations in the strength of the D1 footwall and fault zone. The first observation, of course, is the contrast between the corrugated and antithetic fault-bearing region of the footwall where most of our dive observations were made and the non-corrugated, devoid of antithetic faults in the eastern domain. We proposed earlier that this contrast is associated with a change in the rheological behavior of shear zones in the D1 fault zone, from brittle and possibly stronger in the corrugated region to semi-brittle and probably weaker in the non-corrugated region. The other observation concerns the direction of the observed corrugations.

Corrugations at dome-shaped detachment fault surfaces of the MAR are parallel to sub-parallel to the spreading direction (Cann et al., 1997; Smith et al., 2006; MacLeod et al., 2009). This is also the case at domal ODF surfaces documented in the eastern SWIR, near our study area (Cannat et al., 2009). However, the dominant trend of hectometer and decameter-spaced corrugations documented in this study is N25°, at an angle to the N355-N10 spreading direction derived from magnetic anomalies (Cannat et al., 2006; Patriat and Segoufin, 1988; Lemaux et al., 2002). NNE-trending ridges, which we interpret as mega-corrugations, have the same discordant trend (Figure 2a). Note that the more northerly spreading direction is also consistent with the orientation of fault scarps and volcanic ridges in the axial valley (Figure 1b). The interpretation we propose is that this reflects a clockwise rotation of strain. This rotation would affect an ~10 km-long stretch of D1: in the shipboard bathymetry, NNE-trending ridges are detected over about 7 km along the axis (Figure 2a), and benches that signal antithetic normal faults can be traced west at least 10 km, all the way to the more volcanically active domain mapped during ROV dive 641 (not

considered in our study; Figure 1b). Such a deca-kilometer-scale, clockwise strain rotation could result from an along-axis change in the D1 exhumation rates, with slightly faster rates in the non-corrugated, probably weaker, eastern domain, which, based solely on shipboard bathymetry at this point, extends east at least 35 km along-axis (Figure 1a). This interpretation would, of course, have to be tested with new microbathymetry and dive observations. Enigmatic NNW-trending undulations of the seafloor, spaced by ~500m and up to 100 m-high, are visible in the shipboard bathymetry on the north flank of the footwall at the longitude of dive 649 (Figure 1b). There is no reported equivalent to these structures in the axial valley seafloor that is thought to represent the older portions of the D2 exhumed surface (Sauter et al., 2013). Could they also be due to the 3D internal deformation of the D1 footwall? Are these complexities expressed because D1 is in its early stages of development? Or is the corrugated domain we investigated characteristic of nearly amagmatic ODFs when they approach more magmatic regions of the ridge? If so, why would such transitional regions of the ODF fault zone develop less of the fluid-enhanced serpentinite gouges?

2.6 Conclusions

We present results from an ROV, shipboard bathymetry, and microbathymetry survey of the exposed fault surfaces of two consecutive (D2 and D1) flip-flop detachment faults in the northern axial valley wall of the SWIR at 64°35'E. This investigation provided microbathymetry, outcrop visual observations, and in situ samples to constrain several aspects of the anatomy of these detachment fault zones. Our main findings and preferred interpretations are as follows:

1- The axial valley wall from bottom to top exposes variably deformed serpentinized peridotites, with very uncommon gabbro dikes, and the top of the wall, as well as the scarps that limit blocks of the degraded D1 breakaway, expose highly deformed material, including serpentinites microbreccia and gouge, with a low northerly dip, consistent with them being exposed fault rocks from the previous D2 detachment. Our observations, therefore support the nearly amagmatic, flip-flop

ODFs interpretation (Sauter et al., 2013). The width of the D1 degraded breakaway confirms the ~300 kyr age estimation (Cannat et al., 2019) for the initiation of the D1 detachment.

2- The objective of the ROVSMOOTH cruise was to characterize the geology of the smooth ultramafic seafloor domains (Cannat et al., 2006) formed by eastern SWIR nearly amagmatic ODFs. Yet we have documented corrugations and NNE-trending broad ridges that we interpret as mega-corrugations in the lower slopes of the D1 exposed footwall. We have also documented sets of recent and probably active small offset antithetic normal faults that dissect these ridges and the corrugated terranes. By contrast, in a more easterly part of the study area, the exposed D1 fault surface is indeed smooth, with no corrugations. The difference between the two areas, corrugated and non-corrugated, is also expressed in the abundance of serpentinite microbreccia and gouges: they are up to 8 m-thick in the smooth domain and only a few decimeter-thick and spatially less continuous in the corrugated domain. We propose that these gouge-microbreccia intervals develop when hydrous fluids are available in the fault zone.

3- Our observations of the exposed D1 and D2 fault zones and the indented and lobate shape of the D1 emergence lead us to propose that the damage domain of these two ODFs is very thick, with fault splays linking around pluri-hectometer-sized phacoids of less deformed serpentinized peridotites. These linked fault splays, each corresponding to at least 100 m of more intensely deformed rocks, could correspond to the seismic reflectors imaged at depths down to 5 km below the D1 emergence (Momoh et al., 2017). These reflectors are found over an across-fault distance of ~1.5 km, which may be the thickness of the D1 damage zone. This is substantially more than documented at domal corrugated ODFs from more magmatic ridge settings. The thickness of deformed rocks in individual fault splays (at least 100 m) is comparable, but the nature of the deformed rocks is not: ultracataclastic and gouge intervals are uncommon at these more magmatic domal ODFs, while sheared serpentinites commonly contain talc, amphibole and/or chlorite.

4- Our observations document along-axis variations of the characteristics of the D1 footwall, with an eastern non-corrugated smooth domain and a more westerly domain that has corrugations, NNE-trending ridges (mega-corrugations?), and small offset antithetic normal faults, and where ultracataclastic and gouge horizons are not as developed. This corrugated domain is also where the axial valley wall is higher. Together, these characteristics point to a stronger D1 fault and footwall. Another intriguing characteristic of this corrugated domain is that the corrugations and the NNE-trending ridges make a 15-25° clockwise angle to the spreading direction. We propose that such a clockwise strain rotation over a deca-kilometer scale could also be due to along-axis changes in the fault and footwall strength, with a weaker fault and footwall in the non-corrugated domain to the east. This 3D perspective poses a possible challenge to 2D numerical models of oceanic detachment faults and emphasizes the intricate complexity of geological processes.

2.7 Chapter 2-Figures (1-15)

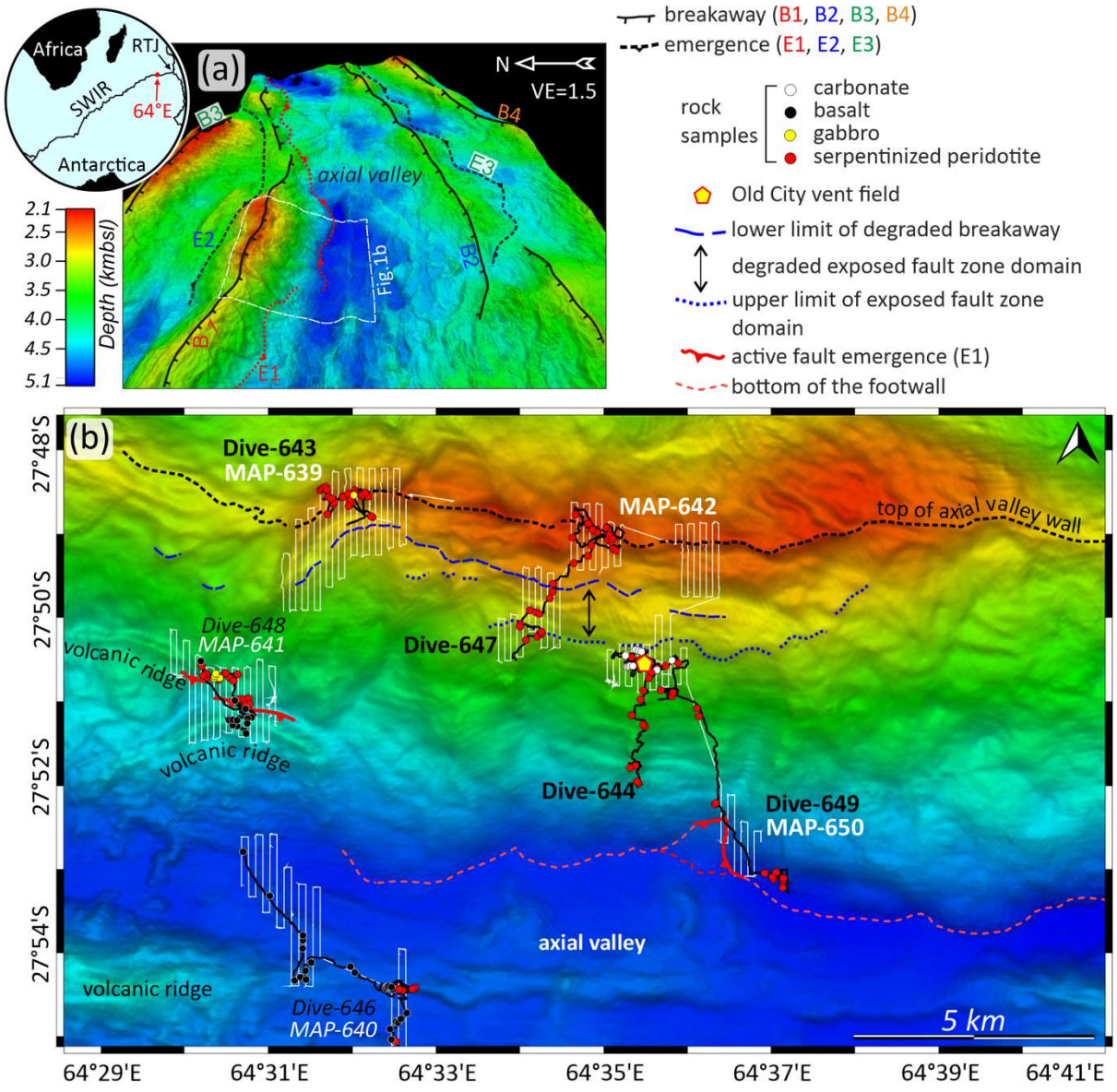

***Figure 1**: Regional context and location of ROV dives. (a) 3D view of shipboard bathymetry (view toward east) over the 64°35' E near axis region of the eastern SWIR. This view highlights the breakaways (B1 to B4) and emergences (E1 to E3) of recent axial detachments (Sauter et al., 2013). (b) shipboard bathymetry in map view (location in a), focusing over the axial valley and the northern axial valley wall, corresponding respectively to the hanging wall and footwall of active detachment D1. Tracks of ROV microbathymetry surveys are shown as white lines, tracks of ROV exploration dives in black, and the primary lithology of recovered samples is indicated with circular-colored symbols. ROV dives analyzed in this paper are numbered in bold. The two blue dashed lines are limits traced based on combining bathymetry and dive geological observations: long dashes for the base of the degraded breakaway domain and short dashes for the base of the degraded exposed fault zone domain (see text).*

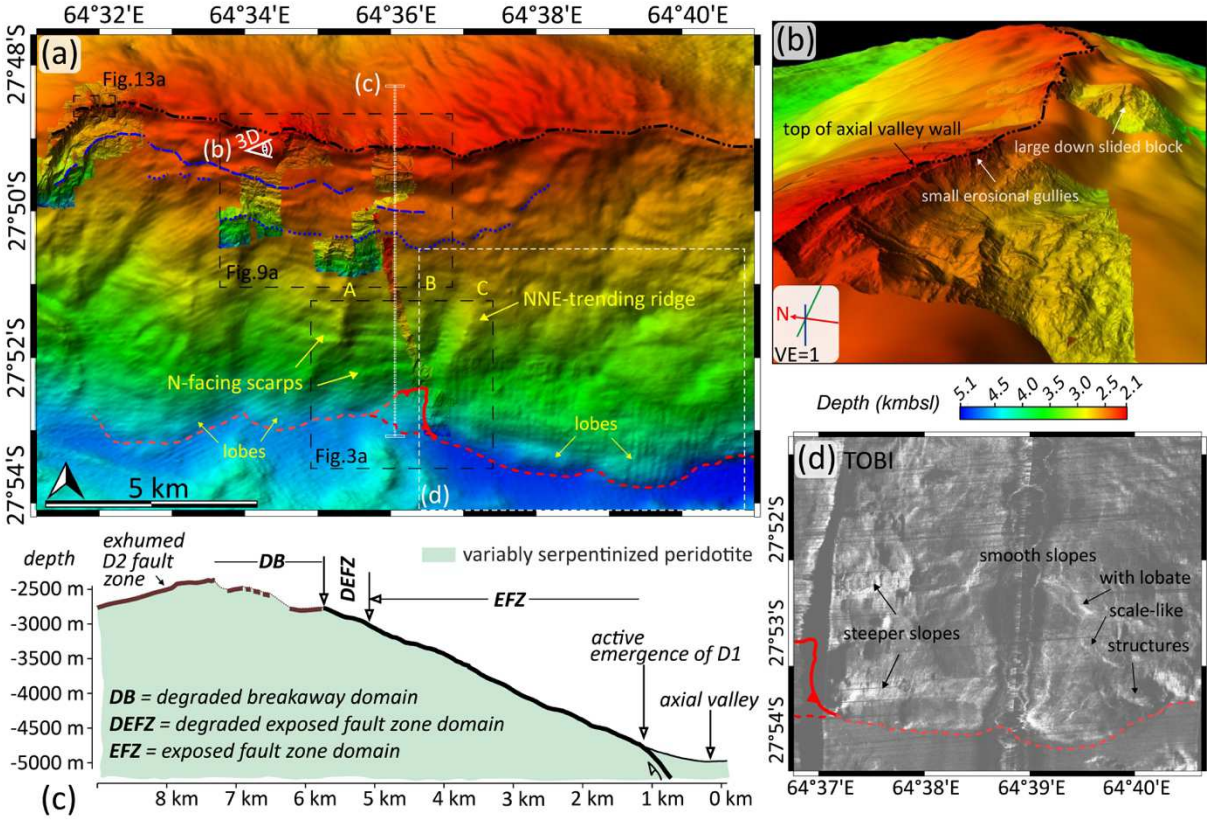

***Figure 2**: Map scale characteristics of the D1 footwall. (a) Microbathymetry for ROV dives 639, 642, and 650 overlain on shipboard bathymetry (color scale in b). Color scales for microbathymetry as in detailed Figures 3a, 9a, and 15b (located by insets). Symbols for D1 emergence, base of degraded fault zone domain, bottom of degraded breakaway domain, and top of footwall, as in Figure 1b. Illumination from the 315°N direction emphasizes north-facing scarps, particularly in the bottom half of the wall. NNE-trending ridges A, B, and C are numbered as in Figure 3a. (b) Perspective view of the upper portion of the axial valley wall and the degraded breakaway region, located in a, showing hectometer to kilometer-scale slid blocks, rigid or internally deformed, and more recent and smaller scale erosional gullies in the steepest scarps. (c) Morpho-tectonic interpretation of a north-south cross-section (positioned in a) of the exhumed detachment fault (D1) footwall, no vertical exaggeration. (d) Seafloor reflectivity image (TOBI; Sauter et al. 2013; located in a), showing the smooth eastern lower slopes of the footwall, with lobate, scale-like structures and two regions of steeper slopes.*

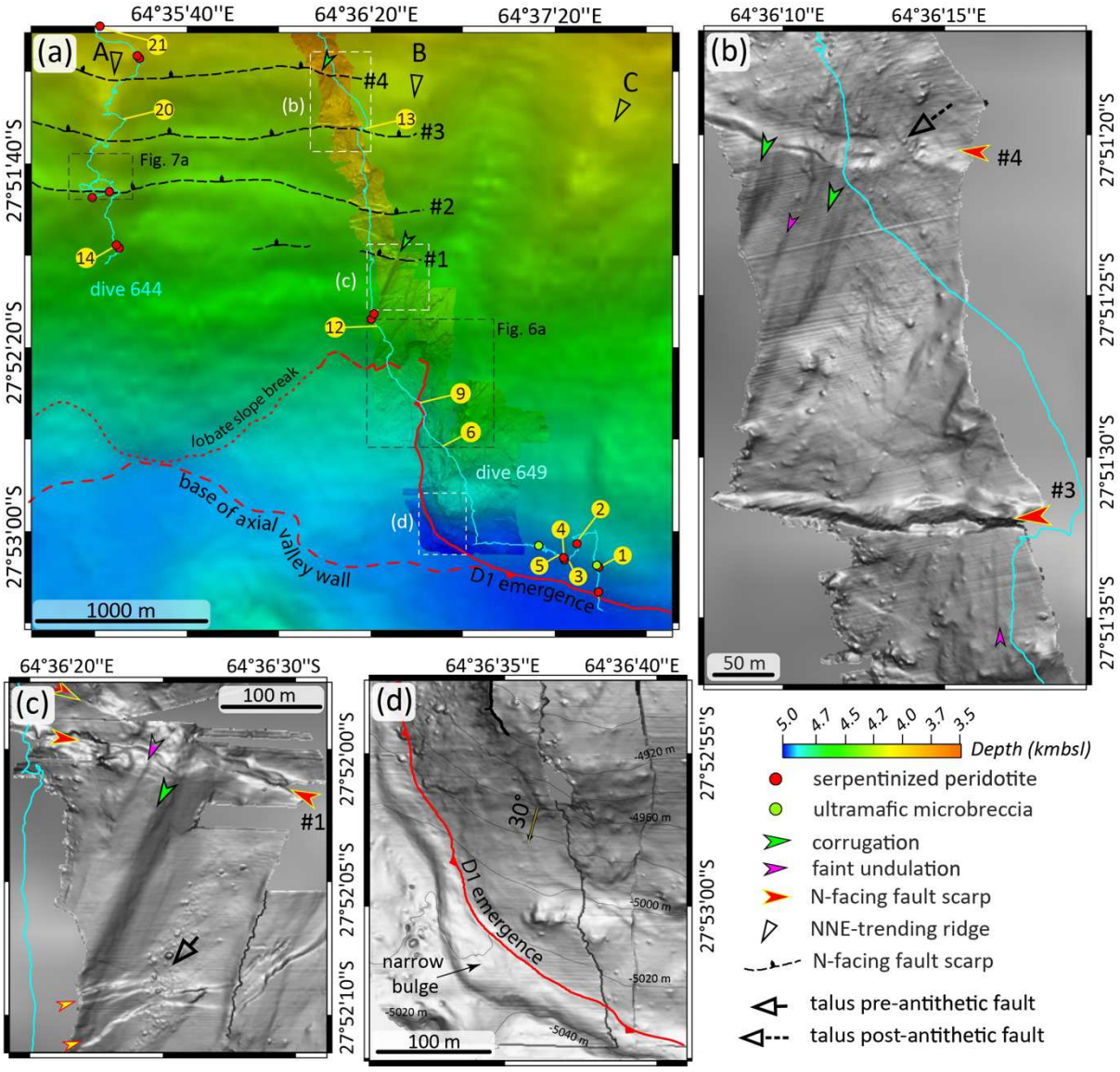

***Figure 3**: Bathymetric map of the lower slopes of the D1 detachment footwall, located in Figure 2a. (a) Microbathymetry (dive 650; located in Figure 1b), overlain on shipboard bathymetry, same depth scale. Red and green dots show the location and lithology of the samples collected in these lower slopes along the tracks of dives 644 and 649. Numbers in yellow circles correspond to the location of seafloor video snapshots shown in Figures 4, 5, and 8. Other video snapshots from dives 644 and 649 are located and shown, respectively, in Supplementary Figures 1 and 2. Panels (b), (c), and (d) are grey-shaded details of the microbathymetry located in (a).*

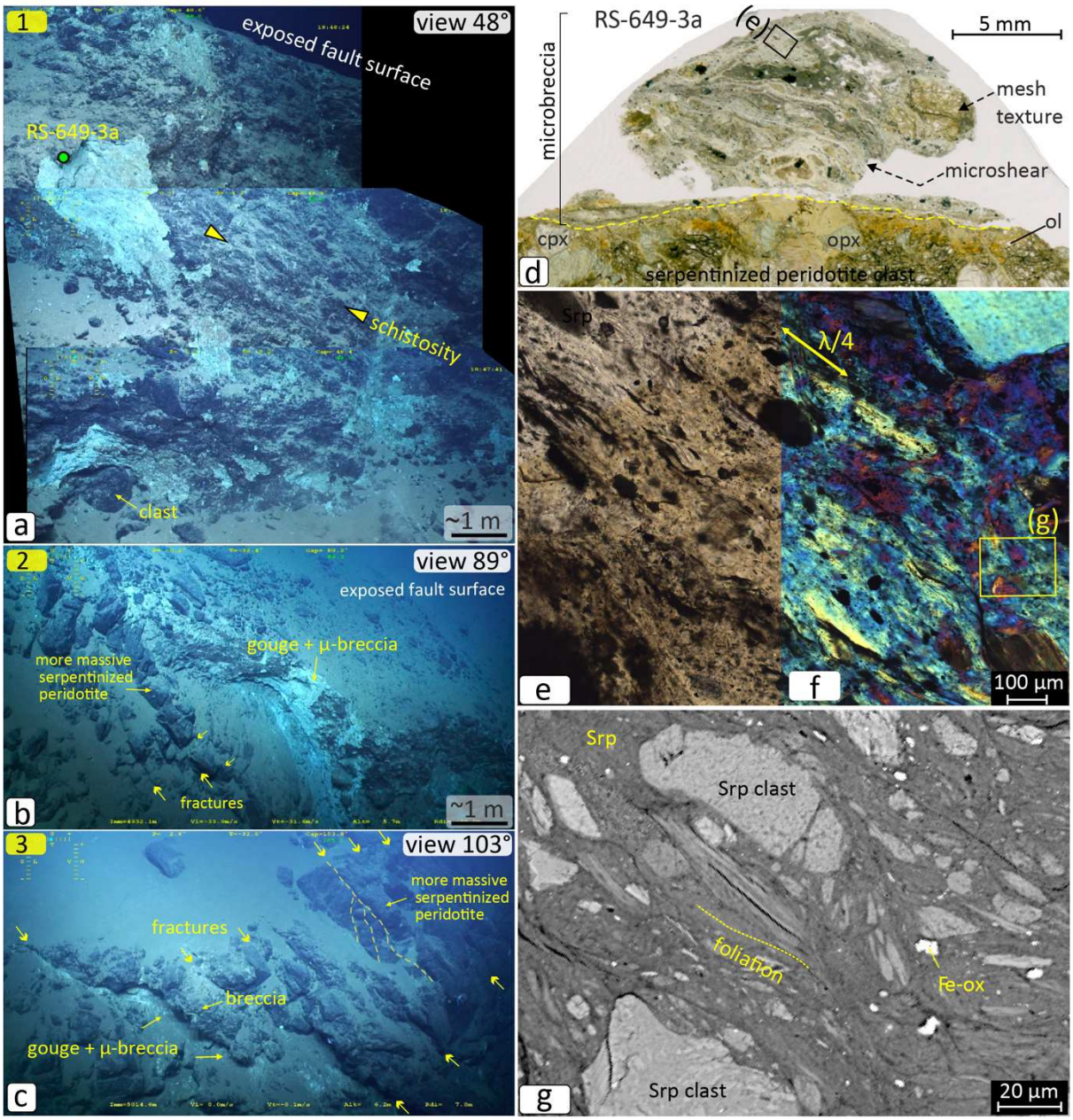

Figure 4: *Lower slopes of the D1 detachment footwall. Selected ROV snapshots (numbers in yellow in the upper left corner correspond to locations in Figure 3a, and microstructure of highly sheared sample RS-649-3a. (a) photomontage of 3 ROV snapshots showing a ~8 m-thick horizon of serpentinite gouge and microbreccia. South-dipping planar surface at the top is the exposed fault surface. Outcrop has a rough schistosity parallel to this fault surface. Location of sample RS-649-3a is shown. (b) side view of planar exposed fault surface with ~1 m of gouge/microbreccia over more massive serpentinized peridotite with set of sub-parallel fractures (dipping south 30-45°). (c) another side view shows that several meters below the main exposed fault surface (it is outside the view to the right; field of view ~12 m in foreground), some fractures are also lined with pale green gouge/microbreccia material. Also shown in the background of (c) are sets of conjugate steeper fractures in more massive serpentinized peridotite. (d) Full thin section view of sample RS-649-3a (natural light) from gouge-microbreccia horizon in (a) shows a ~10 mm-thick microclast-bearing sheared domain, which corresponds to the pervasive schistosity of the outcrop (a). (e) closer view of a sheared*

interval in natural light, located in (d). (f) detail of (e) in polarized light with an additional wave plate showing a strong crystallographic preferred orientation of the sheared serpentine. (g) Backscattered electron (BSE) image located in (f) shows elongated, angular to subrounded serpentinite (Srp) microclasts in the sheared serpentine matrix.

***Figure 5**: Selected ROV snapshots, dive 649, lower slopes of the detachment footwall. Numbers in yellow in the upper left corner correspond to locations in Figure 3a. (a) Outcrop is made of blocky serpentinized peridotites with a gouge and microbreccia shear zone, ~50 cm-thick, gently south-dipping, overlying more massive, yet locally schistose serpentinized peridotite, with set of conjugate, steeper south-dipping fractures, some filled with whitish sheared serpentinite material. (b) detail of shear zone with slightly rotated serpentinized peridotite blocks separated by sheared fractures also filled with white sheared material. Geometry is consistent with top to the south, normal displacement. (c) Here, the gently south-dipping exposed fault surface is made of serpentinized peridotites with anastomosing fractures delimitating sigmoidal phacoids. Small amounts of whitish gouge and microbreccia material are found in neck and peripheral domains.*

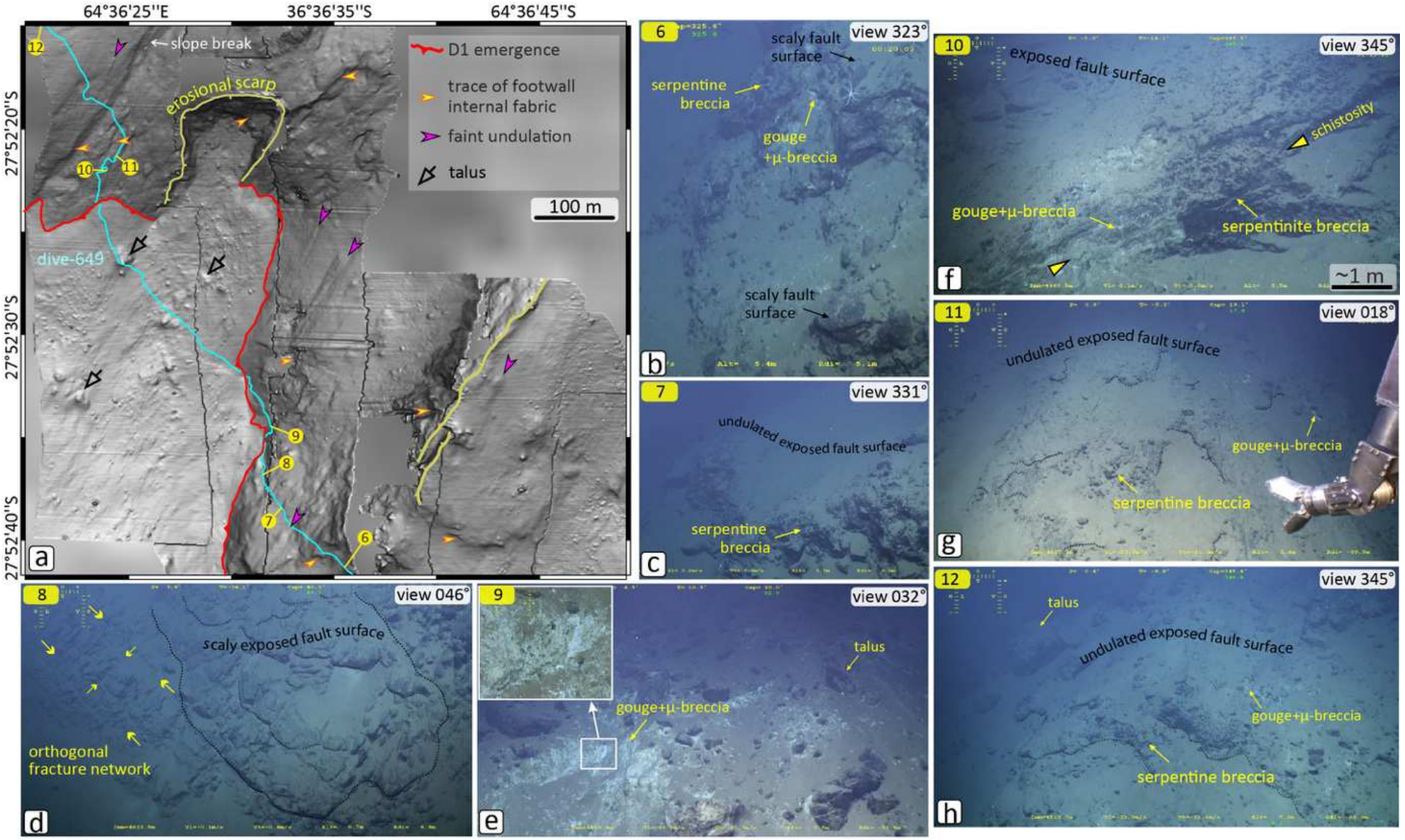
64°36'25''E
36°36'35''S
64°36'45''S
27°52'20''S
27°52'30''S
27°52'40''S
slope break
erosional scarp
D1 emergence
trace of footwall internal fabric
faint undulation
talus
100 m
dive-649
a
b
scaly fault surface
serpentine breccia
gouge +μ-breccia
c
undulated exposed fault surface
d
scaly exposed fault surface
orthogonal fracture network
e
talus
f
exposed fault surface
schistosity
gouge+μ-breccia
serpentinite breccia
~1 m
g
h

Figure 6: *Lower slopes of axial valley wall along the track of ROV dive 649. (a) Microbathymetry (dive 650; located in Figures 1b and 2a), shaded grey scale. Numbers in yellow circles correspond to the location of seafloor video snapshots shown in panels b to h (field of view ~15-20 m in foreground except in f). Other video snapshots from dive 649 are located and shown, respectively, in Supplementary Figures 1 and 2. To the west, the exhumed fault surface emerges with a 25-35° south or southwest-facing slope from more gentle slopes that expose talus deposits. This fault surface locally bears faint undulations. Slope breaks and erosional scarps provide windows into the internal fabric of the fault zone: planar features with an apparent dip to the south. In (b) and (c), the exposed fault surface dips S to SSW in brecciated serpentinized peridotite with occasional gouge-bearing microbreccia intervals. In (d) and (e), the exposed fault surface dips to the SW. In (d), it consists of scaly fractures in a relatively massive serpentinized peridotite outcrop with prominent preexisting orthogonal fractures (the apparent dip of the dominant set is to the south). In (e), the exposed fault surface has a more gentle dip and is made of at least 1 m of serpentinite gouge and microbreccia. In (f), a small erosional scarp shows at least 0.5 m of microbreccia over schistose serpentinized peridotite beneath the planar exposed fault surface. In (g) and (h), the exposed fault surface corresponds to at least 1 m of brecciated serpentine and is undulated (amplitude <1 m over 15-20 m). Scaly and pullout structures on these undulated fault planes are consistent with downdip, undulation-parallel normal displacement.*

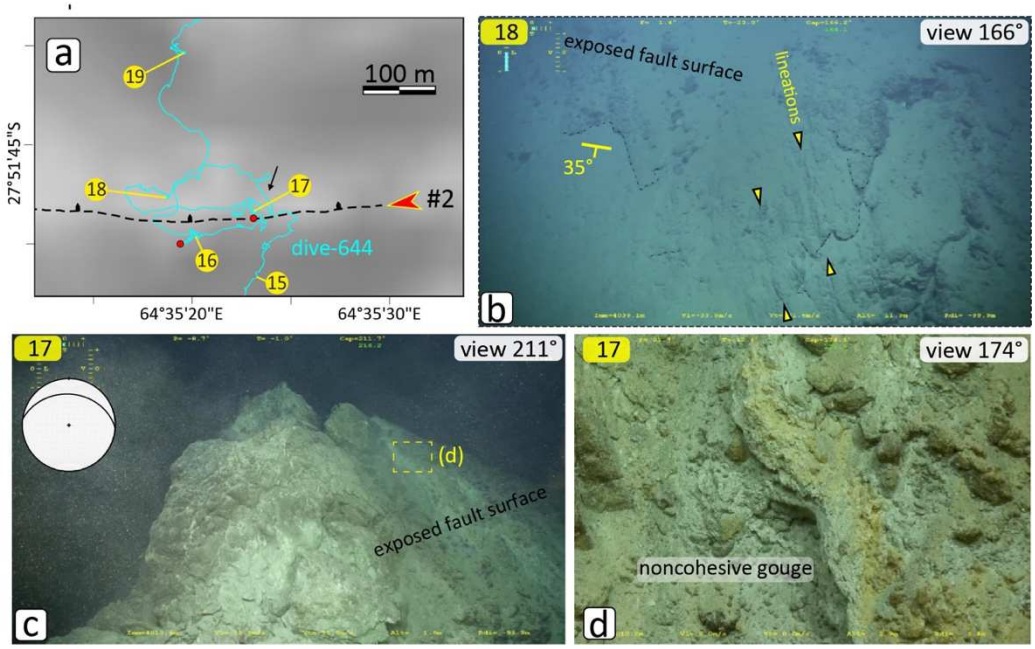

Figure 7*: North-facing, antithetic fault scarp along the track of dive 644. (a) Map view of dive 644 track around antithetic fault scarp #2 (located in Fig. 3a). Numbers in yellow circles correspond to the location of seafloor video snapshots shown in panels b to d (field of view ~15-20 m in foreground except in (d), and in Figure 8b The scarp exposes a north dipping fault plane, with steep west-dipping lineations and scaly and pullout structures consistent with normal displacement. (c) Another view of the north-dipping fault plane, lined with at least 1 m of non-cohesive gouge (d).*

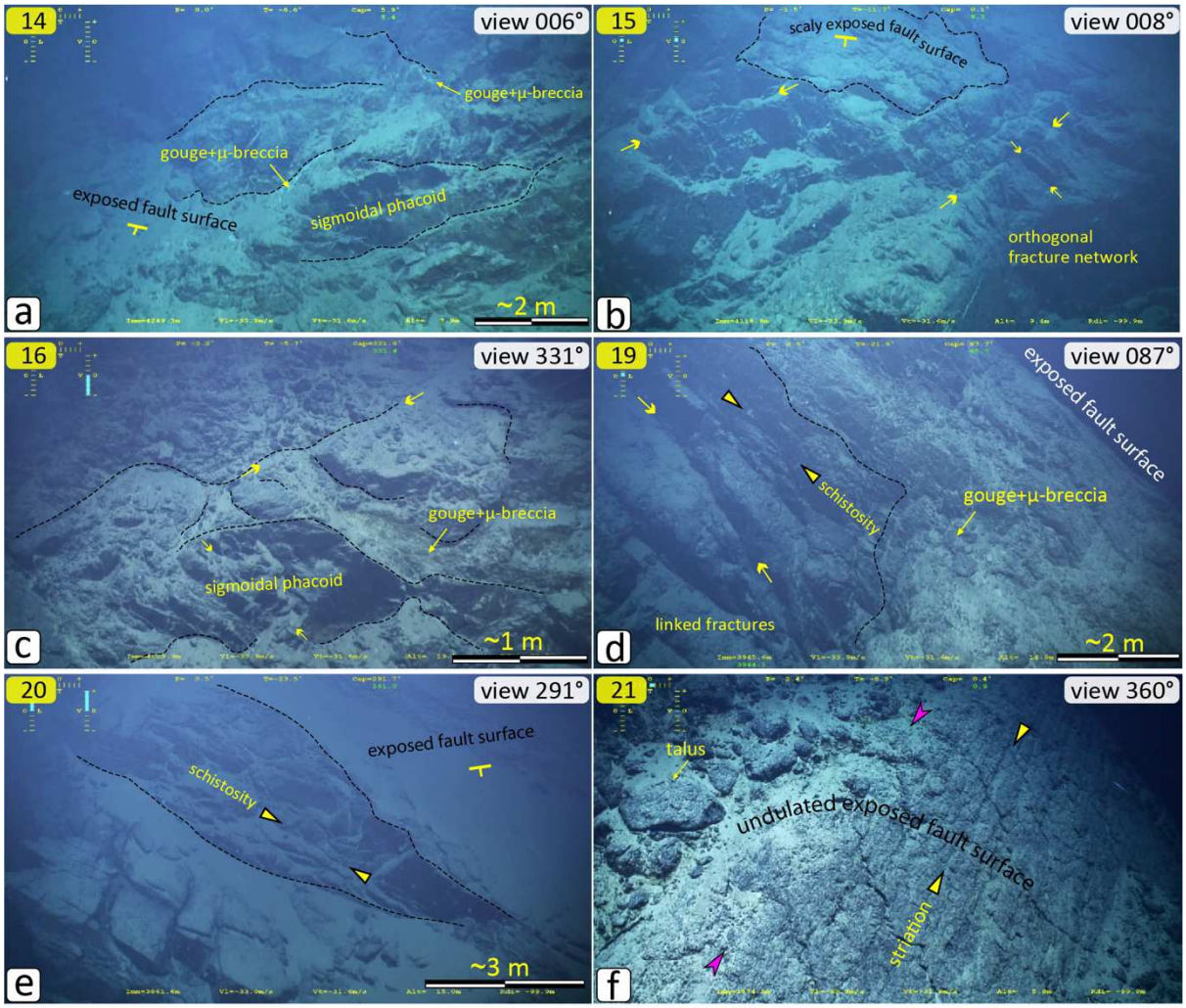

Figure 8: *Selected ROV snapshots along NNE-trending ridge A, dive 644. Numbers in yellow in the upper left corner correspond to locations in Figures 3a and 7a. In (a), (b), and (c), a dominant set of fractures dips to the S or SW. In (a) and (c), these fractures define sigmoidal phacoids and are locally outlined by gouge and microbreccia (up to ~50 cm-thick in c). In (b), these fractures are planar, defining an orthogonal network, and similar to Figure 6d, there is a discordant, later, south-dipping scaly fault plane in the background. In (d), an erosional scarp reveals the deformation beneath the south-dipping planar fault plane, with ~1 m of gouge and microbreccia, over serpentinized peridotite with concordant schistosity and sigmoidal phacoids. (e) is on the east flank of ridge A, and exposed fault planes have a dominant, slope-parallel, southeast dip. They isolate decameter-long flat sigmoidal phacoids in serpentinized peridotite that has a platy schistosity/cleavage. (f) Shows an undulated striated exposed fault surface (undulation trends NNE, field of view ~10 m).*

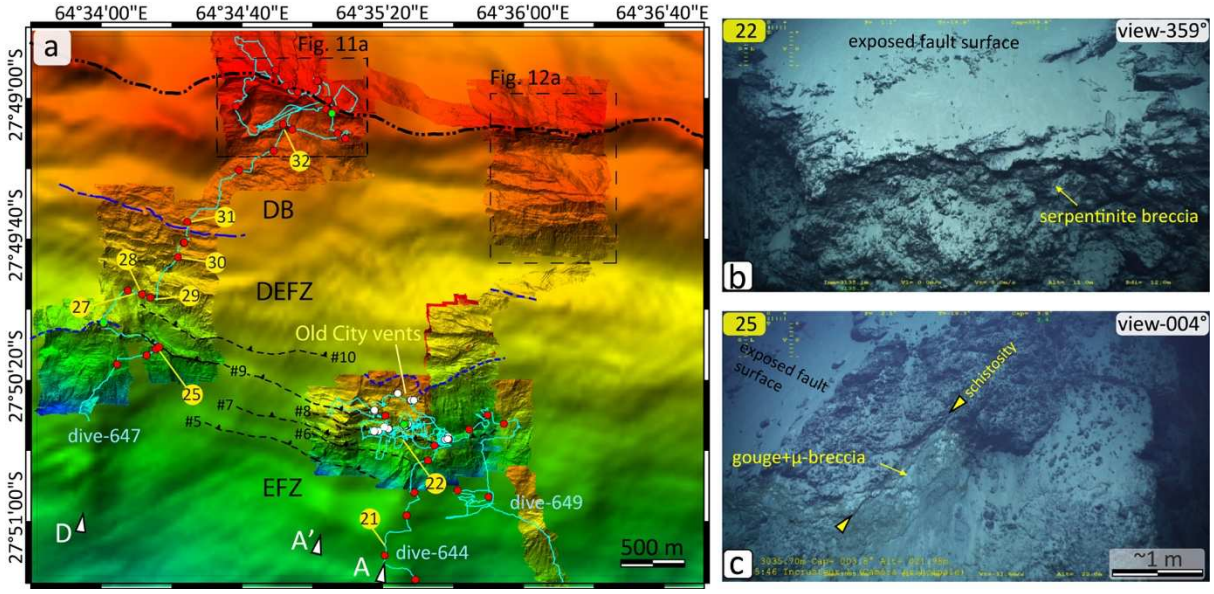

Figure 9: *Middle and upper slopes of the axial valley wall along the tracks of ROV dives 644, 647, and 649. (a) Microbathymetry (dives 642 and 650; located in Figures 1a and 2b), overlain on shipboard bathymetry, same depth scale as in Fig. 2a. Numbers in yellow circles correspond to the location of seafloor video snapshots shown in panels b and c (field of view ~15-20 m in foreground), and in Figure 10. Other dive video snapshots from dives 644, 647, and 649 are located and shown in Supplementary Figures 2, 4. Blue and purple lines are proposed limits between the EFZ (exposed fault zone) and DEFZ (degraded exposed fault zone) and between the DEFZ and the DB (degraded breakaway) domains. A, A', and D are NNE-trending ridges, as in Figures 2a. Dashed black lines numbered 5 to 10 are north-facing, antithetic fault scarps. (b) and (c) are selected ROV snapshots showing exposed D1 fault surfaces in the upper slopes of the EFZ domain, near the Old City vents (b), and further to the west along dive 647 (c).*

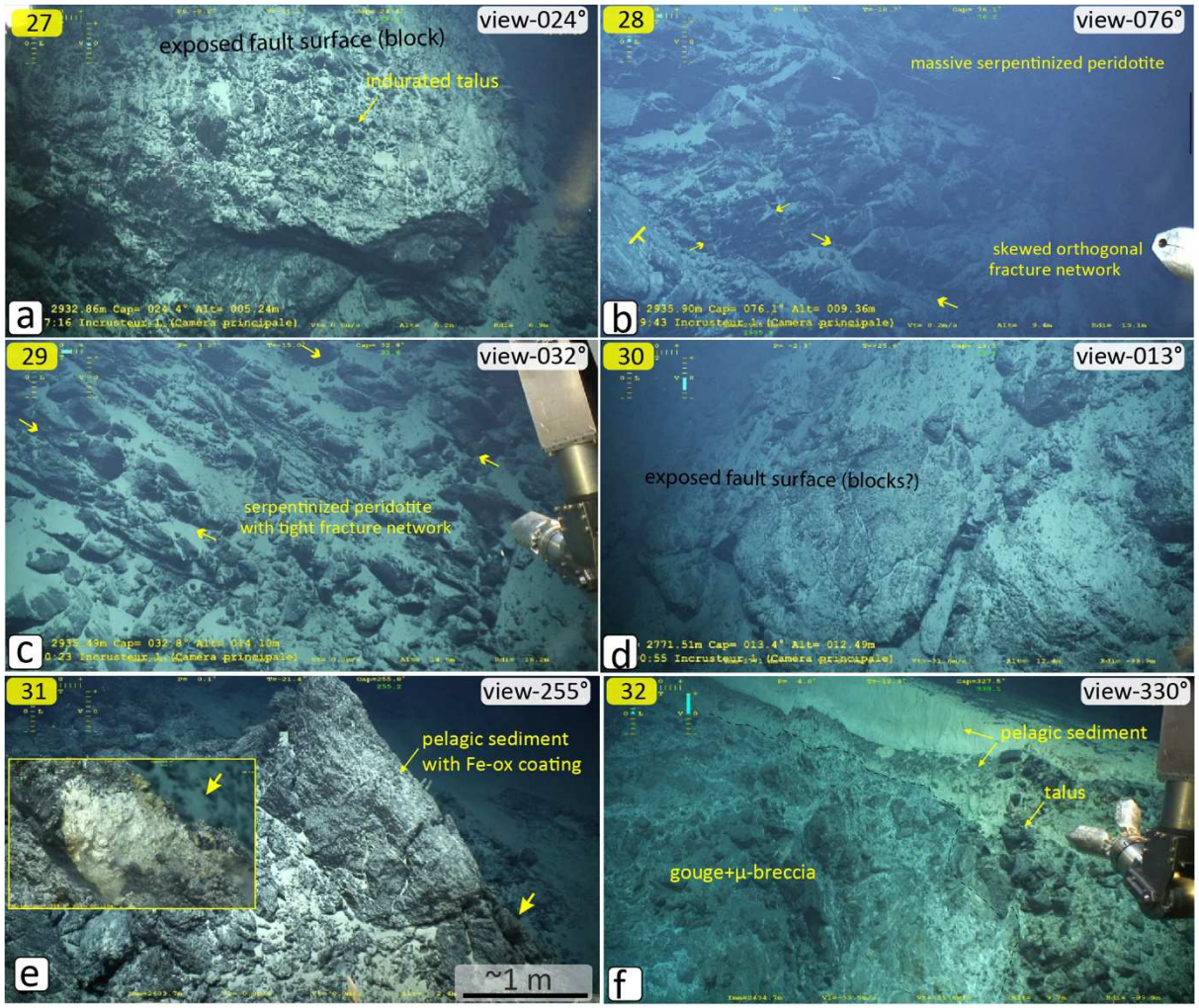

Figure 10: *Selected ROV snapshots in the DEFZ (degraded exposed fault zone; a to d) and DB (degraded breakaway; e and f) domains, dive 647. Numbers in yellow in the upper left corner correspond to locations in Figure 9a. (a) Exposed fault surface, probably a large block, covered with semi-indurated talus. (b) Large outcrop of massive serpentinized peridotite with conjugate fractures: the secondary set of north-dipping fractures may have been rotated from orthogonality due to normal displacement on dominant, south-dipping fractures. (c) Another large outcrop, with tight subparallel to linked southeast-dipping fractures. (d) Exposed fault surfaces, blocks, or outcrops. (e) First encounter with thick (>1.5 m) and iron-manganese oxide-coated, semi-indurated pelagic sediments characteristic of the exposed D2 fault surface (Figure 11b). (f) Foliated serpentinite gouge and microbreccia with ~1 m-thick cover of pelagic sediment on top of a slid block just south of the top of the axial valley wall (Figure 11a).*

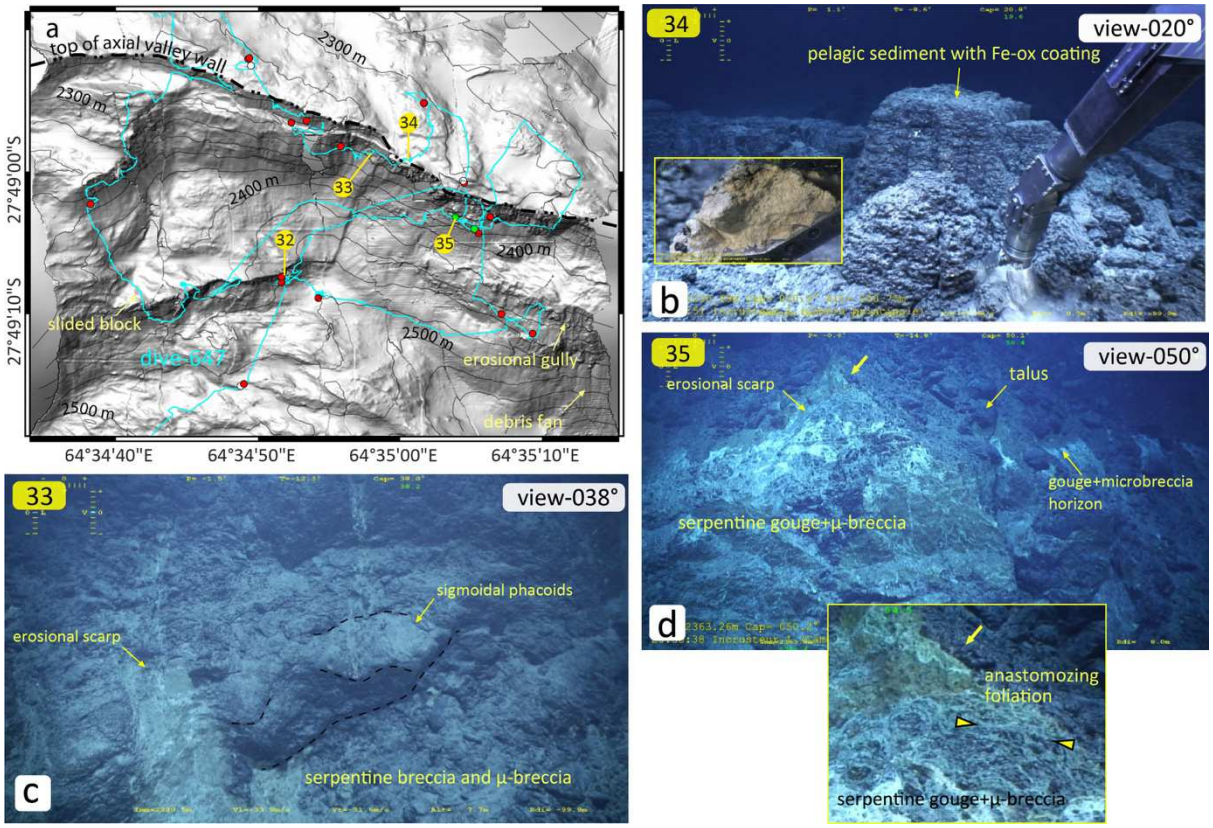

Figure 11: *D2 exposed fault surface explored during dive 647 along the top of the axial valley wall. (a) Shaded microbathymetry (dive 642, map located in Figure 9a) showing the track of dive 647 and the location of rock samples. Numbers in yellow circles correspond to the location of seafloor video snapshots shown in panels b, c, and d (field of view ~15-20 m in foreground). Other dive video snapshots from dive 647 are located and shown in Supplementary Figures 3, and 4. (b) Thick (>1.5 m) and iron-manganese oxide-coated, semi-indurated pelagic sediments on top of the wall (exposed D2 fault surface). (c) Large outcrop of serpentinite breccia and microbreccia with north-dipping schistosity and sigmoidal phacoids, ~40 m below the exposed fault surface. (d) Large outcrop of serpentinite breccia, microbreccia, and gouge, with north-dipping, anastomosing foliation, ~55 m below the exposed fault surface.*

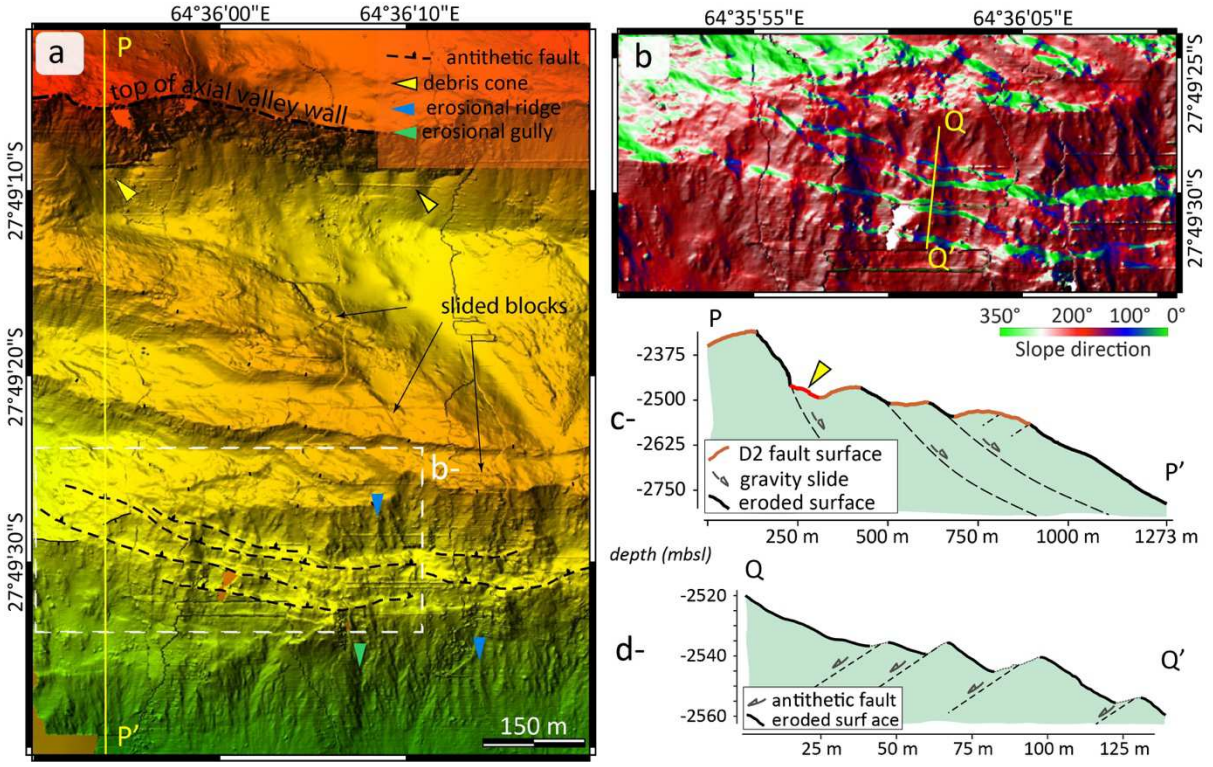

Figure 12: *Mass-wasting and antithetic faults in the degraded breakaway (DB) domain. (a) Microbathymetry (dive 642, map located in Figure 9a, same depth color scale). The edge of three, hectometer-sized slid blocks are eroded in the form of more recent gullies, erosional ridges, and debris cones. (b) Slope direction map (located in a) showing detail of WNW-trending antithetic fault scarps cutting through erosional ridges along the edge of the southernmost slid block. (c) Topographic section located in a. (d) Topographic section located in b.*

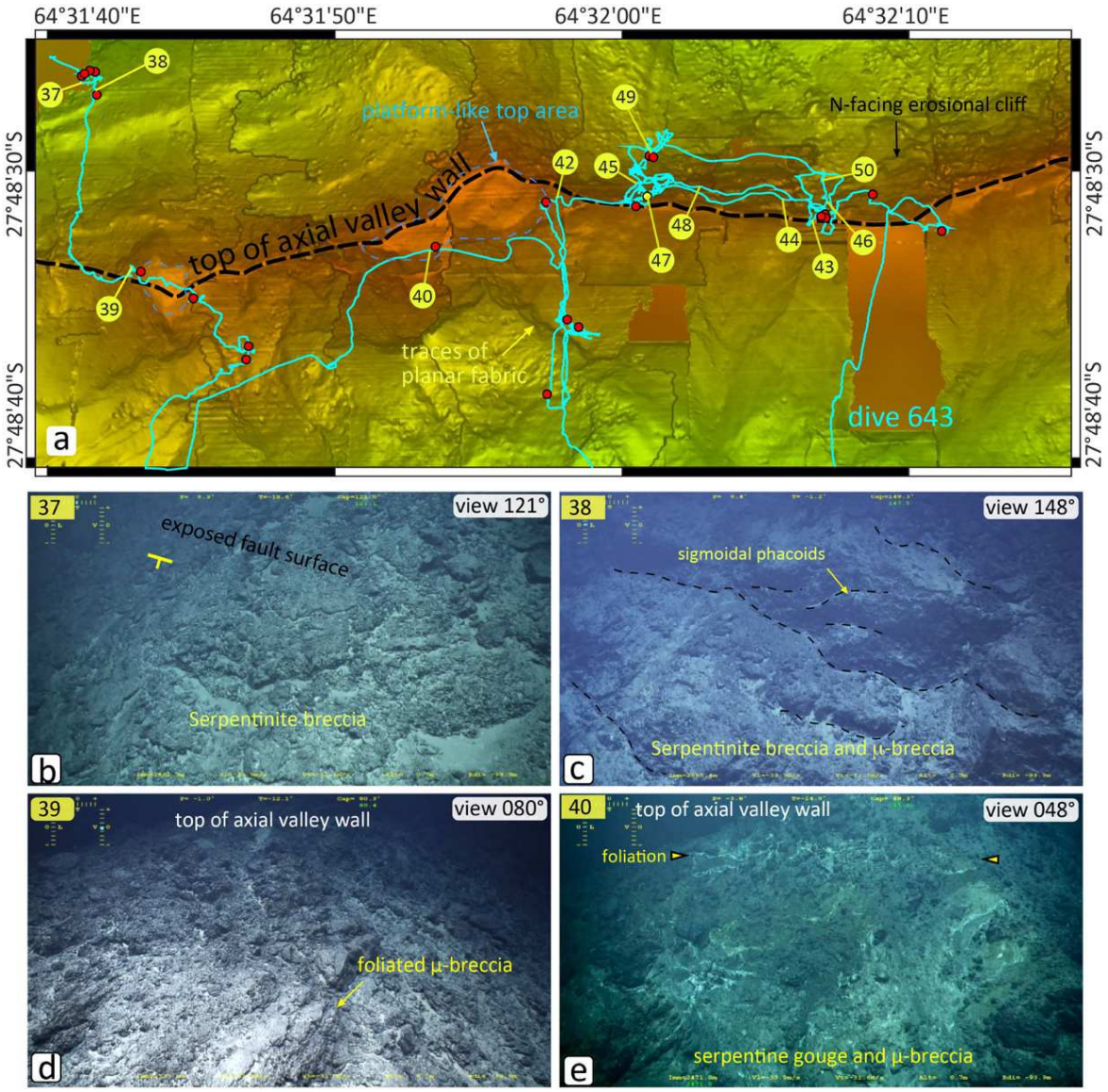

Figure 13: *D2 exposed fault surface explored during dive 643 in the west of the study area. (a) Microbathymetry (dive 639, map located in Figure 2a, same depth color scale) shows the location of rock samples and of the track of dive 643. Numbers in yellow circles correspond to the location of seafloor video snapshots shown in panels b to e (field of view ~15-20 m in foreground) and in Figure 14. Other dive video snapshots from dive 643 are located and shown in Supplementary Figures 5a and 6. The top of the axial valley wall in this region is limited by erosional head scarps on both its south and north sides. It, therefore, forms a narrow ridge with steep scarps on both sides. (b) and (c) brecciated serpentinized peridotites exposed a bit downslope on the northern flank of the axial valley wall. (d) and (e) serpentinite gouge and microbreccia with north-dipping (d), or sub-horizontal anastomosing (e) foliation, exposed in platform-like sections of the top of the axial valley wall.*

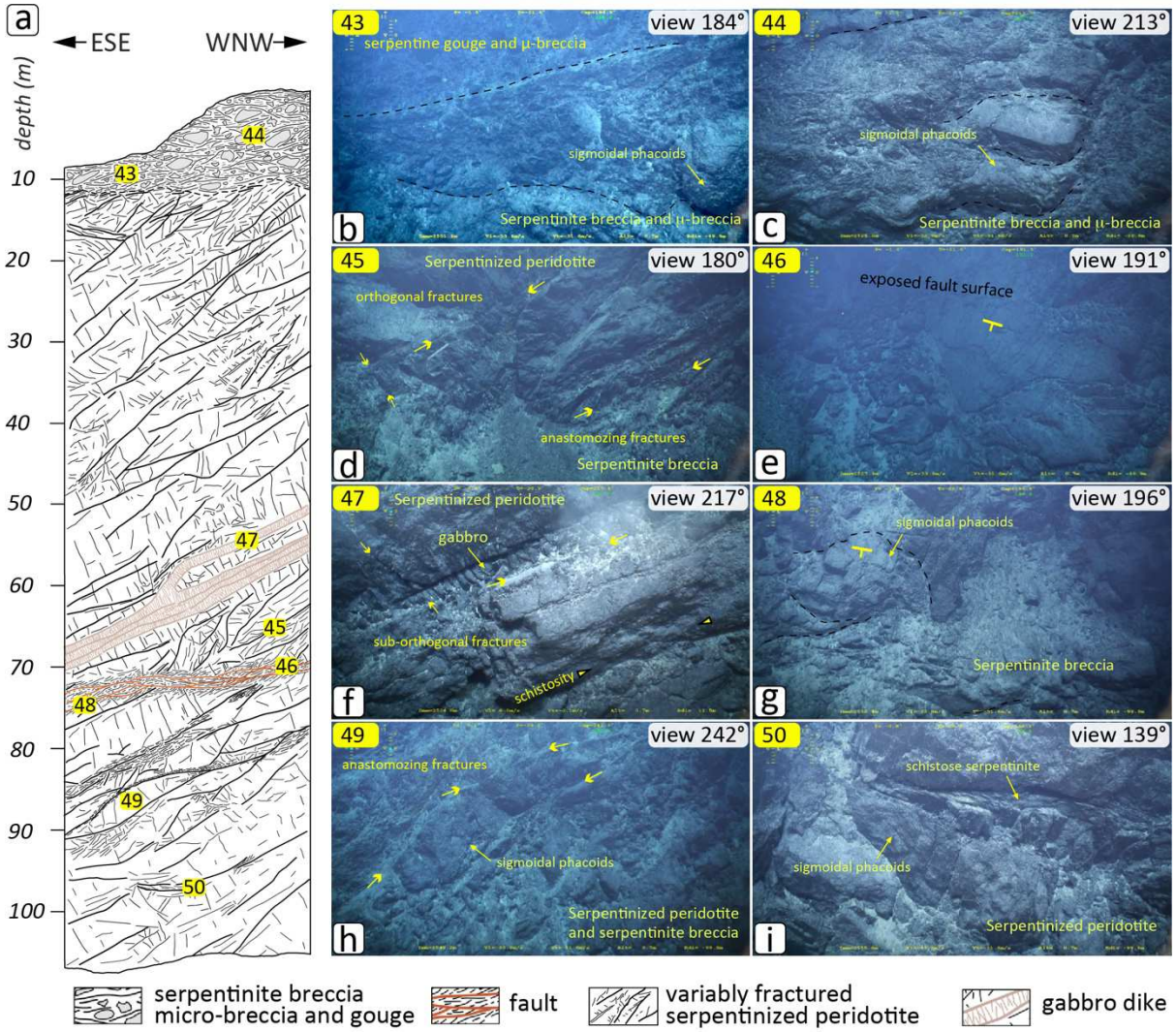

Figure 14: *A generalized litho-structural log of the D2 detachment fault zone based on dive 647 observations made along the ~100 m-high, north-facing erosional cliff at the top of the axial valley wall (Figure 13a). Numbers in yellow circles in (a) correspond to the seafloor video snapshots shown in panels b to i (field of view ~15-20 m in foreground) and to locations in Figure 13a. The top of the wall exposes the most deformed facies (serpentinite gouge, microbreccia, and breccia), with gently dipping to horizontal sigmoidal foliations, resting unconformably on variably deformed serpentinized peridotites. These have ESE-dipping structures, ranging from massive with sets of orthogonal fractures (d and f) to brecciated with sigmoidal fractures and local schistose intervals (d and h). Midway down the cliff, there is an N-dipping exposed fault surface (e). The dominant set of sigmoidal fractures in the brecciated serpentinites below this fault also dips to the north (g).*

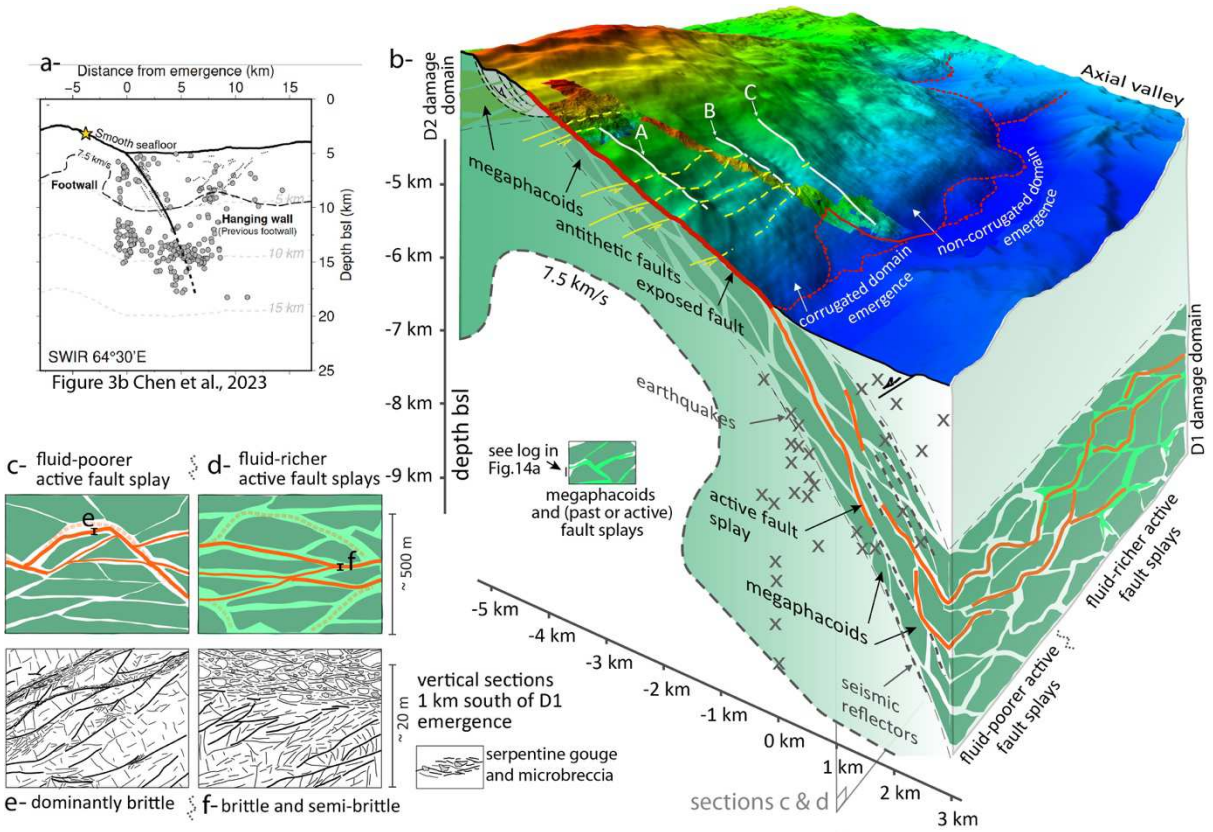

Figure 15. *Possible anatomy of the D1 footwall and damage zone, down to ~9 km below its emergence. a- Synthetic sketch used to constrain the conceptual sketch in (b), showing the distribution of earthquakes recorded in the 64°30'E SWIR region over two, 2-3 weeks long periods in 2014 and 2016 (Chen et al., 2023), the 7.5 km/s Vp isovelocity contour from Corbalan et al. (2021), and the trace of seismic reflectors from Momoh et al. (2017). b- 3D conceptual sketch drawn from (a), seafloor topography, and our geological results. The width of the damage zone (~1 km) is inferred from the distribution of seismic reflectors. The size of megaphacoids (domains of moderately fractured serpentinized peridotite) is inferred from hectometer to kilometer-sized lobate structures and indentations of the D1 emergence. c- and d- Conceptual sketches of the D1 fault zone, about 1 km south of its emergence, emphasizing the difference between the corrugated western region, with dominantly brittle deformation, and the non-corrugated, smooth eastern region, with fluid-enhanced semi-brittle deformation. e- and f- Outcrop-scale sketches of active fault splay in c- and d-, based on dive observations. See text for further explanations.*

2.8 Cited references:

Bickert, M., Lavier, L. and Cannat, M., 2020. How do detachment faults form at ultraslow mid-ocean ridges in a thick axial lithosphere?. *Earth and Planetary Science Letters*, *533*, p.116048.

Bickert, M., Cannat, M., Tommasi, A., Jammes, S. and Lavier, L., 2021. Strain localization in the root of detachment faults at a melt-starved mid-ocean ridge: a microstructural study of Abyssal Peridotites from the Southwest Indian Ridge. *Geochemistry, Geophysics, Geosystems*, *22*(5), p.e2020GC009434.

Bonnemains, D., Escartín, J., Mével, C., Andreani, M. and Verlaguet, A., 2017. Pervasive silicification and hanging wall overplating along the 13° 20′ N oceanic detachment fault (M id-A tlantic R idge). *Geochemistry, Geophysics, Geosystems*, *18*(6), pp.2028-2053.

Boschi, C., Früh-Green, G.L., Delacour, A., Karson, J.A. and Kelley, D.S., 2006. Mass transfer and fluid flow during detachment faulting and development of an oceanic core complex, Atlantis Massif (MAR 30 N). *Geochemistry, Geophysics, Geosystems*, *7*(1).

Buck, W.R., 1988. Flexural rotation of normal faults. *Tectonics*, *7*(5), pp.959-973.

Buck, W.R., Lavier, L.L. and Poliakov, A.N., 2005. Modes of faulting at mid-ocean ridges. *Nature*, *434*(7034), pp.719-723.

Cannat, M. and Casey, J.F., 1995, June. An ultramafic lift at the Mid-Atlantic Ridge: successive stages of magmatism in serpentinized peridotites from the 15 N region. In *Mantle and Lower Crust Exposed in Oceanic Ridges and in Ophiolites: Contributions to a Specialized Symposium of the VII EUG Meeting, Strasbourg, Spring 1993* (pp. 5-34). Dordrecht: Springer Netherlands.

Cannat, M., Lagabrielle, Y., Bougault, H., Casey, J., de Coutures, N., Dmitriev, L. and Fouquet, Y., 1997. Ultramafic and gabbroic exposures at the Mid-Atlantic Ridge: Geological mapping in the 15 N region. *Tectonophysics*, *279*(1-4), pp.193-213.

Cannat, M., Rommevaux-Jestin, C., Sauter, D., Deplus, C. and Mendel, V., 1999. Formation of the axial relief at the very slow spreading Southwest Indian Ridge (49 to 69 E). *Journal of Geophysical Research: Solid Earth*, *104*(B10), pp.22825-22843.

Cannat, M., Sauter, D., Mendel, V., Ruellan, E., Okino, K., Escartin, J., Combier, V. and Baala, M., 2006. Modes of seafloor generation at a melt-poor ultraslow-spreading ridge. *Geology*, *34*(7), pp.605-608.

Cannat, M., Sauter, D., Bezos, A., Meyzen, C., Humler, E. and Le Rigoleur, M., 2008. Spreading rate, spreading obliquity, and melt supply at the ultraslow spreading Southwest Indian Ridge. *Geochemistry, Geophysics, Geosystems*, *9*(4).

Cannat, M., Sauter, D., Escartín, J., Lavier, L. and Picazo, S., 2009. Oceanic corrugated surfaces and the strength of the axial lithosphere at slow spreading ridges. *Earth and Planetary Science Letters*, *288*(1-2), pp.174-183.

Cannat, M., Sauter, D., Lavier, L., Bickert, M., Momoh, E. and Leroy, S., 2019. On spreading modes and magma supply at slow and ultraslow mid-ocean ridges. *Earth and Planetary Science Letters*, *519*, pp.223-233.

Casey, J.F., 1997. Comparison of major-and trace-element geochemistry of abyssal peridotites and mafic plutonic rocks with basalts from the MARK region of the Mid-Atlantic Ridge. In *Proceedings of the Ocean Drilling Program. Scientific Results* (Vol. 153, pp. 181-241).

Casini, L., Maino, M., Sanfilippo, A., Ildefonse, B. and Dick, H.J., 2021. High-Temperature Strain Localization and the Nucleation of Oceanic Core Complexes (16.5° N, Mid-Atlantic Ridge). *Journal of Geophysical Research: Solid Earth*, *126*(9), p.e2021JB022215.

Chen, J., Crawford, W.C. and Cannat, M., 2023. Microseismicity and lithosphere thickness at a nearly-amagmatic oceanic detachment fault system. *Nature Communications*, *14*(1), p.430.

Corbalán, A., Nedimović, M.R., Louden, K.E., Cannat, M., Grevemeyer, I., Watremez, L. and Leroy, S., 2021. Seismic velocity structure along and across the ultraslow-spreading Southwest Indian ridge at 64 30′ E showcases flipping detachment faults. *Journal of Geophysical Research: Solid Earth*, *126*(10), p.e2021JB022177.

Demartin, B.J., Sohn, R.A., Canales, J.P. and Humphris, S.E., 2007. Kinematics and geometry of active detachment faulting beneath the Trans-Atlantic Geotraverse (TAG) hydrothermal field on the Mid-Atlantic Ridge. *Geology*, *35*(8), pp.711-714.

Dick, H.J., Natland, J.H., Alt, J.C., Bach, W., Bideau, D., Gee, J.S., Haggas, S., Hertogen, J.G., Hirth, G., Holm, P.M. and Ildefonse, B., 2000. A long in situ section of the lower ocean crust: results of ODP Leg 176 drilling at the Southwest Indian Ridge. *Earth and planetary science letters*, *179*(1), pp.31-51.

Dick, H.J., Ozawa, K., Meyer, P.S., Niu, Y., Robinson, P.T., Constantin, M., Hebert, R., Maeda, J., Natland, J.H., Hirth, G. and Mackie, S., 2002. 10. Primary silicate mineral chemistry of a 1.5-km section of very slow spreading lower ocean

crust: ODP hole 735B, Southwest Indian ridge. *Proceedings of Ocean Drilling Program, Scientific Results, 000. College Station, TX: Ocean Drilling Program*, pp.1-60.

Escartín, J. and Cannat, M., 1999. Ultramafic exposures and the gravity signature of the lithosphere near the Fifteen-Twenty Fracture Zone (Mid-Atlantic Ridge, 14–16.5 N). *Earth and Planetary Science Letters*, *171*(3), pp.411-424.

Escartín, J., Mével, C., MacLeod, C.J. and McCaig, A.M., 2003. Constraints on deformation conditions and the origin of oceanic detachments: The Mid-Atlantic Ridge core complex at 15 45′ N. *Geochemistry, Geophysics, Geosystems*, *4*(8).

Escartín, J., Smith, D.K., Cann, J., Schouten, H., Langmuir, C.H. and Escrig, S., 2008. Central role of detachment faults in accretion of slow-spreading oceanic lithosphere. *Nature*, *455*(7214), pp.790-794.

Escartin, J., Mevel, C., Petersen, S., Bonnemains, D., Cannat, M., Andreani, M., Augustin, N., Bézos, A., Chavagnac, V., Choi, Y. and Godard, M., 2017. Tectonic structure, evolution, and the nature of oceanic core complexes and their detachment fault zones (13 20′ N and 13 30′ N, Mid Atlantic Ridge). *Geochemistry, Geophysics, Geosystems*, *18*(4), pp.1451-1482.

Hansen, L.N., Cheadle, M.J., John, B.E., Swapp, S.M., Dick, H.J., Tucholke, B.E. and Tivey, M.A., 2013. Mylonitic deformation at the Kane oceanic core complex: Implications for the rheological behavior of oceanic detachment faults. *Geochemistry, Geophysics, Geosystems*, *14*(8), pp.3085-3108.

John, B.E., 1987. Geometry and evolution of a mid-crustal extensional fault system: Chemehuevi Mountains, southeastern California. *Geological Society, London, Special Publications*, *28*(1), pp.313-335.

Karson, J.A., Früh-Green, G.L., Kelley, D.S., Williams, E.A., Yoerger, D.R. and Jakuba, M., 2006. Detachment shear zone of the Atlantis Massif core complex, Mid-Atlantic Ridge, 30 N. *Geochemistry, Geophysics, Geosyste*

Kelemen, P.B., Kikawa, E., Miller, D.J., Abe, N., Bach, W., Carlson, R.L., Casey, J.F., Chambers, L.M., Cheadle, M., Cipriani, A. and Dick, H.J.B., 2007. Leg 209 Summary: Processes in a 20-km-Thick Conductive Boundary Layer beneath the Mid-Atlantic Ridge, 14°-16° NProceedings of the Ocean Drilling Program, 209 Scientific Results. In *Proceedings of the Ocean Drilling ProgramProceedings of the Ocean Drilling Program, 209 Scientific Results* (Vol. 209, pp. 1-33). Kelemen, PB, Kikawa, E., and Miller, DJ (Eds.).

Lecoeuvre, A., Ménez, B., Cannat, M., Chavagnac, V. and Gérard, E., 2021. Microbial ecology of the newly discovered serpentinite-hosted Old City hydrothermal field (southwest Indian ridge). *The ISME journal*, *15*(3), pp.818-832.

Little, T.A., Webber, S.M., Mizera, M., Boulton, C., Oesterle, J., Ellis, S., Boles, A., van der Pluijm, B., Norton, K., Seward, D. and Biemiller, J., 2019. Evolution of a rapidly slipping, active low-angle normal fault, Suckling-Dayman metamorphic core complex, SE Papua New Guinea. *Bulletin*, *131*(7-8), pp.1333-1363.

MacLeod, C.J., Escartin, J., Banerji, D., Banks, G.J., Gleeson, M., Irving, D.H.B., Lilly, R.M., McCaig, A.M., Niu, Y., Allerton, S. and Smith, D.K., 2002. Direct geological evidence for oceanic detachment faulting: The Mid-Atlantic Ridge, 15 45′ N. *Geology*, *30*(10), pp.879-882.

MacLeod, C.J., Searle, R.C., Murton, B.J., Casey, J.F., Mallows, C., Unsworth, S.C., Achenbach, K.L. and Harris, M., 2009. Life cycle of oceanic core complexes. *Earth and Planetary Science Letters*, *287*(3-4), pp.333-344.

Mével, C., Cannat, M., Gente, P., Marion, E., Auzende, J.M. and Karson, J.A., 1991. Emplacement of deep crustal and mantle rocks on the west median valley wall of the MARK area (MAR, 23 N). *Tectonophysics*, *190*(1), pp.31-53.

Mizera, M., Little, T.A., Biemiller, J., Ellis, S., Webber, S. and Norton, K.P., 2019. Structural and geomorphic evidence for rolling-hinge style deformation of an active continental low-angle normal fault, SE Papua New Guinea. *Tectonics*, *38*(5), pp.1556-1583.

Minshull, T.A., Muller, M.R. and White, R.S., 2006. Crustal structure of the Southwest Indian Ridge at 66 E: Seismic constraints. *Geophysical Journal International*, *166*(1), pp.135-147.

Momoh, E., Cannat, M., Watremez, L., Leroy, S. and Singh, S.C., 2017. Quasi-3-D seismic reflection imaging and wide-angle velocity structure of nearly amagmatic oceanic lithosphere at the ultraslow-spreading Southwest Indian Ridge. *Journal of Geophysical Research: Solid Earth*, *122*(12), pp.9511-9533.

Momoh, E., Cannat, M. and Leroy, S., 2020. Internal structure of the oceanic lithosphere at a melt-starved ultraslow-spreading mid-ocean ridge: insights from 2-D seismic data. *Geochemistry, Geophysics, Geosystems*, *21*(2), p.e2019GC008540.

Olive, J.A., Behn, M.D. and Tucholke, B.E., 2010. The structure of oceanic core complexes controlled by the depth distribution of magma emplacement. *Nature Geoscience*, *3*(7), pp.491-495.

Parnell-Turner, R., Sohn, R.A., Peirce, C., Reston, T.J., MacLeod, C.J., Searle, R.C. and Simão, N.M., 2017. Oceanic detachment faults generate compression in extension. *Geology*, *45*(10), pp.923-926.

Parnell-Turner, R., Escartín, J., Olive, J.A., Smith, D.K. and Petersen, S., 2018. Genesis of corrugated fault surfaces by strain localization recorded at oceanic detachments. *Earth and Planetary Science Letters*, *498*, pp.116-128.

Parnell-Turner, R., Sohn, R.A., Peirce, C., Reston, T.J., MacLeod, C.J., Searle, R.C. and Simão, N.M., 2021. Seismicity trends and detachment fault structure at 13 N, Mid-Atlantic Ridge. *Geology*, *49*(3), pp.320-324.

Patriat, P. and Segoufin, J., 1988. Reconstruction of the central Indian Ocean. *Tectonophysics*, *155*(1-4), pp.211-234.

Picazo, S., Cannat, M., Delacour, A., Escartín, J., Rouméjon, S. and Silantyev, S., 2012. Deformation associated with the denudation of mantle-derived rocks at the Mid-Atlantic Ridge 13°–15° N: The role of magmatic injections and hydrothermal alteration. *Geochemistry, Geophysics, Geosystems*, *13*(9).

Picazo, S., Manatschal, G., Cannat, M. and Andréani, M., 2013. Deformation associated to exhumation of serpentinized mantle rocks in a fossil Ocean Continent Transition: The Totalp unit in SE Switzerland. *Lithos*, *175*, pp.255-271.

Pressling, N., Morris, A., John, B.E. and MacLeod, C.J., 2012. The internal structure of an oceanic core complex: An integrated analysis of oriented borehole imagery from IODP Hole U1309D (Atlantis Massif). *Geochemistry, Geophysics, Geosystems*, *13*(9).

Sauter, D., Cannat, M., Rouméjon, S., Andreani, M., Birot, D., Bronner, A., Brunelli, D., Carlut, J., Delacour, A., Guyader, V. and MacLeod, C.J., 2013. Continuous exhumation of mantle-derived rocks at the Southwest Indian Ridge for 11 million years. *Nature Geoscience*, *6*(4), pp.314-320.

Schroeder, T. and John, B.E., 2004. Strain localization on an oceanic detachment fault system, Atlantis Massif, 30 N, Mid-Atlantic Ridge. *Geochemistry, Geophysics, Geosystems*, *5*(11).

Schroeder, T., Cheadle, M.J., Dick, H.J., Faul, U., Casey, J.F. and Kelemen, P.B., 2007. Nonvolcanic seafloor spreading and corner-flow rotation accommodated by extensional faulting at 15 N on the Mid-Atlantic Ridge: A structural synthesis of ODP Leg 209. *Geochemistry, Geophysics, Geosystems*, *8*(6).

Smith, D.K., Cann, J.R. and Escartín, J., 2006. Widespread active detachment faulting and core complex formation near 13 N on the Mid-Atlantic Ridge. *Nature*, *442*(7101), pp.440-443.

Smith, D.K., Escartín, J., Schouten, H. and Cann, J.R., 2008. Fault rotation and core complex formation: Significant processes in seafloor formation at slow-spreading mid-ocean ridges (Mid-Atlantic Ridge, 13–15 N). *Geochemistry, Geophysics, Geosystems*, *9*(3).

Smith, D.K., Schouten, H., Dick, H.J., Cann, J.R., Salters, V., Marschall, H.R., Ji, F., Yoerger, D., Sanfilippo, A., Parnell-Turner, R. and Palmiotto, C., 2014. Development and evolution of detachment faulting along 50 km of the Mid-Atlantic Ridge near 16.5° N. *Geochemistry, Geophysics, Geosystems*, *15*(12), pp.4692-4711.

Spencer, J.E., 1999. Geologic continuous casting below continental and deep-sea detachment faults and at the striated extrusion of Sacsayhuaman, Peru. *Geology*, *27*(4), pp.327-330.

Tucholke, B.E., Lin, J. and Kleinrock, M.C., 1998. Megamullions and mullion structure defining oceanic metamorphic core complexes on the Mid-Atlantic Ridge. *Journal of Geophysical Research: Solid Earth*, *103*(B5), pp.9857-9866.

Tucholke, B.E., Behn, M.D., Buck, W.R. and Lin, J., 2008. Role of melt supply in oceanic detachment faulting and formation of megamullions. *Geology*, *36*(6), pp.455-458.

Chapter 3

Strain localization in the brittle domain during detachment faulting in a nearly amagmatic ultraslow spreading context: 64°35'E Southwest Indian Ridge

Souradeep Mahato*, Mathilde Cannat, Isabelle Martinez

Institut de Physique du Globe de Paris, UMR 7154 -CNRS, Université Paris Cité, Paris, France

Key points: Foliated microbreccia, fault gouge, strain localization, active detachment fault, magma-starved MOR section, Particle size distribution (PSD), Fractal distribution, lithosphere strength

3.1 Abstract

The 64°E region of the eastern SWIR is a melt-poor end-member region of the MOR system. Magma focusing on axial volcanoes leaves >50km wide along-axis corridor, where seafloor spreading occurs almost entirely via detachment faults (Sauter et al., 2013). These faults exhume mantle-derived rocks on the seafloor in alternate polarity (flip-flop faulting). They root into domains of grain size reduction of the fresh peridotite at the base of the brittle-ductile transition domain (Bickert et al., 2021). Here, we document strain localization microstructures formed in partially serpentinized ultramafic rocks in shallower regions of the detachment fault zone

Most samples in our study are serpentinite micro-breccia and gouge from exhumed detachment fault surfaces. These samples are tectonically brecciated with clast-rich and clast-poor domains and a matrix made of microcrystalline serpentine. Textural evidence indicates that brecciation in all samples postdated partial serpentinization of the peridotite. The most highly sheared microdomains display semi-brittle deformation: serpentinite microclasts are fractured but are also partially dissolved and replaced by syn-tectonic chrysotile fibers forming a fine-grained matrix, with a strong shape and crystallographic preferred orientation. Based on both outcrop-scale and sample-scale observations, we propose that syn-tectonic crystallization of the chrysotile fibers was favored by hydrous fluids circulating in the detachment fault zone. Brittle deformation experiments show that chrysotile gouges have very low frictional strength, comparable to talc, in low temperature, water-saturated conditions, but that their strength increases at higher temperature and confining pressure. Dissolution-precipitation processes such as documented in our samples could, however, reduce the strength contrast between chrysotile gouges in the shallower and deeper portions of the detachment faults. The strength of the fault zone also depends on whether the weak gouge line is substantial or only minor portions of the active fault splays. The strength of the fault zones is, therefore, expected to vary primarily due to the distribution, thickness, and interconnectedness of the chrysotile gouge layers, with the presence of hydrous fluids playing a crucial role in these

variations. Our results contrast with observations made at more magmatically robust oceanic detachments, where assemblages of talc-amphibole-chlorite and serpentine formed by the hydrous alteration of mafic-ultramafic protoliths and by metasomatism by hydrous fluids that have altered mafic lithologies commonly localize deformation.

3.2 Introduction

[1] A significant portion of the oceanic lithosphere is accreted through large (>10 km) offset detachment faulting along slow-spreading mid-oceanic ridges (Ocean Detachment Faults or ODFs; Cann et al., 1997; Smith et al., 2006; Cannat et al., 2006; Escartín et al., 2008). These faults are crucial fluid circulation conduits within the upper oceanic lithosphere (Jons et al., 2009; McCaig et al., 2010; Roumejon & Cannat, 2014; Andreani et al., 2007). They have a steep angle at depth (deMartin et al., 2007; Parnell Turner et al., 2017) and are assumed to root into or just above the brittle-ductile transition (BDT) domain (Lavier et al., 2000; Olive et al., 2010; Hansen et al., 2013; Bickert et al., 2021). In ridge contexts that develop these detachment faults, microseismicity studies point to depths of the BDT, representing the axial brittle lithospheric thickness of ~8-12 km for the slow-spreading Mid-Atlantic ridge (MAR) (deMartin et al., 2007; Parnell-Turner et al., 2017), and ~15-20 km for the ultraslow-spreading Southwest Indian ridge (SWIR; Schlindwein & Schmid, 2016; Grevemeyer et al., 2019; Tao et al., 2020; Chen et al., 2023) and for the Gakkel and Knipovich ridges (Schlindwein & Schmid, 2016; Meier et al., 2021). However, numerical models that rely only on cohesion weakening as a function of increasing strain predict that large offset detachment faults do not develop in a brittle axial lithosphere that is thicker than 10 kilometers (Lavier et al., 2000; Lavier & Buck, 2002). Additional weakening mechanisms involving a larger decrease in the effective strength of the fault rocks are therefore needed for detachment faults to form in a thick axial lithosphere. This is illustrated by numerical models that also reduce the friction coefficient above a critical amount of strain and do produce detachments in thick lithosphere conditions (Sandiford et al., 2021; Bickert et al., 2020; Mezri et al., submitted). The direct study

of fault rocks outcropping and sampled at exposed ODF surfaces is critical to constrain these models.

Such studies have, to this date, mostly concerned ODFs that formed in contexts of low to moderate magmatism at both the MAR and SWIR. These detachment fault zones show localized deformation up to 70 m below the exposed fault surfaces, with schistose intervals and anastomosing fractures (Schroeder and John, 2004; Karson et al., 2006; Boschi et al., 2006; Schroeder et al., 2007; Escartin et al., 2017; Bonnemains et al., 2017). There have been no reports there of meter to decameter-thick intervals of cataclastic serpentinite such as those documented in fossil Ocean Continent Transition (OCT) detachments (Manatschal and Muntener, 2009; Picazo et al., 2013).

The fault rocks exposed in magmatically active ODF contexts typically contain semi-brittle shear zones that contain deformed and recrystallized hydrous minerals such as amphibole, chlorite, and/or talc, in addition to serpentine (Schroeder and John, 2004; Boschi et al., 2006; Schroeder et al., 2007; Picazo et al., 2012; Escartin et al., 2003). These minerals formed, for the most part from hydrothermal alteration of serpentinized peridotites that contained veins of gabbroic rocks (Cannat & Casey, 1995; Boschi et al., 2006; Hansen et al., 2013; Picazo et al., 2012; Schroeder & John, 2004; Casini et al., 2021; Jons et al., 2009; Albers et al., 2019). An origin from the alteration of ultramafic fault rocks by Si-Al-Fe-rich hydrothermal fluids, resulting from the prior alteration of gabbroic materials, is also proposed in some cases (Escartín et al., 2003; Boschi et al., 2006; McCaig et al., 2007; Picazo et al., 2012; Früh-Green et al., 2017). The existence of a gabbroic component in or near the fault is, therefore, key to facilitate strain localization in the brittle lithosphere.

In the absence or near absence of magma, which is the case for ODFs developed in a few regions of the Southwest Indian (Cannat et al., 2006; Sauter et al., 2013) and Gakkel (Michael et al., 2003), ultraslow spreading ridges, it is unlikely that hydrous minerals developed from the alteration of gabbros will have a significant impact on strain localization. Indeed, detachment faults in nearly amagmatic sections of the Eastern SWIR expose serpentinized peridotites onto the seafloor, with rare basalts

(Sauter et al., 2013), and the proportion of serpentinized peridotite samples that do contain veins of gabbroic material is much lower than at more magmatically robust ODFs (Paquet et al., 2017; Rouméjon et al., 2015; Bickert et al., 2023). Outcrops of detachment fault zones in this nearly amagmatic context (Mahato and Cannat, in prep.) are more comparable to those documented at fossil OCTs (Manatschal and Muntener, 2009; Picazo et al., 2013), with meter to decameter-thick intervals of cataclastic serpentinites, microbreccia, and gouge.

In this paper, we study deformation microstructures of samples collected during ROV dives of the ROVSMOOTH cruise (Cannat et al., doi:10.17600/16002000) from the most deformed microbreccia and gouge intervals (Figure 1). For the purpose of comparison, we also include a few gouge samples from the exposed surface of two smaller offset normal faults that dissect the exposed detachment surfaces in the same area. Previous sample scale studies of serpentinized peridotites in this nearly amagmatic region of the SWIR have focused on the serpentinization processes (Rouméjon and Cannat, 2014; Rouméjon et al., 2015) on deformation and strain localization processes in fresh peridotites in the root zones of the detachments, at and below the brittle-ductile transition (BDT; Bickert et al., 2021); and on the evidence for the percolation of small amounts of seawater-derived fluids in the detachment fault zone, down to the BDT domain (Bickert et al., 2023). This paper is, therefore, the first sample-scale study focused on deformation and strain localization processes in the upper, brittle, and already partially serpentinized regions of nearly amagmatic ODFs. We describe the samples' microstructures, including clast size distribution, we analyze the major element composition of the clasts, and discuss the possible consequences of our results in terms of the effective strength of the fault rocks in the brittle region of the ODFs. In this discussion, we refer to other studies of cataclastic serpentinites based on field samples (fossil OCT in SE Switzerland; Picazo et al., 2013; Franciscan Complex in California, USA; Hirauchi and Yamaguchi, 2007; and serpentinites exposed along the San Andreas fault system; Andreani et al., 2005), and on samples deformed in laboratory experiments (Tesei et al., 2018; Behnsen & Faulkner, 2012; Moore et al., 1997, 2004; Moore & Lockner, 2011).

3.3 Geological setting of the samples

[1] The south-facing wall of the axial valley at the 64°35'E SWIR region (Figure 1) is the exposed footwall of the currently active D1-detachment fault (Sauter et al., 2013; Cannat et al., 2019). This region of the SWIR is characterized by "flip-flop" detachment faulting (Reston & McDermott, 2011), where a new detachment fault cuts through the footwall of a preceding detachment fault with opposite polarity (Sauter et al., 2013). This flip-flop ODF regime has been active for at least the past 10 myr, exposing ultramafic seafloor in the two diverging plates (Sauter et al., 2013). This study concerns samples collected in the SWIR axial region from the two most recent ODFs. D1 is the presently active, south-facing detachment; it has been active for only ~300 kyrs (Cannat et al., 2019), its footwall forms the 2500 m-high northern axial valley wall (Figure 1), and it dissected the D2, north-facing ODF (proposed to have been active for ~1.5 myr; Sauter et al., 2013).

Microearthquakes in the study area have been relocated down to 15 km below the seafloor (bsf), indicating that the brittle lithosphere there is at least that thick (Chen et al., 2023). Seismic refraction data indicate that the crust is 3 to 5 km thick (Momoh et al., 2017; Corbalan et al., 2021). Based on seafloor geology (Sauter et al., 2013), this crust is interpreted as made primarily of variably serpentinized peridotites (Momoh et al., 2017; Corbalan et al., 2021). Several planar seismic reflectors, up to 1.5 km apart in the across fault direction, dip ~50° to the south and are imaged down to ~5 km bsf (Momoh et al., 2017). These reflectors are interpreted as fault damage associated with ODF D1 (Momoh et al., 2017). D1 emerges near the bottom of the northern axial valley wall (Figure 1), except in the western part of the study area, where the lower slopes of the wall are covered by basalt flows emitted at a curved volcanic ridge at ~4170 mbsl (meters below sea level). The most recent D1-related displacement in this western region appears to occur above this volcanic ridge, at a south-dipping normal fault with a dip of ~40-45° and a horizontal throw of at least 150 m (Figures 2e and d; Tominaga et al., in prep.). Another small offset normal fault surface sampled for this study (fault dip of ~55° to the south; horizontal fault throw

~75m) dissects the thin volcanic cover in the axial valley floor and exposes D2 fault rocks at depths of 4880 mbsl (Figure 2g; Tominaga et al., in prep.).

The other samples in the study (Figure 1) come from intervals of serpentinite gouge and microbreccia in the exposed fault zone of the D1 or D2 detachments (Table 1). Map and outcrop scale characteristics of these exposed fault zones are documented in Mahato and Cannat (in prep.; Chapter 2 of this thesis manuscript). This larger-scale geological and tectonic study shows that both the D1 and the D2 fault zones are probably made of several anastomosing fault splays that link around large, up to kilometer-scale phacoids of less fractured serpentinized peridotite. Deformation in these fault splays varies in intensity over >100 m, from widely-spaced arrays of sub-parallel fractures to tightly linked fractures defining hecto to decameter scale phacoids, to cataclastic intervals with breccia, microbreccia, and gouge (check summary of the observed outcrop scale structures in the conceptual sketches of Figure 14b to e).

Serpentinite gouge and microbreccia horizons are the most deformed rocks in this structural sequence. They have distinctive pale green to yellow colors that contrast with the darker serpentinized peridotites (Figure 2b and d). They occur as laterally continuous, meter to plurimeter-thick layers in the core of the exposed fault splays (Figure 2c). They also occur as centimeter to decimeter-thick discontinuous horizons in the periphery of some sigmoidal phacoids (Figure 2a). Preliminary thin section observations of microshear zones in gouge and microbreccia samples (Mahato and Cannat, in prep.; figure 4d-g of chapter 2) suggest localized semi-brittle deformation, syn-kinematic growth of serpentine fibers, and dissolution of some microclasts. Combined with outcrop scale observations, this led Mahato and Cannat (in prep. and Chapter 2) to hypothesize that the development of these gouge horizons is favored by syn-kinematic access to hydrous fluids. This hypothesis is, as we will see, supported by the more detailed study presented here.

D1 gouge and microbreccia samples come from ~4980 mbsl just above the emergence of the detachment in the east (ROV dive 649; Figure 1) and from exposed,

D1 fault surfaces at depths of ~2970-3190 mbsl, near the Old City vent field (Lecoeuvre et al., 2021; Figure 1). In addition, the relatively small offset fault explored during ROV dive 648 (Figure 1) probably reworks gouge and microbreccia horizons formed in the D1 fault zone (Figure 2 e and f). D2 gouge and microbreccia samples come from the erosional south-facing scarp explored during ROV dive 647 at the top of the axial valley wall (Figure 1) and from the north-facing exposed D2 fault surfaces on the northern flank of this wall in the west of the study area (ROV dive 643; Figure 1). D2 gouge and microbreccia are also exposed in the south-facing scarp formed by the small offset normal fault explored in the axial valley floor during ROV dive 646 (Figures 1 and 2g), A summary of the geological context of the 14 gouge and microbreccia samples selected for this study is proposed in Table 1, and ROV dive video snapshots documenting each sampling site are shown in Supplementary Figure 1. Due to the fragile nature of these rocks, a water-tight box designed for microbiological sampling (biobox) was used to collect most of them, preventing them from being washed away in the ROV basket. Thin section-size fragments of these fragile samples were then selected for thin-section preparation (Figure 3). Several had to be indurated with epoxy (for example, Figure 3f).

3.4 Methods

We selected 14 of the 18 collected gouge and microbreccia samples (Table 1) to characterize their mineralogy and texture. We used a combination of optical microscopy, with or without the addition of a 550 (λ) retardation plate under cross-polarised light, Raman spectroscopy, and scanning electron microscopy (SEM). We also measured clast and matrix mineral compositions using an electron microprobe. Finally, we used SEM images acquired under several magnifications to analyze clast (particle) size distributions (PSD).

Raman Spectroscopy. We used the Raman micro-spectrometer LabRAM HR Evolution Horiba (Institut de Physique du Globe de Paris, France) to identify the serpentine species. The spectra were collected within the 3400-3800 cm^{-1} range using

a 488 nm laser, a five mW effective power source, and a 50X objective lens. Each spectrum was collected for 120 seconds and repeated twice. To correct the baseline and find peaks, we utilized the KnowItAll (@Wiley Science Solutions) software package, referencing previously reported peaks for specific serpentine species minerals (Tarling et al., 2018; Roumejon et al., 2015).

Scanning Electron Microscopy (SEM). We acquired electron back-scattered images to characterize microstructures and overall chemical variations. We used the scanning electron microscope (SEM) (Institut de Physique du Globe de Paris, France).

Electron Microprobe. We used a Cameca SX-100 electron microprobe (platform CAMPARIS, Sorbonne Université, Paris) to measure major element concentrations in clasts and matrix, with a constant acceleration voltage of 15 kV and a beam current of 10 nA. The spot size was ~2 μm, and the counting time was 190 s.

Particle Size Distribution. We used SEM images acquired at several magnifications (Figure 4a, b) to quantify particle size distributions (in our case, particles are clasts in the microbreccia and gouge) with the ImageJ free software (Rasband, 2007). Clasts appear brighter than the finer-grained matrix and were identified using automatic brightness thresholding, occasionally adjusting manually for improved detection (Figures 4c and d). Then, clasts were automatically measured from the scaled images. Due to their lesser resolution, SEM images acquired at smaller magnifications (Figure 4a) do not identify the smallest clasts. Alternatively, images acquired at higher magnifications cover only a small area (Figure 4b) and may not be representative of the overall distribution of smaller clasts in the lower magnification image. For this reason, we chose to analyze and compare PSD data separately for each magnification.

To visualize and analyze the data, we used log-log plots of the cumulative number of particles greater than a given size *N(l)* versus *l,* where *l* is the square root of the clast area (Figure 4e). A fractal distribution of particle size, described by $N(l) = C(l)^{-D}$ (Turcotte, 1986; Glazner & Mills, 2012) corresponds to a straight line of slope -D in

N(l) versus *l* log-log plots. PSD data in natural and laboratory fault rocks do not, however, systematically show self-similarity, and PSD might also show exponential or linear distributions (e.g., Keulen et al., 2007). We wrote a Matlab script to group the clasts by unique *l* values and to assign an *N* value to each group. Following Glazner and Mills (2012), this method sidesteps arbitrary bin sizes (Supplementary Figure 4d-f) in traditional binning (e.g., Turcotte, 1986) and offers finer data granularity. Prior to analyzing the results in terms of linearity and D values, we set an upper bound for l values considered at each magnification to correspond to *N*=20. The choice of this upper boundary is arbitrary, designed to exclude underrepresented larger clasts (Figure 4e). For all magnifications (e.g., 28X, 1000X in Figure 4), the data towards the smaller clast sizes show a deviation from linearity (or follows another power law distribution with a different D-value) below a certain threshold (e.g., $l < 12$ μm for 28X; $l < 0.62$ μm for 1000X, in Figure 4e). For low-magnification images (e.g., 28X in Figure 4e), this deviation is likely a detection issue due to the lower resolution (pixel/μm). For high-magnification images (e.g., 1000X in Figure 4e), deviations in smaller clast sizes are not fully explained by resolution issues and may, as we will see, result from actual microscale characteristics of the samples.

Our study focuses on the most deformed intervals that have the smallest clast sizes. When investigating linear fits to the power-law distributions, we used the deviation value determined above as a lower bound for clast sizes considered at each magnification; then, instead of using the N=20 bound for the larger clast sizes (as shown in Figure 4e), we manually selected the larger size bound in order to ensure the best linear fit. This manual selection approach was used in previous PSD studies (e.g., Blenkinsop, 1991; Melosh et al., 2014) whenever data did not define a single linear trend over the full range of resolved particle sizes.

3.5 Results

3.5.1. Microstructures, mineralogy, and mineral compositions of microbreccia samples

The fragments of gouge and microbreccia samples selected for this study contain clast sizes up to ~2.5 cm long (Figure 3). Larger, up to a few decimeter-sized clasts are,

however, seen in the corresponding outcrops (for example, in Figure 2d and f). Some fragments are clast-poor and foliated (Figure 3b), others are clast-rich. The clasts visible in these fragments come in different shapes: angular, elongated, and subrounded (Figure 3e). In several samples, the matrix is carbonated (Figure 3d; Table 1). In thin sections, most samples from the D1 and D2 exposed fault zones (Table 1 and Figures 5a and 6a) contain microshear bands up to ~ 15 mm thick (Figures 5c, 5e, 6c, and 6e) alternating with and warping around more clast-rich (clasts surface % > 50) microdomains up to ~10 mm wide (Figures 5d and 6d). Sample RS-646-12 (Figure 7b, d and f), collected from the D2 fault zone exposed by a small offset normal fault in the axial valley floor, locally has a clast-poor matrix, with subrounded microclasts in a fine-grained serpentine matrix that shows no preferred orientation (Figure 7f). Samples collected from the planes of smaller offset normal faults during ROV dives 646 and 648 (Table 1 and Figure 7a, c, and e) lack the mm-thick, clast-poor, shear bands. Their matrix is mostly clast-rich and made of clasts with no shape nor crystallographic fabric. There are, however, occasional clasts that do include sheared microdomains (Supplementary Figure 2b-c). We interpret these clasts as reworked fragments of the D1 (ROV dive 648) or D2 (ROV dive 646) fault zones that are cut by these smaller offset faults.

The clasts are made of serpentinized peridotite, in some cases with a typical mesh texture developed after olivine (Figure 5d) or bastite texture developed after pyroxene (Figure 7c-d). The presence of bastite and mesh textured clasts indicates that the brecciation process followed serpentinization. Mesh texture clasts primarily consist of lizardite, evidenced by characteristic Raman peaks at 3685 and 3703/3704 cm^{-1} (Figure 5b; Auzende et al., 2004; Tarling et al., 2018). Clasts in the sheared domains also feature lizardite, lizardite, and chrysotile (peaks at 3691 and 3697/3698 cm-1), and polyhedral serpentine (Figure 5b, 6b and Supplementary Figure 3). Compositionally, the serpentinite clasts align with typical SWIR serpentinites (Roumejon & Cannat, 2014; Roumejon et al., 2015), characterized by Mg# numbers of 86-97 (Figure 8a; Table 3). While serpentine in the clasts also has typical total oxides and SiO2 contents, serpentine in the fine-grained matrix is commonly depleted (total

oxide < 70 wt%; SiO2 contents < 38 wt%; Figure 8a). We interpret these characteristics as due to the porosity of the fine-grained serpentine matrix.

Only a few samples (Table 1) retain olivine relicts in the mesh cores (Figure 5d). The Mg# numbers of these olivine relicts (Table 2: ~90-91.5) are consistent with data from other abyssal peridotite samples in the study area (Seyler et al., 2003). The same is true for the orthopyroxene, spinel, and most clinopyroxene relicts found in partially serpentinized clasts (Table 2 and Supplementary Table 1). In two samples from the western part of the study area, some clinopyroxene clasts have higher TiO_2 contents (> 0.5 wt%; Figure 8b; Table 2) and higher FeO contents (> 6 wt%), than abyssal peridotites, consistent with a gabbroic origin, by comparison with data from documented gabbroic suites from the SWIR (Atlantis Massif, Dick et al., 2002; and our study area, Paquet et al., 2016). Yet other relict minerals in the same samples, and the abundance of serpentine, indicate a primarily ultramafic primary mineralogy.

One sample (RS-644-23), a domain contains extensively fractured CPX with high CaO contents (>25 wt%; Table 3) and very low TiO_2 and Al_2O_3 (<1 wt%; Table 3), indicating a hydrothermal origin (Stakes et al., 1991), which therefore predated the brittle deformation of the sample. Chlorite clasts were also observed in those samples that contain gabbro-derived cpx clasts (Table 3). In a sheared microdomain of one of these samples, we observed dissolution/reaction rims around a few serpentine clasts (Figure 9a). The sheared matrix in this microdomain is made of serpentine with a crystallographic fabric, and contains a few flakes of chlorite. The cores of these rimmed serpentine clasts are Al and Fe-poor (Figure 9b). The rims are Al and Fe enriched and probably made of a mixture of serpentine and chlorite. The serpentine in the sheared matrix has intermediate compositions (Figure 9b). These textural and chemical relations suggest syn to post tectonic metasomatism by a fluid enriched in Al and Fe, probably through local interactions with chlorite and gabbroic clinopyroxene clasts.

3.5.2. Clast-poor and clast-rich microdomains: SEM Microstructural Analysis

The matrix of clast-poor, foliated microdomains in samples of gouge and microbreccia samples from D1 and D2 fault zones show constructive bluish-green to blue interference colors when viewed under cross-polarized light with a retardation plate (Figures 5c and 6c). This indicates that the slow crystallographic axes of the serpentine crystals in this fine-grained matrix are oriented sub-parallel to the foliation. In these foliated domains, SEM images also show that the matrix occupies a greater area than the total area of the clasts (typically > 50% of total area based on quantitative analyses with ImageJ). The clasts predominantly show an elongated tabular form (up to ~100 μm long) alongside phacoidal, sigmoidal, and augen shapes (up to ~200-250 μm long), with a significant number of them aligning parallel to the foliation (Figures 5e, 6e, 10a and 10d). The smaller clasts, sometimes only ~ 5-12 μm in size, are commonly rounded or oval-shaped and have poorly defined boundaries with the matrix (Figures 10c, 10d, 11c, and 11d). Raman spectra analysis reveals that these rounded clasts and the sheared matrix are made of chrysotile (Figures 5b, e, and 6b, e). Other clasts are also made of chrysotile or of a composite of chrysotile mixed with lizardite and polygonal serpentine phases (Figures 5b, e, 6b, and Supplementary Figure 3). The chrysotile in the matrix is microcrystalline (a few micrometers in length at the most; Figure 10d). There are also elongated clasts up to ~50 μm that are made of fibrous chrysotile (Figure 10d).

The matrix in the clast-rich domain of gouge and microbreccia samples from D1 and D2 fault zones is also made of chrysotile based on Raman spectra (Supplementary Figure 3) and also appears microcrystalline. However, it is not foliated (Figure 10b and c) and has no preferred crystallographic orientation. Clasts are mostly angular, mostly made of lizardite and lizardite-chrysotile composites, have no shape fabric (Figure 10b and c), and typically occupy a greater total area than the matrix (typically > 50% of total area based on quantitative analyses with ImageJ). Larger clasts show edge abrasion (Figures 5d and 10e), and bastites typically break into tablet-shaped fragments (Figure 11c). SEM images show that several clast-rich microdomains are

dissected by thin clast-poor microshear zones (Figure 11a). Also, within several broader microshear zones, the foliated matrix wraps around lenticular-shaped clast-rich domains up to a few hundred μm in size (Figures 5e, 10a, 10c, and 11a). These microtextures are consistent with a chronology with the clast-rich microbreccia predating the formation of the foliated microshears.

Gouge and microbreccia samples collected in the exposed surface of small offset faults dominantly have a clast-rich microtexture similar to clast-rich domains observed in detachment fault zone samples (Figure 7c and e). They do not show foliated intervals that can be followed at thin section scale (Figure 7a). Some samples from the small offset fault plane explored during ROV dive 648 (Figures 1, 2e, and 2f) do, however, contain clasts of foliated, clast-poor material, and we interpret these as reworked fragments of the D1 fault material that is dissected by the fault (Figure 2e).

Sample RS646-12 comes from an extensively altered outcrop of the D2 fault zone, exposed by a small offset fault in the axial valley floor (Figures 2g and 7a). It has a specific microstructure with microdomains that have a greater proportion of matrix and less angular clasts than the clast-rich microdomains in all the other samples (Figure 7d and f), but no foliation and no crystallographic fabric of the serpentine matrix (Figure 7f). This microtexture could be related to the extensive hydrous alteration of the corresponding outcrop.

3.5.3. Micro-scale processes and particle size distribution (PSD) in clast-poor vs. clast-rich micro-domains

Our objective here is to provide a quantitative textural description of the finest-grained portions of the microbreccia and gouge samples based on PSD data obtained from BSE images with the highest magnification (800X and 1000X). As explained in the method section, PSD data obtained at such magnifications have a small area coverage but do resolve the smallest sub-micron particle sizes.

We first look into the PSD data obtained at a 1000X magnification in the clast-poor, foliated domains of gouge-microbreccia samples (Figure 12). Among the smallest identified particles, most are probably genuine clasts resulting from intense fragmentation and abrasion in the sheared matrix, yet most also display a weak BSE contrast with the matrix and contorted, commonly ill-defined boundaries (Figure 12d). Some of these low-contrast particles are aligned and appear not to be clasts but brighter portions of elongated and fibrous chrysotile grains that may have formed by local growth from the matrix (Figure 12d). Particles in the size range considered for log-log linear fitting ($0.62 < l < 2.42$ μm for the example in Figure 12; see Method) follow a fractal distribution (with a D-value of 1.69 in Figure 12). Contours of smaller particles are even less clearly defined and do not have the requisite numbers (*N)* in each l group to sustain a power-law distribution (Figure 12a). One plausible explanation is that a sizable fraction of the smallest particles underwent dissolution and recrystallization, eventually merging with the matrix.

We now compare the PSD obtained in the clast-rich and clast-poor domains of 4 representative samples using BSE images acquired at 800X (Figure 13). RS-648-25 comes from the fault plane of a smaller offset fault that dissects D1 fault zone exposures (Figure 2e). It does not contain clast-poor domains. RS-646-12 comes from a highly altered exposure of the D2 fault zone in the axial valley floor (Figure 2g). RS-643-05 comes from a D2 fault zone exposure (Figure 2b), and RS-649-3 from a D1 fault zone exposure (Figure 2c and d). Both samples contain clast-rich and foliated clast-poor domains.

For the sheared clast-poor domains (samples from the D1 and D2 detachment fault zones; Figure 13g and i), we have seen that the smallest particles identified and measured in the PSD data of are not all clasts, while clasts in the larger size range considered in our PSD study (a few microns) have contorted limits that suggest that they have been partially dissolved into the matrix. These two characteristics might explain slightly higher D-values (fractal dimensions) than in the clast-rich domains of the same samples (1.79 and 1.82 against 1.62 and 1.55, respectively; Figure 12 b and

c). Higher D values in these clast-poor domains may also result from higher finite strain, leading to enhanced clast size reduction (Heilbronner and Keulen, 2006). Whatever the case, the measured D-values for both clast-rich and clast-poor domains fall within the range of previously reported D-values for cataclastic fault rocks and gouges in the field (1 to 2.5; Rousell et al., 2003; Storti et al., 2003; Billi, 2005; Clark et al., 2006), and in laboratory experiment (0.7 to 2.5; Marone & Scholz, 1989; Sammis et al., 1987; Amitrano and Schmittbuhl, 2002; Keulen et al., 2007).

For clast-rich domains, this PSD study shows that clasts in the most fine-grained portions of each sample have similar size distributions in detachment fault zone samples, and in the fault gouge of a smaller offset fault (RS-648-25). Clast size distribution therefore confirms the visual similarity between these microbrecciated domains, and suggests that this ultracataclastic microstructure is not dependant on the cumulative net slip of the fault. A similar conclusion was reached by Wilson et al. (2005) and Reches & Dewers (2005), from the comparison of fault gouges from the San Andreas fault (cumulated displacement of about 160 km), with a gouge formed after a single earthquake and only 0.4m displacement in a south african gold mine. These authors further proposed that these gouges formed by dynamic rock pulverization during earthquake propagation.

Finally, the atypical class-poor domains of sample RS-646-12 (non-foliated matrix, more rounded clasts, and a larger clasts to matrix proportion than other D1 or D2 clast-poor domains; Figures 7f and 13e and f) represent clear outliers texturally and display variable PSD patterns. In the portion of this sample represented in Figure 13e (clast-poor texture 1), the PSD is, for the most part, non-fractal (Figure 13a), and the small range of clast sizes over which it is log-log linear, have a significantly lower D value (0.81) than clast-rich (1.46 to 1.62) and clast-poor (1.79 and 1.82) domains in the other samples, and in other regions of this same sample that contain more clasts in the smaller, ~0.6-3 μm range (e.g., clast-poor texture 2; Figure 13f). Our preferred explanation is that this low D-value results from the static dissolution of most clasts in this size range into the microcrystalline matrix of this atypical sample (Figure 13e).

3.6 Discussion

3.6.1. In what conditions and over what depths did the studied microbreccia and gouges form?

Gouge and microbreccia from the exposed planes of the two small offset (< 140 m; Tominaga et al., in prep.) normal faults sampled for this study formed within ~150 m of the seafloor. They lack the clast-poor, foliated shear bands that characterize samples from the D1 and D2 exposed detachment surfaces, but their clast-rich microstructure is similar to that of these D1 and D2 samples. This indicates, as explained in section 4.3, that this clast-poor cataclastic structure is independent of fault displacement. It also shows that it can form up to very shallow depths. The clast-poor foliated shear bands, when present, dissect and wrap around clasts of the clast-rich microbreccia (Figures 10a, 10c, and 11a). The shape and crystallographic preferred orientation of the small chrysotile fibers in the matrix of these clast-poor domains, the imbrication and the elongated shape of the clasts, are similar to microstructures produced by frictional deformation processes in the laboratory at temperatures down to 25°C (Tesei et al., 2018). However, several observations point to additional, non-frictional mechanisms being active during the deformation of our samples.

While most clasts in clast-rich domains are angular and retain the lizardite and lizardite+chrysotile±polygonal serpentine mineralogy of the original serpentinized peridotite, most clasts in clast-poor domains are elongated or sigmoid-shaped, and made of chrysotile, commonly with the chrysotile fibers nearly aligned in the foliation of the matrix (Figures 5, 6, 10d, and 11d). The change of clasts shape and the crystallographic orientation could be explained by abrasion, rotation and spalling in the deforming matrix, but the change in mineralogy indicates that dissolution and crystallization processes were also involved. In Figure 11b, a clast of bastite, with a lizardite+chrystotile mineralogy, is broken and enclosed in the foliated chrysotile matrix. In Figure 9a, in a sample that contains gabbroic clasts, rims of Al and Fe-rich serpentine (probably a mix of serpentine and chlorite) form around serpentine clasts. This indicates metasomatism and points to the involvement of a fluid. Outcrop-scale

ROV observations also suggest that hydrous fluids play a role in the formation of the gouge and microbreccia horizons (Mahato and Cannat, in prep.; Chapter 2).

Chrysotile may crystallize over a large range of temperatures (T <400°C; Chernosky et al., 1988; Evans, 2004). Actually, the formation of gouges in the complex anastomosing fabric of the D1 or D2 detachment damage zones is not expected to occur at a single depth/temperature but potentially over a large part of the brittle axial lithosphere (Figure 14a and Mahato and Cannat, in prep.; Chapter 2). Based on local seismicity records, this would be ~15 km bsf in our study area (Chen et al., 2023). Regarding the formation of the gouge and microbreccia studied here, this broad range can be reduced to temperatures < 400°C (Figure 14a) to allow for pre (the peridotites in our samples were serpentinized prior to brecciation) and syntectonic (crystallization of chrysotile) serpentine stability. Chrysotile has been shown to form at very low temperature, near surface conditions and therefore we cannot constrain the lower bound of this temperature range (Evans, 2004). However, the dissolution and crystallization processes involved in the formation of the chrysotile matrix would be enhanced at higher temperatures. Pyroxene geothermometry suggests that high-stress semi-brittle deformation microstructures form at temperatures of at least 800°C in fresh peridotite samples from our study area (Bickert et al., 2021). If we consider a linear geothermal gradient, and equate the base of the seismogenic lithosphere to this 800°C brittle-ductile transition, then 400°C would be reached at 7.5 km bsf (Figure 14a). However, in a context where hydrothermal circulations can impact local geotherms, a given temperature does not correspond to a fixed depths: it can be deeper in hydrothermal downflow regions, shallower in hydrothermal upflow zones.

Most recorded local earthquakes (~40 events/day, local magnitudes <1 to 3.2) occur in the 8 to 13 km bsf depth range (Figure 14a; Chen et al., 2023). Temperatures there are most likely > 400°C, too hot for serpentine to form. However, earthquakes are also recorded up to depths of 1 km bsf, in the fault zone and in the adjacent footwall and hanging wall (Figure 14a). If the formation of the clast-rich cataclastic textures does occur during earthquakes, as proposed for similar microtextures by Wilson et al.

(2005) and Reches & Dewers (2005), it might accompany some of these earthquakes. Further displacement on the newly formed fault splays, facilitated by fluids, could then produce the clast-poor microshears over a range of depths and temperatures.

3.6.2. What are the consequences of the microstructural observations in terms of strength of the lithosphere?

Laboratory experiments show that the frictional strength of water-saturated chrysotile gouge is very low (Moore et al., 1997; 2004; Tesei et al., 2018). Their friction coefficient can be as low as 0.1 at 100°C and a confining pressure of 40 MPa, and increases at higher temperatures and confining pressure to 0.55 at 280°C and 200 MPa in the Moore et al. (2004) study. This drastic change in friction coefficient is explained by progressive dewatering of the fine-grained fibrous aggregate (Moore et al., 1997; Moore and Lockner, 2004). It is accompanied by a change from velocity strengthening in the lower temperature range to velocity weakening at higher temperatures and confining pressures (Moore et al., 2004). Experimental data, therefore, suggest that faults lined by chrysotile gouge exhibit contrasted rheological behavior, weak and possibly creep-dominated at relatively shallow depths, and stronger and prone to earthquakes at higher temperatures and confining pressures (Moore et al., 2004).

Natural fault zones that are lined by phyllosilicate gouges commonly show textural evidence for syn-tectonic dissolution-precipitation processes comparable to those described in the clast-poor domains of our samples: localized hydrous fluid influx in cataclastic domains promotes the alteration of frictionally stronger minerals, to weaker phyllosilicates that form interconnected layers (Wallis et al., 2015). These mixed frictional-viscous deformation processes have been investigated experimentally and found to significantly reduce the rock strength (Niemeijer & Spiers, 2005; 2007). Because dissolution-precipitation processes should be more active at higher temperatures, this effect could reduce the strength contrast predicted by Moore et al.

(2004) between the shallower and deeper portions of faults lined by chrysotile gouge in regions where hydrous fluids are accessible.

Outcrops of the D1 detachment fault zone in our study area show strong contrasts in terms of the thickness and lateral continuity of the gouge-microbreccia intervals (Mahato and Cannat, in prep.; Chapter 2). This is interpreted as due to the contrasted availability of hydrous fluids at scales of several hundred meters, between different regions of the fault zone, or between different fault splays in the kilometer-thick damage zone (Figure 14a and Mahato and Cannat, in prep.; Chapter 2). Regions or splays that are not lined by the meter to plurimeter-thick gouge layers are expected to be stronger, even at shallow depths. The fault strength in these regions would be expected to be similar to that of the fractured serpentinized peridotites up to several tens of meters away from the gouge horizons in the more fluid-rich regions or splays (Figure 14b and c), where chrysotile-bearing gouge are thin and line only some of the anastomosing fractures (Figure 14d). Numerical models of mid-ocean ridge tectonics in a magma-starved context (e.g., Bickert et al., 2020; Sandiford et al., 2021; Mezri et al., submitted) typically apply a single lower friction coefficient (chosen from the experimental deformation literature on lizardite and chrysotile) for strongly deformed serpentinized peridotites in fault zones. Although making these models more complex is not the point, our results indicate that the strength of these fault zones can vary substantially depending on the availability of hydrous fluids.

3.6.3. Fault strength at nearly amagmatic versus more magmatic axial detachment fault systems

Deformation experiments indicate that the frictional strength of water saturated chrysotile gouge can be as low as that of talc (friction coefficients 0.1-0.3; Morrow et al., 2000; Moore and Lockner, 2004; Escartin et al., 2008; Chen et al., 2017), the weakest mineral found in the talc±tremolite±chlorite±serpentine schists that characterize more magmatically-robust mid-ocean ridge detachment faults (MacLeod et al., 2002; Escartin et al., 2003; Schroeder and John, 2004; Boschi et al., 2006; Picazo et al., 2012). In the right conditions of fluid accessibility, the strength of nearly

amagmatic flip-flop detachment faults could therefore be as low as that of more magmatic detachment faults.

Yet the larger kilometer-scale structure of the fault zones appears different in the two contexts. More magmatic detachments expose dome-shaped corrugated fault surfaces (Smith et al., 2008; MacLeod et al., 2002; Escartin et al., 2017), while the eastern SWIR flip-flop detachments, in regions where chrysotile gouges are abundant, expose non-corrugated fault surfaces, with evidence for a complex, km-scale anastomosing fault splays structure (Mahato and Cannat, in prep.; Chapter 2). The detection of several planar seismic reflectors interpreted as damage zones and distant by up to 1.8 km in the D1 fault zone (Figure 14a; Momoh et al., 2017) is consistent with this large-scale anastomosing fault splays and phacoids structure. Another clear difference is that earthquakes at more magmatic detachments mostly align along the fault plane (deMartin et al., 2007; Parnell-Turner et al., 2017), while below the active D1 detachment, earthquakes occur over a broad domain that includes part of the footwall and hanging wall, with no clear alignment on the fault (Figure 14a; Chen et al., 2023).

These contrasted characteristics suggest that deformation occurs in a more localized fault zone at more magmatically active detachments. We hypothesize that this may be caused not so much by differences in rheology occurring in the serpentinized upper brittle lithosphere but by differences in strain localization in deeper, hotter levels. Magmatically active mid-ocean ridge detachments are commonly hypothesized to root just above or even into gabbroic melt-mush zones (e.g., Cannat et al., 1991; Dick et al., 2019; Picazo et al., 2012a; Hanson et al., 2013). In this context, the weaker gabbros and surrounding veined peridotites, first fresh, then hydrothermally altered into talc±tremolite±chlorite±serpentine assemblages, facilitate strain localization from the brittle-ductile transition domain upward (Picazo et al., 2012a; Hanson et al., 2013). By contrast, in the nearly amagmatic flip-flop detachment context of our study area, sample studies indicate that deformation in the brittle-ductile transition domain is delocalized into widespread fractures and grain-

size reduction shear zones (Bickert et al., 2021; 2023). We lack preserved outcrops and samples to really document what then happens in the brittle domain at temperatures above serpentine stability (between ~400°C and ~700°C; Figure 14a), but hydrous minerals such as talc and amphibole, that could be stable in this range of temperatures and help localize strain, are not common in the recovered ultramafic samples (Rouméjon et al., 2015; Bickert et al., 2023).

3.6.4. Conclusions

We analyze the deformation microtextures of samples of serpentinite microbreccia and gouge from the most highly deformed intervals of two exposed flip-flop detachment fault zones (D1 and D2) in the 64°35'E SWIR nearly amagmatic spreading corridor. We also analyze samples of serpentinite gouge from smaller offset normal faults that dissect the D1 or D2 exposed fault surfaces. Our main findings and preferred interpretations are as follows:

1- All samples contain clast-rich micro domains formed by brittle fracturing of already serpentinized peridotites. Samples from the D1 and D2 detachments also contain thin foliated and clast-poor horizons in which clast dissolution and precipitation of a fine-grained chrysotile matrix has occurred. As already shown in other fault contexts, the clast size distribution in clast-rich domains appears independant of displacement on the fault (ODF or small offset normal fault). Chrysotile's ability to crystallize across a broad range of temperatures (below 400°C) means its presence in gouges and, subsequently, the occurrence of these gouge-bearing horizons can span various depths in the ODFs damage zone.

2- Experimental deformation studies highlight that the frictional strength of water-saturated chrysotile gouge at low and moderate temperatures is comparable to that of talc, which is common (with other minerals such as chlorite and amphibole, that result from the hydrous alteration of gabbro-

peridotite mixtures or metasomatism by a Si-rich hydrothermal fluid) in deformed rocks from more magmatic mid-ocean ridge detachment faults. At higher temperature and confining pressure, brittle deformation experiments show that the strength of the crysotile gouge increases. This might suggest that fault splays lined by chrysotile gouge are stronger deeper in the damage zone of ODFs. However, fluid-enhanced dissolution-precipitation processes such as observed in the clast-poor domains of our samples are likely to further weaken the chrysotile gouge in these deeper levels. The rheology of the gouges, however, is not the only control on fault strength: the thickness, extent, and outcrop to fault-scale interconnectivity of the gouge and microbreccia horizons also control the overall strength of the fault zone.

3- While in the right fluid conditions, nearly amagmatic flip-flop detachment faults lined by chrysotile gouge could be as weak as talc-lined more magmatic detachments, these fault zones differ significantly. The eastern SWIR ODFs appear to have thicker damage zones with pluri-hectomer-sized phacoids of less deformed serpentinized peridotite between linked fault splays. We postulate that such thick damage might originate might not result so much from differences in the rheology of the upper brittle lithosphere, but could be inherited from a less localized deformation in the brittle ductile transition domain.

3.7 Chapter 3-Figures (1-14)

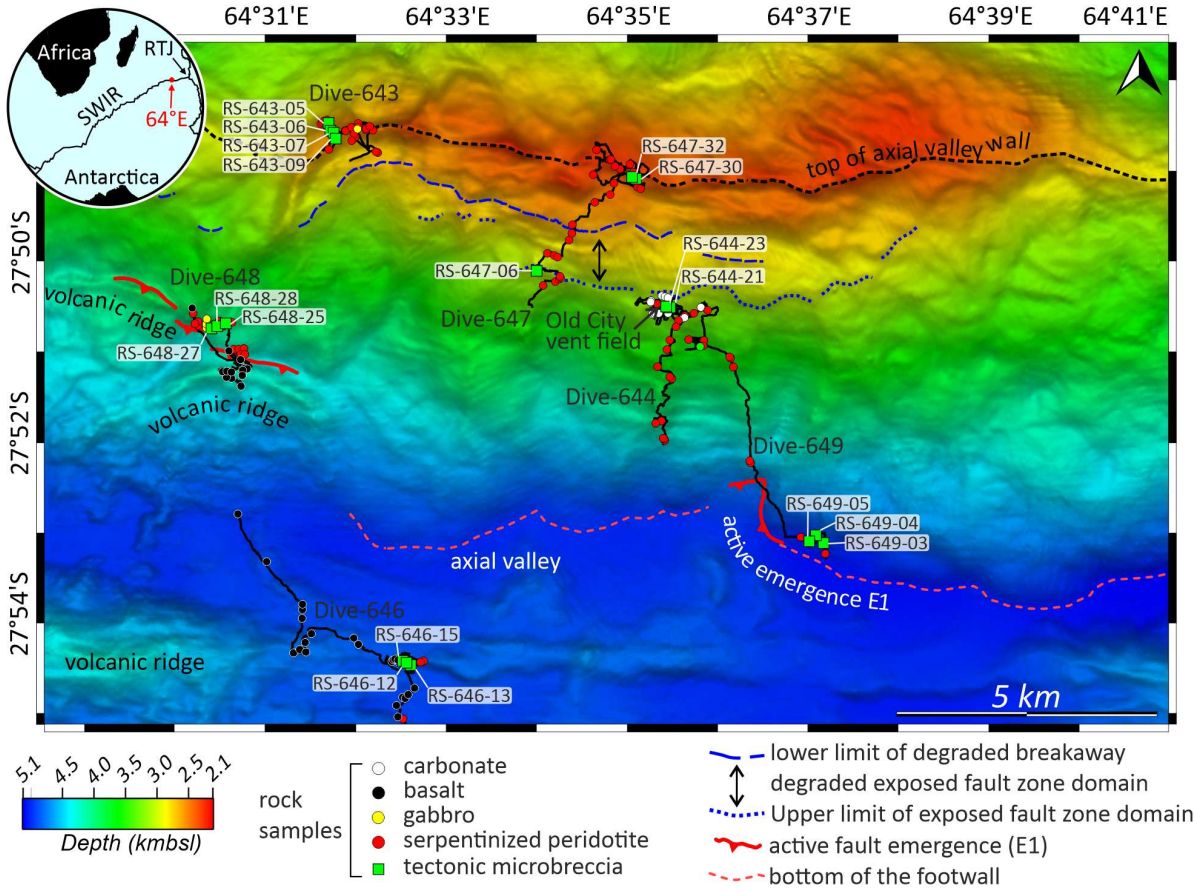

Figure 1: *Shaded relief bathymetry map showing the tectonic setup of the young active detachment fault (D1), which cuts through the older and inactive D2 detachment footwall in the 64.5°E ridge region. From bottom to top, the south-facing axial valley wall has three major structural domains, namely the (1) exposed fault zone (EFZ) domain, (2) degraded exposed fault zone (DEFZ) domain, and (3) degraded breakaway (DB) domain, (Mahato and Cannat, in prep.). To the east of longitude 64°32'E, spreading is almost fully amagmatic; to the west, it is in part accommodated by the emplacement of volcanic ridges (Sauter et al., 2013). Gouge-bearing tectonic microbreccia samples studied in this paper (green squares with labels) were collected from exposed fault surfaces during ROV dives 643 to 649 of the ROVSMOOTH cruise (Cannat et al., doi:10.17600/16002000; dive tracks shown as black line).*

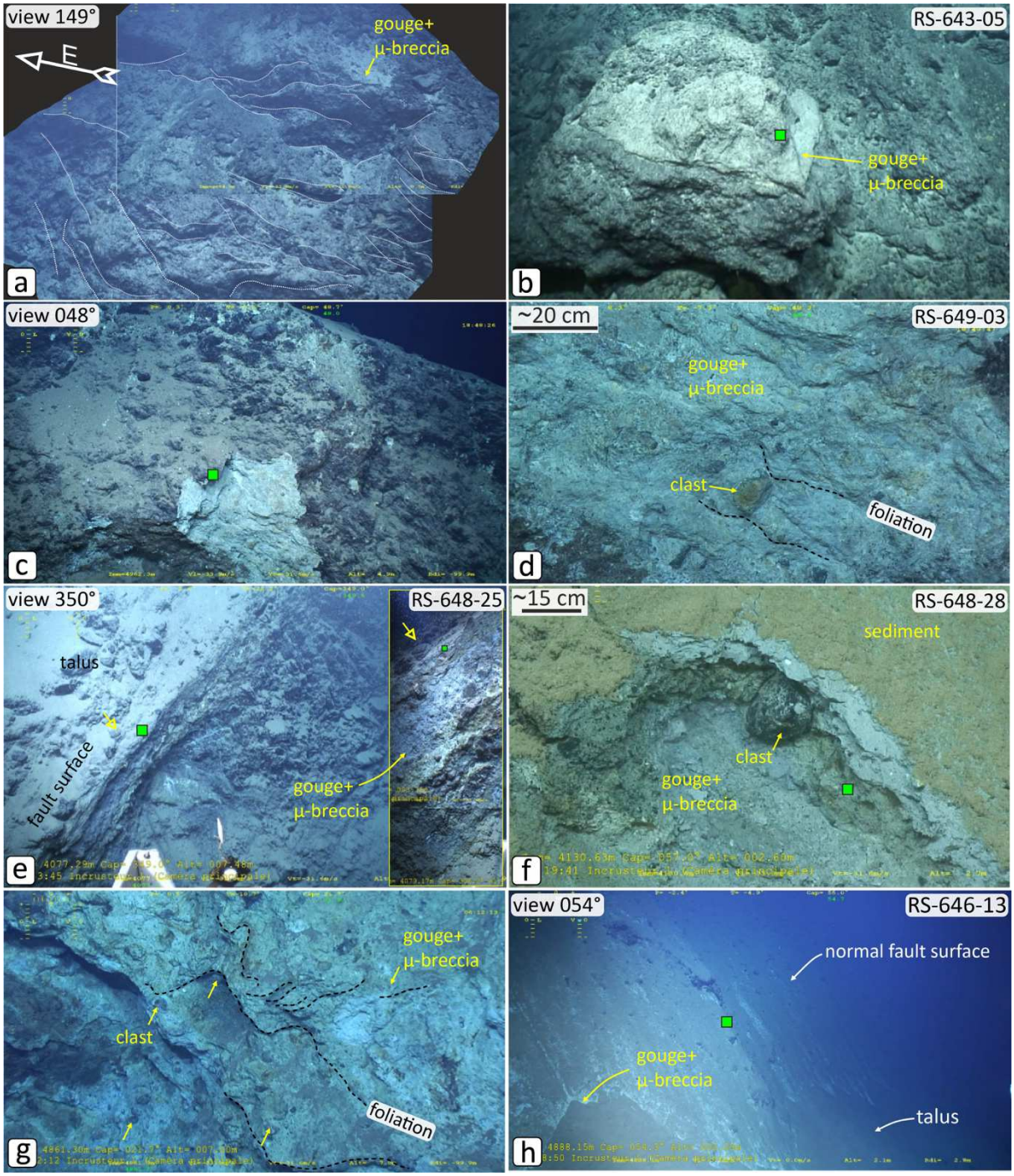

***Figure 2**: A selection of ROV dive video snapshots showing sites where the serpentinite gouge and microbreccia samples analyzed in this study were collected (selected video snapshots for all sampling sites are shown in Supplementary Figure 1). a- Mosaic of several snapshots showing linked fractures and sigmoidal phacoids near the location of sample RS-643-05, D2 exposed fault zone (location in Figure 1). b- Closer view of decimeter-thick interval of gouge and microbreccia at sample RS-643-05 location, ~5 m downslope from the outcrop shown in a. c- A plurimeter-thick interval of serpentine breccia, microbreccia and gouge just below the exposed D1 fault surface. The vertical field of view at the center of the frame is about ~5-6 meters. The outcrop is coated with iron-manganese oxide, except in the fresh erosional scarp where sample RS-649-03 was collected (Figure 1). d- Close-up view of the freshly exposed part*

of the outcrop in c-, showing warped foliation around sub-rounded clasts of serpentinized peridotite. e- An erosional scarp exposes D1 fault rocks (brecciated serpentinized peridotite) below the plane of a relatively small offset normal fault explored during ROV dive 648 (location of sample RS-648-25, from decimeter-thick fault gouge layer). f- A close-up view of the same south-dipping fault place at the location of sample RS-648-28. The fragile gouge includes subrounded clasts of serpentinized peridotite. g- A 4-5 meter-thick horizon of D2 microbreccia and gouge is exposed by the small offset normal fault shown in h-. Sample RS-646-12 comes from this formation, a few meters out of the frame. Note the similarity with D1 microbreccia and gouge in d-. h- Lightly sedimented plane of small offset normal fault that dissects the thin lava cover and exposes D2 fault rocks in the axial valley floor. Sample RS-646-13 comes from the thin layer of gouge along this plane.

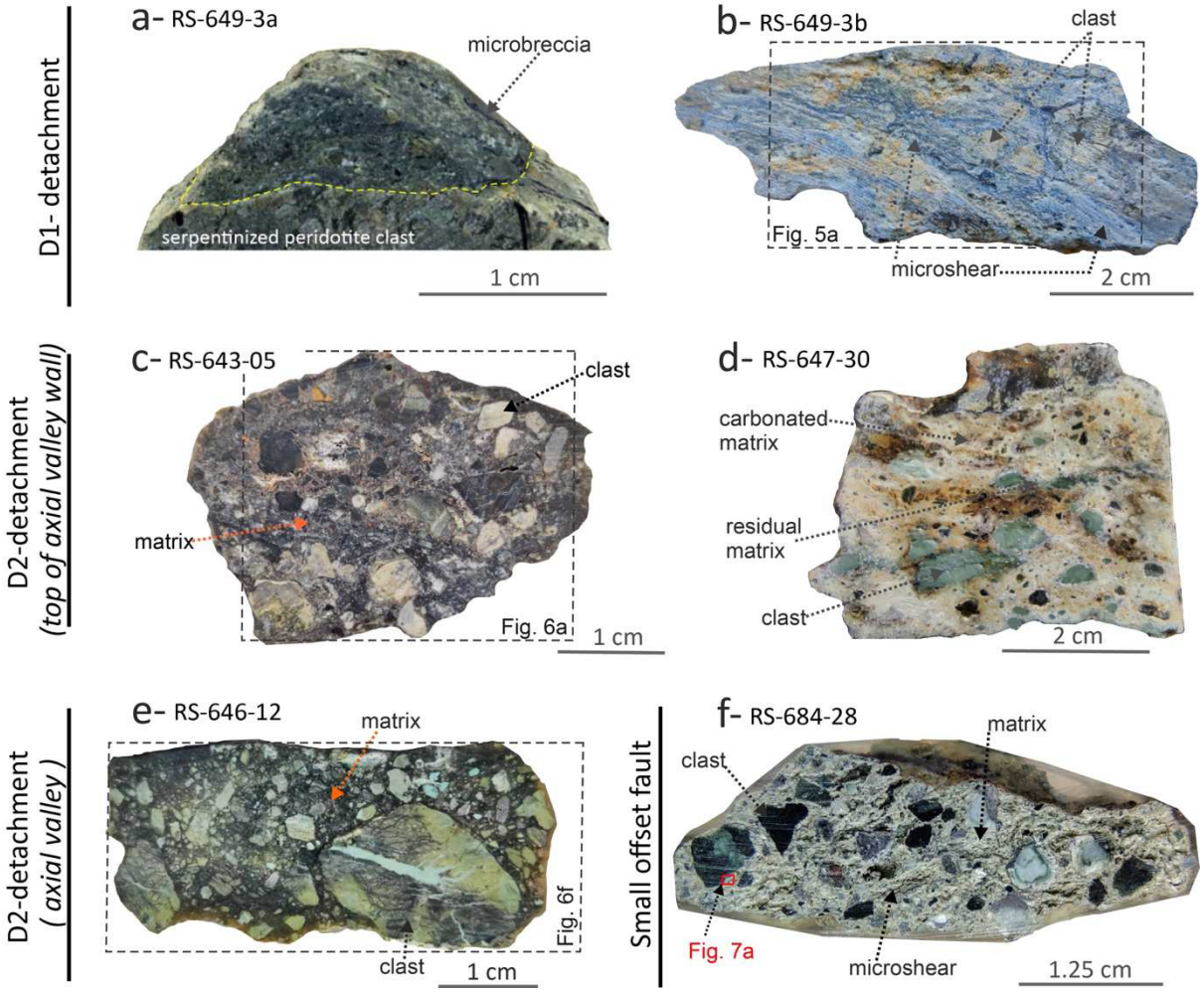

Figure 3*: Thin section-size fragments of the gouge-bearing micro-breccias sampled from the D1-detachment fault zone (a-b); the D2-detachment fault zone (c-d); the smaller offset fault plane explored during dive 648 (Figures 1, 2e and 2f) in the western part of the D1 footwall (e); and the small offset fault explored during dive 646 (Figures 1, and 2h) in the axial valley (f). a and b are two separate fragments from the same outcrop (Figure 2c and d). a- Sample RS-649-3a is a subrounded clast that contains part of a serpentinized peridotite clast with its microbrecciated matrix (a clast of clast). b- Sample RS-649-3b is a fragment of the more fragile foliated matrix visible in the close-up view of Figure 2d. c- Sample RS-643-05 (Figure 2b) contains angular to subangular clasts in a sheared matrix. d- Sample RS-647-30 (Figure 1) is a matrix-dominated, extensively carbonated microbreccia with fully serpentinized peridotite clasts. e- Sample RS-646-12 (Figure 2g): microbreccia made of randomly oriented subrounded to rounded clasts of serpentinite. f- Sample RS-648-28 (Figures 1 and 2f) contains angular to subangular angular clast of serpentinite in a crudely foliated matrix.*

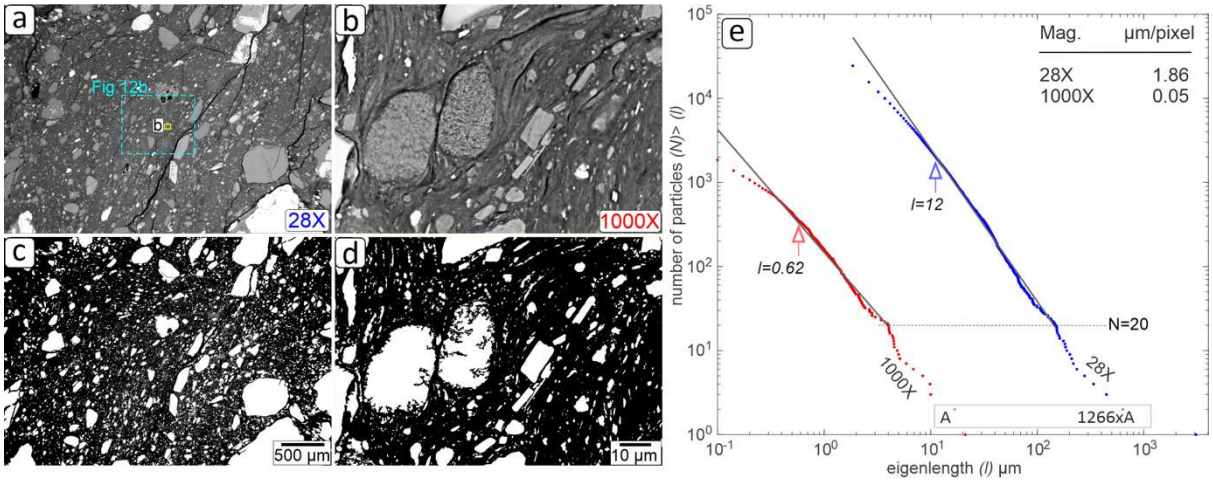

Figure 4: *Methodology for particle (clast) size distribution (PSD) measurements in sample RS-649-3, using backscattered electron (BSE) images and the ImageJ software. (a-b). BSE images were acquired at 28X and 1000X magnification. The higher-magnification (1000X) image resolves smaller clasts but corresponds to a very small subset of the area under 28X magnification. (c-d) Processed images: particles identified as clasts in white, matrix in black. (e) Log-log plot of the cumulative number of particles N(l) greater than a given size l, where l is the square root of the clast area, for clasts identified with the 28X and 1000X magnifications. Linear regression lines are fitted from a larger clasts size bound set to correspond to N(l) =20. PSD data for smaller clast sizes shows a deviation below a certain threshold (l < 12 µm for 28X; l < 0.62 µm for 1000X) in relation to the linear regression fit. For low-magnification images (e.g., 28X), this deviation is likely a detection issue due to the lower resolution (µm/pixel).*

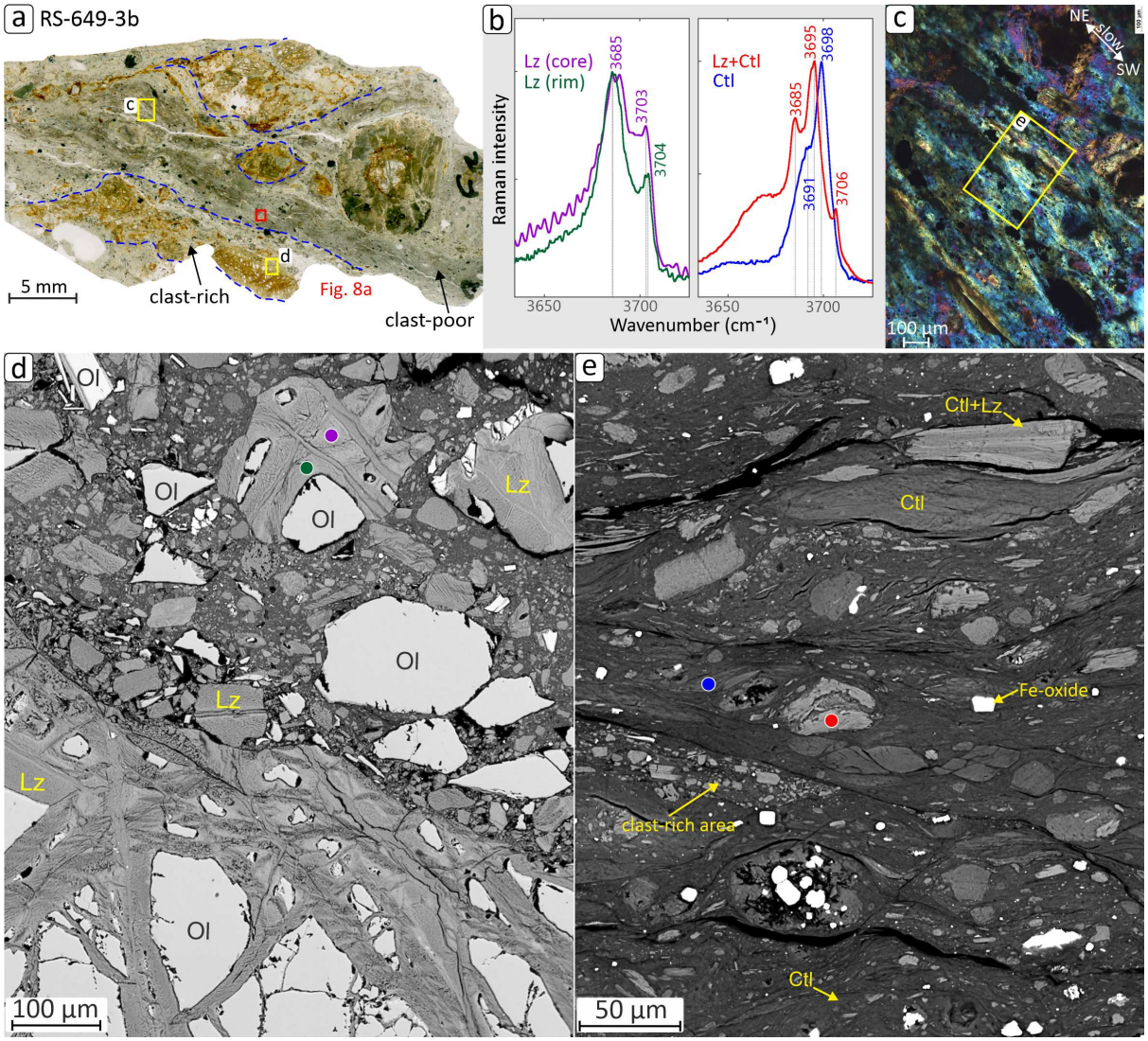

Figure 5: *Microstructure details of a representative sample (RS-649-3) from the D1 detachment fault zone. Abbreviations: (Ol) olivine, (Lz) Lizardite, (Ctl) chrysotile. The positions of the relocated images are indicated by yellow and red boxes. (a) Whole thin section under natural light showing the foliated clast-poor domains warping around more clast-rich domains. (b) Selected Raman spectra for clasts and matrix, located as color dots in panels d and e: mesh textured clasts are primarily made of lizardite, while the matrix in sheared domains and some of the smaller clasts are made of chrysotile. (c) The clast-poor domain shows a well-defined serpentine crystallographic fabric, as shown by the bluish-green color under cross-polarized light with a retardation plate. (d) BSE image from the clast-rich domain shows randomly oriented angular to sub-angular clasts of mesh texture serpentine and olivine in darker fine-grained matrix. (e) BSE image from the foliated clast-poor domain shows elongated, sigmoidal, and sub-rounded clasts that are preferentially oriented along local shear bands.*

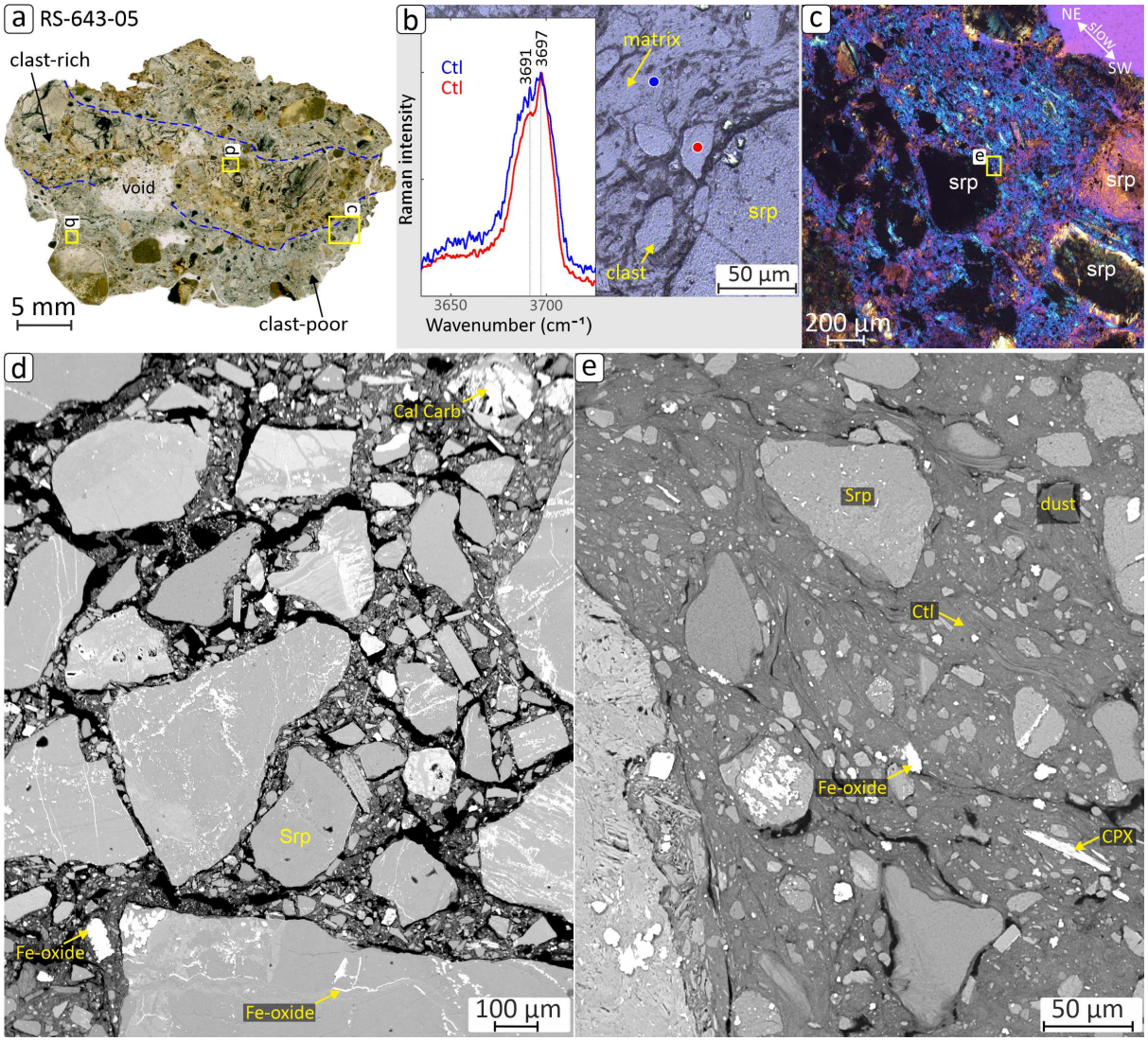

Figure 6: *Microstructure details of a representative sample (RS-643-05) from the D2 detachment fault zone. Abbreviations: (srp) serpentinite, (cpx) clinopyroxene, (Ctl) chrysotile, (cal carb) calcium carbonate mineral. Fractures and voids (white in natural light and black in BSE images) were created during sample collection and preparation due to the fragile nature of the rock. The positions of the relocated images are indicated by yellow boxes. (a) Whole thin section under natural light showing the foliated clast-poor domains warping around more clast-rich domains. (b) Selected Raman spectra for clasts and matrix, located as color dots in reflected light microphotograph of a clast-poor domain. (c) The clast-poor domain shows a well-defined serpentine crystallographic fabric, as shown by the bluish-green color under cross-polarized light with a retardation plate. (d) BSE image from the clast-rich domain shows randomly oriented angular to sub-angular clasts of serpentinite in darker fine-grained matrix. (e) BSE image from the foliated clast-poor domain shows elongated and sub-rounded clasts that are preferentially oriented along local shear bands.*

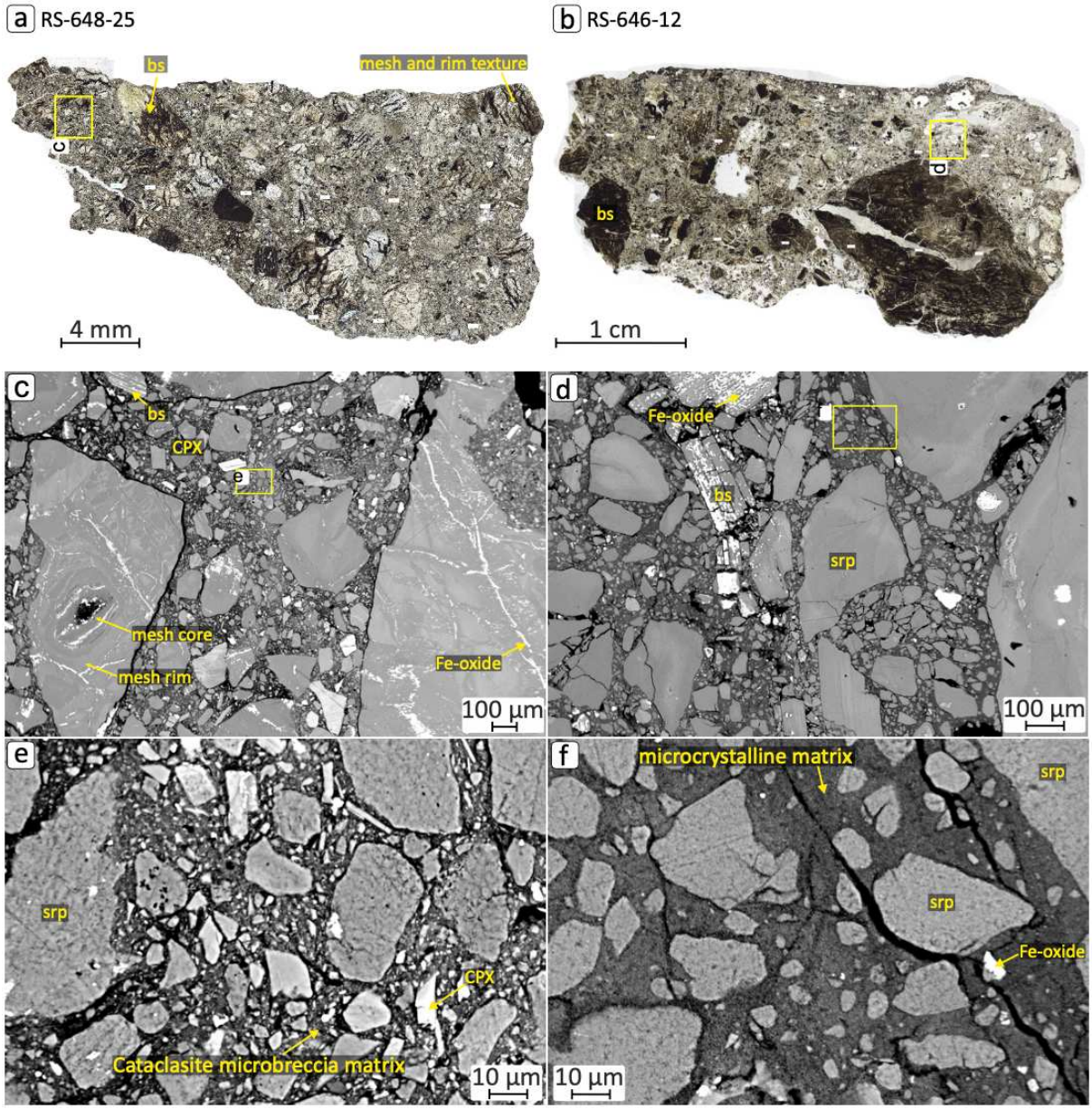

Figure 7: *Microstructure details of samples RS-648-25 (from smaller offset normal fault plane) and RS-646-12 (D2 fault zone exposed in axial valley floor). Abbreviations: (srp) serpentinite, (bs) bastite, (cpx) clinopyroxene. The positions of the relocated images are indicated by yellow boxes. (a-b) Whole thin sections under natural light, showing their clast-rich texture. (c) BSE image of sample RS-648-25 shows angular clasts of mesh texture serpentine, serpentinite, and bastite. (d) BSE image of sample RS-646-12 shows angular to subrounded clasts of mesh texture serpentine, serpentinite, and bastite. (e-f) Close-up BSE views of samples RS-648-25 (e) and RS-646-12 (f). In (e) the fine-grained matrix is clast-rich, with angular microclasts. In (f), the fine-grained matrix is clast-poor, and the clasts are sub rounded. However, the microcrystalline matrix shows no foliation and the clasts do not have a shape fabric.*

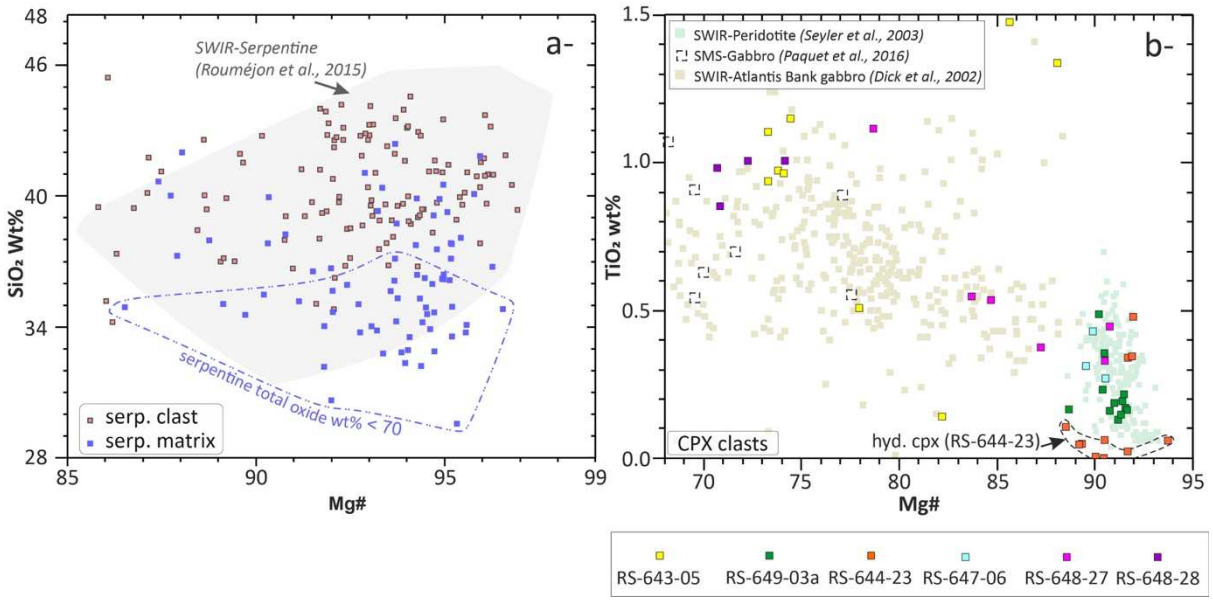

Figure 8: *Major element composition of serpentine (a) and clinopyroxene (b) in selected gouge and microbreccia samples (Table 2 and Supplementary Table X). Mg#= (Mg/Mg+Fe+Mn). (a) SiO2 wt.% vs Mg# in serpentine clasts and matrix. (b) TiO2 wt.% vs Mg# in clinopyroxene clasts.*

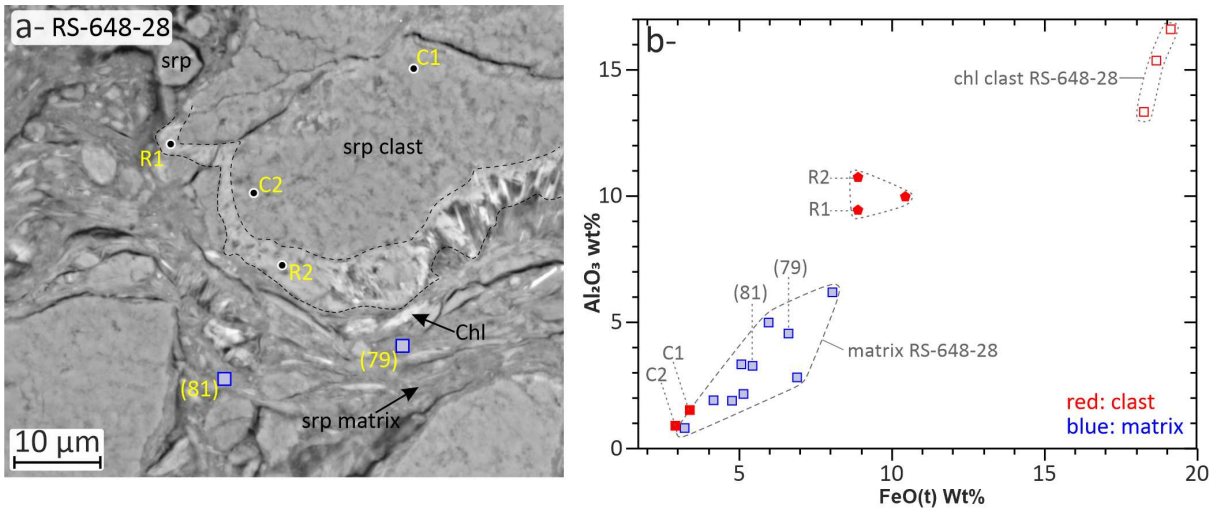

Figure 9: *Dissolution/reaction rims around a serpentine clast in sample RS-648-28, that contains gabbro-derived cpx and chlorite clasts. (a) BSE image. The dissolution/reaction rim is lighter than the core of the serpentine clast. (b) Al2O3 vs. FeO wt% in serpentine and chlorite in clasts and in sheared matrix.*

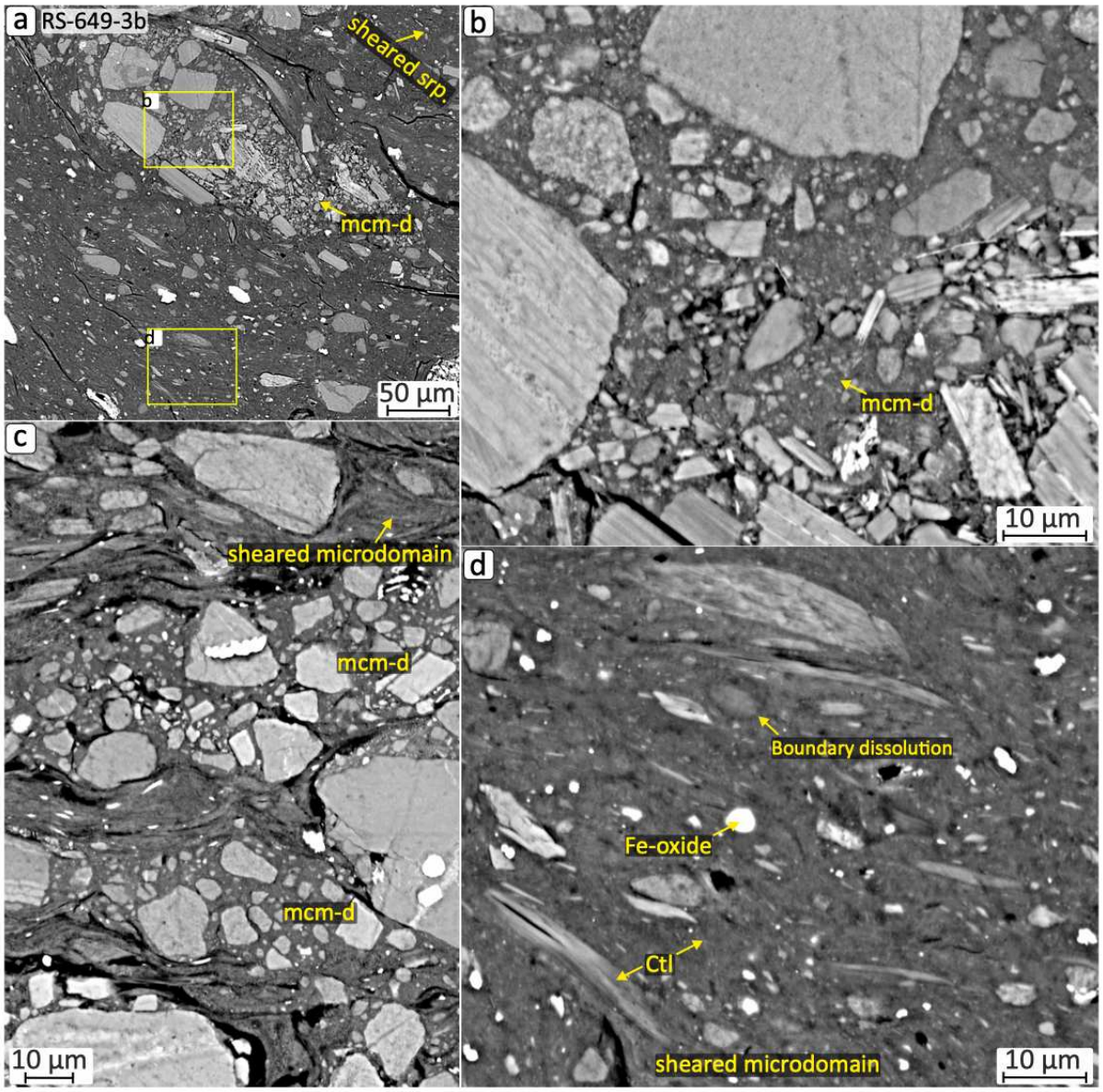

Figure 10: *BSE images of representative microtextures in clast-rich and clast-poor domains in D1 gouge and microbreccia sample RS-649-3. Abbreviations: (mcm-d)* ***m****icro****c****rystalline* ***m****atrix-****d****omain, (Ctl) chrysotile. (a) a clast-rich microdomain is surrounded by a clast-poor microdomain (b) zoomed-in image of the clast-rich domain in a- shows that its serpentine matrix is microcrystalline. (c) Zoomed-in image of the same sample showing that clast-rich domains are themselves clasts in the clast-poor, foliated matrix. (d) zoomed-in image of the clast-poor domain in a- shows a foliated serpentine matrix and rounded clasts interpreted as in the process of being dissolved and/or recrystallized.*

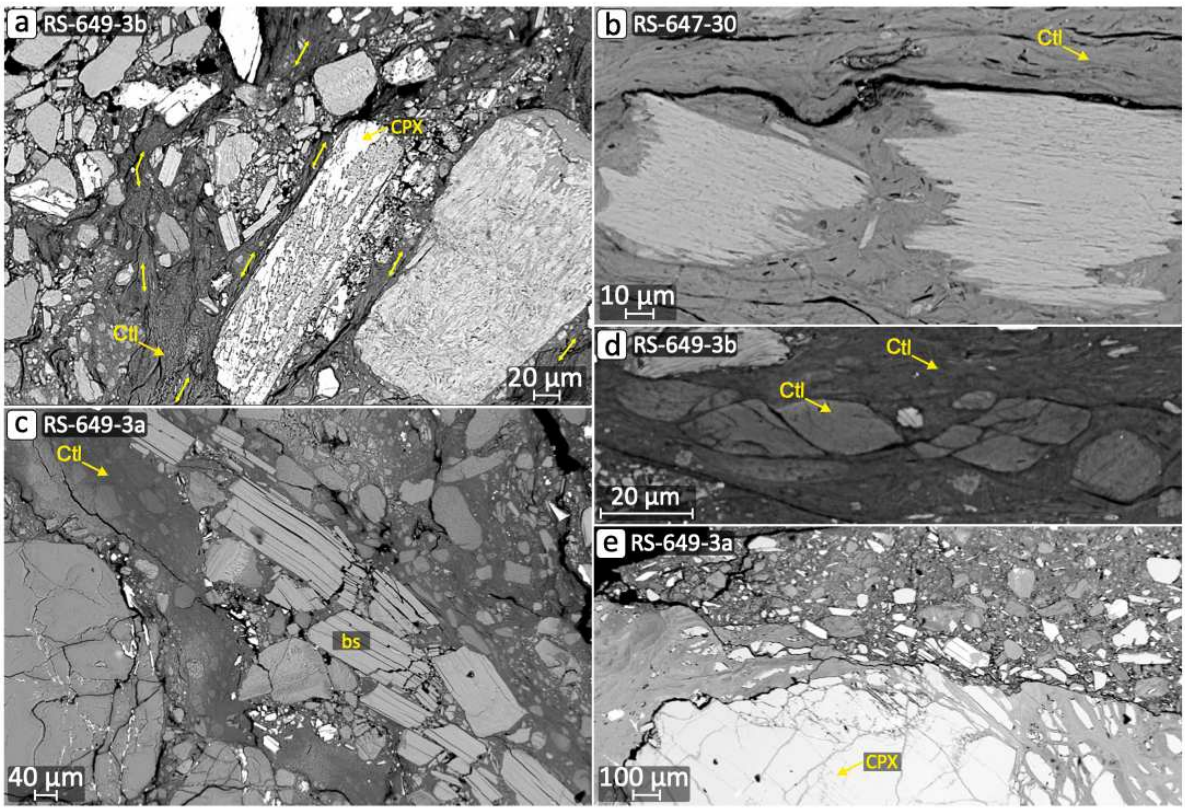

Figure 11: *BSE images of representative microtextures in clast-rich and clast-poor domains of gouge and microbreccia samples RS-649-3 (D1 exposed fault zone) and RS-647-30 (D2 exposed fault zone). Abbreviations: (CPX) clinopyroxene, (Ctl) chrysotile. (a) clast-poor microshear zones dissect a clast-rich domain; (b) Serpentine clast embedded in a sheared matrix is boudinaged and partially dissolved/recrystallized; (c) Bastite in clast-rich domain is fractured and delaminated parallel to its lamellae to form elongated tablet-shaped microclasts; (d) breaking of augen-shaped chrysotile clasts and (e) edge abrasion of a large serpentinized peridotite clast, contributing relatively fresh clinopyroxene clasts to the surrounding microbreccia domain.*

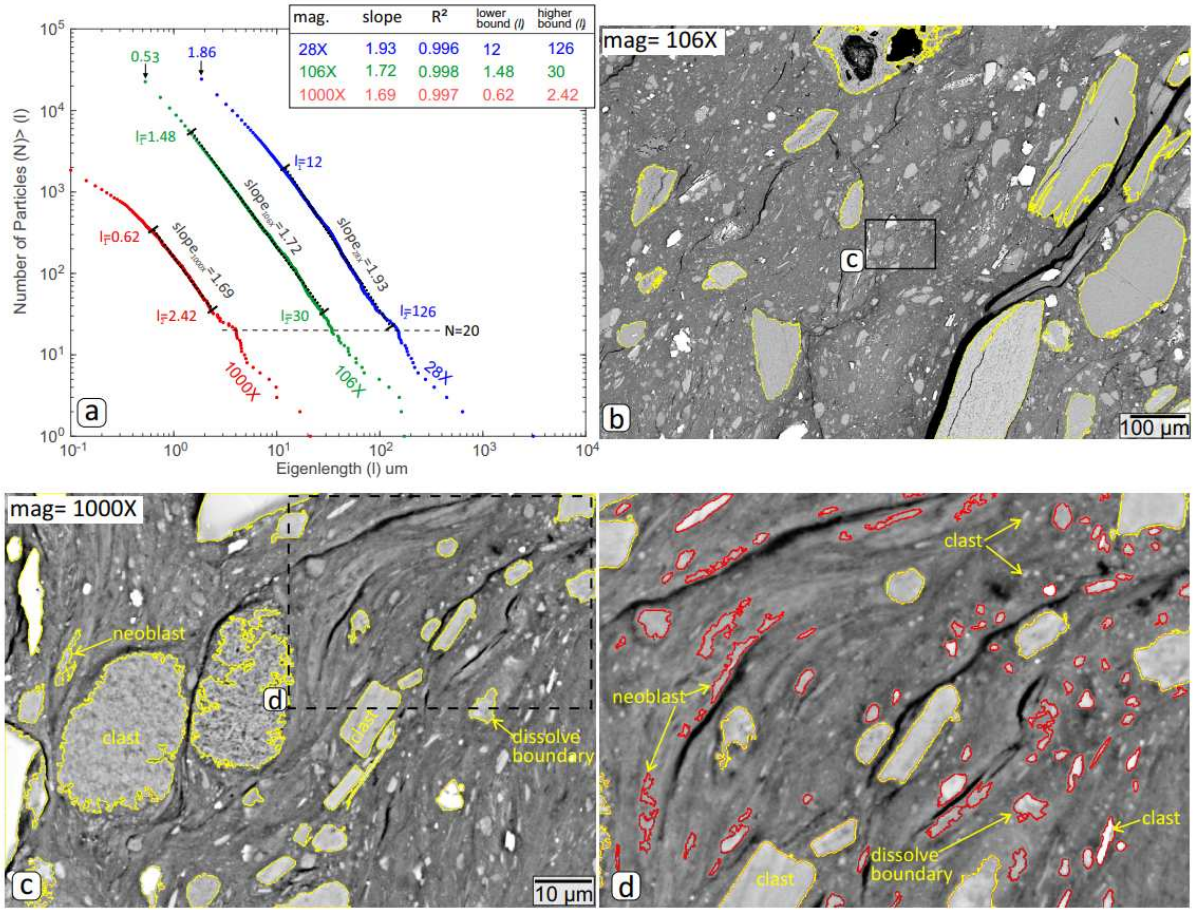

Figure 12: *Particles (clasts) size distribution obtained at several magnifications (e.g., 28X, 106X, and 1000X) in clast-poor, foliated microdomains of gouge-microbreccia sample RS-649-3. a- Log-log plot of the cumulative number of particles N(l) greater than a given size l, where l is the square root of the clast area, for clasts identified at 28X, 106X, and 1000X magnifications. Linear regression lines are fitted between the deviation value determined as a lower bound for clasts sizes at each magnification (Figure 4), and a manually selected larger size bound that ensures the best linear fit (Method section). The slope (D) of the regression lines is magnification-dependent. b- BSE image at 106X magnification, located in 28X magnification BSE image of Figure 4a. Clasts with yellow contours are larger than the 30 mm upper bound for the linear fit in a-. c- BSE image at 1000X magnification, located in b. Clasts with yellow contours are larger than the 2.42 mm upper bound for the linear fit in a-. d- Zoomed view of a portion of c-. Particles with blue contours are smaller than the 0.62 mm lower bound for the log-log linear fit in a-. Particles with red contours are larger than this lower bound, and smaller than the 2.42 mm upper bound for the log-log linear fit in a-. These particles have a weak BSE contrast with the matrix, and contorted limits, consistent with partial dissolution/recrystallization.*

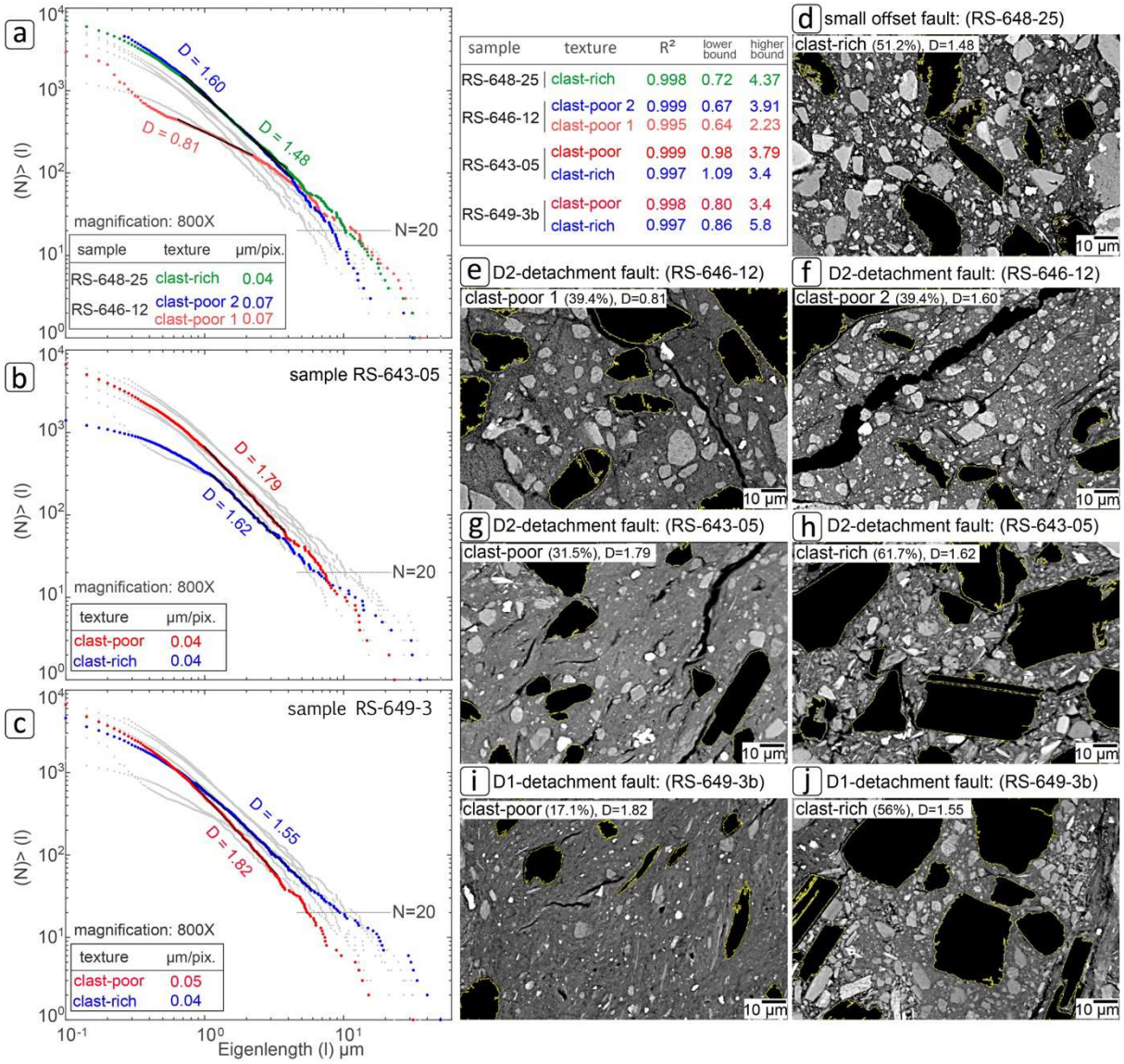

Figure 13: *Comparison of particle size distribution (PSD) in clast-rich (clasts % > 50) and clast-poor domains of 4 representative samples (Table 1 and text). Panels a-, b- and c- show log-log plots of the cumulative number of particles N(l) greater than a given size l, where l is the square root of the clast area, for clasts identified at 800X magnification. In each plot, the values in grey are the PSD distributions in the other panels, shown for comparison. D values correspond to linear regression lines fitted in each case between the deviation value determined as a lower bound for smaller clasts sizes (Method section) and a manually selected larger size bound that ensures the best linear fit. Panels d- to j- show the corresponding 800X magnification BSE images. Clasts with l corresponding to N(l) < 20 are contoured in yellow and blacked out.*

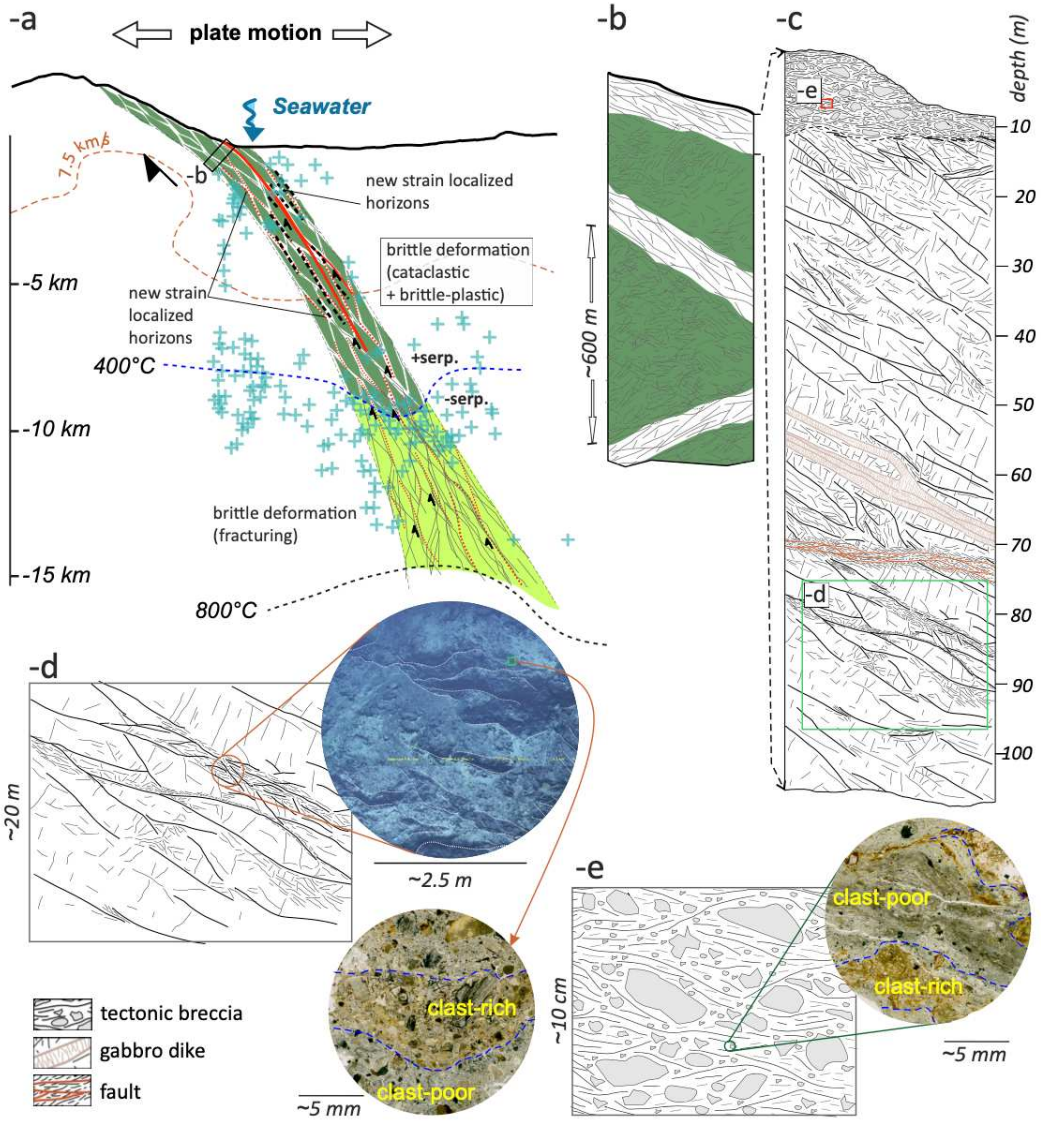

Figure 14: *A conceptual sketch of whole lithosphere-scale (a), outcrop-scale (b, c), and sample-scale (d, e) strain localization in the serpentine stability domain during nearly amagmatic axial detachment faulting. a- Whole lithosphere sketch after Bickert et al. (2022). The 800°C isotherm depth is constrained to approximately 15 km based on petrological observations (Bickert et al., 2021) and the distribution of microearthquakes (Chen et al., 2023; blue crosses). The 400°C isotherm limits the stability of serpentine minerals. Also shown are the 7.5 km/s Vp iso-velocity contour (Corbalan et al., 2021) and the trace of seismic reflectors inferred to correspond to fault damage (Momoh et al., 2017; dashed lines). b- Conceptual sketch of the fault's damage zone, with anastomosing fault splays wrapping around hectometer-scale phacoids of more moderately deformed serpentinized peridotites. c- Lithostratigraphy of an exhumed fault splay, based on ROV dive observations (Mahato and Cannat, in prep.;*

Chapter 2). Gouge and microbreccia occur in two settings: in decimeter-thick horizons of localized strain associated with anastomosing fractures (d; for example, sample RS-643-05; Figure 2a and b), and in meter to plurimeter-thick horizons (e; for example sample RS-649-03; Figure 2c and d). While these settings differ at the outcrop scale, the associated microstructures are similar.

3.8 Chapter 3-Tables (1-3)

Table 1: Outcrop and textural summary of selected ultramafic microbreccia samples

Regional tectonic setting	nature of the outcrop	Sample No.:	Matrix carbonation	Microbreccia/gouge texture	
				Clast rich domain (clast area> matrix area)	clast poor domain (clast area<matrix area)
D2-detachment fault zone (top of the axial valley wall)	anastomosing FZ with 10-15 cm thick gouge bearing microbreccia zone	RS-643-05	0	microcrystalline srp. matrix	sheared srp. matrix
	schistose north-dipping outcrop	RS-643-06	90%	_	_
	schistose north-dipping outcrop	RS-643-07	95%	microcrystalline srp. matrix	_
	few tens of cm thick breccia outcrop	RS-643-09	100%	_	_
	about 50-60 m thick exposed FZ	RS-647-30	80%	microcrystalline srp. matrix	sheared srp. matrix
D2-detachment fault zone (axial valley)	Few meters thick, schistose gouge bearing microbreccia horizon	RS-646-12	0	cataclastic srp matrix	microcrystalline srp. matrix
D1-detachment fault zone	south dipping striated fault surface	RS-647-06	100%	matrix is totally replaced by carb.	
	about 8 m thick gouge bearing FZ	RS-649-3a	0	microcrystalline srp. matrix	sheared srp. matrix
		RS-649-3b	0	microcrystalline srp. matrix	sheared srp. matrix
	few meters thick south-dipping FZ fault zone breccia, one of the Old City sites	RS-644-21	60%	microcrystalline srp. matrix	sheared srp. matrix
		RS-644-23	10-15?%	_	sheared srp. matrix
Small offset faults	about 1.5 m thick exposed gouge bearing fault breccia/microbreccia	RS-648-25	0	cataclastic srp. matrix	
	south-dipping fault surface	RS-648-27	0	little to none recryst. of the srp. matrix	
	about 1 m thick gouge bearing fault breccia/microbreccia	RS-648-28	0	microcrystalline srp. matrix	sheared matrix
	normal faults on D1-hanging wall with about 100 meters of vertical offset	RS-646-13	0	microcrystalline/cataclastic matrix, with relict of sheared matrix	

Table 2: Representative spot analyses of primary clast mineralogy from selected microbreccia samples located in Table 1.

Samples	RS-649-3a	RS-649-3b	RS-647-06	RS-649-3a	RS-647-06	RS-649-3a	RS-647-06	RS-644-23	RS-648-27	RS-648-27	RS-648-28	RS-643-05	RS-649-3a	RS-644-23
Point	29	196	b	14	c	40	e	359	244	239	157	261	2	352
Mineral type	ol	ol	ol	opx	opx	cpx•	cpx•	cpx•	cpx•	cpx°	cpx°	cpx°	spl	spl
SiO_2	40.56	41.39	41.09	55.06	55.85	51.59	51.59	51.41	50.86	52.08	51.44	49.89	0.05	0.05
TiO_2	0	0	0	0.11	0.13	0.13	0.27	0.47	0.45	1.12	1.01	1.15	0.06	0.05
Al_2O_3	0.02	0.03	0	3.60	4.10	5.93	6.83	5.68	5.81	3.24	3.16	3.48	49.40	52.08
FeO	9.64	8.88	9.97	6.12	6.63	2.62	3.15	2.50	2.77	6.99	8.59	8.54	12.72	11.23
MnO	0.10	0.10	0.13	0.10	0.22	0	0	0.01	0.03	0.26	0.30	0.23	0	0
MgO	50.56	49.31	48.78	33.40	32.20	15.28	15.90	16.22	15.50	15.01	14.32	14.34	18.75	20.01
CaO	0.07	0.04	0.02	1.45	0.97	22.04	21.79	22.54	23.36	21.35	20.76	20.75	0.02	0.18
Na_2O	0	0	0.02	0.06	0.04	0.87	0.72	0.80	0.56	0.68	0.86	0.94	0.01	0.02
K_2O	0.03	0	0	0	0	0	0.01	0	0	0	0	0.01	0	0
Cr_2O_3	0.01	0	0	0.58	0.68	1.55	0.95	0.86	1.12	0.04	0.01	0.03	18.33	13.40
NiO	0.53	0.37	0.46	0.13	0.17	0.10	0.11	0.07	0	0.01	0.01	0.02	0.25	0.27
Cl	0	0	0	0	0	0	0	0	0.01	0	0	0.03	0	0
F	0	0	0	0	0	0	0	0	0	0	0	0	0	0
Total	101.52	100.12	100.47	100.61	100.99	100.11	101.32	100.56	100.48	100.76	100.45	99.40	99.58	97.29
Mg#	90.24	90.72		90.53		91.21	90.06	91.98	90.78	78.68	74.16	74.44	72.42	76.06

cpx• : cpx from peridotite protolith; cpx° : cpx from magmatic protolith e.g., gabbro

Table 3: Representative spot analyses of secondary clast and matrix mineralogy from selected microbreccia samples located in Table 1.

Sample	RS-644-23	RS-648-27	RS-648-28	RS-643-05	RS-649-3a	RS-649-3b	RS-647-06	RS-644-23	RS-643-05	RS-647-30	RS-646-12	RS-648-27	RS-648-28	RS-649-3a	RS-649-3b	RS-644-23	RS-643-05	RS-647-30	RS-646-12	RS-648-28	RS-647-30	RS-644-23
Point	331	235	128	256	46	200	x	353	280	314	374	227	166	60	169	355	266	286	383	132	296	364
Minerals	cpx©	chl	chl	chl	srp clast	srp clast	srp clast	srp clast	srp clast	srp clast	srp clast	srp clast	srp clast	srp matrix	srp matrix	srp matrix	srp matrix	srp matrix	srp matrix	srp matrix	carbonate	carbonate
SiO_2	54.79	31.57	29.76	31.37	41.44	43.19	41.40	43.58	41.95	43.97	41.86	41.14	39.77	37.57	37.76	39.28	37.85	41.84	37.27	40.68	0.11	0.04
TiO_2	0.06	0.04	0.05	0	0.02	0.01	0	0.04	0.01	0.01	0.01	0.13	0.11	0	0.04	0	0.02	0.01	0	0.01	0	0.02
Al_2O_3	0.03	14.94	16.61	15.68	1.88	1.06	0.23	1.14	0.18	0.30	1.25	4.93	4.21	1.03	0.98	1.06	1.01	0.17	0.99	6.19	0.01	0
FeO	3.06	15.16	19.11	19.13	3.52	2.75	4.99	4.65	4.60	4.14	4.96	7.57	14.14	3.46	3.52	3.29	2.84	2.80	6.95	8.05	0	0.06
MnO	0.04	0.55	0.13	0.06	0.07	0.03	0.04	0.01	0.07	0.16	0.08	0.04	0.29	0.07	0.13	0.12	0.06	0.05	0.13	0.02	0	0.01
MgO	16.64	24.02	21.30	21.76	39.08	39.71	37.55	38.91	38.9	37.26	36.45	29.92	29.58	36.03	33.51	36.94	32.03	37.73	28.93	31.48	0.03	0
CaO	25.75	0.10	0.06	0.13	0.04	0.01	0.14	0.06	0.05	0.04	0.04	3.11	0.22	0.02	0.04	0.66	0.02	0.12	0.05	0.13	58.7	50.51
Na_2O	0.03	0.07	0.08	0.04	0.03	0	0.01	0.02	0.07	0.02	0.06	0.36	0.17	0.04	0.02	0.09	0.2	0.13	0.59	0.06	0.06	0.18
K_2O	0	0.02	0.02	0	0.03	0.01	0	0	0.01	0.03	0.03	0.06	0.04	0	0	0.03	0.02	0.03	0.06	0	0.01	0
Cr_2O_3	0.02	0	0	0	0.35	0.44	0	0.02	0.01	0	0	0.9	0.85	0.01	0	0	0.05	0.01	0	0.03	0	0
NiO	0.02	0.01	0.07	0.04	0.19	0.12	0.41	0.14	0.4	0	0.24	0.06	0.12	0.21	0.30	0.12	0.20	0.10	0.73	0.07	0	0.04
Cl	0	0.03	0	0.03	0.02	0.01	0.13	0.03	0.22	0.02	0.07	0.04	0.12	0.08	0.27	0.09	0.3	0.12	0.12	0.08	0	0.02
F	0	0	0	0	0	0	0	0	0	0	0	0	0	0	0	0	0	0	0	0	0	0
Total	100.45	86.52	87.2	88.24	86.66	87.33	84.90	88.59	86.46	85.94	85.03	88.28	89.61	78.51	76.57	81.65	74.60	83.11	75.82	86.79	59	51
Mg#	90.52	73.15	66.36	66.91	95.10	96.22	92.01	93.71	93.68	91.92	92.81	87.50	78.50	94.80	94.24	95.08	95.17	95.94	87.92	87.43	_	_

cpx©: cpx of hydrothermal origin

3.9 References:

Albers, E., Schroeder, T. and Bach, W., 2019. Melt impregnation of mantle peridotite facilitates high-temperature hydration and mechanical weakening: Implications for oceanic detachment faults. *Geochemistry, Geophysics, Geosystems*, *20*(1), pp.84-108.

Amitrano, D. and Schmittbuhl, J., 2002. Fracture roughness and gouge distribution of a granite shear band. *Journal of Geophysical Research: Solid Earth*, *107*(B12), pp.ESE-19.

Andréani, M., Boullier, A.M. and Gratier, J.P., 2005. Development of schistosity by dissolution–crystallization in a Californian serpentinite gouge. *Journal of Structural Geology*, *27*(12), pp.2256-2267.

Andréani, M., Mével, C., Boullier, A.M. and Escartin, J., 2007. Dynamic control on serpentine crystallization in veins: Constraints on hydration processes in oceanic peridotites. *Geochemistry, Geophysics, Geosystems*, *8*(2).

Auzende, A.L., Daniel, I., Reynard, B., Lemaire, C. and Guyot, F., 2004. High-pressure behaviour of serpentine minerals: a Raman spectroscopic study. *Physics and Chemistry of Minerals*, *31*, pp.269-277.

Seyler, M., Cannat, M. and Mevel, C., 2003. Evidence for major-element heterogeneity in the mantle source of abyssal peridotites from the Southwest Indian Ridge (52 to 68 E). *Geochemistry, Geophysics, Geosystems*, *4*(2).

Behnsen, J. and Faulkner, D.R., 2012. The effect of mineralogy and effective normal stress on frictional strength of sheet silicates. *Journal of Structural Geology*, *42*, pp.49-61.

Bickert, M., Lavier, L. and Cannat, M., 2020. How do detachment faults form at ultraslow mid-ocean ridges in a thick axial lithosphere?. *Earth and Planetary Science Letters*, *533*, p.116048.

Bickert, M., Cannat, M., Tommasi, A., Jammes, S. and Lavier, L., 2021. Strain localization in the root of detachment faults at a melt-starved mid-ocean ridge: a microstructural study of Abyssal Peridotites from the Southwest Indian Ridge. *Geochemistry, Geophysics, Geosystems*, *22*(5), p.e2020GC009434

Bickert, M., Cannat, M. and Brunelli, D., 2023. Hydrous fluids down to the semi-brittle root zone of detachment faults in nearly amagmatic ultra-slow spreading ridges. *Lithos*, *442*, p.107084.

Blenkinsop, T.G., 1991. Cataclasis and processes of particle size reduction. *pure and applied geophysics*, *136*, pp.59-86.

Billi, A., 2005. Grain size distribution and thickness of breccia and gouge zones from thin (< 1 m) strike-slip fault cores in limestone. *Journal of Structural Geology*, *27*(10), pp.1823-1837.

Bonnemains, D., Escartín, J., Mével, C., Andreani, M. and Verlaguet, A., 2017. Pervasive silicification and hanging wall overplating along the 13° 20′ N oceanic detachment fault (M id-A tlantic R idge). *Geochemistry, Geophysics, Geosystems*, *18*(6), pp.2028-2053.

Boschi, C., Früh-Green, G.L., Delacour, A., Karson, J.A. and Kelley, D.S., 2006. Mass transfer and fluid flow during detachment faulting and development of an oceanic core complex, Atlantis Massif (MAR 30 N). *Geochemistry, Geophysics, Geosystems*, *7*(1).

Cannat, M., Mével, C. and Stakes, D., 1991. Normal ductile shear zones at an oceanic spreading ridge: tectonic evolution of Site 735 gabbros (southwest Indian Ocean). In *Von Herzen, RP, Robinson, PT, et al., Proc. ODP, Sci. Results* (Vol. 118, pp. 415-429).

Cannat, M. and Casey, J.F., 1995, June. An ultramafic lift at the Mid-Atlantic Ridge: successive stages of magmatism in serpentinized peridotites from the 15 N region. In *Mantle and Lower Crust Exposed in Oceanic Ridges and in Ophiolites: Contributions to a Specialized Symposium of the VII EUG Meeting, Strasbourg, Spring 1993* (pp. 5-34). Dordrecht: Springer Netherlands.

Cannat, M., Lagabrielle, Y., Bougault, H., Casey, J., de Coutures, N., Dmitriev, L. and Fouquet, Y., 1997. Ultramafic and gabbroic exposures at the Mid-Atlantic Ridge: Geological mapping in the 15 N region. *Tectonophysics*, *279*(1-4), pp.193-213.

Cannat, M., Sauter, D., Mendel, V., Ruellan, E., Okino, K., Escartin, J., Combier, V. and Baala, M., 2006. Modes of seafloor generation at a melt-poor ultraslow-spreading ridge. *Geology*, *34*(7), pp.605-608.

Cannat, M., Sauter, D., Lavier, L., Bickert, M., Momoh, E. and Leroy, S., 2019. On spreading modes and magma supply at slow and ultraslow mid-ocean ridges. *Earth and Planetary Science Letters*, *519*, pp.223-233.

Casini, L., Maino, M., Sanfilippo, A., Ildefonse, B. and Dick, H.J., 2021. High-Temperature Strain Localization and the Nucleation of Oceanic Core Complexes (16.5° N, Mid-Atlantic Ridge). *Journal of Geophysical Research: Solid Earth*, *126*(9), p.e2021JB022215.

Chernosky, J.V., Berman, R.G. and Bryndzia, L.T., 1988. Stability, phase relations, and thermodynamic properties of chlorite and serpentine group minerals. *Reviews in Mineralogy and Geochemistry*, *19*(1), pp.295-346.

Chen, X., Elwood Madden, A.S. and Reches, Z.E., 2017. The frictional strength of talc gouge in high-velocity shear experiments. *Journal of Geophysical Research: Solid Earth*, *122*(5), pp.3661-3676.

Chen, J., Crawford, W.C. and Cannat, M., 2023. Microseismicity and lithosphere thickness at a nearly-amagmatic oceanic detachment fault system. *Nature Communications*, *14*(1), p.430.

Clerc, C., Boulvais, P., Lagabrielle, Y. and de Saint Blanquat, M., 2014. Ophicalcites from the northern Pyrenean belt: a field, petrographic and stable isotope study. *International Journal of Earth Sciences*, *103*, pp.141-163.

Corbalán, A., Nedimović, M.R., Louden, K.E., Cannat, M., Grevemeyer, I., Watremez, L. and Leroy, S., 2021. Seismic velocity structure along and across the ultraslow-spreading Southwest Indian ridge at 64 30′ E showcases flipping detachment faults. *Journal of Geophysical Research: Solid Earth*, *126*(10), p.e2021JB022177.

Demartin, B.J., Sohn, R.A., Canales, J.P. and Humphris, S.E., 2007. Kinematics and geometry of active detachment faulting beneath the Trans-Atlantic Geotraverse (TAG) hydrothermal field on the Mid-Atlantic Ridge. *Geology*, *35*(8), pp.711-714.

Dick, H.J., Ozawa, K., Meyer, P.S., Niu, Y., Robinson, P.T., Constantin, M., Hebert, R., Maeda, J., Natland, J.H., Hirth, G. and Mackie, S., 2002. 10. Primary silicate mineral chemistry of a 1.5-km section of very slow spreading lower ocean crust: ODP hole 735B, Southwest Indian ridge. *Proceedings of Ocean Drilling Program, Scientific Results, 000. College Station, TX: Ocean Drilling Program*, pp.1-60.

Dick, H.J., Macleod, C.J., Blum, P., Abe, N., Blackman, D.K., Bowles, J.A., Cheadle, M.J., Cho, K., Ciazela, J., Deans, J.R. and Edgcomb, V.P., 2019. Dynamic accretion beneath a slow-spreading ridge segment: IODP Hole 1473A and the Atlantis Bank Oceanic Core Complex. *Journal of Geophysical Research: Solid Earth*, *124*(12), pp.12631-12659.

Escartín, J., Mével, C., MacLeod, C.J. and McCaig, A.M., 2003. Constraints on deformation conditions and the origin of oceanic detachments: The Mid-Atlantic Ridge core complex at 15 45′ N. *Geochemistry, Geophysics, Geosystems*, *4*(8).

Escartín, J., Smith, D.K., Cann, J., Schouten, H., Langmuir, C.H. and Escrig, S., 2008. Central role of detachment faults in accretion of slow-spreading oceanic lithosphere. *Nature*, *455*(7214), pp.790-794.

Escartin, J., Mevel, C., Petersen, S., Bonnemains, D., Cannat, M., Andreani, M., Augustin, N., Bézos, A., Chavagnac, V., Choi, Y. and Godard, M., 2017. Tectonic structure, evolution, and the nature of oceanic core complexes

and their detachment fault zones (13 20′ N and 13 30′ N, Mid Atlantic Ridge). *Geochemistry, Geophysics, Geosystems*, *18*(4), pp.1451-1482.

Evans, B.W., 2004. The serpentinite multisystem revisited: chrysotile is metastable. *International Geology Review*, *46*(6), pp.479-506.

Glazner, A.F. and Mills, R.D., 2012. Interpreting two-dimensional cuts through broken geologic objects: fractal and non-fractal size distributions. *Geosphere*, *8*(4), pp.902-914.

Grevemeyer, I., Hayman, N.W., Lange, D., Peirce, C., Papenberg, C., Van Avendonk, H.J., Schmid, F., de La Peña, L.G. and Dannowski, A., 2019. Constraining the maximum depth of brittle deformation at slow-and ultraslow-spreading ridges using microseismicity. *Geology*, *47*(11), pp.1069-1073.

Hansen, L.N., Cheadle, M.J., John, B.E., Swapp, S.M., Dick, H.J., Tucholke, B.E. and Tivey, M.A., 2013. Mylonitic deformation at the Kane oceanic core complex: Implications for the rheological behavior of oceanic detachment faults. *Geochemistry, Geophysics, Geosystems*, *14*(8), pp.3085-3108.

Hanson, R.E., Puckett Jr, R.E., Keller, G.R., Brueseke, M.E., Bulen, C.L., Mertzman, S.A., Finegan, S.A. and McCleery, D.A., 2013. Intraplate magmatism related to opening of the southern Iapetus Ocean: Cambrian Wichita igneous province in the Southern Oklahoma rift zone. *Lithos*, *174*, pp.57-70.

Heilbronner, R. and Keulen, N., 2006. Grain size and grain shape analysis of fault rocks. *Tectonophysics*, *427*(1-4), pp.199-216.

Hirauchi, K.I. and Yamaguchi, H., 2007. Unique deformation processes involving the recrystallization of chrysotile within serpentinite: implications for aseismic slip events within subduction zones. *Terra Nova*, *19*(6), pp.454-461.

Jöns, N., Bach, W. and Schroeder, T., 2009. Formation and alteration of plagiogranites in an ultramafic-hosted detachment fault at the Mid-Atlantic Ridge (ODP Leg 209). *Contributions to Mineralogy and Petrology*, *157*, pp.625-639

Karson, J.A., Früh-Green, G.L., Kelley, D.S., Williams, E.A., Yoerger, D.R. and Jakuba, M., 2006. Detachment shear zone of the Atlantis Massif core complex, Mid-Atlantic Ridge, 30 N. *Geochemistry, Geophysics, Geosystems*, *7*(6).

Keulen, N., Heilbronner, R., Stünitz, H., Boullier, A.M. and Ito, H., 2007. Grain size distributions of fault rocks: A comparison between experimentally and naturally deformed granitoids. *Journal of Structural Geology*, *29*(8), pp.1282-1300.

Lavier, L.L., Buck, W.R. and Poliakov, A.N., 2000. Factors controlling normal fault offset in an ideal brittle layer. *Journal of Geophysical Research: Solid Earth*, *105*(B10), pp.23431-23442.

Lavier, L.L. and Buck, W.R., 2002. Half graben versus large-offset low-angle normal fault: Importance of keeping cool during normal faulting. *Journal of Geophysical Research: Solid Earth*, *107*(B6), pp.ETG-8.

MacLeod, C.J., Escartin, J., Banerji, D., Banks, G.J., Gleeson, M., Irving, D.H.B., Lilly, R.M., McCaig, A.M., Niu, Y., Allerton, S. and Smith, D.K., 2002. Direct geological evidence for oceanic detachment faulting: The Mid-Atlantic Ridge, 15 45′ N. *Geology*, *30*(10), pp.879-882.

Manatschal, G. and Müntener, O., 2009. A type sequence across an ancient magma-poor ocean–continent transition: the example of the western Alpine Tethys ophiolites. *Tectonophysics*, *473*(1-2), pp.4-19.

Marone, C. and Scholz, C.H., 1989. Particle-size distribution and microstructures within simulated fault gouge. *Journal of Structural Geology*, *11*(7), pp.799-814.

McCaig, A.M., Cliff, R.A., Escartin, J., Fallick, A.E. and MacLeod, C.J., 2007. Oceanic detachment faults focus very large volumes of black smoker fluids. *Geology*, *35*(10), pp.935-938.

McCaig, A.M., Delacour, A., Fallick, A.E., Castelain, T. and Früh-Green, G.L., 2010. Detachment fault control on hydrothermal circulation systems: Interpreting the subsurface beneath the TAG hydrothermal field using the isotopic and geological evolution of oceanic core complexes in the Atlantic. *Diversity of Hydrothermal Systems on Slow Spreading Ocean Ridges, Geophys. Monogr. Ser*, *188*, pp.207-240.

Meier, M., Schlindwein, V., Scholz, J.R., Geils, J., Schmidt-Aursch, M.C., Krüger, F., Czuba, W. and Janik, T., 2021. Segment-scale seismicity of the ultraslow spreading Knipovich Ridge. *Geochemistry, Geophysics, Geosystems*, *22*(2), p.e2020GC009375.

Momoh, E., Cannat, M., Watremez, L., Leroy, S. and Singh, S.C., 2017. Quasi-3-D seismic reflection imaging and wide-angle velocity structure of nearly amagmatic oceanic lithosphere at the ultraslow-spreading Southwest Indian Ridge. *Journal of Geophysical Research: Solid Earth*, *122*(12), pp.9511-9533.

Moore, D.E., Lockner, D.A., Ma, S., Summers, R. and Byerlee, J.D., 1997. Strengths of serpentinite gouges at elevated temperatures. *Journal of Geophysical Research: Solid Earth*, *102*(B7), pp.14787-14801.

Moore, D.E., Lockner, D.A., Tanaka, H. and Iwata, K., 2004. The coefficient of friction of chrysotile gouge at seismogenic depths. *International Geology Review*, *46*(5), pp.385-398.

Moore, D.E. and Lockner, D.A., 2011. Frictional strengths of talc-serpentine and talc-quartz mixtures. *Journal of Geophysical Research: Solid Earth*, *116*(B1).

Niemeijer, A.R. and Spiers, C.J., 2005. Influence of phyllosilicates on fault strength in the brittle-ductile transition: Insights from rock analogue experiments. *Geological Society, London, Special Publications*, *245*(1), pp.303-327.

Niemeijer, A.R. and Spiers, C.J., 2007. A microphysical model for strong velocity weakening in phyllosilicate-bearing fault gouges. *Journal of Geophysical Research: Solid Earth*, *112*(B10).

Olive, J.A., Behn, M.D. and Tucholke, B.E., 2010. The structure of oceanic core complexes controlled by the depth distribution of magma emplacement. *Nature Geoscience*, *3*(7), pp.491-495.

Paquet, M., Cannat, M., Brunelli, D., Hamelin, C. and Humler, E., 2016. Effect of melt/mantle interactions on MORB chemistry at the easternmost S outhwest I ndian R idge (61°–67° E). *Geochemistry, Geophysics, Geosystems*, *17*(11), pp.4605-4640.

Parnell-Turner, R., Sohn, R.A., Peirce, C., Reston, T.J., MacLeod, C.J., Searle, R.C. and Simão, N.M., 2017. Oceanic detachment faults generate compression in extension. *Geology*, *45*(10), pp.923-926.

Picazo, S., Cannat, M., Delacour, A., Escartín, J., Rouméjon, S. and Silantyev, S., 2012. Deformation associated with the denudation of mantle-derived rocks at the Mid-Atlantic Ridge 13°–15° N: The role of magmatic injections and hydrothermal alteration. *Geochemistry, Geophysics, Geosystems*, *13*(9).

Picazo, S., Manatschal, G., Cannat, M. and Andréani, M., 2013. Deformation associated to exhumation of serpentinized mantle rocks in a fossil Ocean Continent Transition: The Totalp unit in SE Switzerland. *Lithos*, *175*, pp.255-271.

Rasband, W.S., 2007. ImageJ, US national institutes of health. *http://rsb. info. nih. gov/ij/(1997-2007)*.

Reches, Z.E. and Dewers, T.A., 2005. Gouge formation by dynamic pulverization during earthquake rupture. *Earth and Planetary Science Letters*, *235*(1-2), pp.361-374.

Reston, T.J. and McDermott, K.G., 2011. Successive detachment faults and mantle unroofing at magma-poor rifted margins. *Geology*, *39*(11), pp.1071-1074.

Rouméjon, S. and Cannat, M., 2014. Serpentinization of mantle-derived peridotites at mid-ocean ridges: Mesh texture development in the context of tectonic exhumation. *Geochemistry, Geophysics, Geosystems*, *15*(6), pp.2354-2379.

Roumejon, S., Cannat, M., Agrinier, P., Godard, M. and Andreani, M., 2015. Serpentinization and fluid pathways in tectonically exhumed peridotites from the Southwest Indian Ridge (62–65 E). *Journal of Petrology*, *56*(4), pp.703-734.

Rousell, D.H., Fedorowich, J.S. and Dressler, B.O., 2003. Sudbury Breccia (Canada): a product of the 1850 Ma Sudbury Event and host to footwall Cu–Ni–PGE deposits. *Earth-Science Reviews*, *60*(3-4), pp.147-174.

Sammis, C., King, G. and Biegel, R., 1987. The kinematics of gouge deformation. *Pure and Applied Geophysics*, *125*, pp.777-812.

Sandiford, D., Brune, S., Glerum, A., Naliboff, J. and Whittaker, J.M., 2021. Kinematics of footwall exhumation at oceanic detachment faults: solid-block rotation and apparent unbending. *Geochemistry, Geophysics, Geosystems*, *22*(4), p.e2021GC009681.

Sauter, D., Cannat, M., Rouméjon, S., Andreani, M., Birot, D., Bronner, A., Brunelli, D., Carlut, J., Delacour, A., Guyader, V. and MacLeod, C.J., 2013. Continuous exhumation of mantle-derived rocks at the Southwest Indian Ridge for 11 million years. *Nature Geoscience*, *6*(4), pp.314-320.

Schlindwein, V. and Schmid, F., 2016. Mid-ocean-ridge seismicity reveals extreme types of ocean lithosphere. *Nature*, *535*(7611), pp.276-279.

Schroeder, T. and John, B.E., 2004. Strain localization on an oceanic detachment fault system, Atlantis Massif, 30 N, Mid-Atlantic Ridge. *Geochemistry, Geophysics, Geosystems*, *5*(11).

Schroeder, T., Cheadle, M.J., Dick, H.J., Faul, U., Casey, J.F. and Kelemen, P.B., 2007. Nonvolcanic seafloor spreading and corner-flow rotation accommodated by extensional faulting at 15 N on the Mid-Atlantic Ridge: A structural synthesis of ODP Leg 209. *Geochemistry, Geophysics, Geosystems*, *8*(6).

Smith, D.K., Cann, J.R. and Escartín, J., 2006. Widespread active detachment faulting and core complex formation near 13 N on the Mid-Atlantic Ridge. *Nature*, *442*(7101), pp.440-443.

Storti, F., Billi, A. and Salvini, F., 2003. Particle size distributions in natural carbonate fault rocks: insights for non-self-similar cataclasis. *Earth and Planetary Science Letters*, *206*(1-2), pp.173-186.

Tao, C., Seyfried Jr, W.E., Lowell, R.P., Liu, Y., Liang, J., Guo, Z., Ding, K., Zhang, H., Liu, J., Qiu, L. and Egorov, I., 2020. Deep high-temperature hydrothermal circulation in a detachment faulting system on the ultra-slow spreading ridge. *Nature communications*, *11*(1), p.1300.

Tarling, M.S., Rooney, J.S., Viti, C., Smith, S.A. and Gordon, K.C., 2018. Distinguishing the Raman spectrum of polygonal serpentine. *Journal of Raman Spectroscopy*, *49*(12), pp.1978-1984.

Tesei, T., Harbord, C.W.A., De Paola, N., Collettini, C. and Viti, C., 2018. Friction of mineralogically controlled serpentinites and implications for fault weakness. *Journal of Geophysical Research: Solid Earth*, *123*(8), pp.6976-6991.

Turcotte, D.L., 1986. Fractals and fragmentation. *Journal of Geophysical Research: Solid Earth*, *91*(B2), pp.1921-1926.

Wilson, B., Dewers, T., Reches, Z.E. and Brune, J., 2005. Particle size and energetics of gouge from earthquake rupture zones. *Nature*, *434*(7034), pp.749-752.

Wallis, D., Lloyd, G.E., Phillips, R.J., Parsons, A.J. and Walshaw, R.D., 2015. Low effective fault strength due to frictional-viscous flow in phyllonites, Karakoram Fault Zone, NW India. *Journal of Structural Geology*, *77*, pp.45-61.

Summary of Conclusions

The eastern segments of the Southwest Indian Ridge (SWIR), particularly the 64°35'E and 64°E regions, represent a melt-poor end-member of the global mid-ocean ridge (MOR) system. It contains nearly amagmatic sections, where seafloor spreading is predominantly accommodated by large offset detachment faults, leading to the exposure of mantle-derived rocks on the seafloor. These detachments have a lifetime of 1-2 myr, then a new detachment, with an opposite polarity, takes over. This process is described as flip-flop detachment faulting. This thesis, based on combining shipboard bathymetry, microbathymetry, ROV dive observations, and microstructural observations on rock samples, offers insights into the geology, tectonics, and deformation processes associated with these nearly amagmatic, flip-flop detachment faults.

The axial valley wall in our study area (the 64°E nearly amagmatic section of the SWIR) corresponds to the footwall of the presently active detachment, D1. It exposes variably deformed serpentinized peridotites with very rare gabbro dikes. The summit of this south-facing wall comprises km-sized benches and scarps that represent blocks of the degraded D1 breakaway. These scarps display highly deformed outcrops, consisting of serpentinite microbreccia and gouge-bearing horizons interlayered with relatively less deformed and fractured serpentinized peridotites. These exposed lithologic packages are up to ~100 m thick at places. The orientation and characteristics of these formations suggest that they represent exposures of the previous D2 detachment's fault zone. This evidence strengthens the interpretation of nearly amagmatic, flip-flop ODFs, consistent with prior research (Sauter et al., 2013). Additionally, the across-axis extent of the D1's degraded breakaway verifies the age estimation of around 300 kyr for the initiation of the D1 detachment (Cannat et al., 2019).

Our observations also show significant along-strike axial variations in the D1 footwall features. The coverage of the ROV high-resolution bathymetry and of the ROV observation dives available for this study is limited. However, differences emerge between the eastern smooth, non-corrugated part of the studied area and the western part, in which we identified corrugations comparable to those at more magmatic, domal, and corrugated oceanic detachments. This western corrugated region also displays several hectometer-to-kilometer-wide NNE-trending ridges, which we interpret as mega-corrugations, resulting from the inferred existence of hectometer-to-kilometer-scale phacoids between linked fault splays in the detachment damage zone. This western, corrugated region also displays minor offset recent antithetic normal faults. Both the NNE-trending ridges and the antithetic faults are absent in the non-corrugated region, and the axial valley wall (D1 footwall) is not as high. The other clear difference is that ultracataclastic and gouge layers are thicker and more extensive in the non-corrugated region, and field observations suggest that hydrous fluids in the fault zone could enhance the formation of such gouges. Combined, these characteristics suggest a stronger D1 fault and footwall in the corrugated region. Another intriguing observation is that the trend of corrugations in this region makes a 15-25° clockwise to the spreading direction. We propose that this may result from variations in fault and footwall strength along the axis, possibly linked to the availability of hydrothermal fluids in the detachment fault.

Our study of deformation microtextures has focused on the most deformed serpentinite microbreccia and gouges from the D1 and D2 detachment fault zones. It reveals clast-rich microdomains formed by brittle fracturing of already serpentinized peridotites and foliated, clast-poor microdomains where clast dissolution and the precipitation of a fine-grained chrysotile matrix have occurred. The frictional strength of water-saturated chrysotile gouge at low temperatures is found in deformation experiments to be similar to that of talc, which is commonly found in deformed rocks from more

magmatic mid-ocean ridge detachment faults. However, chrysotile gouge strength increases at increasing temperatures and pressures so that deeper regions of the ODFs' damage zone, lined with chrysotile gouge, could be more robust. However, experimental data also indicates that the fluid-enhanced dissolution-precipitation processes we observed in the samples can weaken the chrysotile gouge in these deeper areas. In addition, the rheology of these gouges is not the sole determinant of fault strength; the thickness, extent, and connectivity of the gouge and microbreccia horizons also likely play crucial roles.

Our findings add to the marked distinctions between the eastern SWIR's nearly amagmatic flip-flop detachment faults and the domal and corrugated detachments at more magmatic ridge settings. We show that the most deformed horizons at the SWIR ODFs are chrysotile-bearing gouges and microbreccia, contrasting with the prevalence of talc, amphibole, and chlorite-bearing serpentinites in strain localization zones of the domal ODFs. The SWIR ODFs also probably have a thicker damage domain with large km-scale phacoids of lesser deformed serpentinized peridotite between linked fault splays. As a working hypothesis, we propose that this thick damage zone may not solely be a result of variations in the rheology of the upper brittle lithosphere. Instead, it might be a legacy of less localized deformation in the transition between the brittle and ductile domains.

Future Perspectives

Based on the findings of this investigation, there are opportunities for further exploration in the future. The aim would be a better understanding of the along-axis availability of the exposed D1 fault geology in relation to hydrous fluids and deformation processes in the detachment fault zone. Using the same approach of acquiring more high-resolution ROV bathymetry, ROV observation

dives, and sampling would be an obvious step. At present, the data is adequate to characterize a region that we discovered is, in fact, corrugated at least locally (although these corrugations are not visible in the shipboard bathymetry) and probably has a stronger fault zone and footwall than regions further to the east. Our observations on the trend of corrugations in this western domain suggest that there might be a clockwise strain rotation caused by this along-axis contrast in fault and footwall strength. We also observe that the inferred emergence of D2 (as shown in Figure 1.17a, Chapter 1), is curvilinear and that this curvilinear shape is centered to where the D1 footwall is the highest. One possibility to explore is that the curvilinear shape of the D2 emergence is not original but results from the deformation of the D1 footwall. This type of curvilinear geometry is visible in the inferred emergence of inactive older detachment faults located off-axis (as depicted in Figure 1.15, Chapter 1). This geometry may reflect the along-axis variation of the fault and footwall strength during the next antithetic detachment.

Chapter 1-References

Albers, E., Schroeder, T. and Bach, W., 2019. Melt impregnation of mantle peridotite facilitates high-temperature hydration and mechanical weakening: Implications for oceanic detachment faults. *Geochemistry, Geophysics, Geosystems*, *20*(1), pp.84-108.

Behnsen, J. and Faulkner, D.R., 2012. The effect of mineralogy and effective normal stress on frictional strength of sheet silicates. *Journal of Structural Geology*, *42*, pp.49-61.

Bernoulli, D. and Weissert, H., 1985. Sedimentary fabrics in Alpine ophicalcites, south Pennine Arosa zone, Switzerland. *Geology*, *13*(11), pp.755-758.

Beslier, M.O., Royer, J.Y., Girardeau, J., Hill, P.J., Boeuf, E., Buchanan, C., Chatin, F., Jacovetti, G., Moreau, A., Munschy, M. and Partouche, C., 2004. A wide ocean-continent transition along the south-west Australian margin: first results of the MARGAU/MD110 cruise. *Bulletin de la Société Géologique de France*, *175*(6), pp.629-641.

Bickert, M., Lavier, L. and Cannat, M., 2020. How do detachment faults form at ultraslow mid-ocean ridges in a thick axial lithosphere?. *Earth and Planetary Science Letters*, *533*, p.116048.

Bickert, M., Cannat, M., Tommasi, A., Jammes, S. and Lavier, L., 2021. Strain localization in the root of detachment faults at a melt-starved mid-ocean ridge: a microstructural study of Abyssal Peridotites from the Southwest Indian Ridge. *Geochemistry, Geophysics, Geosystems*, *22*(5), p.e2020GC009434.

Bickert, M., Cannat, M. and Brunelli, D., 2023. Hydrous fluids down to the semi-brittle root zone of detachment faults in nearly amagmatic ultra-slow spreading ridges. *Lithos*, *442*, p.107084.

Bird, P., 2003. An updated digital model of plate boundaries. *Geochemistry, Geophysics, Geosystems*, *4*(3).

Bonnemains, D., Escartín, J., Mével, C., Andreani, M. and Verlaguet, A., 2017. Pervasive silicification and hanging wall overplating along the 13° 20′ N oceanic detachment fault (M id-A tlantic R idge). *Geochemistry, Geophysics, Geosystems*, *18*(6), pp.2028-2053.

Boschi, C., Früh-Green, G.L., Delacour, A., Karson, J.A. and Kelley, D.S., 2006. Mass transfer and fluid flow during detachment faulting and development of an oceanic core complex, Atlantis Massif (MAR 30 N). *Geochemistry, Geophysics, Geosystems*, *7*(1).

Buck, W.R., Lavier, L.L. and Poliakov, A.N., 2005. Modes of faulting at mid-ocean ridges. *Nature*, *434*(7034), pp.719-723.

Byerlee, J., 1978. Friction of rocks. *Rock friction and earthquake prediction*, pp.615-626.

Canales, J.P., Tucholke, B.E. and Collins, J.A., 2004. Seismic reflection imaging of an oceanic detachment fault: Atlantis megamullion (Mid-Atlantic Ridge, 30 10′ N). *Earth and Planetary Science Letters*, *222*(2), pp.543-560.

Canales, J., Xu, M., Tucholke, B.E., Collins, J.A. and Dubois, D.L., 2007, December. The sub-seafloor structure of Mid-Atlantic Ridge core complexes. In *AGU Fall Meeting Abstracts*(Vol. 2007, pp. T51F-06).

Canales, J.P., Tucholke, B.E., Xu, M., Collins, J.A. and DuBois, D.L., 2008. Seismic evidence for large-scale compositional heterogeneity of oceanic core complexes. *Geochemistry, Geophysics, Geosystems*, *9*(8).

Candela, T. and Renard, F., 2012. Segment linkage process at the origin of slip surface roughness: Evidence from the Dixie Valley fault. *Journal of Structural Geology*, *45*, pp.87-100.

Cannat, M., Mével, C. and Stakes, D., 1991. Normal ductile shear zones at an oceanic spreading ridge: tectonic evolution of Site 735 gabbros (southwest Indian Ocean). In *Von Herzen, RP, Robinson, PT, et al., Proc. ODP, Sci. Results* (Vol. 118, pp. 415-429).

Cannat, M., 1993. Emplacement of mantle rocks in the seafloor at mid-ocean ridges. *Journal of Geophysical Research: Solid Earth*, *98*(B3), pp.4163-4172.

Cannat, M. and Casey, J.F., 1995, June. An ultramafic lift at the Mid-Atlantic Ridge: successive stages of magmatism in serpentinized peridotites from the 15 N region. In *Mantle and Lower Crust Exposed in Oceanic Ridges and in Ophiolites: Contributions to a Specialized Symposium of the VII EUG Meeting, Strasbourg, Spring 1993* (pp. 5-34). Dordrecht: Springer Netherlands.

Cannat, M., Lagabrielle, Y., Bougault, H., Casey, J., de Coutures, N., Dmitriev, L. and Fouquet, Y., 1997. Ultramafic and gabbroic exposures at the Mid-Atlantic Ridge: Geological mapping in the 15 N region. *Tectonophysics*, *279*(1-4), pp.193-213.

Cannat, M., Rommevaux-Jestin, C., Sauter, D., Deplus, C. and Mendel, V., 1999. Formation of the axial relief at the very slow spreading Southwest Indian Ridge (49 to 69 E). *Journal of Geophysical Research: Solid Earth*, *104*(B10), pp.22825-22843.

Cannat, M., Rommevaux-Jestin, C. and Fujimoto, H., 2003. Melt supply variations to a magma-poor ultra-slow spreading ridge (Southwest Indian Ridge 61° to 69° E). *Geochemistry, Geophysics, Geosystems*, *4*(8).

Cannat, M., Sauter, D., Mendel, V., Ruellan, E., Okino, K., Escartin, J., Combier, V. and Baala, M., 2006. Modes of seafloor generation at a melt-poor ultraslow-spreading ridge. *Geology*, *34*(7), pp.605-608.

Cannat, M., Sauter, D., Escartín, J., Lavier, L. and Picazo, S., 2009. Oceanic corrugated surfaces and the strength of the axial lithosphere at slow spreading ridges. *Earth and Planetary Science Letters*, *288*(1-2), pp.174-183.

Cannat, M., Mangeney, A., Ondréas, H., Fouquet, Y. and Normand, A., 2013. High-resolution bathymetry reveals contrasting landslide activity shaping the walls of the Mid-Atlantic Ridge axial valley. *Geochemistry, Geophysics, Geosystems*, *14*(4), pp.996-1011.

Cannat, M., Sauter, D., Lavier, L., Bickert, M., Momoh, E. and Leroy, S., 2019. On spreading modes and magma supply at slow and ultraslow mid-ocean ridges. *Earth and Planetary Science Letters*, *519*, pp.223-233.

Cheadle, M. and Grimes, C., 2010. To fault or not to fault. *Nature Geoscience*, *3*(7), pp.454-456.

Chen, J. (1992). Oceanic crustal thickness versus spreading rate. *Geophysical Research Letters, (8),* 753–756.

Chen, J., Crawford, W.C. and Cannat, M., 2023. Microseismicity and lithosphere thickness at a nearly-amagmatic oceanic detachment fault system. *Nature Communications*, *14*(1), p.430.

Chernosky, J.V., Day, H.W. and Caruso, L.J., 1985. Equilibria in the system MgO–SiO2–H2O: Experimental determination of the stability of Mg-anthophyllite. *American Mineralogist*, *70*(3-4), pp.223-236.

Childs, C., Watterson, J. and Walsh, J.J., 1995. Fault overlap zones within developing normal fault systems. *Journal of the Geological Society*, *152*(3), pp.535-549.

Christensen, N.I., 1978. Ophiolites, seismic velocities and oceanic crustal structure. *Tectonophysics*, *47*(1-2), pp.131-157.

Corbalán, A., Nedimović, M.R., Louden, K.E., Cannat, M., Grevemeyer, I., Watremez, L. and Leroy, S., 2021. Seismic velocity structure along and across the ultraslow-spreading Southwest Indian ridge at 64 30′ E showcases flipping detachment faults. *Journal of Geophysical Research: Solid Earth*, *126*(10), p.e2021JB02217.

Demartin, B.J., Sohn, R.A., Canales, J.P. and Humphris, S.E., 2007. Kinematics and geometry of active detachment faulting beneath the Trans-Atlantic Geotraverse (TAG) hydrothermal field on the Mid-Atlantic Ridge. *Geology*, *35*(8), pp.711-714.

Detrick, R., Collins, J., Stephen, R. and Swift, S., 1994. In situ evidence for the nature of the seismic layer 2/3 boundary in oceanic crust. *Nature*, *370*(6487), pp.288-290.

Dick, H.J.B., 1989. Abyssal peridotites, very slow spreading ridges and ocean ridge magmatism. *Geological Society, London, Special Publications*, *42*(1), pp.71-105.

Dick, H.J., Natland, J.H., Alt, J.C., Bach, W., Bideau, D., Gee, J.S., Haggas, S., Hertogen, J.G., Hirth, G., Holm, P.M. and Ildefonse, B., 2000. A long in situ section of the lower ocean crust: results of ODP Leg 176 drilling at the Southwest Indian Ridge. *Earth and planetary science letters*, *179*(1), pp.31-51.

Dick, H.J., Ozawa, K., Meyer, P.S., Niu, Y., Robinson, P.T., Constantin, M., Hebert, R., Maeda, J., Natland, J.H., Hirth, G. and Mackie, S., 2002. 10. Primary silicate mineral chemistry of a 1.5-km section of very slow spreading lower ocean crust: ODP hole 735B, Southwest Indian ridge. *Proceedings of Ocean Drilling Program, Scientific Results, 000. College Station, TX: Ocean Drilling Program*, pp.1-60.

Dick, H.J., Lin, J. and Schouten, H., 2003. An ultraslow-spreading class of ocean ridge. *Nature*, *426*(6965), pp.405-412.

Escartin, J., Hirth, G. and Evans, B., 1997. Effects of serpentinization on the lithospheric strength and the style of normal faulting at slow-spreading ridges. *Earth and Planetary Science Letters*, *151*(3-4), pp.181-189.

Escartín, J. and Cannat, M., 1999. Ultramafic exposures and the gravity signature of the lithosphere near the Fifteen-Twenty Fracture Zone (Mid-Atlantic Ridge, 14–16.5 N). *Earth and Planetary Science Letters*, *171*(3), pp.411-424.

Escartin, J., Hirth, G. and Evans, B., 2001. Strength of slightly serpentinized peridotites: Implications for the tectonics of oceanic lithosphere. *Geology*, *29*(11), pp.1023-1026.

Escartín, J., Mével, C., MacLeod, C.J. and McCaig, A.M., 2003. Constraints on deformation conditions and the origin of oceanic detachments: The Mid-Atlantic Ridge core complex at 15 45′ N. *Geochemistry, Geophysics, Geosystems*, *4*(8).

Escartín, J., Smith, D.K., Cann, J., Schouten, H., Langmuir, C.H. and Escrig, S., 2008. Central role of detachment faults in accretion of slow-spreading oceanic lithosphere. *Nature*, *455*(7214), pp.790-794.

Escartin, J., Mevel, C., Petersen, S., Bonnemains, D., Cannat, M., Andreani, M., Augustin, N., Bézos, A., Chavagnac, V., Choi, Y. and Godard, M., 2017. Tectonic structure, evolution, and the nature of oceanic core complexes and their detachment fault zones (13 20′ N and 13 30′ N, Mid Atlantic Ridge). *Geochemistry, Geophysics, Geosystems*, *18*(4), pp.1451-1482.

Evans, B.W., 2004. The serpentinite multisystem revisited: chrysotile is metastable. *International Geology Review*, *46*(6), pp.479-506.

Ferrill, D.A., Morris, A.P., Stamatakos, J.A. and Sims, D.W., 2000. Crossing conjugate normal faults. *AAPG bulletin*, *84*(10), pp.1543-1559.

Früh-Green, G.L., Orcutt, B.N., Green, S.L., Cotterill, C., Morgan, S., Akizawa, N., Bayrakci, G., Behrmann, J.H., Boschi, C., Brazleton, W.J. and Cannat, M., 2017. Expedition 357 summary. *Proceedings of the International Ocean Discovery Program*, *357*.

Garcés, M. and Gee, J.S., 2007. Paleomagnetic evidence of large footwall rotations associated with low-angle faults at the Mid-Atlantic Ridge. *Geology*, *35*(3), pp.279-282.

Gente, P., Pockalny, R.A., Durand, C., Deplus, C., Maia, M., Ceuleneer, G., Mével, C., Cannat, M. and Laverne, C., 1995. Characteristics and evolution of

the segmentation of the Mid-Atlantic Ridge between 20 N and 24 N during the last 10 million years. *Earth and Planetary Science Letters*, *129*(1-4), pp.55-71.

Grevemeyer, I., Hayman, N.W., Lange, D., Peirce, C., Papenberg, C., Van Avendonk, H.J., Schmid, F., de La Peña, L.G. and Dannowski, A., 2019. Constraining the maximum depth of brittle deformation at slow-and ultraslowspreading ridges using microseismicity. *Geology*, *47*(11), pp.1069-1073

Hansen, L.N., Cheadle, M.J., John, B.E., Swapp, S.M., Dick, H.J., Tucholke, B.E. and Tivey, M.A., 2013. Mylonitic deformation at the Kane oceanic core complex: Implications for the rheological behavior of oceanic detachment faults. *Geochemistry, Geophysics, Geosystems*, *14*(8), pp.3085-3108.

Heezen, B.C., 1960. The rift in the ocean floor. *Scientific American*, *203*(4), pp.98-114.

Hooft, E.E.E., Detrick, R.S., Toomey, D.R., Collins, J.A. and Lin, J., 2000. Crustal thickness and structure along three contrasting spreading segments of the Mid-Atlantic Ridge, 33.5–35 N. *Journal of Geophysical Research: Solid Earth*, *105*(B4), pp.8205-8226.

Ildefonse, B., Blackman, D.K., John, B.E., Ohara, Y., Miller, D.J. and MacLeod, C.J., 2007. Oceanic core complexes and crustal accretion at slow-spreading ridges. *Geology*, *35*(7), pp.623-626.

Jackson, J. and McKenzie, D., 1999. A hectare of fresh striations on the Arkitsa Fault, central Greece. *Journal of Structural Geology*, *21*(1), pp.1-6.

Jenkins, D.M., Holland, T.J. and Clare, A.K., 1991. Experimental determination of the pressure-temperature stability field and thermochemical properties of synthetic tremolite. *American Mineralogist*, *76*(3-4), pp.458-469.

John, B.E., 1987. Geometry and evolution of a mid-crustal extensional fault system: Chemehuevi Mountains, southeastern California. *Geological Society, London, Special Publications*, *28*(1), pp.313-335.

John, B.E. and Cheadle, M.J., 2010. Deformation and alteration associated with oceanic and continental detachment fault systems: Are they similar. *Diversity of Hydrothermal Systems on Slow Spreading Ocean Ridges, Geophys. Monogr. Ser*, *188*, pp.175-205.

Jöns, N., Bach, W. and Schroeder, T., 2009. Formation and alteration of plagiogranites in an ultramafic-hosted detachment fault at the Mid-Atlantic Ridge (ODP Leg 209). *Contributions to Mineralogy and Petrology*, *157*, pp.625-639.

Karson, J.A. and Dick, H.J.B., 1983. Tectonics of ridge-transform intersections at the Kane Fracture Zone. *Marine Geophysical Researches*, *6*(1), pp.51-98.

Karson, J.A., 1998. Internal structure of oceanic lithosphere: A perspective from tectonic windows. *Geophysical Monograph-American Geophysical Union*, *106*, pp.177-218.

Karson, J.A., Früh-Green, G.L., Kelley, D.S., Williams, E.A., Yoerger, D.R. and Jakuba, M., 2006. Detachment shear zone of the Atlantis Massif core complex, Mid-Atlantic Ridge, 30 N. *Geochemistry, Geophysics, Geosystems*, *7*(6).

Lavier, L.L., Roger Buck, W. and Poliakov, A.N., 1999. Self-consistent rolling-hinge model for the evolution of large-offset low-angle normal faults. *Geology*, *27*(12), pp.1127-1130.

Lavier, L.L., Buck, W.R. and Poliakov, A.N., 2000. Factors controlling normal fault offset in an ideal brittle layer. *Journal of Geophysical Research: Solid Earth*, *105*(B10), pp.23431-23442.

Lavier, L.L. and Buck, W.R., 2002. Half graben versus large-offset low-angle normal fault: Importance of keeping cool during normal faulting. *Journal of Geophysical Research: Solid Earth*, *107*(B6), pp.ETG-8.

Lin, J., Purdy, G.M., Schouten, H., Sempere, J.C. and Zervas, C., 1990. Evidence from gravity data for focusedmagmatic accretionalong the Mid-Atlantic Ridge. *Nature*, *344*(6267), pp.627-632.

Macdonald, K.C., 1982. Mid-ocean ridges: Fine scale tectonic, volcanic and hydrothermal processes within the plate boundary zone. *Annual Review of Earth and Planetary Sciences*, *10*(1), pp.155-190.

MacLeod, C.J., Escartin, J., Banerji, D., Banks, G.J., Gleeson, M., Irving, D.H.B., Lilly, R.M., McCaig, A.M., Niu, Y., Allerton, S. and Smith, D.K., 2002. Direct geological evidence for oceanic detachment faulting: The Mid-Atlantic Ridge, 15 45′ N. *Geology*, *30*(10), pp.879-882.

Manatschal, G. and Bernoulli, D., 1999. Architecture and tectonic evolution of nonvolcanic margins: Present-day Galicia and ancient Adria. *Tectonics*, *18*(6), pp.1099-1119.

Manatschal, G., Froitzheim, N., Rubenach, M. and Turrin, B.D., 2001. The role of detachment faulting in the formation of an ocean-continent transition: insights from the Iberia Abyssal Plain. *Geological Society, London, Special Publications*, *187*(1), pp.405-428.

McCaig, A.M., Cliff, R.A., Escartin, J., Fallick, A.E. and MacLeod, C.J., 2007. Oceanic detachment faults focus very large volumes of black smoker fluids. *Geology*, *35*(10), pp.935-938.

Michael, P.J., Langmuir, C.H., Dick, H.J.B., Snow, J.E., Goldstein, S.L., Graham, D.W., Lehnert, K., Kurras, G., Jokat, W., Mühe, R. and Edmonds, H.N., 2003. Magmatic and amagmatic seafloor generation at the ultraslow-spreading Gakkel ridge, Arctic Ocean. *Nature*, *423*(6943), pp.956-961.

Miller, D.J. and Christensen, N.I., 1997. Seismic velocities of lower crustal and upper mantle rocks from the slow-spreading Mid-Atlantic Ridge, south of the Kane Transform Zone (MARK). In *Proceedings-ocean drilling program scientific results* (pp. 437-456). National Science Foundation.

Momoh, E., Cannat, M., Watremez, L., Leroy, S. and Singh, S.C., 2017. Quasi-3-D seismic reflection imaging and wide-angle velocity structure of

nearly amagmatic oceanic lithosphere at the ultraslow-spreading Southwest Indian Ridge. *Journal of Geophysical Research: Solid Earth*, *122*(12), pp.9511-9533.

Moore, D.E., Lockner, D.A., Ma, S., Summers, R. and Byerlee, J.D., 1997. Strengths of serpentinite gouges at elevated temperatures. *Journal of Geophysical Research: Solid Earth*, *102*(B7), pp.14787-14801.

Moore, D.E., Lockner, D.A., Tanaka, H. and Iwata, K., 2004. The coefficient of friction of chrysotile gouge at seismogenic depths. *International Geology Review*, *46*(5), pp.385-398.

Moore, D.E. and Lockner, D.A., 2008. Talc friction in the temperature range 25–400 C: Relevance for fault-zone weakening. *Tectonophysics*, *449*(1-4), pp.120-132.

Moore, D.E. and Lockner, D.A., 2011. Frictional strengths of talc-serpentine and talc-quartz mixtures. *Journal of Geophysical Research: Solid Earth*, *116*(B1).

Morris, A., Gee, J.S., Pressling, N., John, B.E., MacLeod, C.J., Grimes, C.B. and Searle, R.C., 2009. Footwall rotation in an oceanic core complex quantified using reoriented Integrated Ocean Drilling Program core samples. *Earth and Planetary Science Letters*, *287*(1-2), pp.217-228.

Muller, M.R., Minshull, T.A. and White, R.S., 1999. Segmentation and melt supply at the Southwest Indian Ridge. *Geology*, *27*(10), pp.867-870.

Müntener, O. and Manatschal, G., 2006. High degrees of melt extraction recorded by spinel harzburgite of the Newfoundland margin: The role of inheritance and consequences for the evolution of the southern North Atlantic. *Earth and Planetary Science Letters*, *252*(3-4), pp.437-452.

Nicholls, I.A., Ferguson, J., Jones, H., Marks, G.P. and Mutter, J.C., 1981. Ultramafic blocks from the ocean floor southwest of Australia. *Earth and Planetary Science Letters*, *56*, pp.362-374.

Ohara, Y., Yoshida, T., Kato, Y. and Kasuga, S., 2001. Giant megamullion in the Parece Vela backarc basin. *Marine Geophysical Researches*, *22*(1), pp.47-61.

Ohara, Y., Fujioka, K., Ishii, T. and Yurimoto, H., 2003. Peridotites and gabbros from the Parece Vela backarc basin: unique tectonic window in an extinct backarc spreading ridge. *Geochemistry, Geophysics, Geosystems*, *4*(7).

Okino, K., Matsuda, K., Christie, D.M., Nogi, Y. and Koizumi, K.I., 2004. Development of oceanic detachment and asymmetric spreading at the Australian-Antarctic Discordance. *Geochemistry, Geophysics, Geosystems*, *5*(12).

Olive, J.A. and Dublanchet, P., 2020. Controls on the magmatic fraction of extension at mid-ocean ridges. *Earth and Planetary Science Letters*, *549*, p.116541.

Paquet, M., Cannat, M., Brunelli, D., Hamelin, C. and Humler, E., 2016. Effect of melt/mantle interactions on MORB chemistry at the easternmost S

outhwest I ndian R idge (61°–67° E). *Geochemistry, Geophysics, Geosystems*, *17*(11), pp.4605-4640.

Parnell-Turner, R., Sohn, R.A., Peirce, C., Reston, T.J., MacLeod, C.J., Searle, R.C. and Simão, N.M., 2017. Oceanic detachment faults generate compression in extension. *Geology*, *45*(10), pp.923-926.

Parnell-Turner, R., Escartín, J., Olive, J.A., Smith, D.K. and Petersen, S., 2018. Genesis of corrugated fault surfaces by strain localization recorded at oceanic detachments. *Earth and Planetary Science Letters*, *498*, pp.116-128.

Parnell-Turner, R., Sohn, R.A., Peirce, C., Reston, T.J., MacLeod, C.J., Searle, R.C. and Simão, N.M., 2021. Seismicity trends and detachment fault structure at 13 N, Mid-Atlantic Ridge. *Geology*, *49*(3), pp.320-324.

Patriat, P. and Segoufin, J., 1988. Reconstruction of the central Indian Ocean. *Tectonophysics*, *155*(1-4), pp.211-234.

Peacock, D.C.P., 2002. Propagation, interaction and linkage in normal fault systems. *Earth-Science Reviews*, *58*(1-2), pp.121-142.

Péron-Pinvidic, G. and Manatschal, G., 2009. The final rifting evolution at deep magma-poor passive margins from Iberia-Newfoundland: a new point of view. *International Journal of Earth Sciences*, *98*(7), pp.1581-1597.

Phipps Morgan, J., Parmentier, E.M. and Lin, J., 1987. Mechanisms for the origin of mid-ocean ridge axial topography: Implications for the thermal and mechanical structure of accreting plate boundaries. *Journal of Geophysical Research: Solid Earth*, *92*(B12), pp.12823-12836.

Picazo, S., Cannat, M., Delacour, A., Escartín, J., Rouméjon, S. and Silantyev, S., 2012. Deformation associated with the denudation of mantle-derived rocks at the Mid-Atlantic Ridge 13°–15° N: The role of magmatic injections and hydrothermal alteration. *Geochemistry, Geophysics, Geosystems*, *13*(9).

Picazo, S., Manatschal, G., Cannat, M. and Andréani, M., 2013. Deformation associated to exhumation of serpentinized mantle rocks in a fossil Ocean Continent Transition: The Totalp unit in SE Switzerland. *Lithos*, *175*, pp.255-271.

Planert, L., Flueh, E.R. and Reston, T.J., 2009. Along-and across-axis variations in crustal thickness and structure at the Mid-Atlantic Ridge at 5 S obtained from wide-angle seismic tomography: Implications for ridge segmentation. *Journal of Geophysical Research: Solid Earth*, *114*(B9).

Poliakov, A.N. and Buck, W.R., 1998. Mechanics of stretching elastic-plastic-viscous layers: Applications to slow-spreading mid-ocean ridges. *Geophysical Monograph-American Geophysical Union*, *106*, pp.305-324.

Raleigh, C.B. and Paterson, M.S., 1965. Experimental deformation of serpentinite and its tectonic implications. *Journal of Geophysical Research*, *70*(16), pp.3965-3985.

Reston, T.J., Weinrebe, W., Grevemeyer, I., Flueh, E.R., Mitchell, N.C., Kirstein, L., Kopp, C. and Kopp, H., 2002. A rifted inside corner massif on the Mid-Atlantic Ridge at 5 S. *Earth and Planetary Science Letters*, *200*(3-4), pp.255-269.

Reston, T.J. and McDermott, K.G., 2011. Successive detachment faults and mantle unroofing at magma-poor rifted margins. *Geology*, *39*(11), pp.1071-1074.

Rouméjon, S. and Cannat, M., 2014. Serpentinization of mantle-derived peridotites at mid-ocean ridges: Mesh texture development in the context of tectonic exhumation. *Geochemistry, Geophysics, Geosystems*, *15*(6), pp.2354-2379.

Roumejon, S., Cannat, M., Agrinier, P., Godard, M. and Andreani, M., 2015. Serpentinization and fluid pathways in tectonically exhumed peridotites from the Southwest Indian Ridge (62–65 E). *Journal of Petrology*, *56*(4), pp.703-734.

Sandiford, D., Brune, S., Glerum, A., Naliboff, J. and Whittaker, J.M., 2021. Kinematics of footwall exhumation at oceanic detachment faults: solid-block rotation and apparent unbending. *Geochemistry, Geophysics, Geosystems*, *22*(4), p.e2021GC009681.

Sauter, D. and Cannat, M., 2010. The ultraslow spreading Southwest Indian ridge. *Diversity of hydrothermal systems on slow spreading ocean ridges*, *88*, pp.153-173.

Sauter, D., Cannat, M., Rouméjon, S., Andreani, M., Birot, D., Bronner, A., Brunelli, D., Carlut, J., Delacour, A., Guyader, V. and MacLeod, C.J., 2013. Continuous exhumation of mantle-derived rocks at the Southwest Indian Ridge for 11 million years. *Nature Geoscience*, *6*(4), pp.314-320.

Schlindwein, V. and Schmid, F., 2016. Mid-ocean-ridge seismicity reveals extreme types of ocean lithosphere. *Nature*, *535*(7611), pp.276-279.

Schroeder, T. and John, B.E., 2004. Strain localization on an oceanic detachment fault system, Atlantis Massif, 30 N, Mid-Atlantic Ridge. *Geochemistry, Geophysics, Geosystems*, *5*(11).

Searle, R.C., Cannat, M., Fujioka, K., Mével, C., Fujimoto, H., Bralee, A. and Parson, L., 2003. FUJI Dome: A large detachment fault near 64° E on the very slow-spreading southwest Indian Ridge. *Geochemistry, geophysics, geosystems*, *4*(8).

Seyler, M., Cannat, M. and Mevel, C., 2003. Evidence for major-element heterogeneity in the mantle source of abyssal peridotites from the Southwest Indian Ridge (52 to 68 E). *Geochemistry, Geophysics, Geosystems*, *4*(2).

Small, C. and Sandwell, D.T., 1992. An analysis of ridge axis gravity roughness and spreading rate. *Journal of Geophysical Research: Solid Earth*, *97*(B3), pp.3235-3245.

Sandwell, D.T., Smith, W.H., Gille, S., Jayne, S., Soofi, K. and Coakley, B., 2001. Bathymetry from space: White paper in support of a high-resolution, ocean altimeter mission. *Int. Geophys. Ser*, *69*, pp.1049-1062.

Sauter, D. and Cannat, M., 2010. The ultraslow spreading Southwest Indian ridge. *Diversity of hydrothermal systems on slow spreading ocean ridges*, *88*, pp.153-173.

Schlindwein, V. and Schmid, F., 2016. Mid-ocean-ridge seismicity reveals extreme types of ocean lithosphere. *Nature*, *535*(7611), pp.276-279.

Smith, D.K., Cann, J.R. and Escartín, J., 2006. Widespread active detachment faulting and core complex formation near 13 N on the Mid-Atlantic Ridge. *Nature*, *442*(7101), pp.440-443.

Smith, D.K., Escartín, J., Schouten, H. and Cann, J.R., 2008. Fault rotation and core complex formation: Significant processes in seafloor formation at slow-spreading mid-ocean ridges (Mid-Atlantic Ridge, 13–15 N). *Geochemistry, Geophysics, Geosystems*, *9*(3).

Spencer, J.E., 1999. Geologic continuous casting below continental and deep-sea detachment faults and at the striated extrusion of Sacsayhuaman, Peru. *Geology*, *27*(4), pp.327-330.

Standish, J.J., Dick, H.J., Michael, P.J., Melson, W.G. and O'Hearn, T., 2008. MORB generation beneath the ultraslow spreading Southwest Indian Ridge (9–25 E): Major element chemistry and the importance of process versus source. *Geochemistry, Geophysics, Geosystems*, *9*(5).

Summers, R. and Byerlee, J., 1977, May. A note on the effect of fault gouge composition on the stability of frictional sliding. In *International Journal of Rock Mechanics and Mining Sciences & Geomechanics Abstracts* (Vol. 14, No. 3, pp. 155-160). Pergamon.

Takahashi, M., Uehara, S.I., Mizoguchi, K., Shimizu, I., Okazaki, K. and Masuda, K., 2011. On the transient response of serpentine (antigorite) gouge to stepwise changes in slip velocity under high-temperature conditions. *Journal of Geophysical Research: Solid Earth*, *116*(B10).

Tapponnier, P. and Francheteau, J., 1978. Necking of the lithosphere and the mechanics of slowly accreting plate boundaries. *Journal of Geophysical Research: Solid Earth*, *83*(B8), pp.3955-3970.

Tolstoy, M., Harding, A.J. and Orcutt, J.A., 1993. Crustal thickness on the Mid-Atlantic Ridge: Bull's-eye gravity anomalies and focused accretion. *Science*, *262*(5134), pp.726-729.

Tucholke, B.E. and Lin, J., 1994. A geological model for the structure of ridge segments in slow spreading ocean crust. *Journal of Geophysical Research: Solid Earth*, *99*(B6), pp.11937-11958.

Tucholke, B.E., Lin, J. and Kleinrock, M.C., 1998. Megamullions and mullion structure defining oceanic metamorphic core complexes on the Mid-Atlantic Ridge. *Journal of Geophysical Research: Solid Earth*, *103*(B5), pp.9857-9866.

Tucholke, B.E. and Sibuet, J.C., 2007. Leg 210 synthesis: Tectonic, magmatic, and sedimentary evolution of the Newfoundland-Iberia rift. In *Proceedings of the Ocean Drilling Program, scientific results* (Vol. 210, pp. 1-56). College Station, TX: Ocean Drilling Program.

Tucholke, B.E., Behn, M.D., Buck, W.R. and Lin, J., 2008. Role of melt supply in oceanic detachment faulting and formation of megamullions. *Geology*, *36*(6), pp.455-458.

Yu, Z., Li, J., Niu, X., Rawlinson, N., Ruan, A., Wang, W., Hu, H., Wei, X., Zhang, J. and Liang, Y., 2018. Lithospheric structure and tectonic processes constrained by microearthquake activity at the central ultraslow-spreading Southwest Indian Ridge (49.2° to 50.8° E). *Journal of Geophysical Research: Solid Earth*, *123*(8), pp.6247-6262.

White, R. S., McKenzie, D., & O'Nions, R. K. (1992). Oceanic crustal thickness from seismic measurements and rare earth element inversions. *Journal of Geophysical Research: Solid Earth, 97(B13)*:19683–19715.

Whitmarsh, R.B. and Sawyer, D.S., 1996. The ocean/continent transition beneath the Iberia Abyssal Plain and continental-rifting to seafloor-spreading processes. In *Proceedings-ocean Drilling Program Scientific Results* (pp. 713-736). National Science Foundation.

Whitmarsh, R.B., Manatschal, G. and Minshull, T.A., 2001. Evolution of magma-poor continental margins from rifting to seafloor spreading. *Nature*, *413*(6852), pp.150-154.

Whitney, D.L., Teyssier, C., Rey, P. and Buck, W.R., 2013. Continental and oceanic core complexes. *Bulletin*, *125*(3-4), pp.273-298.

Yu, Z., Li, J., Niu, X., Rawlinson, N., Ruan, A., Wang, W., Hu, H., Wei, X., Zhang, J. and Liang, Y., 2018. Lithospheric structure and tectonic processes constrained by microearthquake activity at the central ultraslow-spreading Southwest Indian Ridge (49.2° to 50.8° E). *Journal of Geophysical Research: Solid Earth*, *123*(8), pp.6247-6262.

Appendix

6.1 Chapter 2: Supplementary Figures (1-7)

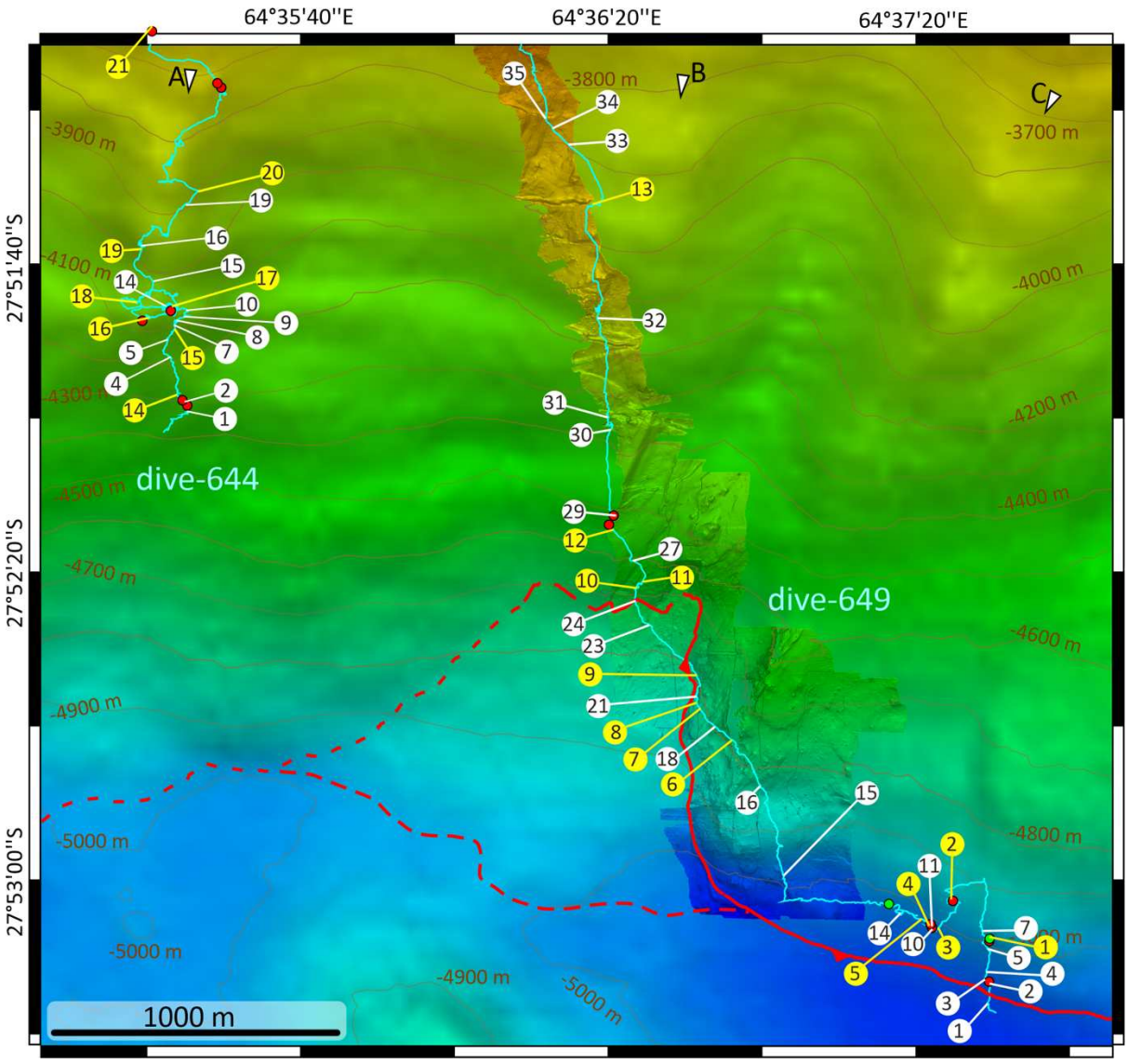

Supplementary Figure 1: *The map (a selected area from map-650, located in Figure 1) displays a detailed microbathymetry along dive-649 overlaid on the shipboard bathymetry. White circles numbered 1 to 35 indicate the locations of photographs in Supplementary Figure 2 for dive 649, and white circles numbered 1 to 19 indicate the locations of photographs for dive 644.*

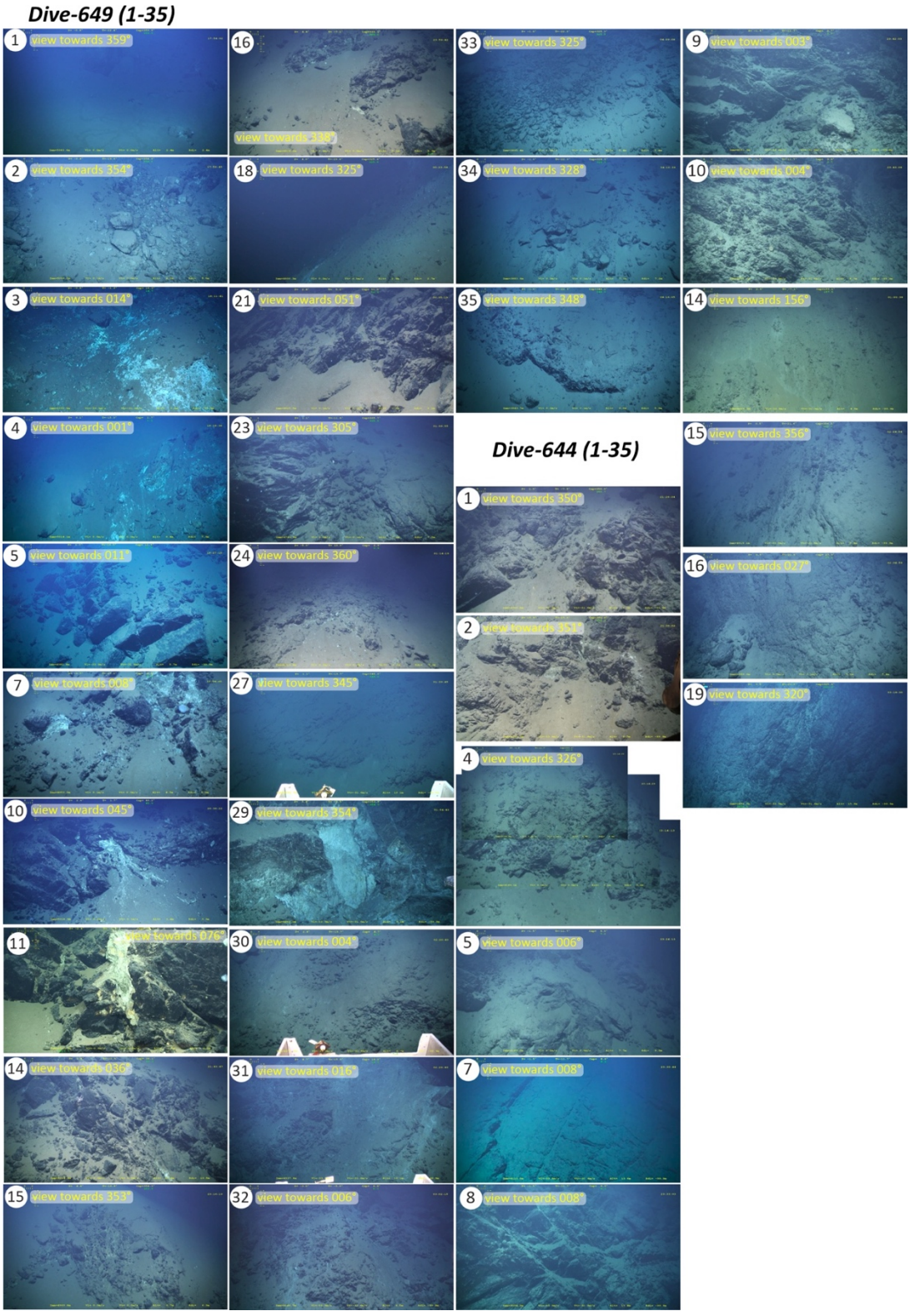

Supplementary Figure 2: *ROV dive video snapshots show outcrop scale structures of the exhumed D1 detachment fault zone along dive 649 and 644. Supplementary Figure 1 displays the locations of these video snapshots.*

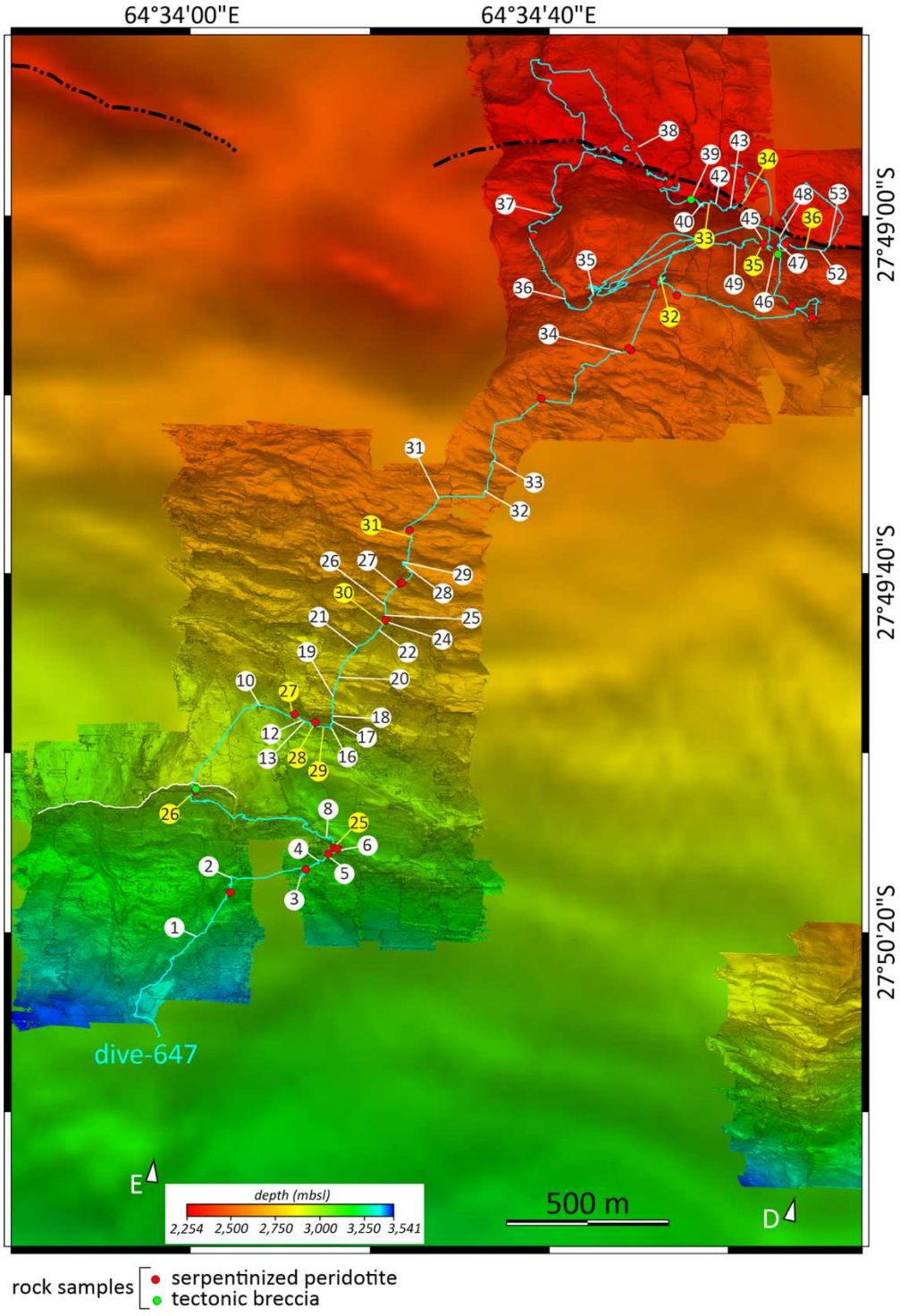

Supplementary Figure 3: *The map (a selected area from map-642, located in Figure 1) displays a detailed microbathymetry along dive-647 overlaid on the shipboard bathymetry. White circles numbered 1 to 53 indicate the locations of video snapshots in Supplementary Figure 4 for dive 647.*

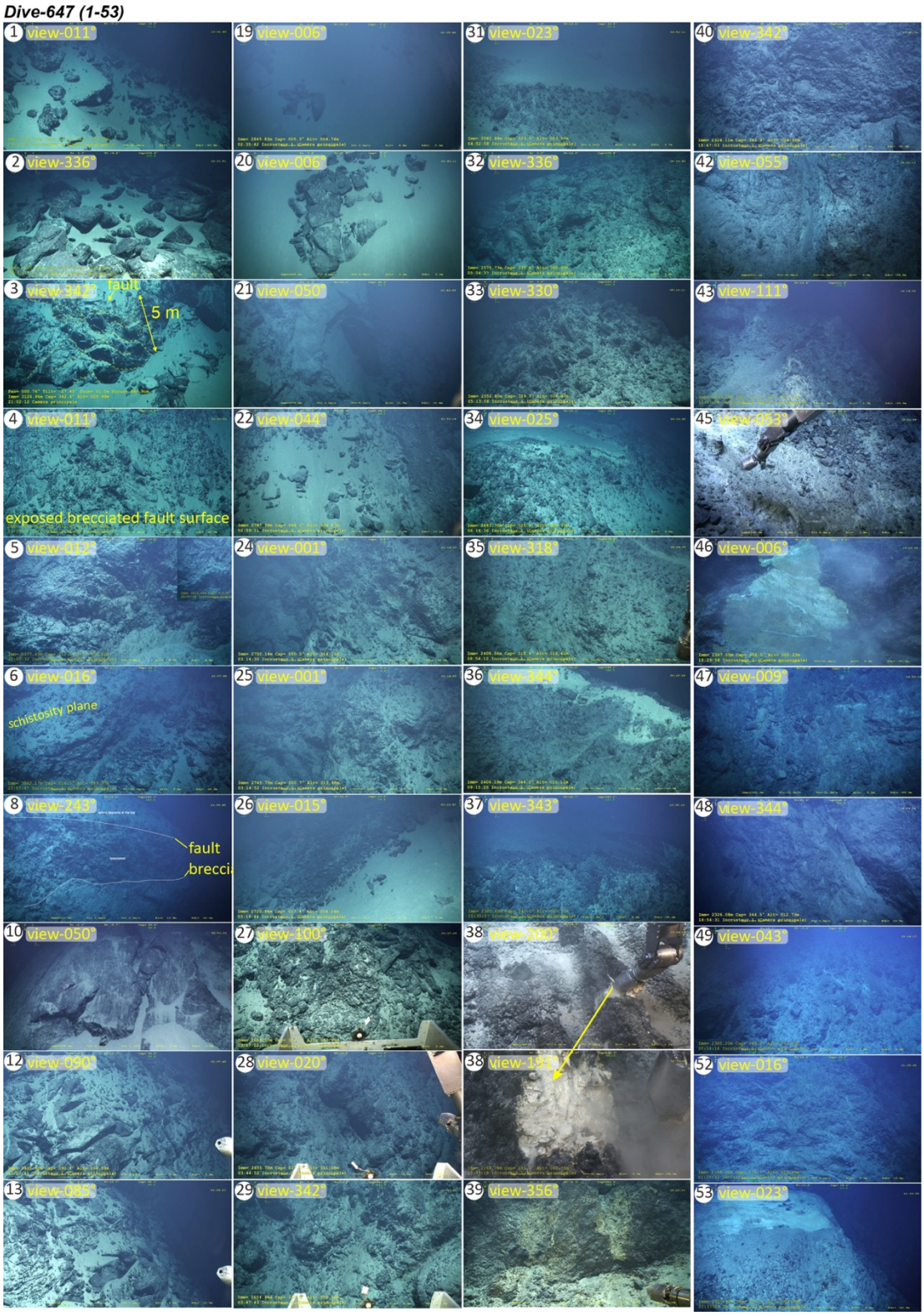

Supplementary Figure 4: *ROV dive video snapshots show outcrop scale structures of the exhumed D1 fault zone (photos 3-8), degraded exposed fault zone (photos 10-29), and degraded breakaway (photos 31-53) along the dive 647. Supplementary Figure 3 displays the locations of these video snapshots.*

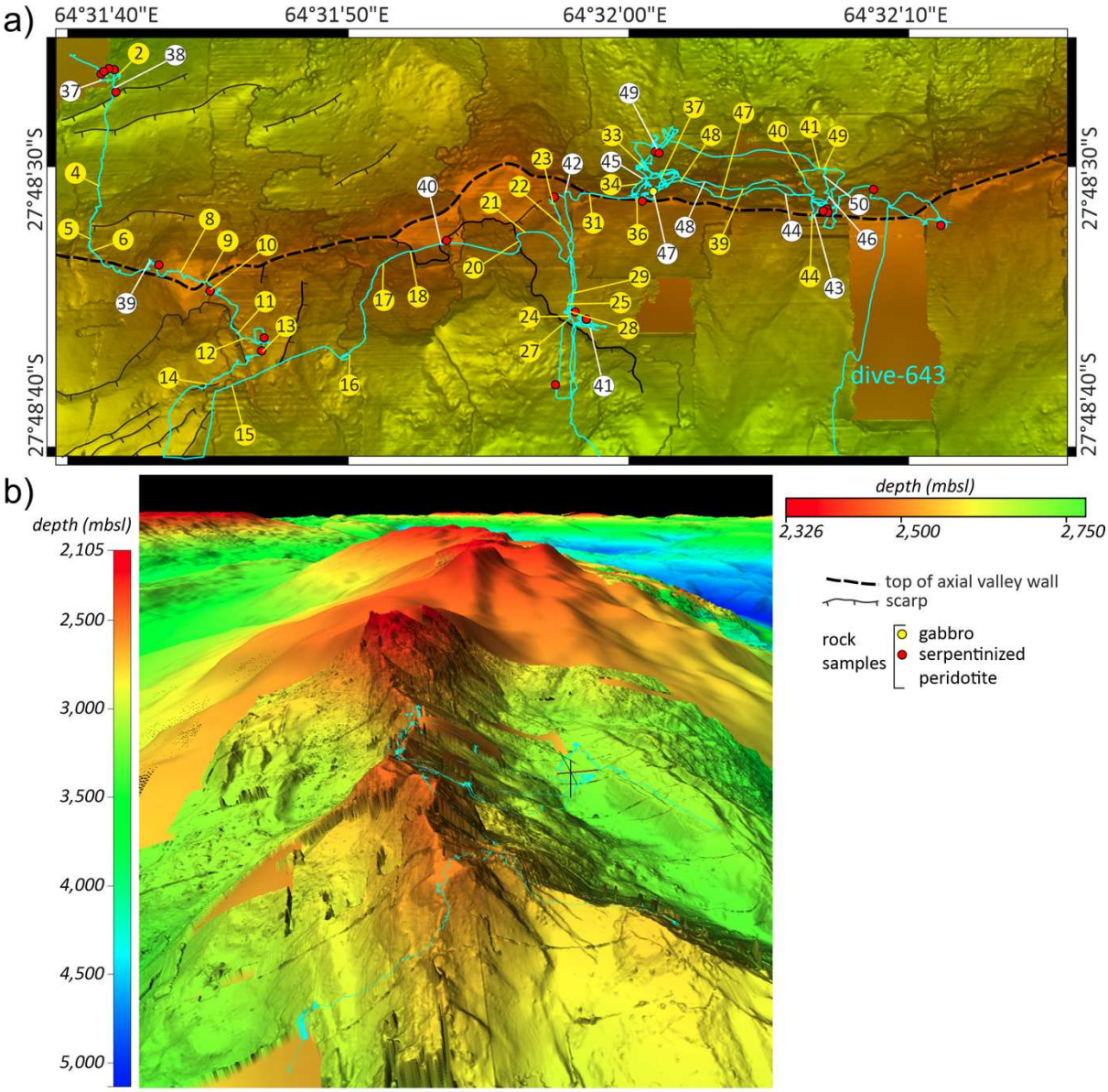

Supplementary Figure 5: *(a) a selected area of map-639 (located in Figure 1) displays a detailed microbathymetry along dive-643. The thick black dashed line represents the top of the axial valley wall, and yellow circles numbered 2 to 49 indicate the locations of video snapshots in supplementary figure 6 for dive 643. (b) 3D perspective view of map a- from west to east, showing the narrow ridge structure along the top of the axial valley wall.*

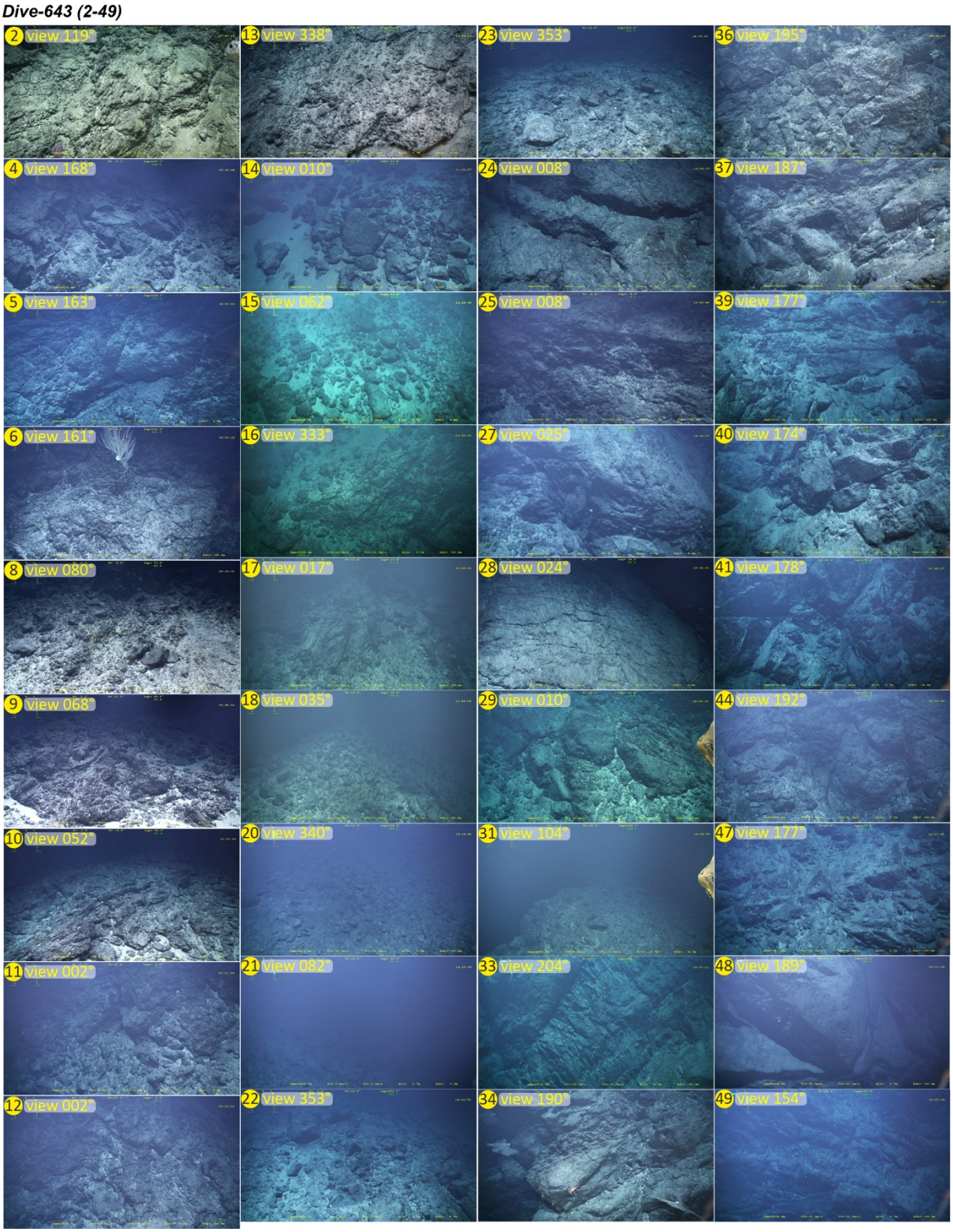

Supplementary Figure 6: *ROV dive video snapshots show outcrop scale structures of the exhumed D2 fault zone (photos 2-49) along dive 643. Supplementary Figure 5 displays the locations of these video snapshots.*

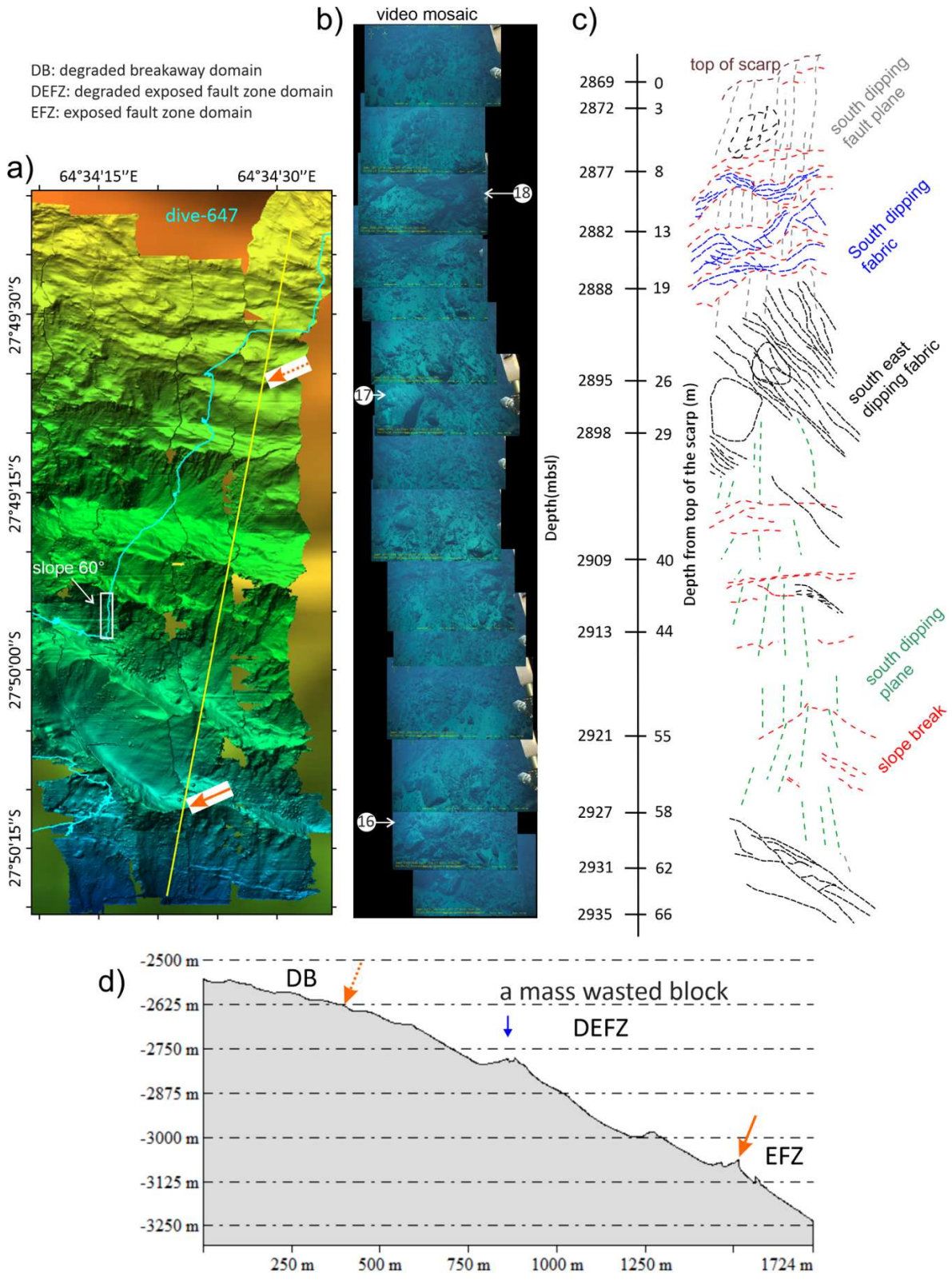

Supplementary Figure 7: *(a) Detailed microbathymetry map (a part of map-647) of the DEFZ. (b) A video mosaic of a 60° south sloping face, located in a-. (c) An interpretative sketch corresponding to the video mosaic in b-, showing different rock fabrics along the ~70 m high section. (d) Topography of the DEFZ, located in a-.*

6.2 Chapter 3: Supplementary Figures (1-4)

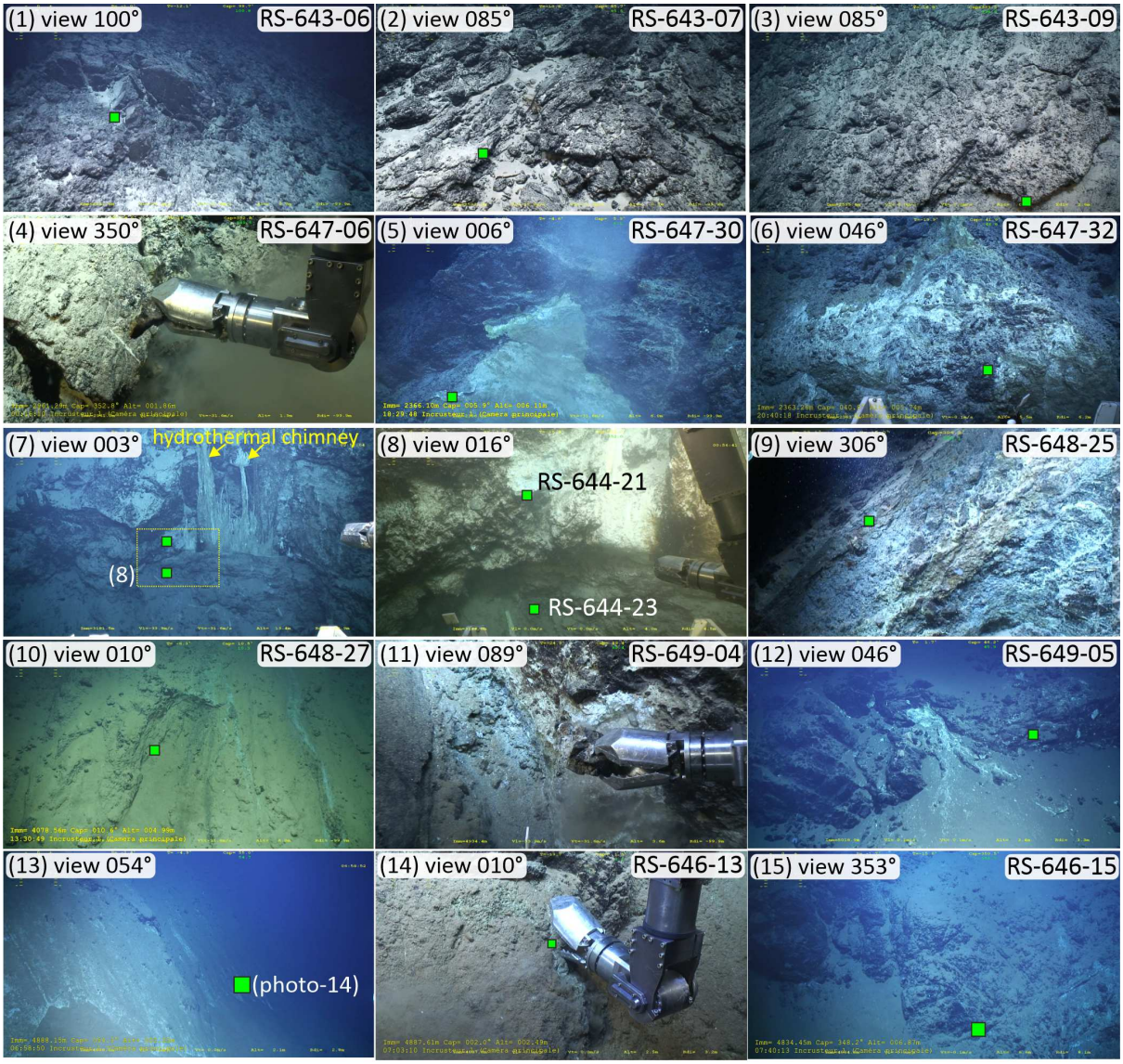

Supplementary Figure 1: *Video snapshots showing outcrop settings of the recovered serpentine microbreccia samples. Outcrop locations correspond to the sample numbers located in Figure 1.*

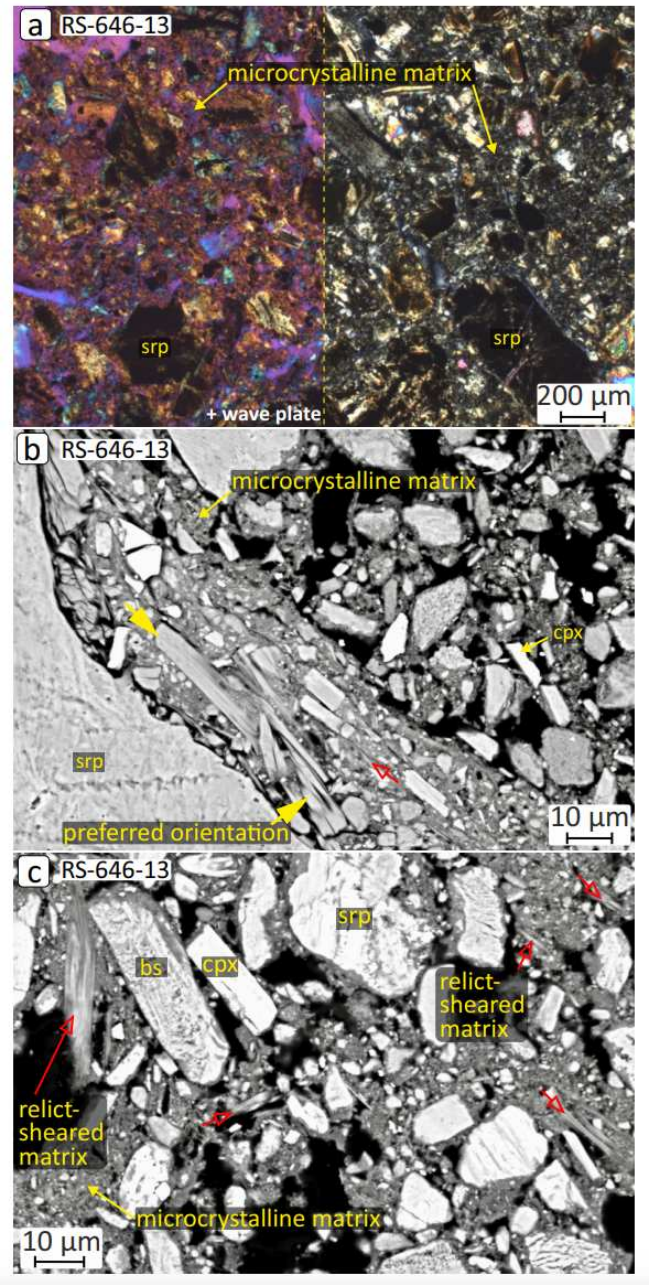

Supplementary Figure 2: *Microphotographs and SEM images of sample RS-646-13 (see Table 1), (a) matrix has no preferred orientation, as seen under cross-polarized light and with a retardation plate. (b) A high-resolution BSE image shows microcrystalline and cataclastic matrix except for protected areas by larger clasts; in the protected areas, the clast shows a shape-preferred orientation, and clasts or relict of the sheared serpentine matrix (Similar-looking chrysotile clasts/fibers can be seen in Figure 10d) is often visible in the cataclastic domains, as shown in (c).*

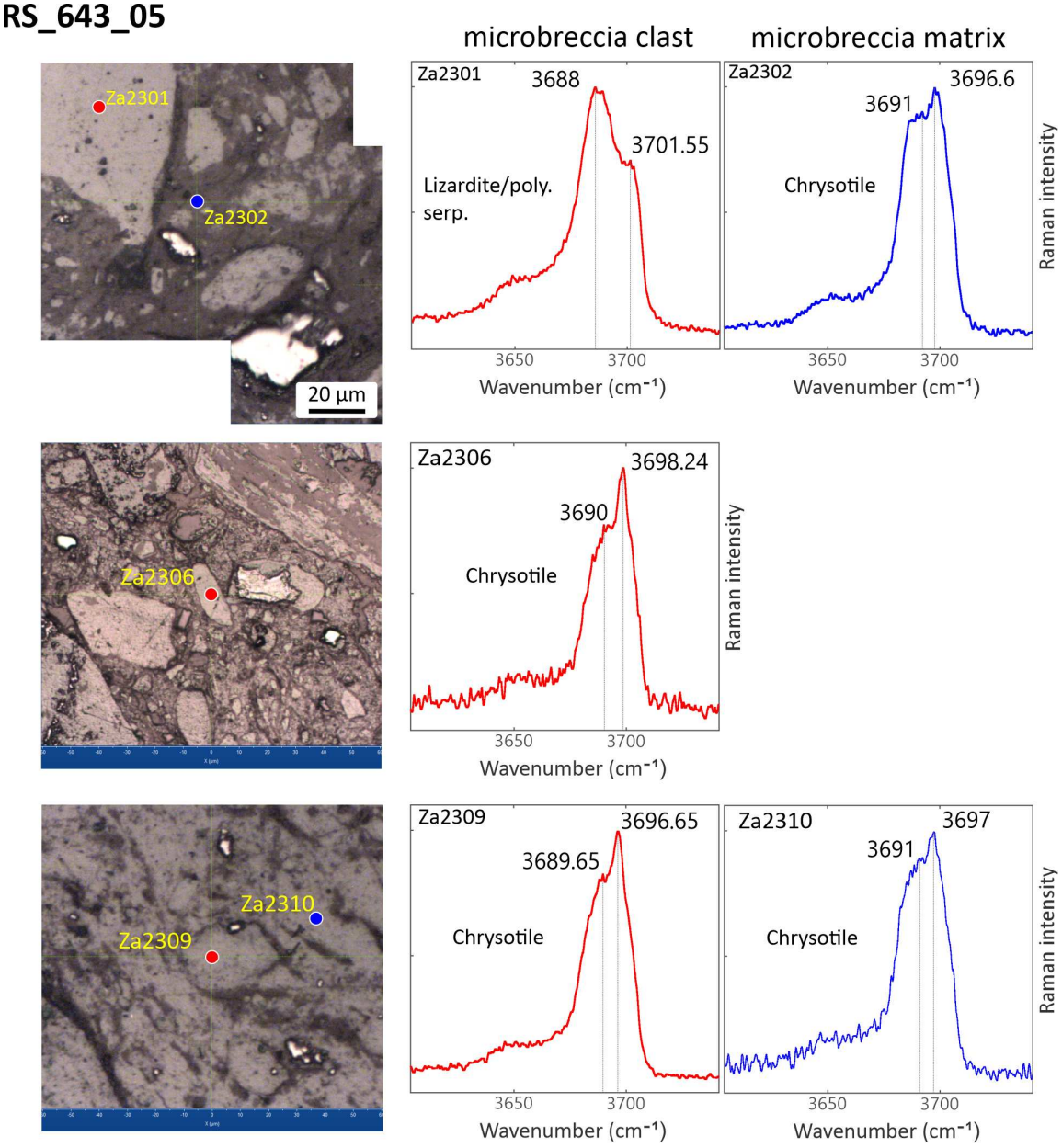

***Supplementary Figure 3**: Representative Raman spot analyses of microbreccia clasts and matrix*

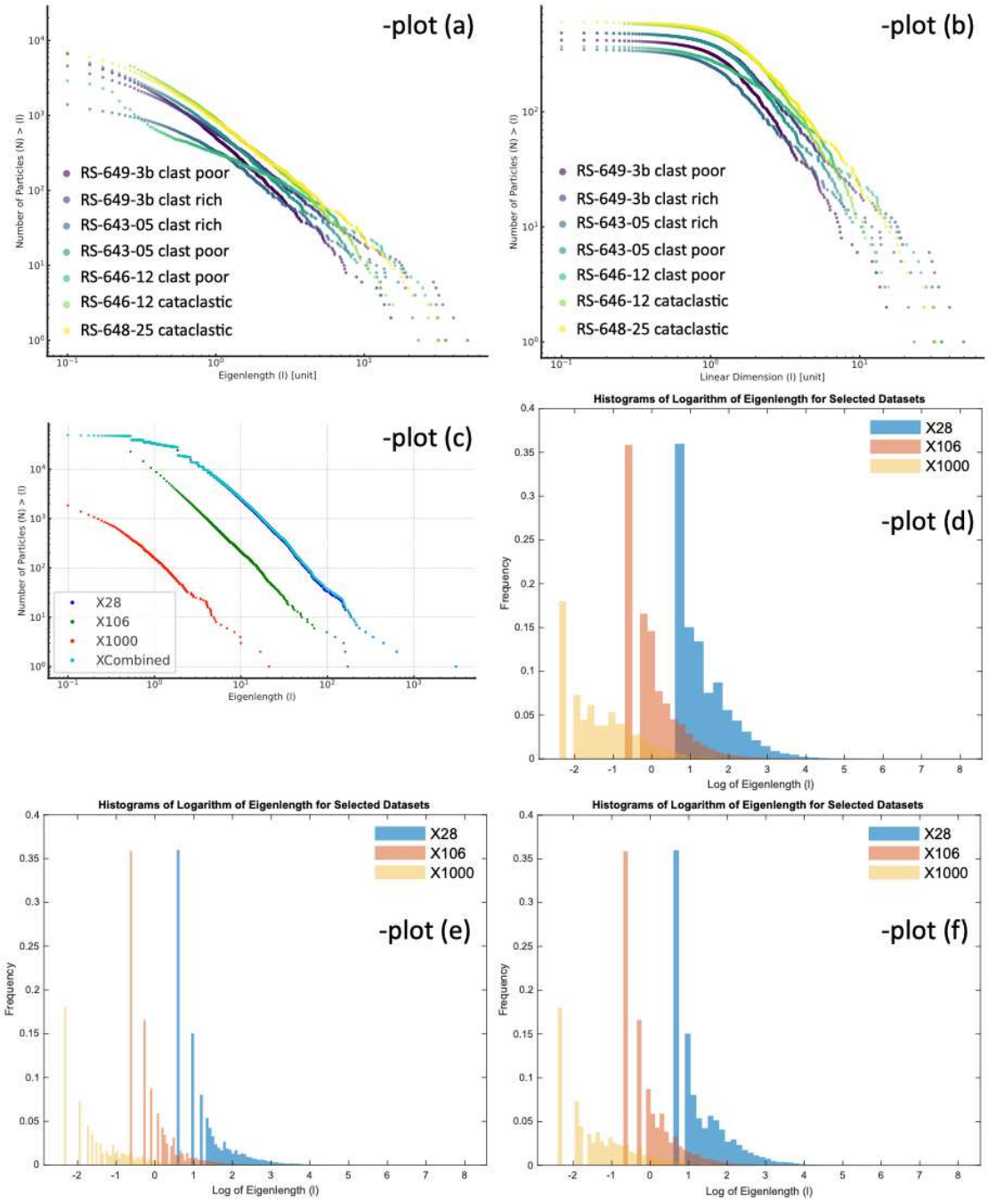

Supplementary Figure 4: *figures a- and b- show the nature of the log-log plot for particle size distribution when different methodologies are applied. The main difference lies in the initial steps, where the script for Plot (a) does a direct ranking before grouping by unique eigenlength values, while the Plot (b) script starts with grouping by unique values and then assigns ranks based on group sizes before transforming these into a descending rank array. Thus, Plot (a) Initially deals with raw, ungrouped data, preserving the original granularity of the data. It allows for detailed analysis at different stages, before and after grouping by unique eigenlength values. On the other*

hand, in plot (b), Initial grouping can potentially lose some details of the data distribution, as it operates on grouped ranks rather than the raw data points. We preferred plot (a). (c) shows when data collected at different magnifications (28X, 106X, 1000X) or at different scales are combined (XCombined), it not only merges the distinct distribution patterns observed in individual datasets at different magnifications but can also lead to a phenomenon where the smaller particles, which are more abundantly captured at higher magnifications, dominate the lower end of the size distribution. This leads to a horizontal tail in the log-log plot, representing a plateau in the number of particles for the smaller size classes similar to plot (b). (d-e-f) shows the effect of traditional binning on particle size distribution when different bin numbers are used. The number of bins for (d) is 30; for (e) is 100 and (f) is 50.

6.3 Chapter 3: Supplementary Table 1

Supplementary Table 1*: The table contains information on the geolocations of all the recovered tectonic microbreccia samples during the ROVSMOOTH cruise and their CNRS-IGSN codes*

Regional tectonic setting	Sample No.:	IGSN code	Latitude	Longitude	depth(mbsl)
D2-detachment fault zone	RS_643_05	CNRS0000001105	27°48.456' S	64°31.696' E	2670
	RS_643_06	CNRS0000001106	27°48.559' S	64°31.721' E	2531
	RS_643_07	CNRS0000001107	27°48.574' S	64°31.752' E	2503
	RS_643_09	CNRS0000001109	27°48.610' S	64°31.782' E	2537
	RS_647_30	CNRS0000001218	27°49.068' S	64°35.087' E	2367
	RS_647_32	CNRS0000001220	27°49.054'S	64°35.065' E	2362
	RS_646_12	CNRS0000001168	27°54.447' S	64°32.571' E	4862
D1-detachment fault zone	RS_647_06	CNRS0000001194	27°50.072' S	64°34.007' E	2972
	RS_649_03	CNRS0000001270	27°53.130' S	64°37.160' E	4962
	RS_649_04	CNRS0000001271	27°53.043' S	64°37.077' E	4934
	RS_649_05	CNRS0000001272	27°53.101' S	64°37.031' E	5018
	RS_648_25	CNRS0000001253	27°50.700' S	64°30.420' E	4078
	RS_648_27	CNRS0000001255	27°50.712' S	64°30.379' E	4127
	RS_648_28	CNRS0000001256	27°50.732' S	64°33.990' E	4143
	RS_644_21	CNRS0000001148	27°50.551' S	64°35.441' E	3184
	RS_644_23	CNRS0000001149	27° 50.552' S	64°35.439' E	3186
Hanging wall of D1-detachment	RS_646_13	CNRS0000001169	27°54.452' S	64°32.593' E	4888
	RS_646_15	CNRS0000001171	27°54.429' S	64°32.525' E	4836